4-2016

Ultra-thin boron nitride films by pulsed laser deposition: Plasma diagnostics, synthesis, and device transport

Nicholas Robert Glavin
Purdue University

PURDUE UNIVERSITY
GRADUATE SCHOOL
Thesis/Dissertation Acceptance

This is to certify that the thesis/dissertation prepared

By Nicholas Robert Glavin

Entitled

Ultra-thin Boron Nitride Films by Pulsed Laser Deposition: Plasma Diagnostics, Synthesis, and Device Transport

For the degree of Doctor of Philosophy

Is approved by the final examining committee:

Timothy S. Fisher
Chair

Andrey A. Voevodin

Ronald G. Reifenberger

Amy Marconnet

To the best of my knowledge and as understood by the student in the Thesis/Dissertation Agreement, Publication Delay, and Certification Disclaimer (Graduate School Form 32), this thesis/dissertation adheres to the provisions of Purdue University's "Policy of Integrity in Research" and the use of copyright material.

Approved by Major Professor(s): Timothy S. Fisher

Approved by: Jay P. Gore 4/19/2016

Head of the Departmental Graduate Program Date

ULTRA-THIN BORON NITRIDE FILMS BY PULSED LASER DEPOSITION: PLASMA DIAGNOSTICS, SYNTHESIS, AND DEVICE TRANSPORT

A Dissertation

Submitted to the Faculty

of

Purdue University

by

Nicholas Robert Glavin

In Partial Fulfillment of the

Requirements for the Degree

of

Doctor of Philosophy

May 2016

Purdue University

West Lafayette, Indiana

For my wonderful and supporting wife Erika, and all of my family and friends.

ACKNOWLEDGEMENTS

The work accompanied in this document is made possible through a host of supporting individuals that I have had the pleasure of knowing and working with. First, I would like to acknowledge the love and support from my parents, family and friends, with whom this process would have not been possible. Their continued encouragement and understanding is a blessing, and I cannot state enough how much of a positive influence they have been on the completion of this program. In particular, my current fiancée and future wife Erika has been the most important person in my life and has been with me through every step of this process. For that, I am eternally grateful.

The Air Force Research Laboratory has been a wonderful place to work, with an impressive and supportive group of people. Dr. Andrey Voevodin went above and beyond as my technical mentor by supporting my technical efforts and constantly challenging me to be a better scientist. Dr. Chris Muratore, Dr. Michael Check, Dr. Michael Mcconney, Mr. Adam Waite, and Dr. Amber Reed have all provided technical support in completion of the projects discussed in this manuscript. Mr. Arthur Safriet and Mr. John Bultman deserve a special place in this section with their design of various one-of-a-kind PLD equipment and constant support. Without these two individuals, I would have been significantly delayed in many of my deadlines, and thanks to their rapid response and problem solving skills, the equipment was operating at optimal efficiency, with new and upgraded capabilities, and was back up and running quickly. I would like

to thank Dr. Michael Jespersen for support in performing much of the X-ray Photoelectron Spectroscopy, as well as Dr. Jianjun Hu for support with the TEM imaging. For those that I have missed from the Air Force Research Laboratory, I apologize, and you all deserve thanks and praise.

Two academic collaborators have helped in completion and evaluation of the device testing discussed in Chapter 6. My many collaborative efforts with Dr. Aman Haque from Penn State University allowed us to build a nanofabricator to accomplish the thermal transport measurements, and his student Mr. Baoming Wang was very helpful in his in-situ TEM knowledge. I would like to thank both of them for accommodating me in the lab in my trips to Penn State University. Also, Dr. Goutam Koley from Univ. of South Carolina aided in the measurement of the fabricated graphene devices, and I much appreciate his expertise and guidance.

I have met many exceptional people in my time at Purdue University, and I would like to especially single out my advisor, Dr. Fisher. He and I had discussed the possibility of a distance learning PhD four years ago, and I know this would not have been possible without his advisement. It was not an easy task, and some pioneering effort was required, but I am very grateful of his accommodation to my studies. Also, many members from Dr. Fisher's group have been helpful in this process, including Dr. Anurag Kumar, Dr. Alfredo Tuesta, Mr. Majed Alfrefae, Dr. Rajib Paul, and others; thank you for welcoming me into the group. I would also like to express thanks to my committee members Dr. Amy Marconnet and Dr. Ron Reifenberger, whom I have had many fruitful discussions. Finally, I would like to acknowledge the many people in the

School of Mechanical Engineering from Purdue University and thank them for the continued support.

TABLE OF CONTENTS

Page

LIST OF TABLES ix

LIST OF FIGURES x

LIST OF SYMBOLS xix

ABSTRACT xxii

CHAPTER 1. INTRODUCTION 1

CHAPTER 2. LITERATURE REVIEW 5

2.1 Introduction to boron nitride 5

2.2 Synthesis routes towards 2D hexagonal boron nitride 10

2.2.1 Mechanical and liquid exfoliation 12

2.2.2 Chemical vapor deposition 13

2.2.3 Physical vapor deposition growth techniques 20

2.2.4 Pulsed laser deposition of thick boron nitride coatings 23

2.3 Plasma spectroscopy approaches in preparation of BN thin films 26

2.4 Dielectric and protective characteristics of 2D boron nitride films and coatings 28

2.4.1 Dielectrics in next generation nanoelectronic devices 28

2.4.2 Vertical tunneling device and behavior 30

2.4.3 Applications for *h*-BN in protective coatings 34

2.5 Thermal transport behavior in 2D and ultra-thin materials 37

2.5.1 In-plane thermal conductivity of ultra-thin boron nitride films 38

2.5.2 Thermal conductance at BN interfaces 48

2.6 Summary of the literature review and objectives of study 52

CHAPTER 3. TEMPORALLY AND SPATIALLY RESOLVED PLASMA SPECTROSCOPY IN PULSED LASER DEPOSITION OF ULTRA-THIN BORON NITRIDE FILMS 55

Page

3.1 Motivation and background info 55
3.2 Experimental methodology 55
3.3 Spatially-dependent plasma behavior 59
3.4 Temporally dependent plasma behavior at the substrate location 63
3.5 Impact of plasma conditions on boron nitride film growth 69
3.6 Summary of mechanisms for ultra-thin BN growth 72
CHAPTER 4. GROWTH OF FEW-LAYER, LARGE AREA HEXAGONAL BORON NITIRDE BY PULSED LASER DEPOSITION 75
4.1 Growth of 2D *h*-BN 75
4.2 Experimental methodology 78
4.3 Impact of the working distance on plasma dynamics 81
4.4 Influence of substrate surface templating for *h*-BN formation 86
4.5 Electrical characterization of crystalline *h*-BN 88
4.6 Summary for *h*-BN growth by PLD 90
CHAPTER 5. AMORPHOUS BORON NITRIDE: A UNIVERSAL, ULTRA-THIN DIELECTRIC FOR TWO-DIMENSIONAL NANOELECTRONICS 92
5.1 Background information on reduced temperature boron nitride growth 92
5.2 Experimental methodology 94
5.3 Demonstration of low temperature processing benefits using PLD 96
5.4 Structural and chemical bonding analysis of substrate agnostic *a*-BN films 98
5.5 Correlation of nucleation and growth behavior of ultra-thin boron nitride with localized electrical performance 101
5.6 Device-scale electronic behavior and properties 104
5.7 Comparison of device-scale electrical properties of current dielectric materials 109
5.8 Summary of low temperature growth of *a*-BN for flexible nanoelectronics 110
CHAPTER 6. TRANSPORT BEHAVIOR IN NANOELECTRONIC BORON NITRIDE FILMS AND DEVICES 112
6.1 Graphene device performance on ultra-thin *h*-BN and *a*-BN films 113
6.1.1 Preparation of boron nitride and graphene for device testing 114

Page

6.1.2 Graphene device performance 116
6.2 Thermal conductivity of pulsed laser deposited boron nitride thin films 119
6.2.1 Formulation of bridge structure and annealing of BN thin films 120
6.2.2 Thermal transport measurements in suspended films....123
6.3 Engineering thermal interface conductances at boron nitride device interfaces 128
6.3.1 Experimental setup for thermal conductance measurements....131
6.3.2 Optimization of thermal conductance at *a*-BN/metal interfaces 133
6.4 Summary of transport in *a*-BN and *h*-BN dielectrics for graphene devices 143
CHAPTER 7. CONCLUSIONS....145
LIST OF REFERENCES....150
APPENDICES
APPENDIX A: Large area *a*-BN growth....164
APPENDIX B: Steady State Plasma Emission Spectra....166
VITA....190
PUBLICATIONS....191

LIST OF TABLES

Table Page

5.1 Comparison of electronic properties of thin film *a*-BN, CVD deposited *h*-BN, single crystal *h*-BN, thermally grown SiO_2, and ultra-thin *a*-BN described in this work.....110

LIST OF FIGURES

Figure Page

2.1 a) Structure of hexagonal and cubic boron nitride, reproduced from [18] with permission from the Royal Society of Chemistry, and b) phase diagrams of the expected crystalline transition between *c*-BN and *h*-BN, reprinted with permission from [17], Copyright 2016 American Chemistry Society. 6

2.2 Representation of the most common boron nitride nanostructures in 2D, 1D, and 0D from [18] with permission from the Royal Society of Chemistry. 8

2.3 a) Identification of 1-4 layer *h*-BN sheets using an optical microscope and a 590 nm yellow filter, reproduced from [19] with permission from John Wiley and Sons Publishing, b) cross sectional TEM images of *h*-BN sheets ranging from 2 to 10 layers reprinted from [20] with permission from Elsevier, c) Raman response of E_{2g} mode in *h*-BN sheets and d) peak position as a function of layers, reproduced from [19] with permission from John Wiley and Sons Publishing. 9

2.4 Representation of growth methodologies for 2D materials (inset image reprinted by permission from Macmillan publishers LTD: Nature [2], copyright 2013), chemical vapor deposition (CVD) from [27] with permission from Annual Reviews, plasma enhanced chemical vapor deposition (PECVD) reprinted from [28] with permission from Elsevier, physical vapor deposition, mechanical and chemical exfoliation methods reproduced from [29] with permission from the Royal Chemistry Society and reprinted with permission from [30], copyright 2015 American Chemical Society, alternative technique for unzipping nanotubes reprinted by permission from Macmillan Publishers Ltd: Nature [31], copyright 2009, and for substrate thermal composition, reprinted from [32] with permission from the Royal Chemistry Society. 11

Figure Page

2.5 a) An optical top-down view of the as-deposited *h*-BN on Si, b) a close-up TEM micrograph of the hexagonal patterning in h-BN, and c) a cross-sectional view of few-layer *h*-BN growth all reprinted with permission from [43] Copyright 2010 American Chemical Society. Similar images are shown in d) e) and f) from Shi et al. reprinted with permission from [42], copyright 2010 American Chemical Society. The last column in Figure 1 shows g) an SEM image of monolayer triangle formation of *h*-BN, and h) optical image of *h*-BN growth on unpolished and i) highly polished copper foil, all from Kim et al., reprinted with permission from [44], copyright 2011 American Chemical Society. 15

2.6 a) Representative schematic of the triangle formation of h-BN, where the Nitrogen termination is the more energetically favorable termination reprinted with permission from Kim et al. [44], copyright 2011 American Chemical Society, and b) the change in *h*-BN initial grain formation shape as a function of nitrogen and boron chemical concentrations in the CVD furnace reprinted with permission from Stehle et al. [50], copyright 2015 American Chemical Society. 17

2.7 Schematic representing the contract in kinetic (PVD) and thermodynamic (CVD) approaches to film growth where *D* is the diffusion rate and *F* is the incoming deposition flux, center image reprinted by permission from Macmillan Publishers Ltd: Nature [62], copyright 2005. 20

2.8 a) Setup of reactive magnetron sputtering for h-BN films, b) cross-sectional TEM image of few-layer growth on Ru (0001), c) XPS analysis of thickness for the different growth conditions, and d) outlining the three-step process for arbitrarily thick h-BN coatings, all reprinted with permission from [68], copyright 2012 American Chemical Society, e) initial h-BN grain formation with window size of 30 μm, and f) a close-up of a similar image with window size of 9 μm, reprinted from [70] with the permission of AIP Publishing. 22

2.9 TEM cross-sectional image of a three layer sequence of growth starting with amorphous BN and translating to the final c-BN film microstructure, reprinted from Zhang et al. [73], with permission from Elsevier. 25

2.10 a) Optical image and b) schematic of an h-BN/graphene/h-BN device, and c) device performance of gain as a function of operation frequency, reprinted from Han et al. [91], © 2011 IEEE. and d) electron mobility enhancement in graphene on *h*-BN at various temperature as compared to graphene on SiO_2, reprinted with permission from Gannett et al. [92] from AIP Publishing. 29

Figure Page

2.11 a) I-V curves generated from C-AFM studies on mono-, bi-, and tri-layer films, as well as b) thicker films up to 31 layers, reprinted from Lee et al. [96] with the permission of AIP Publishing. In addition, device studies using a setup described in c) and d), and resulting electrical resistivity behavior in multiple layers of *h*-BN in e) and f), all reprinted from with permission of Britnell, et al. [83], copyright 2012 American Chemical Society. 32

2.12 a) SEM images of nickel oxidation at 1,100°C without *h*-BN coating and b) with h-BN coating (no oxidation), and c) weight gain percentage at various temperature, showing the change in oxygenation at these conditions reprinted by permission from Macmillan Publishers Ltd: Nat. Commun. [103], copyright 2013, d) *h*-BN capped MoS_2 gas sensor showing 7 day degradation-free behavior, reprinted with permission from [105], © 2015 IEEE, and e) normalized friction as a function of layered thickness of the exfoliated *h*-BN material, reprinted from [106], reprinted with permission from AAAS. 35

2.13 The Bose-Einstein distribution function at various temperatures. 39

2.14 a) Thermal conductivity contributions from the ZA, TA, LA, and ZO modes in graphene as a function of phonon frequency, reprinted from Singh et al. [112] with permission of AIP Publishing, and b) the mode density of these modes and electrons in graphene at various energies up to 2 x k_BT, reprinted with permission from Fisher [116], World Scientific Publishing. 42

2.15 a) Calculated contribution to the ZA, TA, and LA phonons to overall thermal conductivity in 2D monolayer and few-layer boron nitride films, reprinted with permission from [115], copyright 2012 by the American Physical Society and b) Measured 11 and 5 layer *h*-BN thermal conductivity compared to bulk and monolayer *h*-BN, reprinted with permission from [108], copyright 2013 American Chemical Society. 43

2.16 a) Image of *h*-BN film on micro-electro-mechanical heater device, b) IR thermometry image of the heater supporting the h-BN film, c) close-up of one-dimensional heat transport behavior, and d) energy balance schematic of one-dimensional heat flow with and included term for losses to the ambient all, reprinted from [118] with the permission of AIP Publishing. 46

2.17 Temperature profile of thermal IR measurements of 10 and 20 nm *h*-BN along with modeled conductivities, reprinted from [118] with the permission of AIP Publishing. 47

Figure Page

2.18 Interface thermal conductance between graphene and Au/Ti contacts at various graphene thicknesses (n), reprinted with permission from [119], copyright 2010 American Chemical Society.....51

3.1 a) Computer schematic of deposition chamber setup, b) image of target and substrate inside chamber, and c) schematic of inside the deposition chamber. 56

3.2 Image inside growth chamber indicating locations for BN target, substrate and two collection regions used for spectroscopic analysis. 58

3.3 Broad spectra from Region 1 of ablated plasma from a BN target in vacuum and in 50 mTorr nitrogen gas, and the inset images depict plasma emission 600 ns after the laser interacts with the target at the indicated pressures.....60

3.4 Broad spectra from Region 2 of ablated plasma in a) vacuum and b) 50 mTorr. The scale bars for vacuum and 50 mTorr spectra are 10,000 counts and 100,000 counts, respectively. The inset of each graph displays plasma imaging of full spectra as a function of time after the laser pulse for each corresponding pressure condition.....61

3.5 Time of flight intensities for a) B^+ (345.1 nm), b) N* (748.8 nm), c) N^+ (395.5 nm), and d) N_2^+ (391.4 nm) peaks in Region 2 from ablation of a BN target.....65

3.6 Plasma imaging through narrow bandpass filters for a) N* at 746.8 with a 750 nm filter, and b) N^+ at 395.5 nm with a 400 nm filter at 50 mTorr background gas pressure. The dotted line indicates the location of the substrate and numbers indicate locations of the sapphire (0001) samples.....69

3.7 a) BN ratio and thickness of laser ablated films grown on five sapphire [0001] substrates at different distances from the target at 5 mTorr, 50 mTorr, 100 mTorr, and b) schematics of plasma plume compositions at approximately 3000 ns, and c) 6000 ns after laser pulse.....70

3.8 Example of a cross sectional TEM image of an amorphous BN film grown at room temperature on a sapphire substrate at 50 mTorr nitrogen background pressure. The shown film morphology and thickness uniformity extends microscopically over the entire 5 mm length of the sample. 72

4.1 CCD camera image of plasma emission intensities for 3 cm target-to-substrate working distance at various pressures and time after impact of the laser pulse on the target.....83

Figure Page

4.2 a) Representative XPS scan of the B 1s peak as well as the $\pi \rightarrow \pi^*$ satellite shifted 9 eV from the B *1s* peak, and b) a representative scan of the N *1s* peak. 84

4.3 Boron to nitrogen ratio as a function of nitrogen background pressure within the deposition chamber.....85

4.4 a) Raman spectra from polycrystalline *h*-BN on HOPG, and the inset shows the normalized intensity of the E_{2g} shear mode as a function of nitrogen background pressure; b) Cross-sectional TEM image of approximately 2 nm, polycrystalline *h*-BN on HOPG; and c) ultra-smooth amorphous boron nitride on crystalline sapphire (0001).....87

4.5 Conducting AFM I-V curves of eight spots on a 5 mm x 5 mm BN-coated HOPG sample, and the inset shows the average value of the low-biased tunneling curve. 90

5.1 a) Schematic representation of the pulsed laser deposition setup, b) *a*-BN grown on a 3 inch SiO2/Si wafer and cross-sectional TEM of *a*-BN on Al_2O_3 showing large area uniformity, c) ultra-thin a-BN applied to diverse substrates, including: (1. Kapton™, 2. PDMS, 3. Willow glass™, 4. Polyethylene terephthalate (PET), 5. Carbon cloth, 6. SiO_2/Si, 7. Al_2O_3, 8. Copper foil, 9. HOPG, 10. SiC, 11. Patterned SiO_2, 12. E-beam evaporated chromium, 13. Nickel foil, 14. Magnetron sputtered tungsten) and d) device construct with directly grown *a*-BN and PVD MoS_2 on flexible PET substrate with magnetron sputtered tungsten contacts. 97

5.2 Cross-sectional TEM imaging of amorphous boron nitride growth from room temperature to 200 °C on metal, insulating, 2D material, and flexible substrates (with gold cap layers on top of BN), dotted lines are to aid the reader in identifying *a*-BN material location. Larger area cross-sectional TEMs can be viewed in Figure A.1.....99

5.3 XPS B *1s* and N *1s* regions of < 5 nm a-BN films grown at < 200°C on four representative substrates including magnetron sputtered tungsten (W), 2D PVD MoS_2, Al_2O_3, and PDMS.....100

5.4 a) C-AFM I-V curves of *a*-BN on tungsten and corresponding number of laser pulses, b) C-AFM image and schematic of initial growth stages at 2 pulses, and c) C-AFM image and schematic of cohesive *a*-BN film at critical thickness of 20 pulses.....103

Figure Page

5.5 a) Electrical resistance measurements of continuous *a*-BN films on metallic tungsten at different thicknesses using 40 μm x 40 μm Ti/Au contacts shown in the inset, b) cross-sectional image of the 6 nm *a*-BN device, c) dielectric constant measurements for 6 nm and 16.5 nm films, and d) MoS_2 raman signature of as-deposited (black) and laser annealed (blue) in BN/MoS_2/BN heterostructured stack. 105

5.6 Weibull distribution of device dielectric breakdown measurements on 2.2 nm (30 pulse) *a*-BN sample using Au/Ti contact pads of 40 μm x 40 μm in area. 106

5.7 Bandgap measurement of 8 nm ultra-thin BN on Sapphire (0001) by UV-Vis spectroscopy. 108

6.1 Typical *h*-BN/graphene/*h*-BN "sandwich" device setup, with *h*-BN set up as a smooth, lattice-matched substrate template for graphene devices and as a gate dielectric material. 113

6.2 a) AFM topographical image of annealed BN showing grains with diameter varying from 20 to 40 nm, b) Raman spectra of graphene/BN (red) showing overlap of BN E_{2g} shear mode peak and graphene D peak and *h*-BN film showing E_{2g} peak, and c) SEM image of graphene/BN showing BN grains. 115

6.3 a) Graphene device setup on boron nitride thin films, and b) a representative I-V curve of graphene on 5 nm *a*-BN films, revealing poor performance of the graphene device and observable Dirac point shift. 117

6.4 Graphene device performance on 5 nm *h*-BN compared to traditional SiO_2, with a) a representative IV curve of drain current and back gate voltage, b) hole mobility of graphene on *h*-BN and SiO_2, and c) electron mobility of graphene on the 5 nm *h*-BN. 119

6.5 a) Material stack for freestanding films with initial PLD of BN film grown on SiO_2, then a titanium capping protection layer, followed by a patterned photoresist, b) then the specimen is etched and photoresist removed and c) micromechanically cleaved bridge structure transferred to nanomanipulation stage, d) securing the ends of the BN/Ti specimen and e) removal of the Ti layer for final boron nitride freestanding structure. 121

6.6 TEM images of a) freestanding amorphous BN specimen at room temperature (b) first observed crystallization change at 625 °C and c) corresponding diffraction pattern, d) image of annealed specimen at 650 °C (e) corresponding diffraction pattern showing amorphous to nanocrystalline phase transformation (f) high magnification image showing growth of a crystallite in the amorphous matrix. 123

Figure Page

6.7 Thermal boundary layer profile from near the micro-heater surface to calculate the s term in the heat transfer coefficient, used by permission from [118] and AIP Publishing. 125

6.8 IR temperature measurements of *a*-BN and *h*-BN suspended thin films along with derived thermal conductivity. 127

6.9 TEM images of *h*-BN directly grown by CVD on Al_2O_3 at a) 1000°C and 25 nm thickness, b) 400°C and 7 nm thickness, c) 250°C and 2 nm thickness, d) 250°c and 2 nm thickness followed by post-annealing at 1000°C, and e) table of effective interface thermal conductance measurements of the films grown on Si (111) and Al_2O_3 (0001), all reprinted by permission from [38]. 130

6.10 a) TDTR Device setup for *a*-BN/metal contact thermal conductance evaluation, and b) XPS setup for chemical analysis of BN/metal interface.....133

6.11 Interface conductance TDTR measurements of various metals and metal deposition processes, where “LE” designates low energy, and “HE” designates high energy. 135

6.12 XPS scans of B*1s* and N*1s* areas of the spectra of as-deposited *a*-BN and chemical signature of *a*-BN under a 5 nm Au film deposited by HIPIMS. 138

6.13 XPS spectra of DC and HIPIMS Ti coated *a*-BN films. 140

6.14 XPS Spectra of DC and HIPIMS Al coated *a*-BN films. 141

6.15 The impact of observed *a*-BN surface oxidation to the interface thermal conductance of metal/*a*-BN interfaces with various thin (5 nm) metal contacts and at the performed deposition conditions. 143

Appendix Figure

A.1 Cross-sectional SEM imaging confirming thicknesses and large area uniformity for various BN samples of a) *a*-BN on copper foil, b) BN on W (30 pulses), c) Gold on *a*-BN on PET, d) Gold on *a*-BN on PDMS, and e) Gold/Titanium contacts on BN grown on magnetron sputtered tungsten on an SiO_2 wafer. A higher resolution image of this sample labeled e) was used to verify the thickness of *a*-BN at 16.47 nm for dielectric measurements. 164

A.2 Five topographical AFM images of ultra-thin (< 5 nm) *a*-BN grown on Al_2O_3 at 5 mm separation distances on a 30 mm diameter sample setup. 165

B.1 Collected spectra centered at 300 nm at vacuum conditions.....166

Appendix Figure Page

B.2 Collected spectra centered at 300 nm at 50 mTorr N_2 gas 166

B.3 Collected spectra centered at 350 nm at vacuum conditions.....167

B.4 Collected spectra centered at 350 nm at 50 mTorr N_2 gas 167

B.5 Collected spectra centered at 365 nm at vacuum conditions.....168

B.6 Collected spectra centered at 365 nm at 50 mTorr N_2 gas 168

B.7 Collected spectra centered at 400 nm at vacuum conditions.....169

B.8 Collected spectra centered at 400 nm at 50 mTorr N_2 gas 169

B.9 Collected spectra centered at 400 nm at vacuum conditions (high resolution).....170

B.10 Collected spectra centered at 400 nm at 50 mTorr N_2 gas (high resolution) 170

B.11 Collected spectra centered at 425 nm at vacuum conditions.....171

B.12 Collected spectra centered at 425 nm at 50 mTorr N_2 gas 171

B.13 Collected spectra centered at 450 nm at vacuum conditions.....172

B.14 Collected spectra centered at 450 nm at 50 mTorr N_2 gas 172

B.15 Collected spectra centered at 500 nm at vacuum conditions.....173

B.16 Collected spectra centered at 500 nm at 50 mTorr N_2 gas 173

B.17 Collected spectra centered at 525 nm at vacuum conditions.....174

B.18 Collected spectra centered at 500 nm at 50 mTorr N_2 gas 174

B.19 Collected spectra centered at 550 nm at vacuum conditions.....175

B.20 Collected spectra centered at 550 nm at 50 mTorr N_2 gas 175

B.21 Collected spectra centered at 575 nm at vacuum conditions.....176

B.22 Collected spectra centered at 575 nm at 50 mTorr N_2 gas 176

B.23 Collected spectra centered at 600 nm at vacuum conditions.....177

B.24 Collected spectra centered at 600 nm at 50 mTorr N_2 gas 177

B.25 Collected spectra centered at 625 nm at vacuum conditions.....178

Appendix Figure Page

B.26 Collected spectra centered at 625 nm at 50 mTorr N_2 gas 178

B.27 Collected spectra centered at 650 nm at vacuum conditions.....179

B.28 Collected spectra centered at 650 nm at 50 mTorr N_2 gas 179

B.29 Collected spectra centered at 675 nm at vacuum conditions.....180

B.30 Collected spectra centered at 675 nm at 50 mTorr N_2 gas 180

B.31 Collected spectra centered at 675 nm at vacuum conditions (high resolution).....181

B.32 Collected spectra centered at 675 nm at 50 mTorr N_2 gas (high resolution) 181

B.33 Collected spectra centered at 700 nm at vacuum conditions.....182

B.34 Collected spectra centered at 700 nm at 50 mTorr N_2 gas 182

B.35 Collected spectra centered at 725 nm at vacuum conditions.....183

B.36 Collected spectra centered at 725 nm at 50 mTorr N_2 gas 183

B.37 Collected spectra centered at 750 nm at vacuum conditions.....184

B.38 Collected spectra centered at 750 nm at 50 mTorr N_2 gas 184

B.39 Collected spectra centered at 775 nm at vacuum conditions.....185

B.40 Collected spectra centered at 725 nm at 50 mTorr N_2 gas 185

B.41 Collected spectra centered at 800 nm at vacuum conditions.....186

B.42 Collected spectra centered at 800 nm at 50 mTorr N_2 gas 186

B.43 Collected spectra centered at 825 nm at vacuum conditions.....187

B.44 Collected spectra centered at 825 nm at 50 mTorr N_2 gas 187

B.45 Collected spectra centered at 850 nm at vacuum conditions.....188

B.46 Collected spectra centered at 850 nm at 50 mTorr N_2 gas 188

B.47 Collected spectra centered at 875 nm at vacuum conditions.....189

B.48 Collected spectra centered at 875 nm at 50 mTorr N_2 gas 189

LIST OF SYMBOLS

A	Area, m^2
A_{eff}	Effective contact area, m^2
C_{ox}	Oxide capacitance per unit area, F cm^{-2}
d	Film thickness, m
D	Dimensions, *i. e.* 1, 2 or 3
f	Pump laser frequency, MHz
$f°_{BE}$	Bose-Eisenstein phonon energy distribution
G	Interface thermal conductance, MW m^{-2} K^{-1}
G_{eff}	Effective thermal conductance, MW m^{-2} K^{-1}
g_m	Transconductance, A/V
h	Planck's constant, 4.135668 x 10^{-15} eVs
$\hbar$	Reduced Planck's constant, $h/2\pi$
h_c	Convective heat transfer coefficient, W m^{-2} K^{-1}
h_T	Heat transfer coefficient, W m^{-2} K^{-1}
I	Current, A
k	Thermal conductivity, W m^{-1} K^{-1}
$K(\omega)$	Phonon dispersion relation in K-space as a function of frequency

k_B	Boltzmann constant, 8.617332 * 10^{-5} eV/K
L	Phonon mean free path in nanocrystalline materials, m
l	Thermal penetration depth for TDTR measurements, m
L_c	Channel length, m
l_h	Thermal healing length, m
m	Mass, g
m^*	Electron effective mass, g
M_{2D}	Mode density in a two dimensional material, number of modes per unit volume
P	Convection heat transfer perimeter, m
q_e	Magnitude of electron charge, 1.60217 *10^{-19} J/eV
T	Temperature, K
T_∞	Temperature of the surroundings, K
V	Voltage, V
v_g	Phonon group velocity, m/s
$v_{g,avg}$	Average phonon group velocity, m/s
W_c	Channel width, m
Z	Acoustic impedance
α	Thermal diffusivity, $mm^2\ s^{-1}$
ε	Emissivity, 0.8 for *h*-BN
μ	mass density of the spring in the Acoustic Mismatch Model, mass per volume
μ_{FET}	Graphene FET mobility, $cm^2\ V^{-1}\ s^{-1}$

ν_m	Debye frequency, Hz
σ	Stefan Boltzmann constant, $5.670373 * 10^{-8}$ W m^{-2} K^{-4}
$\tau^{-1}_{bound.}$	Scattering rate contribution due to boundary phonon scattering
τ^{-1}_{eff}	Effective scattering rate, s^{-1}
$\tau^{-1}_{iso.}$	Scattering rate contribution due to isotope scattering, s^{-1}
$\tau^{-1}_{U,p-p}$	Scattering rate contribution due to Umklapp phonon-phonon processes, s^{-1}
Φ_b	Barrier height, eV
Θ_D	Debye Temperature, K
ω	Phonon frequency, Hz

ABSTRACT

Glavin, Nicholas R. Ph.D., Purdue University, May 2016. Ultra-thin Boron Nitride Films Produced by Pulsed Laser Deposition: Plasma Diagnostics, Synthesis, and Device Transport. Major Professor: Dr. Timothy Fisher, School of Mechanical Engineering.

This work describes, for the first time, a pulsed laser deposition (PLD) technique for growth of large area, stoichiometric ultra-thin hexagonal and amorphous boron nitride for next generation 2D material electronics. The growth of boron nitride, in this case, is driven by the high kinetic energies and chemical reactivities of the condensing species formed from physical vapor deposition (PVD) processes, which can facilitate growth over large areas and at reduced substrate temperatures. The use of optical emission spectroscopy during plasma growth provides insight into chemistry, kinetic energies, time of flight data, and spatial distributions within a PVD plasma plume ablated from a boron nitride (BN) target by a KrF laser at different pressures of nitrogen gas. Time resolved spectroscopy and wavelength specific imaging were used to identify and track atomic neutral and ionized species including B^+, B*, N^+, N*, and molecular species including N_2*, N_2^+, and BN. Formation and decay of these species formed both from ablation of the target and from interactions with the background gas were investigated and provided insights into fundamental growth mechanisms of continuous, amorphous boron nitride thin films. The correlation of the plasma diagnostic results with film chemical composition and thickness uniformity studies helped to identify that a predominant

mechanism for BN film formation is condensation surface recombination of boron ions and neutral atomic nitrogen species. These species arrive nearly simultaneously to the substrate location and BN formation occurs microseconds before arrival of majority of N^+ ions generated by plume collisions with background molecular nitrogen. The energetic nature and extended dwelling time of incident N^+ ions at the substrate location was found to negatively impact resulting BN film stoichiometry and thickness. Growth of stoichiometric films was optimized at enriched concentrations of ionized boron and neutral atomic nitrogen in plasma near the condensation surface, providing few nanometer thick films with 1:1 BN stoichiometry and good thicknesses uniformity over macroscopic areas.

By selectively choosing substrates that can facilitate epitaxial hexagonal growth, synthesis of ultra-thin, few-layer hexagonal boron nitride (*h*-BN) was possible using the PLD technique. This process permits growth of thin, polycrystalline *h*-BN at 700 °C, a much lower temperature than that required by traditional growth methods, most typically chemical vapor deposition (CVD). Analysis of the as-deposited films reveals epitaxial-like growth on the nearly lattice matched HOPG substrate, resulting in a nanocrystalline *h*-BN film with grain sizes of approximately 5 nm, and amorphous BN (*a*-BN) on the non-lattice matched sapphire substrates, both with film thicknesses of 1.5-2 nm. Stoichiometric films with boron-to-nitrogen ratios of unity were achieved by adjusting the background pressure within the deposition chamber and the distance between the target and substrate. Conductive atomic force microscopy (C-AFM) measurements of electron tunneling behavior depict a uniform The reduction in deposition temperature and formation of stoichiometric, large-area *h*-BN films by PLD provides a process that is

easily scaled-up for two-dimensional dielectric material synthesis and also presents a possibility to produce very thin and uniform *a*-BN.

The deposited amorphous boron nitride *a*-BN is a very intriguing structural allotrope of boron nitride, as the material in the ultra-thin form has yet to be investigated, especially with regard to the potential use in nanoelectronics. The material can be synthesized in thicknesses from 2 to 17 nm, described in this work, and may offer enhanced properties as a dielectric in flexible electronics. The material is demonstrated to be universal in structure and stoichiometric chemistry on numerous substrates including flexible PDMS, amorphous SiO_2, crystalline Al_2O_3, other 2D materials including graphene, 2D MoS_2, and conducting metals and metal foils. The versatile, large area pulsed laser deposition growth technique is performed at temperatures less than 200°C and without modifying processing conditions, allowing for seamless integration into 2D device architectures. A device-scale dielectric constant of 5.9 ± 0.65 at 1 kHz, breakdown voltage of 9.8 ± 1.0 MV/cm, and bandgap of 4.5 eV were measured for various thicknesses of the ultra-thin *a*-BN material, representing values higher than previously reported chemical vapor deposited (CVD) *h*-BN and nearing single crystal *h*-BN.

Finally, little is known as to how the degree of crystallinity, surface roughness, and other properties of the dielectric will impact 2D device performance. Graphene device performance including electron and hole mobility, as well as Dirac point, were substantially influenced by the presence of the dielectric material. In few-layer graphene films transferred to traditional SiO_2 substrates, as well as SiO_2 substrates coated with 5 nm *a*-BN, the transport properties in graphene were significantly suppressed in

comparison to the annealed nanocrystalline *h*-BN, presumably due to increased scattering events. The weak van der Waals terminated *h*-BN films suppressed these scattering events from the presence of high energy surface optical phonon modes and lack of Coulombic scattering. A two-fold improvement in average hole mobility and a Dirac point shift from > 60V to approximately 3.5V indicate that the influence of hexagonal crystallinity in the channel material is vital for high performance graphene devices.

As the speed of graphene devices continually pushes the limit of 2D physics, thermal management is a constant barrier to overcome in considering reliability and failure mechanisms in high speed RF devices. The dielectric material in the short channel devices will play a critical role in mitigating heat from the semiconductor material. Two mechanisms being considered for hot spot mitigation involve incorporating a high in-plane thermal conductivity material for 2D heat spreading (2D *h*-BN), and ensuring good thermal conductance at interfaces to encourage 3D heat dissipation (covalently terminated *a*-BN). Thermal conductivity measurements of as–deposited *a*-BN and annealed *h*-BN were made possible by a nanofabricated freestanding bridge configuration, where the enhanced surface diffusion allowed for 100 nm *h*-BN grain formation at 600°C. Infrared microscopy and a one-dimensional heat transport model were used to measure both structural configurations of *a*-BN and *h*-BN to have in-plane thermal conductivities of 5 W m^{-1} K^{-1} and 65 W m^{-1} K^{-1}, respectively. In addition to in-plane transport, the dielectric/metal interface will be especially important when it comes to 3D heat dissipation. In this study, the amorphous boron nitride was investigated as a means to enhance thermal conductance at dielectric/metal interfaces. Due to the atomic-scale roughness, covalently terminated bonding, as well as the high Debye

temperature of BN, engineering a high contact thermal conductance is possible using different deposition techniques as a function of metal Debye temperatures. A high thermal conductance of 130 MW m^{-2} K^{-1} was measured on an *a*-BN/aluminum metal interface when the Al was prepared under the proper DC conditions, with a reduction in almost 50% when prepared in sub-optimum conditions using high power impulse magnetron sputtering (HIPIMS).

The dissertation outlines a pathway for a new preparation method for 2D *h*-BN and ultra-thin *a*-BN that has many advantages over traditional dielectric processing. By understanding the fundamental growth mechanisms within the plasma, a knowledge of what is required to formulate high quality electronic materials of only a few nanometers thickness can be achieved. The high temperature *h*-BN and low temperature *a*-BN synthesis described herein represents a step towards commercial routes to high quality dielectric materials for 2D devices. The synthesized films exhibit desirable dielectric and thermal management qualities, as demonstrated in the later sections of this manuscript, that would make for implementation in device structures an exciting possibility.

CHAPTER 1. INTRODUCTION

The nano-scale miniaturization of electronic components has led to recent interest in atomically thin two-dimensional (2D) materials for the possibility of exploiting the advantageous material properties that arise at the atomistic-scale. Unique physical phenomena have been observed upon restricting the material thickness and confining the lattice structure to two-dimensions. Properties including heat transport, energy storage, and electronic behavior can begin to deviate from the bulk crystal as a result of a high surface area to volume ratio and the confinement of energy carriers (electrons and phonons) in the two-dimensional plane. The typical lattice structure within these materials is composed of strong covalent bonds in the plane and weak van der Waals bonds between the planes, resulting in further enhancement of the intra-layer atomic interactions while inhibiting similar interactions in the inter-layer [1-3]. The surge in research in these materials has led to the possibility of revolutionizing electronic devices [4, 5], biological systems [6], energy transport and storage [7-10], and a host of other applications [11, 12].

An entire suite of materials with different band structures [13], material stabilities, carrier mobilities, optoelectronic responses, and many other unique properties have been identified to exist in the two-dimensional form. For the interest of electronic materials, a combination of conducting (graphene), semiconducting (MoS_2 and other transition metal dichalcogenides), and insulating (boron nitride) 2D structures have been explored as a

route to construction of functional, flexible, and tunable devices from their heterostructures [2, 4, 14]. Issues in 2D material integration regarding material compatibility, scale-up, lifetime, and repeatable performance need to be addressed for realization of these materials in real-world applications. In addition, these devices and prototypes are currently limited by the lack of reliable, versatile synthesis techniques for creating complex heterostructures at the industrial-scale and not simply in a laboratory environment.

A new approach towards commercial synthesis of 2D hexagonal-boron nitride (*h*-BN), as well as ultra-thin amorphous-boron nitride (*a*-BN) by pulsed laser deposition (PLD) is discussed in this dissertation. Plasma emission studies during laser ablation of boron nitride enhanced the understanding of appropriate growth conditions and mechanisms required for stoichiometric, large area BN nucleation and growth. This was achieved by in-situ recording and adjusting pulsed plume evolutions to optimize conditions at the condensate surface with the presence of reactive, thermally excited, high mobility, and long diffusion time species. The technique opens up the possibility of preparing high-quality BN films on a wide range of previously incompatible substrates with traditional growth approaches of BN, a possibility to scale the film production to large areas, and achieve very fast growth throughput needed for commercialization. The formation of amorphous and nanocrystalline hexagonal BN thin films (domain sizes approx. 3 nm) was observed on a variety of substrates and temperatures. Key device performance metrics affected by the quality of the dielectric material are discussed including the impact on graphene device performance, the in-plane heat transport within

the dielectric as related to the crystallinity, and the heat conductance at critical dielectric/device interfaces.

A comprehensive literature review presented in Chapter 2 begins with an introduction to nanoscale boron nitride thin films including structural allotropes very similar to the 0D, 1D, and 2D carbon systems. Current state of the art direct growth methodologies of 2D *h*-BN are discussed including mechanical and liquid exfoliation, chemical vapor deposition, and physical vapor deposition, as well as applications for 2D *h*-BN coatings. Progress in the PLD of bulk BN and the spectroscopic studies of plasma diagnostics provide insight into the potential for nanoscale BN synthesis. Finally, thermal transport behavior of 2D *h*-BN and ultra-thin materials is introduced and presents a means of enhancing thermal management for nanoscale devices.

The following chapters present work reflecting a centralized concept of a new deposition technique for ultra-thin boron nitride, understanding critical plasma parameters necessary for the growth of these materials, and the impact that these high quality films can potentially have on 2D material systems. Beginning in Chapter 3, optical emission spectroscopy was explored as a technique to fundamentally understand plasma conditions required for stoichiometric, large area BN growth. In these studies, ionic and neutral species are tracked both spatially and temporally in the formulation of nucleation and growth mechanisms at the substrate surface. Chapter 4 uses lessons learned from the plasma spectroscopy in synthesizing nanocrystalline *h*-BN on lattice matched substrates and temperatures much lower than conventional CVD processing. Structural, chemical, and electronic data further ensures that the films are of high quality for electronics. Amorphous boron nitride is observed on non-lattice matched substrates

and at growth temperatures of < 200°C, as discussed in Chapter 5, making the new dielectric material a very exciting possibility for substrate agnostic flexible systems. Device-scale dielectric measurements reveal enhanced dielectric constant and breakdown from other conventional techniques, without the limitations involving substrate choice and high temperature growth. In Chapter 6, properties of the newly developed nanocrystalline *h*-BN and amorphous *a*-BN films are compared with respect to how the properties will impact critical device metrics including graphene transport in contact with the dielectrics, the in-plane thermal transport behavior, and the interface thermal conductance for 3D thermal management. Finally, Chapter 7 provides for a brief summary of the work performed and described in this manuscript.

CHAPTER 2. LITERATURE REVIEW

2.1 Introduction to boron nitride

Boron nitride (BN) is a non-naturally occurring chemical compound that consists of alternating boron and nitrogen atoms, commonly of great interest to scientists due to the electrical insulating properties, as well as excellent chemical and thermal stability. First synthesized in 1842 by Balmain [15] with molten boric acid and potassium cyanide, the boron and nitrogen containing compound is isoelectronic and isostructural to common carbon systems. Similar to carbon, BN exists in amorphous (*a*-BN) and crystalline forms including hexagonal (*h*-BN), wurtzite (*w*-BN), and cubic (*c*-BN) phases. The two most common crystal phases of interest are the hexagonal and cubic phase, represented in Figure 2.1a, which structurally relate to graphite and diamond, respectively. Cubic boron nitride is the thermodynamically favored composition at reduced temperatures and pressures, and has been shown to be a super-hard material only slightly softer than diamond [16], but superior thermal and chemical stability. The phase diagram of boron nitride in Figure 2.1b from Solozhenko et al. [17], indicates that *c*-BN is the more favorable structure at reduced temperatures and pressures, with a conversion to layered *h*-BN around 1400 °C at atmospheric pressure. Similar to graphite, this layered *h*-BN material is exceptionally exciting for nanoelectronic applications in that the material

retains much of the chemical inertness and insulating properties even at nanometer length scales.

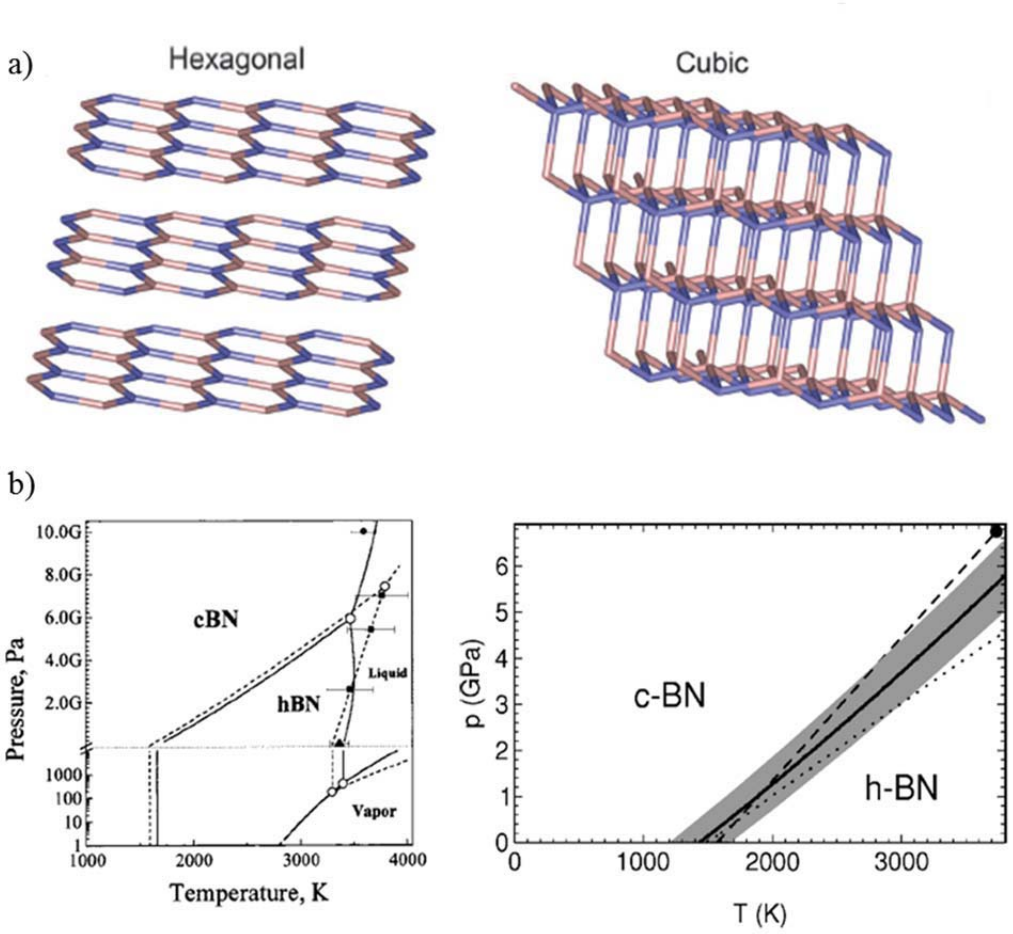

Figure 2.1: a) Structure of hexagonal and cubic boron nitride, reproduced from [18] with permission from the Royal Society of Chemistry, and b) phase diagrams of the expected crystalline transition between *c*-BN and *h*-BN, reprinted with permission from [17], Copyright 2016 American Chemistry Society.

Nano-scale hexagonal boron nitride (*h*-BN) materials have been investigated for use in nanotechnology applications including high speed transistor devices, flexible electronics, and high temperature coatings. Structurally similar to graphene (lattice constant mismatch of 1.2%), *h*-BN nanosheets consist of alternating B and N atoms

arranged in a sp^2-bonded hexagonal lattice structure in-plane such as that depicted in Figure 2.2, with van der Waals interactions between the layered sheets. The boron nitride nanomaterial phases exist in other 0D, 1D, and 2D forms shown in Figure 2.2, similar to carbon material phases (i.e. carbon phases of bucky ball, nanotube, graphene are similar in structure to BN fullerene, BN nanotube, and 2D *h*-BN). The 2D *h*-BN sheets exhibit desirable properties including a wide band gap (5.7 eV), high temperature stability, reasonable dielectric strength, and inertness to many chemical environments. These few-layer sheets have the potential to be utilized as a dielectric in many configurations of 2D nanoelectronic material systems. The atomically thin material can be used as a complementary dielectric material to graphene as it provides an atomically smooth surface free of dangling bonds, high surface optical phonon modes, very high in-plane thermal conductivity, a good tunneling barrier for electrons, and minimal sites for adsorbed surface impurities. These observations have led to experiments involving BN as an ultra-thin gate dielectric as well as a substrate material to create structures such a BN/graphene/BN layers. The use of *h*-BN was shown to markedly increase electron mobility in graphene by several times when compared to traditional dielectric materials such as thermally grown silicon dioxide. Some of these advantageous, and more, will be addressed in subsequent sections, as well as optimal growth procedures for such films.

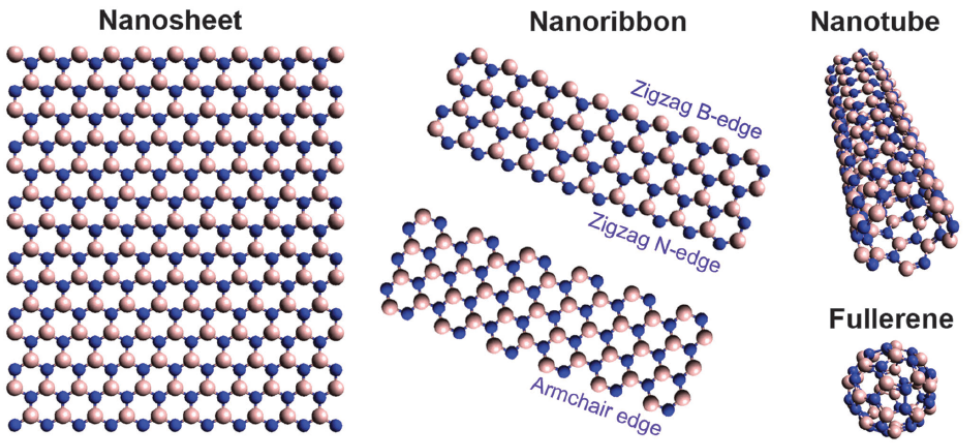

Figure 2.2: Representation of the most common boron nitride nanostructures in 2D, 1D, and 0D from [18] with permission from the Royal Society of Chemistry.

Sheets of *h*-BN are typically evaluated by means of optical microscopy, Raman spectroscopy, cross-sectional and top-down transmission electron microscopy (TEM) imaging, and electrical measurements including conducting atomic force microscopy (C-AFM) and device-scale measurements. Optical microscopy techniques present the ability to identify both single and few-layer flakes, such as the case in Figure 2.3a from Gorbachev et al. [19], where a 590 nm yellow filter was used to clearly identify individual layers. Thicknesses are traditionally verified by means of cross-plane TEM, such as the images shown in Figure 2.3b from Song et al. [20]. This technique is typically time-consuming, but is the most accurate in identifying layer thickness at a local scale, as the direct image of the layered structure and can discern microstructure with moderate ease. The most common structural analysis technique used to identify the presence of the *h*-BN phase is with the use of Raman spectroscopy. In single and few-layer *h*-BN, the E_{2g} mode of the in-plane vibrations within the hexagonal lattice is shifted slightly from the bulk behavior [19], as shown in Figure 2.3c and d from Gorbachev et al.

This shift in peak position as a function of layer thickness from 1369 to 1366 can be used to help loosely decipher monolayer from few and bulk layered structures, however, the exact layer thickness is more precisely measured with micrsocopy techniques.

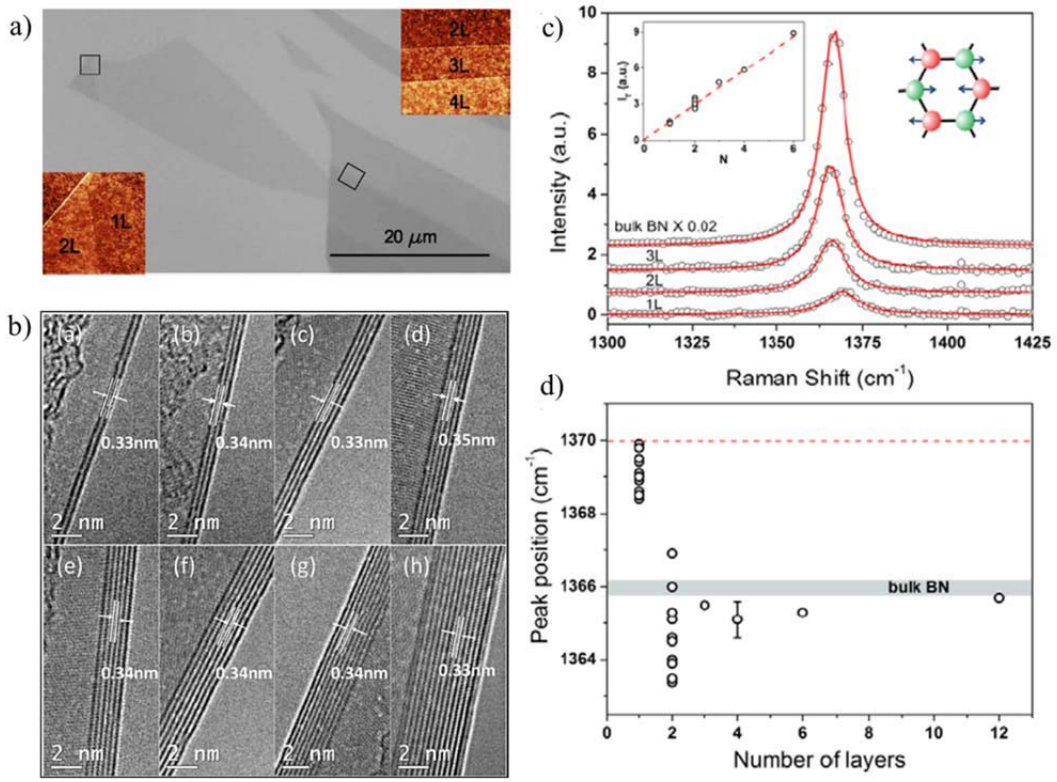

Figure 2.3: a) Identification of 1-4 layer *h*-BN sheets using an optical microscope and a 590 nm yellow filter, reproduced from [19] with permission from John Wiley and Sons Publishing, b) cross sectional TEM images of *h*-BN sheets ranging from 2 to 10 layers reprinted from [20] with permission from Elsevier, c) Raman response of E_{2g} mode in *h*-BN sheets and d) peak position as a function of layers, reproduced from [19] with permission from John Wiley and Sons Publishing.

Few-layer *h*-BN clearly exhibits interesting structural, optical, and electronic properties at the nanoscale that can potentially be highly influential in nanoscale devices in the not-so-distant future. The significant limiting factor for device-scale implementation of 2D *h*-BN (and most other 2D materials) is the lack of ability to

construct these materials at a scale appropriate for commercialization. The following section discusses the very different approaches currently implemented for growth and isolation of 2D *h*-BN.

2.2 Synthesis routes towards 2D hexagonal boron nitride

Since the discovery and isolation of graphene by researchers from the University of Manchester in 2004 [21], and the realization that the confinement of energy carriers to a plane can lead to enhanced material properties including electron mobility [22], heat transport [23], and inherent material flexibility [24, 25], the exploration of growth methodologies for atomic layered 2D materials has been a major field of scientific discovery. The initial separation of these 2D atomic materials were made possible by the careful exfoliation of atomic sheets within bulk crystals, including conducting graphite, semiconducting materials including transition metal dichalcogenides (MoS_2, WS_2, black phosphorous, and others), and insulating layered structures such as hexagonal boron nitride (*h*-BN) [26]. While the exfoliation of bulk crystals can lead to high quality materials at a local scale, researchers have continued to expand and develop direct synthesis methods to grow these materials using techniques that are amenable to larger area device structures. The most popular methodologies include expansion of exfoliation techniques, chemical vapor deposition (CVD), plasma enhanced chemical vapor deposition (PECVD), physical vapor deposition (PVD), and alternative growth techniques including liquid solution processing and electrochemical synthesis, all represented in Figure 2.4.

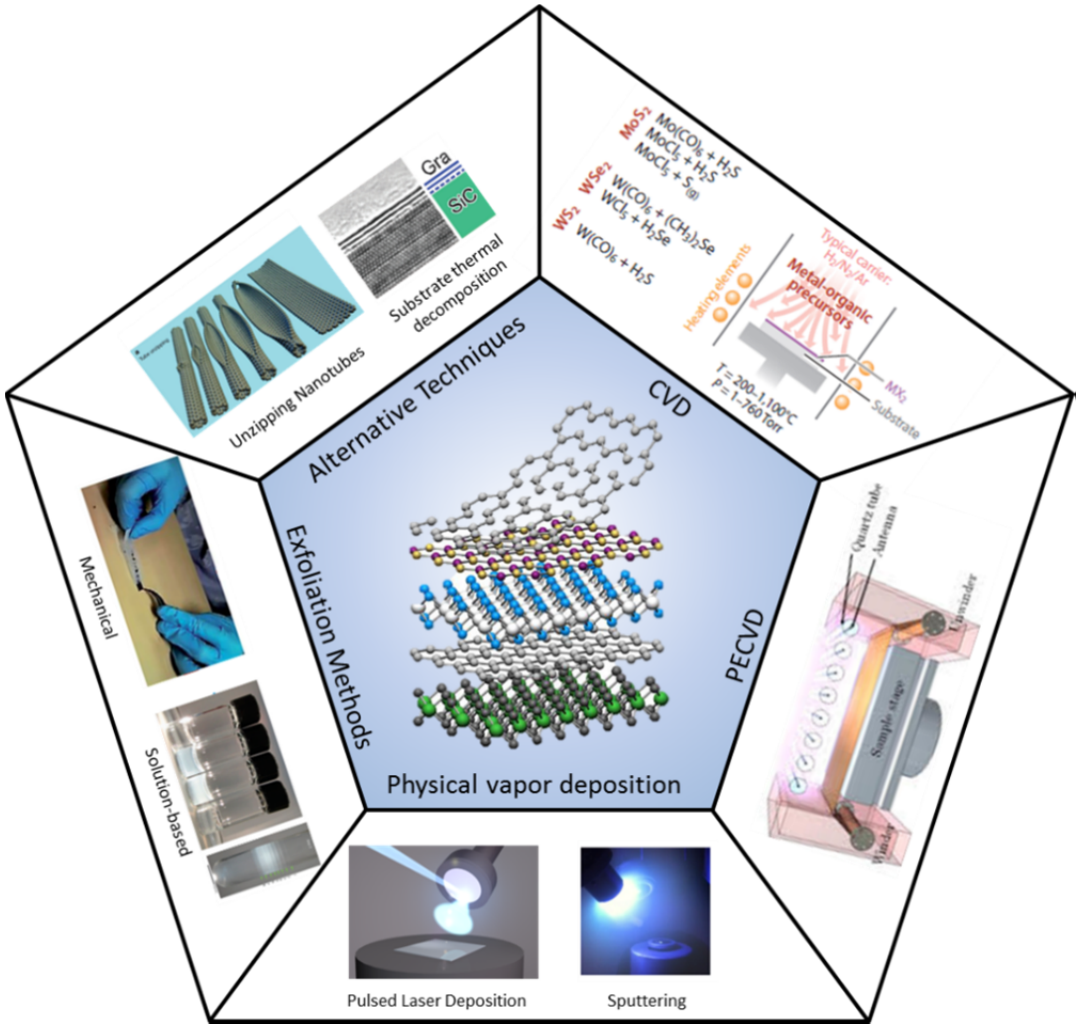

Figure 2.4: Representation of growth methodologies for 2D materials (inset image reprinted by permission from Macmillan publishers LTD: Nature [2], copyright 2013), chemical vapor deposition (CVD) from [27] with permission from Annual Reviews, plasma enhanced chemical vapor deposition (PECVD) reprinted from [28] with permission from Elsevier, physical vapor deposition, mechanical and chemical exfoliation methods reproduced from [29] with permission from the Royal Chemistry Society and reprinted with permission from [30], copyright 2015 American Chemical Society, alternative technique for unzipping nanotubes reprinted by permission from Macmillan Publishers Ltd: Nature [31], copyright 2009, and for substrate thermal composition, reprinted from [32] with permission from the Royal Chemistry Society.

2.2.1 Mechanical and liquid exfoliation

The relative ease of which van der Waals solids can be exfoliated into ultra-thin sheets arises from the presence of covalent bonds in the plane and weak van der Waals bonds between the planes, resulting in strong enhancements of the intra-layer atomic interactions while inhibiting similar interactions in the inter-layer [1]. Bulk layered solids can thus be easily cleaved using mechanical exfoliation, as the van der Waals bonds between the layers (0.1-0.2 eV) are an order of magnitude less strong than the inter-plane bonding (1-2 eV). Mechanical exfoliation is typically performed using an adhesive tape (initially with commercially available 3M scotch-tape™), and ultra-thin layers are isolated on the tape only through several cycles of lift-off steps. The thin flakes can have a wide distribution of thicknesses resulting in low yield of the 2D mono and bi-layer form. Prospects for use of mechanically exfoliated materials in commercial next-generation device constructs are limited, as device heterostructures are built by placing additional 2D exfoliation flakes, metal contacts, and/or other device make-ups must be done carefully, and only after optically identifying the flake(s) of interest first. Despite the limitations, the exfoliation of single materials for use in specific applications can be realized for scalability of some individual 2D materials [29].

While research-scale mechanical exfoliation can isolate very high quality materials, liquid-based exfoliation techniques have begun to show more progress towards commercial applications. Liquid exfoliation of the layered structures is performed by either solvent sonication to physically break into few-layers [33-36], or interstitial intercalation to induce strain and assist in the exfoliation of layers [37]. The 2D material flakes are dispersed in a solvent and separated by various methods, then deposited onto a

substrate by drop-casting, printing, and other methodologies. Although this technique has shown to potentially be a very viable growth technique in the near future, the current discussion in this review will more focus on direct growth techniques for 2D materials.

2.2.2 Chemical vapor deposition

Nucleation and direct growth methodologies for high quality mono- and few-layer h-BN films, as well as many other 2D material counterparts, have been of significant interest within the past decade. The necessity for direct growth, in contrast to the previously discussed exfoliation techniques, is driven by the desire for large area film coverage with strict control of layered thickness as well as eliminating the difficulties associated with the lift-off and transfer processes seen in many exfoliation variations [2, 38]. To date, the progress in growth of 2D insulators including hexagonal-boron nitride has significantly lagged behind comparable conductors and semiconductors (e.g. graphene, transition metal dichalcogenides, and other 2D material systems), as the difficulty in materials processing presents many challenges for device usage [39]. These difficulties include lack of large-area growth required for electronic devices, compatibilities with substrate materials, and required high deposition temperatures (typically >1000°C), each that will be discussed in following sections.

Even as the overall interest in 2D materials has increased substantially since the isolation and initial studies at the University of Manchester [21], monolayer and few-layer h-BN has been directly grown in small domains since the mid 1990's. One of these first isolations of monolayer *h*-BN was made possible by A. Nagashima [40, 41] and was performed by thermal decomposition of borazene ($B_3N_3H_6$) at 700-800°C on metallic

substrates including Ni (111), Pd (111), and Pt(111), which continue to be common substrates for *h*-BN growth. Initial studies using EELS and X-ray Photoelectron Spectroscopy (XPS) led to key observations including the realization of a very low interaction energy between h-BN and the substrate, as well as the extremely slow growth rate for the second layer of *h*-BN from a lack of reactivity on the surface of the monolayer islands. These initial studies were performed with limited interest at the time, but would later influence the 2D materials community substantially nearly a decade later.

Once the exciting discovery of graphene ignited the research in the topic of 2D materials in the mid 2000's, chemical vapor deposition (CVD) become the most prominent growth technique used for single and few-layer 2D materials, including *h*-BN. Demonstration of large area growth of few-layer *h*-BN by atmospheric pressure chemical vapor deposition (APCVD) in early 2010 yielded highly uniform films on copper foil with thicknesses of a few atomic layers [42, 43]. The precursor reactants in these initial studies included ammonia borane (NH_3-BH_3), a solid powder requiring sublimation at temperatures of 120-130°C, as well as a gaseous precursor borazene, also used in initial studies by Nagashima. Both studies were performed at substrate temperatures of 600-700°C for 20-30 minutes of growth in an Ar/H_2 gas mixture, followed by a post-annealing step at 1000°C to further crystallize the multi-layer film. The similarities in film growth and structure for initial efforts in CVD *h*-BN coatings is represented in Figure 2.5, where Figure 2.5a, b, c show an optical image of the few-layer h-BN film, high resolution "top-down" TEM view of the atomic structure, and cross-sectional TEM image of the few-layer h-BN film, respectively, from Song et al. [43], Figure d, e, and f display complementary images using the same techniques from Shi et al. [42], First

growth procedures for the ultra-thin *h*-BN coatings identified many critical issues, common in current growth methods as well, including the necessity to reduce wrinkles, cranks, and pinholes, as the need for uniform, large area coverage is required for many applications.

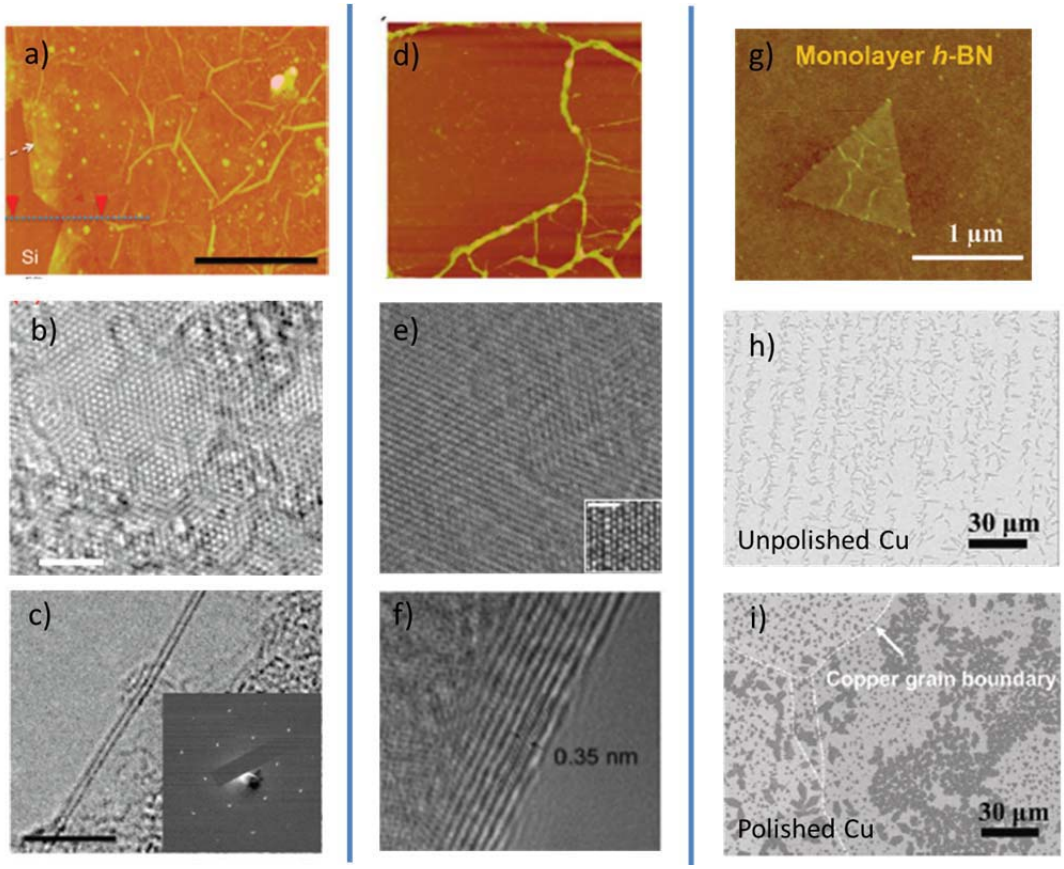

Figure 2.5: a) An optical top-down view of the as-deposited *h*-BN on Si, b) a close-up TEM micrograph of the hexagonal patterning in h-BN, and c) a cross-sectional view of few-layer *h*-BN growth all reprinted with permission from [43] Copyright 2010 American Chemical Society. Similar images are shown in d) e) and f) from Shi et al. reprinted with permission from [42], copyright 2010 American Chemical Society. The last column in Figure 1 shows g) an SEM image of monolayer triangle formation of *h*-BN, and h) optical image of *h*-BN growth on unpolished and i) highly polished copper foil, all from Kim et al., reprinted with permission from [44], copyright 2011 American Chemical Society.

It wasn't until 2012, when Kim, et al. [44], was able to isolate repeatable, triangular domains of single layer *h*-BN by performing the growth at lower pressures (technique known as LPCVD) using Borazane, a gaseous species slightly more environmentally stable than Borazene when decomposed. Advantages of the LPCVD synthesis include increased cleanliness in a vacuum environment, reduced activation energy for *h*-BN formation at lower pressures [45], as well as the reduced effect of kinetics and dynamics of the inlet gas flow for growth [46]. Figure 2.5e is an optical image of one of the triangular domains, with grain sizes on the order of 1 micron. At a single layer, the reactivity of the h-BN is very low, and can lead to incomplete film coverage in this instance of monolayer triangles. Additionally, the surface conditions of the substrate play a critical role in the nucleation density as well as the growth dynamics [47], evidenced by the optical images of the distribution of domains of *h*-BN shown in Figure 2.5h and Figure 2.5i of the same growth conditions on unpolished and polished copper foil, respectively [44].

At the time, it was a surprise that the first domains of h-BN were triangular, in contrast to the traditional hexagonal pattern observed in graphene synthesis on copper foil [48]. Origins of these triangle domains are attributed to low-reactivity of the nitrogen terminated edges, predicted in simulations such as those represented in Figure 2.6a and others [49], that restrict the lateral growth of the triangular domains. As graphene is a monatomic structure, the lack of contrasting edge site nucleation forms a hexagonal pattern similar to the internal structure of the graphene rings. It was observed by Stehle et al. [50] that by altering the location of the substrate in the tube (i.e. further or closer to reactant source), and thus altering the nitrogen-to-boron active species concentrations in

the gas phase at the substrate location, the shape of these few micron-sized domains can be altered from triangle to semi-hexagons, as shown in Figure 2.6b. Further manipulation of gas flow dynamics in the CVD tube (more substantial impact at atmospheric pressure growth) has also proven to control the nucleation shape of the *h*-BN materials from controllable triangles to more advanced structures [51].

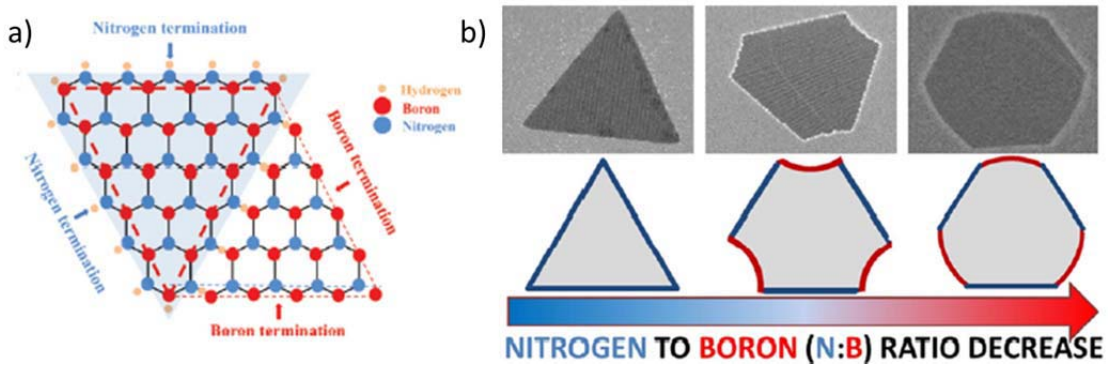

Figure 2.6: a) Representative schematic of the triangle formation of h-BN, where the Nitrogen termination is the more energetically favorable termination reprinted with permission from Kim et al. [44], copyright 2011 American Chemical Society, and b) the change in *h*-BN initial grain formation shape as a function of nitrogen and boron chemical concentrations in the CVD furnace reprinted with permission from Stehle et al. [50], copyright 2015 American Chemical Society.

Beyond *h*-BN growth on copper foils, 2D *h*-BN nucleation and growth has continued to expand to other metals including various crystal orientations of Ni [52-55], Pt [56], Pd [57], and alloys of these materials [58]. Nickel, in particular the (111) crystal orientation, has shown to facilitate high quality *h*-BN growth due to the small lattice mismatch (0.4%). This strain induced by the difference in lattice mismatch is compensated by a slight corrugation of the adlayer, and the periodicity of this depends on the degree of lattice mismatch between the substrate [57]. Grain size of the 2D h-BN can be directly influenced by the surface structure, as exemplified by record high triangular

grain size of 7500 μm^2 on Cu/Al alloys at growth temperatures of 1050°C [58]. The authors attribute the large grain size to the small addition of Al in the alloy, where the nucleation density can be decreased to 60 sites per mm^2, leading to unimpeded, large crystal growth on the surface.

Other interesting 2D structures can be formed by expitaxial lattice interactions between the substrate and *h*-BN. Hexagonal boron nitride nanomesh, a porous material consisting of 12 substrate unit cells with aperture structures 2 nm in width, can be formed on Ru (0001) [59] and Rh (111) by LPCVD techniques used for monolayer growth on other foils [60]. These structures form upon the decomposition of borazine vapor at temperatures at 1100°C, and can have a particular benefit for use in patterning and assembly of nanoparticles such as gold nanoclusters. The change in nanostructure simply by altering the surface lattice structure and texturing conditions highlights the fact that *h*-BN in both the monolayer and few-layer form is extremely surface sensitive during the nucleation and growth process.

The vast majority of CVD synthesis routes have been focused on metallic substrates, as the foils can withstand high temperature synthesis (800-1000°C) and can have expitaxial-like growth effects. Ideally, the 2D material could be grown directly on substrates of greater interest for electronics and other applications. If this would be possible, the requirement for the time and personnel-intensive lift-off and transfer steps would be eliminated, streamlining the device construction process. Prospects for direct growth of *h*-BN on Al_2O_3 and SiO_2, both common substrates for nanoelectronic applications, are discussed by Bresnehan et al. [38, 61]. Key aspects of the *h*-BN growth such as stoichiometry as a function of growth temperature, crystal size, and thermal

transport properties were evaluated to elucidate how the thin *h*-BN films would behave in a graphene device construct. In addition, the enhancement of graphene hole concentration and mobility was evaluated with respect the quality of the as-deposited films on Al_2O_3 and SiO_2. Direct growth of the turbostratic, 2D h-BN films processed at 400°C was shown to possess a higher boron content, however, show the largest increase in mobility of the graphene layered on top of the film, with a 1.5x and 2.5x times increase on Al_2O_3 and SiO_2, respectively.

Multiple variations of chemical vapor deposition to grow 2D materials include metal transformation, chemical vapor transport, powder vaporization, and reactive chemical vapor deposition [27]. In all of these variations, the mechanism for film growth is driven by thermodynamics, as the heat supplied to the substrate is typically the major energy source required for crystal formation (approximately 0.1 eV if substrate is heated to a surface temperature of 1000°C). The thermodynamic process is driven by the atomic mobility, or the lateral diffusion rate, of condensed species on the substrate to form thin films starting at specific, discrete nucleation spots. The deposition rate using this technique can be very slow, where some growths take hours to warm-up and cool-down the chamber of interest, up to an hour of growth time, plus many times there is an addition of an annealing step. Because of this slow growth rate in comparison to the deposition flux, the condensed atomic species are near the equilibrium condition, where the species have a sufficient time to explore their minimal energy representation on the surface before settling into their final configuration [62, 63]. After a critical time, these boundaries will merge together and have been a spot of intense research with regards to

the grain boundary contributions to thermal transport, electron transport, and other physical phenomena.

2.2.3 Physical vapor deposition growth techniques

In contrast to the highly equilibrium, thermodynamically driven processes, such as CVD, 2D materials have also been shown to nucleate and grow crystalline, highly continuous films by means of physical vapor deposition (PVD). In PVD techniques including magnetron sputtering, pulsed laser deposition, molecular beam epitaxy, and others, the plasma generated within a high vacuum chamber can represent ion and electron energies on the order of 1-100 eV. Figure 2.7 schematically represents the different mechanisms, where PVD techniques tend to have a high deposition flux and a relatively low time for atomic surface diffusion [62]. These processes have been known to create metastable and complex structures (including 2D planes), with control of the rate and concentration of species within the plasma [64].

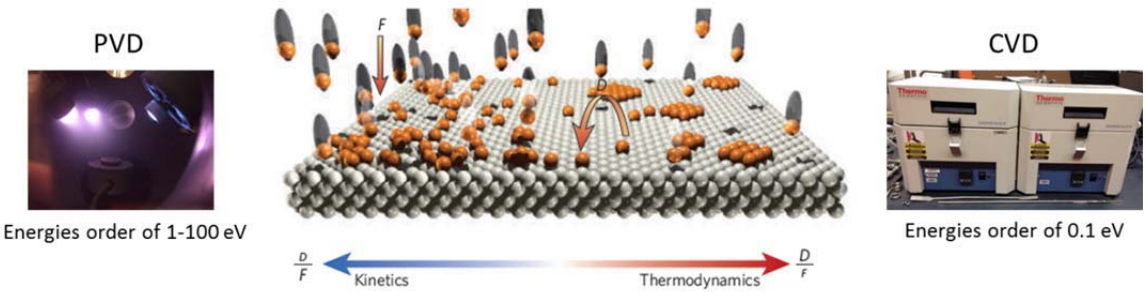

Figure 2.7: Schematic representing the contract in kinetic (PVD) and thermodynamic (CVD) approaches to film growth where *D* is the diffusion rate and *F* is the incoming deposition flux, center image reprinted by permission from Macmillan Publishers Ltd: Nature [62], copyright 2005.

The use of high energy plasmas results in several benefits over conventional CVD approaches including reduced required temperature for *h*-BN formation, large area coverage and versatility in device fabrication. The plasma-based techniques including magnetron sputtering as well as pulsed laser deposition and molecular beam epitaxy have been used to coat very large wafers with uniform, cohesive thin films on the order of 4" in diameter and larger [65]. Due to the high energy plasma species, however, special considerations need to be addressed as to how to control the kinetically driven processes to resist damage to the substrate and reduce the nucleation site density to allow for large area, unimpeded grain formation. An example of a method to control plasma energies is demonstrated in growth of highly uniform 2D MoS_2 growth by magnetron sputtering, where the films demonstrate uniform thicknesses over the entire substrate of less than three angstroms, and the incoming energy must be controlled by an exterior magnetic field to steer the ion species away [66, 67]. The drawback to the high energy process is that the high deposition flux restricts large area grain growth, as the grains in this case are on the order of 20 nm, in contrast to the > 1 μm grains observed in conventional CVD processes. Sutter et al. [68], using a combination of CVD and reactive magnetron sputtering from a boron source in an Ar/N_2 gas mixture (see Figure 2.8a), was able to generate a very slow flux of energetic ions and neutral species to the surface to condense and form uniform, highly crystalline multi-layer *h*-BN on a Ru substrate, shown in Figure 2.8b. With a three-step process combination of initial CVD to seed the growth to less than a monolayer, following by sputtering at high and low temperatures for subsequent multi-layer growth, multiple layers can be formed with a varying degree of thicknesses and stoichiometry, as measured by XPS in Figure 2.8c and d. In addition, pulsed laser

deposition (PLD) studies using very high-energy CO_2 lasers have shown to produce high quality *h*-BN nanosheets that overlap and form on the substrate surface at an even lower temperature of 400°C [69]. These sheets, however, are difficult to control film thickness and resemble exfoliated flakes with regards to distribution of sizes and thicknesses.

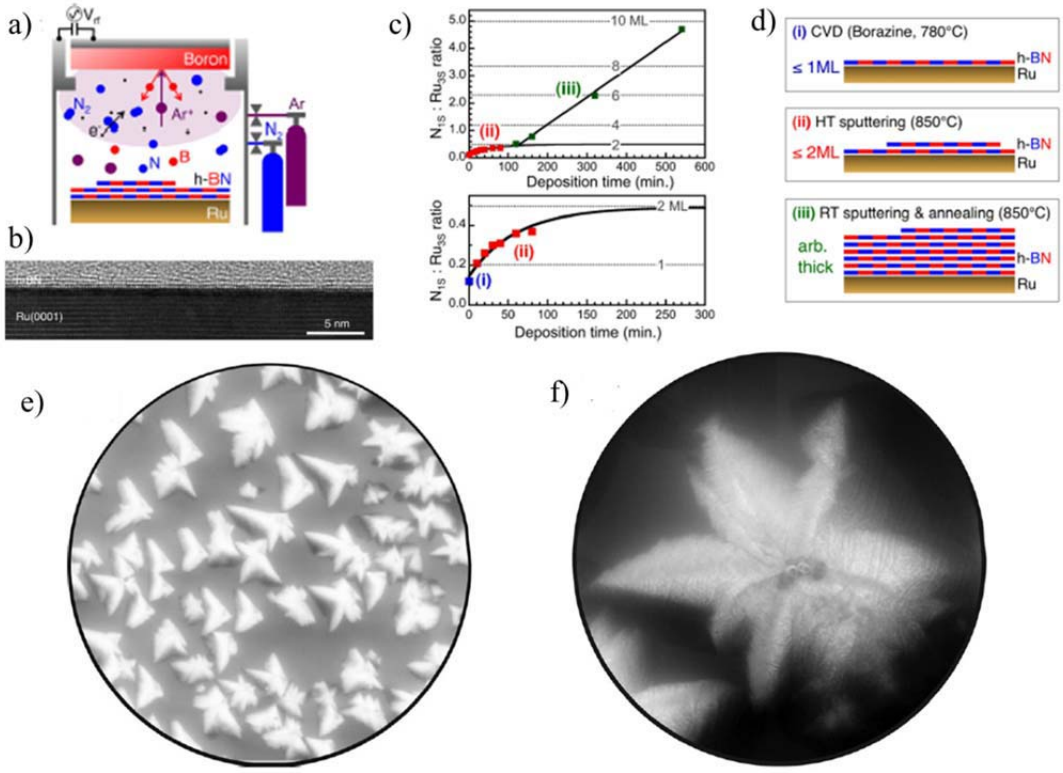

Figure 2.8: a) Setup of reactive magnetron sputtering for h-BN films, b) cross-sectional TEM image of few-layer growth on Ru (0001), c) XPS analysis of thickness for the different growth conditions, and d) outlining the three-step process for arbitrarily thick h-BN coatings, all reprinted with permission from [68], copyright 2012 American Chemical Society, e) initial h-BN grain formation with window size of 30 µm, and f) a close-up of a similar image with window size of 9 µm, reprinted from [70] with the permission of AIP Publishing.

Studies of molecular beam epitaxy of *h*-BN growth on nickel foils by Nakhaie et al. [70] were able to use energy from the molecular ion beam, namely an elemental B and N source, to form large area, cohesive thin films of *h*-BN. The mixture of the high

energy molecular flux, coupled with the high surface temperatures, can lead to interesting meta-stable structures that aren't necessary bound to triangular film formation observed in films grown by CVD. Figure 2.8a and a close-up in Figure 2.8b provides images of MBE growth of *h*-BN that can result in flower-like configurations, which eventually nucleate and grow in ways that aren't traditional in CVD reactor chambers. These can be attributed to the additional kinetic energy [62] supplied by the incoming beam, where the added energy can lead to a reduction in required growth temperature, evidence by growth of these initial crystalline flower-like growths at 730°C.

Two-dimensional hexagonal boron nitride is one of the more interest 2D materials to date, and direct growth methods to understand how to enhance and control the film formation are critical to the future of nanoelectronic devices, anti-corrosive coatings, and other uses. Advances in CVD processing have resulted in extremely large grain size, stoichiometric films, and alternative methods including plasma-based processing techniques could allow for realization of direct-growth device constructs. In order to begin to understand the possibilities of pulsed laser deposition as a methodology for creating ultra-thin boron nitride films for next generation electronics, understanding the critical mechanisms that are important in creating thick boron nitride films is necessary, and discussed in the following section.

2.2.4 Pulsed laser deposition of thick boron nitride coatings

Pulsed Laser Deposition (PLD) is an alternative PVD technique to reactive sputtering and molecular beam epitaxy, where a high energy, focused laser beam pulse causes rapid heating on the face of the target, resulting in both ionized and neutral

components accelerating from the target in the form of a plasma plume normal to the target surface. The plasma plume propagates in the direction of the substrate and can be thermalized by collisions with the background gas, depending on the pressure and target to surface distance. The resulting film quality and composition on the substrate can be affected by parameters including laser wavelength, power, pulse rate, pulse duration, target-to-substrate working distance and relative orientation, background gas type and pressure, and substrate temperature. Whereas alternative PVD techniques present difficulties in preparing complex stoichiometric films due to differing partial pressures of the individual species in the vapor phase, PLD has proven useful in preparing complex thin films due to the rapid, localized heating, and relatively stoichiometric plasmas expelled from the target.

This technique has proven viable for growth of thicker boron nitride films of different crystalline orientations including hexagonal and cubic phases [71], at relatively low temperatures of 650 °C with B:N ratios of approximately one. These thick boron nitride films are well known to have multiple phase transitions within the first 100 nm of growth from the substrate [72]. Figure 2.9 from Zhang et al. [73], shows a cross-sectional TEM of one of these films. The first few nanometers are composed of a <4 nm interfacial amorphous, dense layer. After this initial layer formation, a turbostratic boron nitride phase is formed typically with a thickness of 20-50 nm, which is a polycrystalline version of the hexagonal sp2 bonded crystal structure. Unlike 2D *h*-BN, the turbostratic phase is formed with the basil planes aligned perpendicularly to the substrate. This turbostratic phase eventually advances in thickness and the edges of the basil planes begin to serve as nucleation sites for the resulting cubic boron nitride film microstructure.

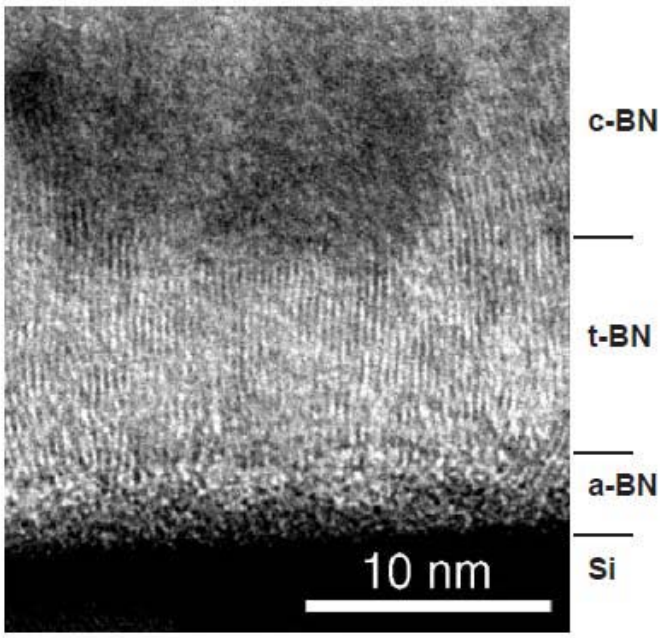

Figure 2.9: TEM cross-sectional image of a three layer sequence of growth starting with amorphous BN and translating to the final c-BN film microstructure, reprinted from Zhang et al. [73], with permission from Elsevier.

Previous PLD studies discussed earlier using very high-energy CO_2 pulsed lasers and various background gases result in a reduction in required substrate temperature for deposition, and formation of overlapping few-layer BNNS flakes at reduced temperatures near 400°C [69, 74]. The PLD technique carried out in the studies highlighted in this dissertation are different in that the formation of cohesive nanoscale thin films either in the nanocrystalline *h*-BN or amorphous phase are observed that do not exhibit cross-plane defects, nucleate cohesively over large areas, and allow for the strict control of film thickness on the wafer-scale using laser ablation.

2.3 Plasma spectroscopy approaches in preparation of BN thin films

Studies of fundamental plasma phenomena of laser ablated plasma from boron nitride targets have aided greatly in the understanding of crystal formation and chemistry of boron nitride films in the amorphous, hexagonal, and cubic phases. Wei et al. [75] were one of the first to investigate the time of flight and velocity of ionized boron (B^+) species expelled from a BN target during ablation by optical emission spectroscopy in a wavelength range from 300-600 nm. Discovery of atomic B^+ velocities close to the target exceeding 10^5 cm/s led to the hypothesis that this species is critical in BN thin film formation. Murray et al. [76] and then Doll et al. [77] both expanded on this by incorporating mass spectroscopy time of flight studies of the B^+ ions and a more detailed optical emission spectroscopy at similar wavelengths, respectively. In the study by Murray et al. the formation of stoichiometric BN in an NH_3 environment was linked to the abundance of (B^+) and (N^+) with a hypothesis on BN formation in gas phase based on the cluster detection by mass-spectroscopy. Additional time of flight and optical spectroscopy studies at different nitrogen background gas pressures and laser powers were conducted by Shin et al. [78] and by Angleraud et al. [79]. These studies confirmed that the plumes consist mainly of neutral and ionized atomic boron with a presence of ionized atomic nitrogen, while the presence of molecular BN in the plasma plumes is negligible. The studies also reported plume confinement and deceleration by collisions with background nitrogen gas, changing BN plume behavior from earlier stage direct propagation to a shockwave formation and hydrodynamically controlled propagation at later stages in plume development [79]. In more recent work from Dutouquet et al. [80], the focus was on identification of BN radicals in the 340-390 nm emission window of the

laser ablated plumes, where the presence of BN was identified but the overall intensity in comparison to atomic emissions was fairly low. These earlier studies clearly highlight the significance of the background gas pressure on the shockwave formation and plume propagation dynamics, plasma plume composition, and possible reaction mechanisms for the film growth.

Most of these earlier plasma studies were directed towards the appropriate growth conditions required for the cubic phase of boron nitride, as the extreme hardness, high thermal conductivity, and chemical stability makes this phase of BN attractive for certain industrial applications including erosion, oxidation resistance, and wear protective coatings [71, 77, 81, 82]. For cubic BN phase formation, the utilization of high kinetic energy of laser ablated B and N species were critical, with translational velocities reported as high as 20-50 km/s depending on the background nitrogen pressure [79]. Observations of nitrogen chemistry at the substrate location and reactions at the substrate surface due to plume collisions with background gas and condensation surface were explored to a lesser degree. Only recently have hexagonal and amorphous phases at the nanoscale thickness scale become of comparable interest [83] for application to electronic and optoelectronic devices. In order to facilitate nanoscale, stoichiometric BN thin film growth, optimization of incoming plasma species composition and energies at the substrate/condensate interface is necessary to aid in the formation of stoichiometric BN while avoiding deterioration under the excessive bombardment by energetic ablated plume species.

2.4 Dielectric and protective characteristics of 2D boron nitride films and coatings

Two dimensional *h*-BN and has been considered for use in many different applications including gate and substrate dielectrics for nanoelectronic devices, anti-corrosive coatings, frictional layered coatings, high temperature resistive layers, and other advanced applications for 2D material systems. The large bandgap (5-6 eV), high temperature and chemical resistivity, and other properties discussed earlier in the chapter, make both the exfoliated *h*-BN and direct-grown *h*-BN material ideal for such applications.

2.4.1 Dielectrics in next generation nanoelectronic devices

Graphene is known for having one of the highest electron and hole mobilities of any material to date, making the 2D material a natural candidate for next generation high speed electronic devices [84]. Initial graphene devices transferred onto traditional SiO_2 substrates were observed to have a reduction in intrinsic transport properties due to adverse interactions with the substrate (>120,000 cm^2/Vs compared to device performance on SiO_2 of approximately 2,000cm^2/Vs) [85, 86]. The carrier mobility in the devices was reduced due to the scattering from charged surface states and impurities in SiO_2, the relatively high surface roughness of the substrate, and the low frequency surface optical phonon modes in SiO_2 [87-89]. Dean et al. [90], was the first to investigate the use of bulk *h*-BN as a substrate material to counteract these effects observed in SiO_2 devices. The strong in-plane bonding of the h-BN substrate was hypothesized to allow for an atomically smooth, inert surface free of dangling bonds or surface charge traps. This was found to be true, as the electronic properties of graphene

including enhanced mobility, reduction in carrier inhomogeneity, and reduced intrinsic doping from the substrate, were substantially improved. Han et al. [91] demonstrated the first exfoliated GFET with *h*-BN integrated in both the substrate and gate dielectric, effectively creating a *h*-BN/Graphene/*h*-BN sandwiched device, as shown in Figure 2.10 a, b, and c. When compared to a traditional GFET device with SiO_2 and Al_2O_3 as dielectrics, an increase of 70% in the peak transconductance (gm) was observed with a higher frequency of operation, as well as a greater than 5x increase in graphene mobility from 1200 cm^2/Vs to 6500 cm^2/Vs. This increase in mobility is also observed in polycrystalline CVD graphene on h-BN, where an increase of greater than three times is observed in Figure 2.10d [92], an effect observed in other device constructs as well [93].

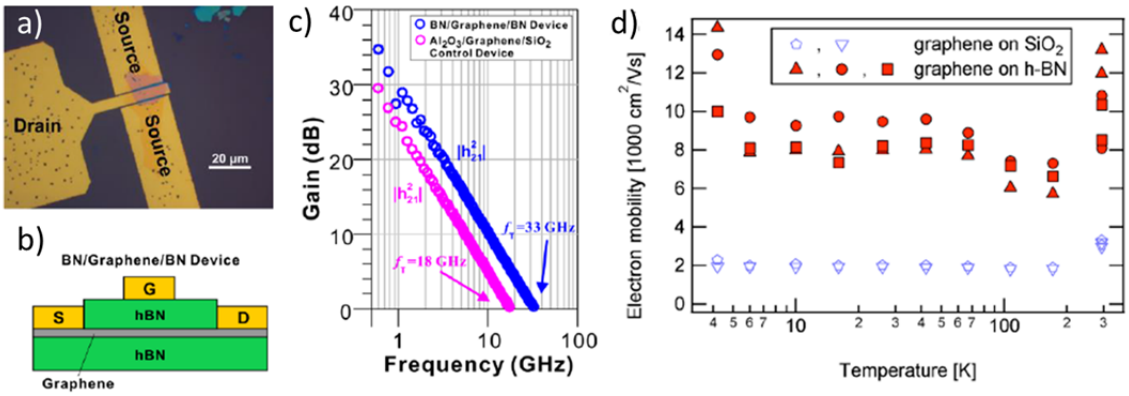

Figure 2.10: a) Optical image and b) schematic of an h-BN/graphene/h-BN device, and c) device performance of gain as a function of operation frequency, reprinted from Han et al. [91], © 2011 IEEE. and d) electron mobility enhancement in graphene on *h*-BN at various temperature as compared to graphene on SiO_2, reprinted with permission from Gannett et al. [92] from AIP Publishing.

Hexagonal boron nitride is also of interest as a key component as a gate dielectric in graphene and other 2D material-based electronic devices. With a dielectric constant of 6, breakdown voltage of 8-10 MV/cm, and bandgap nearing 6 eV [94-96], advantageous

over conventional SiO_2 dielectrics can be realized. In the first demonstration of an all-2D material device, exfoliated h-BN was the choice of gate dielectric with MoS_2 as the working material and graphene as the electrical contacts, providing for a unique device architecture based on all van-der Waals solids [4]. The thickness of *h*-BN in this instance was very thick in this case, around 55 nm. While this device exemplifies rectifying behavior with high quality interfaces between the materials, all of the 2D components were carefully exfoliated and placed in their given location. Thus, the meticulous device construction does not elude to further scale-up required for real world applications. Ideally, devices in the future can incorporate a directly grown synthesis method, such as CVD or PVD growth of *h*-BN, both described earlier. In addition the prospect towards flexible, transparent devices has also been explored [97]. Kim et al. [98] describes device-scale dielectric properties of the CVD grown *h*-BN, where at 15-19 nm, the film measures a dielectric constant of 2-4 with a breakdown of 2.0 ± 0.5 MV/cm. The decrease in breakdown and dielectric constant is attributed to the polycrystallinity of the *h*-BN films, potentially allowing for leakage through the grain boundaries. In order to incorporate *h*-BN as a gate dielectric material in next generation 2D devices, it appears that leakage through these boundaries will be critical with regards to dielectric and device performance.

2.4.2 Vertical tunneling device and behavior

In addition to boron nitride as a substrate material for graphene electronics, few-layer boron nitride has been investigated as a high quality, low dielectric constant barrier material for the 2D vertical electron tunneling devices where electrodes of different

compositions are separated by the layer thickness of the dielectric. These devices rely on the tunneling through the ultra-thin crystalline films layers and allow for the smallest allowable gate lengths down to a single atom, allowing for extremely fast transport.

Tunneling measurements through few-layer, exfoliated h-BN for device constructs is typically performed on a conductive substrate using conductive atomic force microscopy (C-AFM). With effective tip areas typically on the order of 10^3 nm^2, intrinsic property values of the dielectric can be evaluated that are not dependent on typical macro- or microscopic dielectric failure mechanisms including dust particles, cross-plane defects, and grain edges. From these measurements, I-V curves were be generated on pristine crystalline BN flakes of various thicknesses from Lee et al. [96]. At mono, by-, and tri-layer *h*-BN films, direct tunneling was observed as the dominant transport mechanism, shown in Figure 2.11a. Beyond this thickness, the resulting IV curves obeyed a more traditional breakdown behavior. This study indicates that four atomic layers of h-BN is the required thickness to restrict direct tunneling behavior in 2D *h*-BN. Similar studies were performed using a top and bottom graphene electrode setup, shown in Figure 2.11c from Britnell et al. [83]. This setup, using a C-AFM setup depicted in Figure 2.11d, can help identify the tunneling through the BN flake on a device-scale contact setup. With this technique, the thickness and corresponding resistance values can be mapped out as portrayed in Figure 2.11e and f.

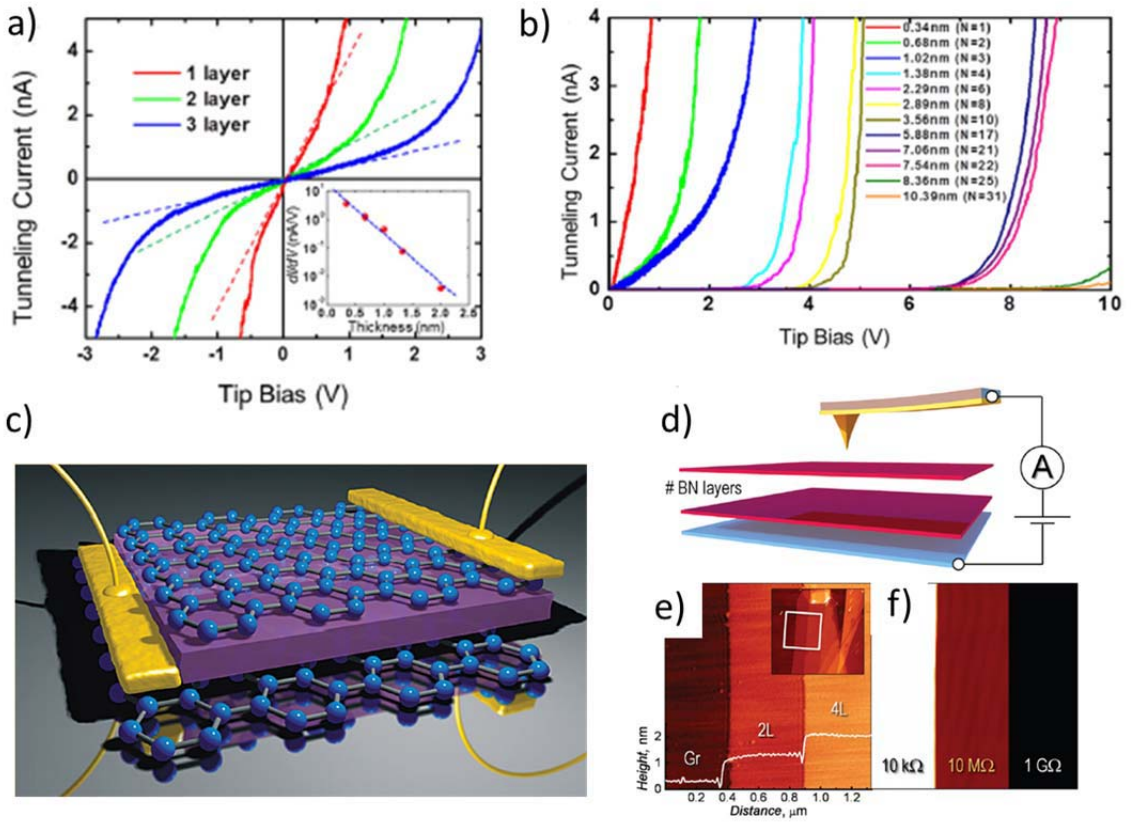

Figure 2.11: a) I-V curves generated from C-AFM studies on mono-, bi-, and tri-layer films, as well as b) thicker films up to 31 layers, reprinted from Lee et al. [96] with the permission of AIP Publishing. In addition, device studies using a setup described in c) and d), and resulting electrical resistivity behavior in multiple layers of *h*-BN in e) and f), all reprinted from with permission of Britnell, et al. [83], copyright 2012 American Chemical Society.

Figure 2.11b clearly shows that there are two regimes associated with tunneling in ultra-thin *h*-BN materials of thicknesses greater than three layers (not direct tunneling). At low biases, the I-V curves will start out linear and then eventually become exponentially dependent at higher biases (typically >0.5 V for monolayer h-BN). At the lower voltages, the tunneling barrier has not been significantly deformed by the applied electric field. Thus, the tunneling current is linearly dependent upon the applied voltage

and exponentially on the thickness of the layered material, as expected for direct tunneling [99]. The tunneling current at this regime can be modeled using the following relationship:

$$I(V) = \frac{A_{eff}\sqrt{m\Phi_B}q_e^2V}{h^2d} * exp\left[\frac{-4\pi\sqrt{m\Phi_B}d}{h}\right], \quad (2.1)$$

where q_e, m, d, and h are the charge of an electron, free electron mass, film thickness, and Planck's constant, respectively. The effective area of contact A_{eff} is typically the area of the contacted tip, and ϕ_B is the barrier height. Direct tunneling was only able to be completely resolved at thicknesses typically less than about 2 nm, as direct tunneling is not measureable in thicker films because of the low probability of electrons tunneling through the barrier.

At higher applied biases, the tunneling is dominated by field-emission tunneling across the barrier, and the voltage dependence becomes quadratic. In this regime, modeling using the Fowler-Nordheim tunneling theory [100] is performed with the following I-V equation:

$$I(V) = \frac{A_{eff}q_e^3mV^2}{8\pi h\Phi_B d^2 m^*} * exp\left[\frac{-8\pi\sqrt{2m^*}\Phi_B^{2/3}d}{3hq_eV}\right], \quad (2.2)$$

and in this relation, m^*/m is 0.26 for *h*-BN. The voltage is high enough at this point to alter the barrier characteristics and a significant reduction in resistivity is observed, leading to a breakdown in the dielectric characteristics within the material.

Determination of the barrier height is critical in understanding electronic behavior of a semiconductor or insulator and the interface of a metal. Depending upon the barrier height and the interface qualities, the Fermi level can potentially be pinned, resulting in

rectifying characteristics within the Schottky barrier. Using the above equations, the barrier height can be determined if the affective contact area is known. Lee et al. [96] measured the barrier height to be 3.07 ± 0.3 eV in h-BN, which is very close to that of traditional SiO2 dielectric (3.25 eV). Another critical piece of information that can be obtained from the C-AFM experiments on tunneling through crystalline materials is the dielectric breakdown strength. In Figure 2.11b, the breakdown strength is shown to be linearly dependent on film thickness up to relatively thick films. Using the constant current method [101], pristine h-BN exfoliated flakes appear to have measured dielectric breakdown strength of 8-10 MV/cm [83, 96], which, like to the barrier height, happens to be a very similar value to that of SiO_2.

2.4.3 Applications for *h*-BN in protective coatings

While certainly *h*-BN has been explored for use in nanoelectronic applications, other technologies utilizing the ultra-thin, layered material have come to life. Thin *h*-BN for corrosion and anti-oxidation coatings, in particular, is a technology that is enabled by the chemical inertness and high temperature stability of *h*-BN [102], to effectively seal the underlying material from exposure to a variety of elements. Initial studies indicate that grown of few-layer h-BN on Ni can withstand oxidation up to temperatures as high as 1,100°C, even in oxygen-rich atmospheres, as displayed in Figure 2.12, with an SEM before (a) and after (b) image [103]. In addition the weight gain as a function of temperature and several different coating thicknesses can be resolved in Figure 2.12c. The coating technique can also be used for other 2D materials, as graphene was shown in the same study to withstand oxidation up to temperatures of 1,000°C. The main reaction

associated with BN and oxygen involves the decomposition of the BN itself into boric acid under the following reaction [104]:

$$2BN + {}^{3}/_{2}\, O_2 = B_2O_3 + N_2$$

The large activation energy required to break this BN molecule (13 eV) lends itself to the explanation as a great anti-oxidation coating, where other oxidation reactions of the underlying substrates can be much lower energies of formation [103].

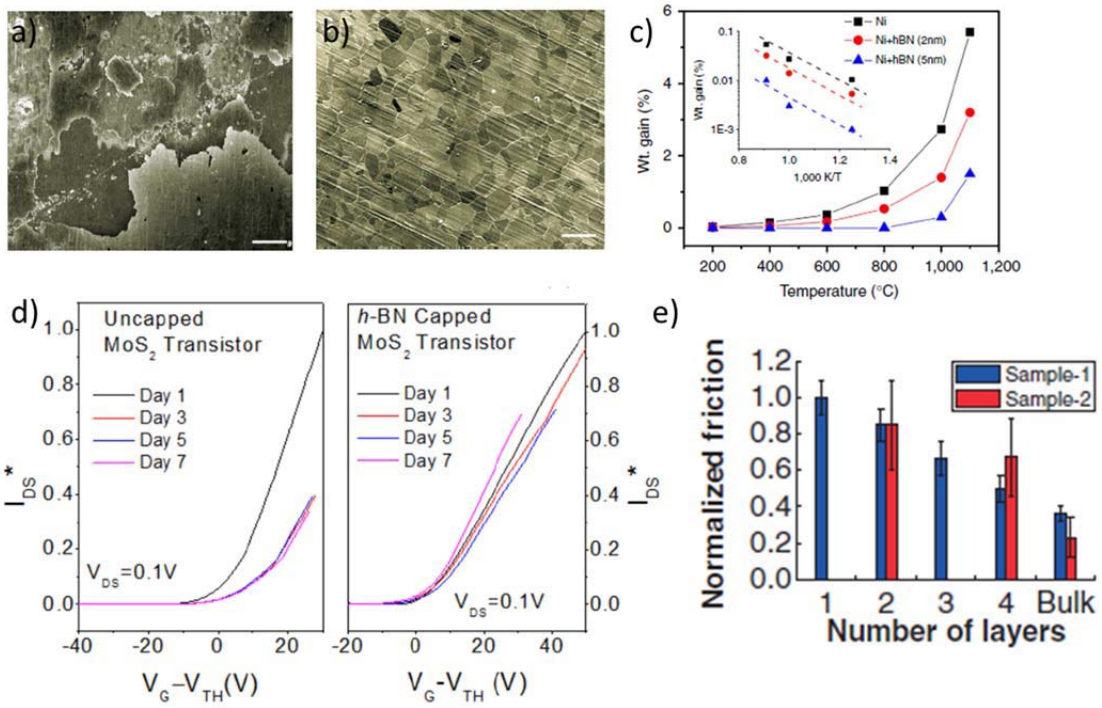

Figure 2.12**:** a) SEM images of nickel oxidation at 1,100°C without *h*-BN coating and b) with h-BN coating (no oxidation), and c) weight gain percentage at various temperature, showing the change in oxygenation at these conditions reprinted by permission from Macmillan Publishers Ltd: Nat. Commun. [103], copyright 2013, d) *h*-BN capped MoS_2 gas sensor showing 7 day degradation-free behavior, reprinted with permission from [105], © 2015 IEEE, and e) normalized friction as a function of layered thickness of the exfoliated *h*-BN material, reprinted from [106], reprinted with permission from AAAS.

The anti-oxidative properties, as well as the ultra-thin nature of 2D h-BN can also be utilized in sensing platforms to effectively seal the active material from the element, but not impede in the sensing capabilities. Take for instance, the study performed by Liu et al. [105], where an MoS_2 transistor setup was used to measure various gases including acetonitrile, ethanol, methanol, and various other gases. When the exfoliated *h*-BN cap protecting the MoS_2, the sensing ability was not degraded, and the life time of the device was extended to a full 7 days when capped, compared to 1 day of working life in the uncapped. IV curves as a function of length of exposure times are in Figure 2.12d.

Due to the inert nature and lack of dangling bonds, as discussed earlier, the *h*-BN material can be an excellent anti-friction coating, similar to many other 2D materials that share the same characteristics [106]. When reducing friction, a monolayer of coverage may actually be detrimental, and a thickness of at least a few layers may be required to reduce the frictional characteristics, as shown in Figure 2.12e. The mechanisms describing this phenomena involves the fact that single layers tend to induce "puckering," where the AFM tip creates out of plane deformation of the 2D material. This effect is then mitigated as the thicknesses increases, and the stiffness of the resulting layers restricts this. Still, flakes of *h*-BN and other materials pose to have a great impact in anti-frictional coatings in the near future.

While only a few sets of applications were touched upon in this section, there are a plethora of potential opportunities for the implementation of ultra-thin and 2D *h*-BN and *a*-BN thin films. Coupled with the exciting material properties, the emergence of a greater understanding of nucleation and growth procedures, and continued push for 2D

implantation into commercial devices, *h*-BN has a very promising future to directly impact many aspects of our daily lives for years to come.

2.5 Thermal transport behavior in 2D and ultra-thin materials

The similarity of the lattice structures, unit cell masses, and phonon dispersions [107] in 2D boron nitride and graphene lend to the observation of very high measured, room temperature in-plane thermal conductivities (k_L=360 W m^{-1} K^{-1} in suspended 5-layer h-BN [108] and above 2000 W m^{-1} K^{-1} in graphene [109]) and relatively low out of plane thermal transport in these materials ($k_{out\ of\ plane,h\text{-}BN}$ = 2 W m^{-1} K^{-1}). The in-plane thermal conductivity in 2D materials can be exceptionally high in relation to the bulk of the material, as quantum confinement in the vertical direction can lead to enhanced carrier mobilities in the plane of the crystal. Also, the weak van der Waals interaction between the layers, as well as high surface to volume raito ensures that the carriers move unimpeded in relation to typical 3D material configurations.

The in-plane thermal conductivity of bulk *h*-BN is reduced by a fifth, compared to graphite, due to the ionic nature of the B-N bond as well as isotopic impurities that are natural to the BN system (19.9% ^{10}B, 80.1% ^{11}B) compared to graphite (98.9% ^{12}C to 1.1% ^{13}C) [110]. The intrinsic in-plane thermal conductivity in *h*-BN is nearly 280 times higher than that for the most commonly used SiO_2 dielectric for current silicon electronic devices. This had led to the hypothesis that *h*-BN can allow for a significant enhancement in the lateral heat spreading and limit hot spot formation at critical device locations.

2.5.1 In-plane thermal conductivity of ultra-thin boron nitride films

The in-plane thermal transport in graphene [111-113] and related carbon materials has extensively been studied, where the thermal conductivity of the similarly structured boron nitride allotropes have only recently become of interest. Preliminary modeling studies using the phonon Boltzmann transport equation first reported in-plane thermal conductivity by Lindsay, et al. on single (SLBN) [114] and multilayer BN (MLBN) [115] using the following relation:

$$k = \frac{1}{D}\sum_j \int \frac{df_{BE}^{\circ}}{dT} \hbar\omega v_g^2 \tau d\omega, \tag{2.3}$$

where f_{BE}° is the Bose-Einstein phonon distribution function, $\hbar$ is reduced Planck's constant, ω is the phonon frequency, v_g is the phonon group velocity, τ is the transmission function, and D is an area term. For two-dimensional *h*-BN, this term can be expressed as $D=(2\pi)^2 N\delta$, where N is the number of layers of boron nitride and δ is the inter-layer spacing (0.333 nm for BN). The integral is evaluated over all of the possible phonon polarizations, which is 6N number of phonon modes for the case of graphene and *h*-BN (LA, TA, ZA, LO, TO, ZO for each layer). The Bose-Einstein distribution function, incorporating quantum statistics, is expressed as the following:

$$f_{BE}^{\circ} = \frac{1}{e^{\frac{\hbar\omega}{k_B T}} - 1}. \tag{2.4}$$

This expression relays the occupation number of phonons at a given frequency and can be any value, as it is not restricted such as the case for Pauli exclusion in electrons. In this expression an important observation occurs that as there is an increase in temperature, the occupation number of both the higher and lower frequency phonon states increases, as shown in an example distribution in Figure 2.13. The access to higher frequency

phonons at these higher temperatures increases the overall thermal energy that is carried by phonons, especially in the moderate to large wave vectors with large group velocities.

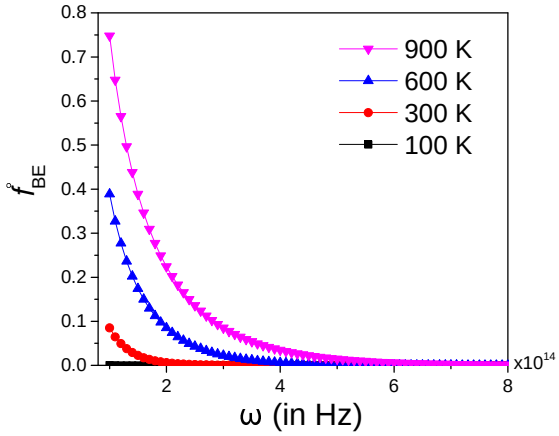

Figure 2.13: The Bose-Einstein distribution function at various temperatures.

One of the more difficult terms to identify in the Boltzmann equation is the transmission function, τ, as this can be a factor of many scattering mechanisms. The term highly depends on temperature and extrinsic system characteristics (e.g., substrate interactions, contamination), and a major source of effort in understanding thermal transport in these types of materials. One way to interpret the transmission function is by using the Matthiessen's rule for scattering events. For the case of *h*-BN, this will account for Umklapp scattering, scattering from isotopic impurities, and grain boundary scattering, and evaluated into an effective scattering rate, τ_{eff}^{-1}, as the inverse of the scattering time, expressed as the following:

$$\tau_{eff}^{-1} = \sum_{scat.proc.j} \tau_j^{-1} = \tau_{U,p-p}^{-1} + \tau_{bound.}^{-1} + \tau_{iso}^{-1}. \quad (2.5)$$

By evaluating each scattering term independently (and assuming that they act independently), a reasonable approximation for the probability of phonon transmission

in-plane can be realized. The Umklapp scattering, which dominates the restriction of heat transfer at higher temperatures because of reasons discussed earlier, can be modeled using Fermi's golden rule for three-phonon scattering or by simpler temperature dependent empirical correlations such as that from the $\tau_{U-p-p}^{-1} = BT\omega^2 e^{-C/T}$. The power law expression here is used in analysis of 2D materials, but is an approximation, as this Umklapp scattering model is more typically applicable to 3D configurations. The scattering term associated with grain boundaries many times is modeled as $\tau_{bound.}^{-1} = \frac{2|v_p|}{L}$, where $|v_p|$ is the average group velocity of the three acoustic phonon modes and L is the phonon mean free path (or in the case of nanocrystalline materials, the grain domain size). The isotopic scattering term is typically modeled using Fermi's golden rule [110]. This term contributes more to thermal conductivity at lower temperatures, however, and it is expected that room temperature contributions to thermal conductivity will be relatively minimal as compared to the phonon-phonon and boundary scattering. Other scattering terms need to be considered in thin *h*-BN film including impurity scattering from the polymer lift-off process as well as non-stoichiometric boron nitride scattering, which can be controlled by the deposition process and discussed in subsequent chapters.

Similar to graphene, it was reported that the acoustic phonons vibrating perpendicular to the layer plane, known as the ZA phonons [112], carry the majority of the heat conduction in *h*-BN. For graphene, these ZA phonons are predicted to contribute an order of magnitude higher to the overall thermal conductivity than the LA , TA, or the low group velocity optical phonon modes, as shown in Figure 2.14a from Singh et al. [112]. Further corroborating the impact of the ZA phonons is the increased measured

thermal conductivity in free-standing specimens than those measured on a substrate, as the out of plane modes are directly influenced by the boundary conditions in the z direction. The ZA phonons have the lowest average group velocity of the acoustic phonons, but have nearly an order of magnitude higher mode density, or the number of carrier half-wavelengths that can fit in a certain area. The mode density of a 2D material is defined as $M_{2D} = \frac{K(\omega)}{\pi}$, where *K(ω)* is the K-space dependence on frequency, or the dispersion relationship of the phonon mode of interest. The LA and TA dispersion relationship can be expressed using the Debye approximation (assumes a linear dispersion and the slope is the average group velocity), where $\omega(K) \approx v_{g,avg}K$, and the ZA mode exhibits a quadratic dispersion, $\omega(K) \approx CK^2$. The differences in dispersion relationships lead to the following mode densities for each branch:

$$M_{2D,LA} = \frac{\omega}{\pi v_{g,LA}}, M_{2D,TA} = \frac{\omega}{\pi v_{g,LA}}, M_{2D,ZA} = \frac{1}{\pi}\sqrt{\frac{\omega}{C}}, \tag{2.6}$$

where *C* is a constant (graphene *C*=5 x 10^{-7} m^2/s). A comparison of the phonon and electron mode densities of graphene from 0 to 50 meV (2 x k_BT) is plotted in Figure 2.14b from Fisher [116]. The availability of many modes for the ZA phonons at many different temperatures to traverse through the material is one of the main reasons why the ZA mode is the primary carrier of thermal transport in graphene and *h*-BN. It is important to note that Figure 2.14b is the number of modes calculated for graphene, which should be very similar to *h*-BN except for the fact that there is no free electron conduction in the insulating material and so the electron contribution to thermal transport will be significantly suppressed.

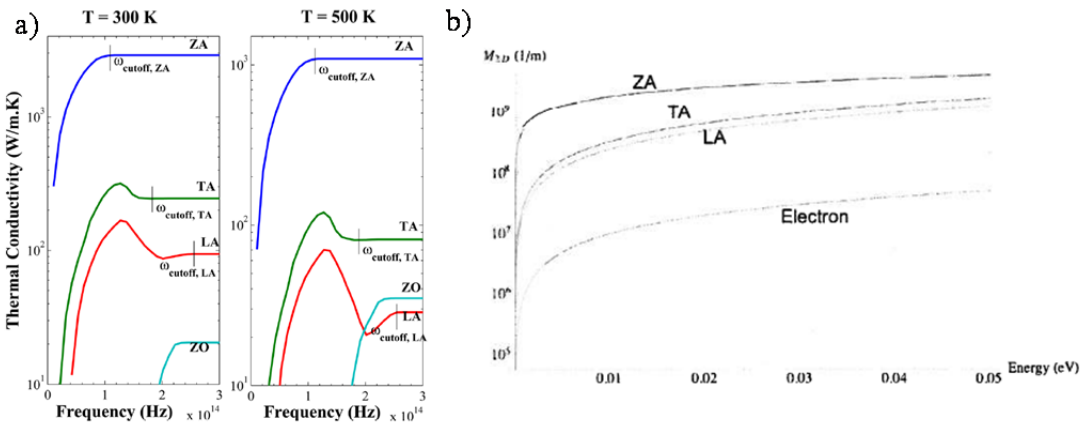

Figure 2.14: a) Thermal conductivity contributions from the ZA, TA, LA, and ZO modes in graphene as a function of phonon frequency, reprinted from Singh et al. [112] with permission of AIP Publishing, and b) the mode density of these modes and electrons in graphene at various energies up to 2 x k_BT, reprinted with permission from Fisher [116], World Scientific Publishing.

Understanding the fundamental scattering mechanisms within the material is required to comprehend the limits of the thermal transport, as they are highly influenced by temperature, external factors, and other material interactions. Initial computational studies in predicting *h*-BN in-plane thermal conductivity include the scattering contributions from anharmonic phonon-phonon interactions (mostly Umklapp scattering rather than Normal type), boundary scattering, and isotopic impurity scattering (present in *h*-BN and not graphene). These studies predict single layer boron nitride (SLBN) to have the highest in-plane thermal conductivity (κ_L at room temperature = 600 W/mK [114]) of bulk and multilayer h-BN, as the symmetry-based selection rule in monolayer 2D crystals strongly suppresses phonon-phonon scattering in the ZA direction, leading to a reduction in thermal conductivity of multi-layer systems ($\kappa_{L,MLBN}/\kappa_{L,SLBN}$ = 0.55), as shown in Figure 2.15a from Lindsay et al. [115]. The overall contributions from the in-

plane TA and LA contributions do not change with number of BN layers, but an increase in the out-of-plane ZA phonon mode arises at the monolayer thickness. This intrinsically makes sense, as the LA and TA phonons traverse in the plane and are not influenced by out of plane restrictions due to weak inter-layer coupling. The total thermal conductivity is then the sum of all of these acoustic phonon contributions and is represented as the black circles in Figure 2.15a. The hollow circles depict in-plane thermal conductivity of hypothetical non-isotopic BN systems. The high level of ^{11}B isotopes are natural in BN systems and result in a lower true thermal conductivity by as much as 38% in monolayer films.

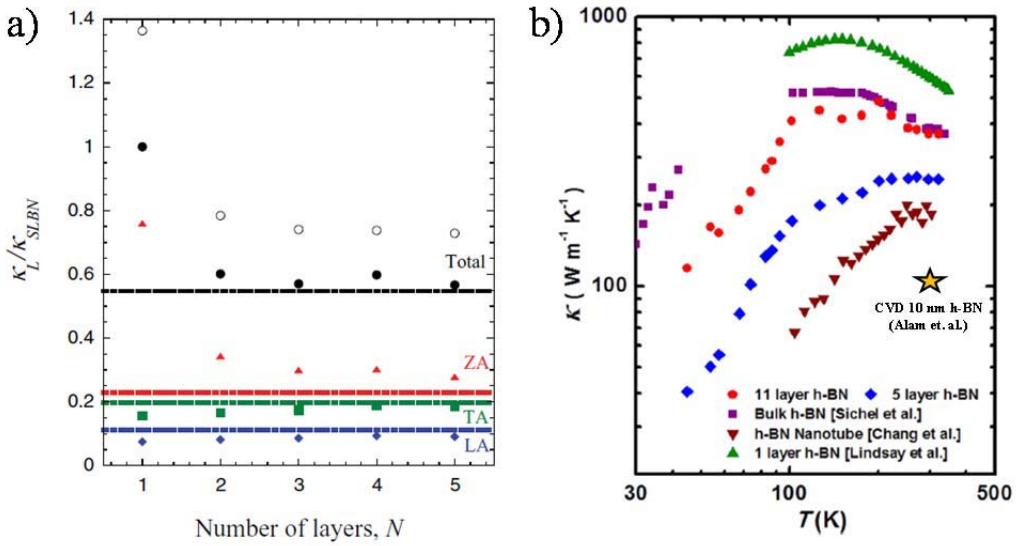

Figure 2.15: a) Calculated contribution to the ZA, TA, and LA phonons to overall thermal conductivity in 2D monolayer and few-layer boron nitride films, reprinted with permission from [115], copyright 2012 by the American Physical Society and b) Measured 11 and 5 layer *h*-BN thermal conductivity compared to bulk and monolayer *h*-BN, reprinted with permission from [108], copyright 2013 American Chemical Society.

It is well known that thermal conductivity is strongly a function of the temperature of the performed measurement, as the phonon density of states shifts and

populates higher frequency modes at elevated temperatures, as evidenced by the Bose-Einstein distribution function from Figure 2.13. In insulators, at temperatures closer to room temperature and above, the availability of higher energy, lower wavelength phonons makes the three-phonon Umklapp scattering more prevalent, which corresponds to a reversal of the phonon wavevector in the first Brillouin zone [116]. This reversal of the wavevector conserves energy but not momentum, and thus heat transfer is restricted in the initial direction of phonon transport by the three-phonon interaction. In considering anharmonic phonon-phonon interactions in 2D materials, three-phonon interactions such as Umklapp scattering are much more prevalent than comparable N-process as well as higher order processes such as four-phonon processes, which are estimated to be much weaker, even at higher temperatures [117]. At lower temperatures, other scattering mechanisms typically become more important, as the high frequency phonon density of states is not highly populated, resulting in very little Umklapp scattering. In exfoliated *h*-BN at temperatures typically below 100K, this contribution to thermal energy scattering is due to a high amount of ^{11}B isotopes as well as impurities induced from the lift-off process required to form free-standing films.

Measured in-plane thermal conductivity of 2D materials can be difficult, as isolation of the material from the substrate is necessary to restrict thermal transport into the substrate material. One established method to directly measure in-plane thermal conductivity of 2D materials is by suspending the material and using micro-Raman thermometry, explained in Balandin et al. [109]. The validity of the measurement technique has been of debate of recent, as the energy transfer process involves a photon-electron-phonon coupling process that is not well understood. Also, the computed

thermal conductivity from these measurements is laser spot-size dependent, revealing that the power absorption primarily leads to generation of longitudinal phonons with short lifetimes, which then have to decay to a ZA phonon mode [112]. Due to the low Raman response in *h*-BN, the technique is most likely not applicable in measuring thermal conductivity of boron nitride systems. To thermally isolate the *h*-BN from the substrate, a free-standing bridge must be created with two contact points, as elaborated in Jo et al. [108], as this allowed for direct measurement of thermal conductivity between two contacts. Thermal conductivity of exfoliated flakes was initially determined using the bridge setup for 5 and 11 layer specimens, and the results including previous measurements on bulk *h*-BN and calculations from SLBN can be shown in Figure 2.15b. The highest in-plane thermal conductivities were predicted in SLBN [114], and measured in the in-plane transport in the bulk form of the hexagonal crystal. The results from this initial study on in-plane thermal transport reflect the behavior in a nearly perfect crystal, as grain boundaries are estimated to be greater than the bridge length of 3 to 7.5 μm.

A more recent study by Alam et al. [118] performed a similar measurement technique, but used a bridge-type setup to measure thermal conductivity of non-pristine polycrystalline-BN growth by CVD. This technique was slightly different than that described in Jo et al. [108], as a thermal imaging camera calibrated to 0.1°C measured the temperature of material in between two electrode pads. In this manuscript, the in-plane thermal conductivity of CVD *h*-BN thin films of approximately 10 and 20 nm in thickness was found to be 100 ± 10 W m^{-1} K^{-1}. The measured thermal conductivity of BN with similar thicknesses to the exfoliated materials show a 50% decrease in thermal conductivity (data pointed added as a star Figure 2.15b), as the scattering at grain

boundaries becomes more prevalent and must be considered in the measurements of thermal conductivity.

The measurement technique is highlighted in detail in the same manuscript [118], and involves both steady state and transient measurement of heat flow by non-contact IR thermometry of the freestanding films placed on a micro-electro-mechanical heater setup. An image of the film configuration and heater setup is depicted in Figure 2.16a. Infrared (IR) thermometry images of the heater and the supported *h*-BN film is shown in Figure 2.16b. In addition, a magnified IR image depicting the one-dimensional heat flow experiment in shown in Figure 2.16c and a simple pin-fin schematic in Figure 2.16d.

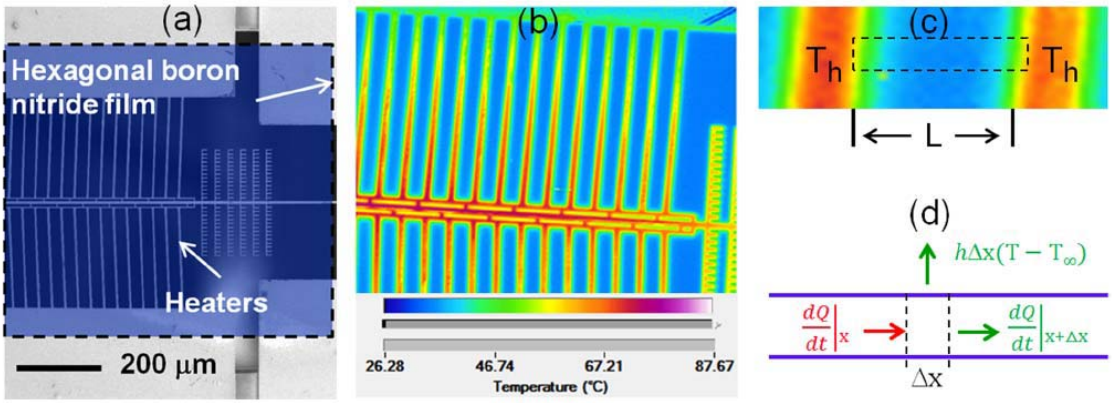

Figure 2.16: a) Image of *h*-BN film on micro-electro-mechanical heater device, b) IR thermometry image of the heater supporting the h-BN film, c) close-up of one-dimensional heat transport behavior, and d) energy balance schematic of one-dimensional heat flow with and included term for losses to the ambient all, reprinted from [118] with the permission of AIP Publishing.

With the one-dimensional heat transfer analysis and methodology described in Alam et al. [118], the thermal conductivity of a calibration sample composed of pure silicon was measured to be 140 W m^{-1} K^{-1}, which is very close to reported literature value. The measured and modeled data of the *h*-BN films deposited by CVD is observed in

Figure 2.17 along with the best model fit for the 20 and 10 nm samples, revealing a thermal conductivity of about 100 W m^{-1} K^{-1}. The hypothetically modeled conductivity of 110 W m^{-1} K^{-1} is displayed as a dotted line and represents a poor fit for the experimental data, indicating that the error in the steady state measurement technique is less than 10%. The steady state technique can also be further validated by the use of transient IR microscopy measurements of thermal diffusivity, α, which is directly related to the density, specific heat, and thermal conductivity. In the analysis of the transient heat dissipation in the freestanding films, the thermal conductivity was measured to be 93 and 97 W m^{-1} K^{-1} for the 20 and 10 nm specimens, respectively, well within 10% of the steady state analysis.

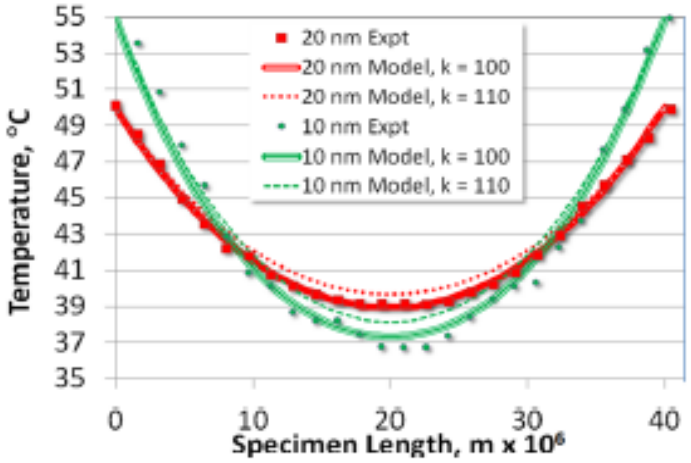

Figure 2.17: Temperature profile of thermal IR measurements of 10 and 20 nm *h*-BN along with modeled conductivities, reprinted from [118] with the permission of AIP Publishing.

Non-exfoliated growth techniques of *h*-BN by means of CVD or PVD will induce the formation of grain boundaries and other scattering mechanisms, and these factors will

be important to understand for the true measurement of thermal transport for device applications. The freestanding technique, among others, described herein can allow for measurement of thermal conductivity under different film qualities. Understanding these limitations regarding in-plane thermal transport will be key in next generation electronics thermal management.

2.5.2 Thermal conductance at BN interfaces

The high in-plane thermal conductivity of *h*-BN has hypothesized to be a main driving force towards integration into next generation nanoelectronic systems, as the ability to spread heat laterally away from the active region could be a mechanism to push to higher power systems that will not overheat. An additional transport mechanism that will become important, especially as the gate lengths are minimized to only a few nanometers, is the interface thermal conductance out-of-plane of the thin layers within the 2D device. As a traditional device is also limited in space, 3D heat dissipation may become especially important, where the lateral distance between device elements can be very small.

Studies of 2D material/metal interface conductance have been performed on graphene [119] and other thin film transition metal dichacolgenide interfaces [120] using time domain thermoreflectance (TDTR). The described technique uses a two-color laser system to evaluate thermal transport at the interface between metal and the underlying substrate. The interface thermal conductance is measured by first sending a “pump” beam to apply heat to a metal-coated substrate and then delaying the time for the “probe” beam to hit the sample. Due to differences in the thermal reflectance properties at

different temperatures, the probe beam will have a different reflectance response at various temperatures. Therefore, by changing the delay time associated with the probe beam, a change in reflectance per unit delay time can be evaluated and an understanding of the thermal response of the material at the metal/substrate interface can be gained. The measure of the in-phase and out-of-phase signals measured with a lock-in amplifier are plotted then as a function of the delay time, which results in the generation of an effective cooling curve. For these measurements, a femtosecond laser system is required, as the spot size can be very small (10μm in diameter) and the pulse length is short enough to restrict significant amounts of conduction laterally or into the bulk substrate. This high aspect ratio of laser spot size to penetration depth makes the TDTR technique selectively sensitive to one-dimensional thermal transport in the direction perpendicular to the sample surface. The thermal interface conductance of the thin film can then be fit to the model elaborated by Cahill [121].

In evaluating the thermal interface conductance of thin 2D materials such as graphene, where the heat from the pump beam will certainly traverse the graphene and penetrate into the bulk substrate, an effective conductance is measured that describes a combination of thermal resistances within the material. Effectively, the comparison is made between the conductance at a metal/substrate interface and the conductance of the system with a 2D material between the same interface. With this approach, in measuring the interface thermal conductance of the ultra-thin BN, the evaluation must be treated as a change in the effective interface conductance between the two materials as the BN/metal and BN/substrate interfaces are compiled into an “effective” conductance term.

Interface thermal conductance has been shown to also depend on properties of the metal contact including the atomic mass difference between the 2D material and Debye temperature of the metal [122]. In graphene, it was determined that the interface conductance was primarily limited by transmission of phonons between the metal and graphene, and not due to electron-phonon scattering. Also, there was not much of a restriction in thermal conductance upon addition of up to 10 graphene layers, as shown in Figure 2.18. The phonon dominated heat transport should definitely be the case for boron nitride, as electron phonon scattering is limited in insulators due to very low free electron mobility. Understanding the phonon modes and the mismatch between the contacts and graphene was vital to ensure good thermal transport. Metal contacts with high Debye temperatures (e.g., Cr, Ni, Ti, Al) are hypothesized to be necessary to increase transport because of the better energy match between the phonon modes of graphene and metal [119].

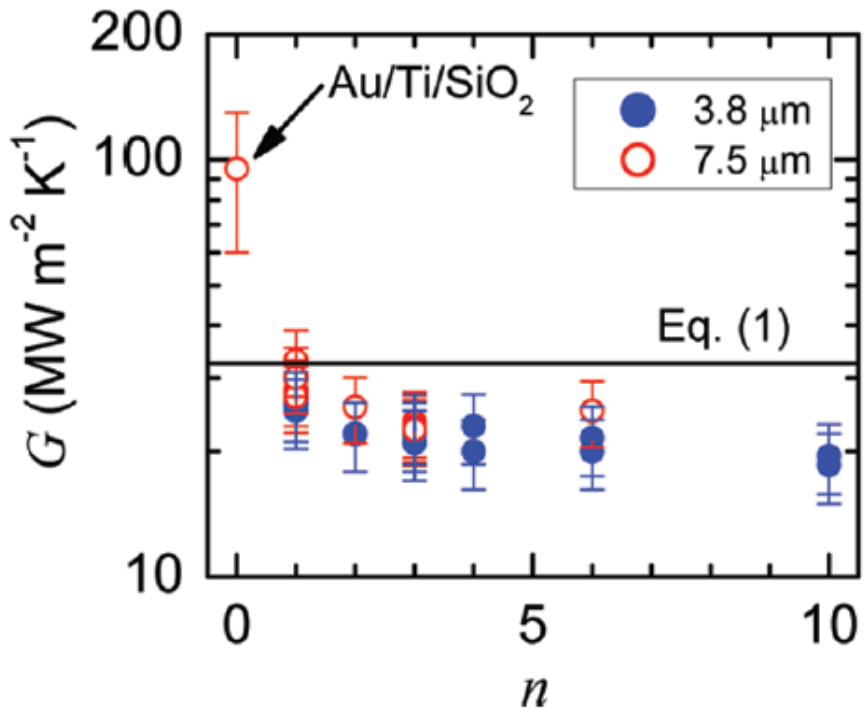

Figure 2.18: Interface thermal conductance between graphene and Au/Ti contacts at various graphene thicknesses (n), reprinted with permission from [119], copyright 2010 American Chemical Society.

In graphene field-effect transistors (GFET), it has been shown that for gate dimensions less than 600 nm, the thermal conductance at graphene/metal contacts will become increasingly important. The dominant path to heat dissipation is governed by the thermal healing length, expressed as the following:

$$l_h = \sqrt{\frac{d k_{in-plane}}{G}}, \tag{2.7}$$

where d is the thickness of graphene, $k_{in\text{-}plane}$ is the thermal conductivity, and G is the thermal conductance. The thermal healing length estimates the length in the plane of the graphene material where the temperature profile due to the Joule heating becomes relatively flat. At this point, the out-of-plane thermal transport will become important, as

predicted in multiple thermal transport studies [119, 123]. In the measurements described in Koh et al. [119], length scales less than twice this characteristic length, the heat dissipates from the graphene through the metal contacts. If the length scale is greater than twice the characteristic length, the phonons will preferentially dissipate to the substrate. The total thermal conductance of a stacked Au/Ti/graphene/SiO_2 heterostructure was measured to be approximately 50 MW m^{-2} K^{-1}, with little dependence of the effective thermal conductance on graphene thickness [119]. The conductance result, G, leads to a calculated thermal healing length, l_h, from the expression above for graphene on a 100 and 300 nm SiO_2 wafer to be 180 and 290 nm, respectively. The thermal transport at graphene/metal and graphene/substrate interfaces have been investigated as means to enhance thermal transport in the out-of-plane direction; however, one of the major locations for hot-spot formation occurs near the gate dielectric. If *h*-BN is set to be a perfect dielectric material for these graphene devices, understanding the thermal transport at the dielectric interfaces is necessary.

2.6 Summary of the literature review and objectives of study

Two-dimensional materials have been one of the fastest growing and exciting fields of scientific research, with the potential to revolutionize a multitude of technology areas. As discussed, one of the major limitations of single layered structures is lack of reliable, repeatable, and large area synthesis techniques at reasonable temperatures and growth times. Hexagonal-boron nitride, in particular, has proved to be especially difficult to synthesize in the 2D form due to the inert surface structure, high required deposition temperatures, and poor device-scale dielectric performance. Synthesis routes

including exfoliation, chemical vapor deposition, and physical vapor deposition are the most explored routes to overcome the current material limitations. Exfoliation of bulk van der Waals *h*-BN allows for the highest crystal quality, perfect for lab-scale device testing, but suffers from a lack of reliable scale-up potential. The most popular direct growth technique, chemical vapor deposition, is driven by thermodynamic crystal growth processes at high temperatures and high quality materials with strict control of film thickness are easily synthesized. However, the resulting triangle domains and non-uniform surface coverage have major hurdles to overcome. In contrast to the thermodynamic CVD processing, physical vapor deposition can allow for a very large area, uniform coating, but the high flux rates and plasma energies restrict the growth of large domains. A very small effort has been made in this area with regards to 2D *h*-BN, with an emphasis specifically on reactive magnetron sputtering and molecular beam epitaxy. Pulsed laser deposition has been a common technique in the late 20th century for synthesizing high quality, thick BN films for hard, high temperature resistant coatings. Due to the relative stoichiometric plasma conditions at plasma energies reasonable to not create defective films, this technique could be a perfect choice for device-scale BN films for next generation 2D material systems. In addition to the absence of scalable synthesis routes, the 2D hetrostructured device development is also restricted by a lack of fundamental knowledge of how the properties and structure of the dielectric material will impact the device performance.

The current study is centered around the PLD deposition technique and exploring the possibility of using PLD-deposited boron nitride for nanoelectronic systems. Objectives in this dissertation include the following:

1. Using optical spectroscopy techniques, fundamentally understand critical plasma conditions including chemistry, plasma energies, spatial distribution, and proper growth conditions to aid in the understanding of 2D, ultra-thin boron nitride material nucleation and growth.
2. Evaluate the temperature dependence and proper surface conditions for formation of 2D *h*-BN at reduced substrate temperatures and over large areas.
3. Explore the possibility of other allotropes of BN, including amorphous and other crystalline variants that are grown at reduced substrate temperatures or on non-lattice matched substrates, and the impact on intrinsic electronic properties crucial to device performance.
4. Explore transport characteristics critical for device performance including electron mobility in the channel, thermal transport in the dielectric, and thermal conductance at devices interfaces will be explored, with a goal of understanding the influence the dielectric material has on 2D devices.

CHAPTER 3. TEMPORALLY AND SPATIALLY RESOLVED PLASMA SPECTROSCOPY IN PULSED LASER DEPOSITION OF ULTRA-THIN BORON NITRIDE FILMS

Chapter 3 derives predominantly from the following published manuscript:

Nicholas R. Glavin, Christopher Muratore, Michael L. Jespersen, Jianjun Hu, Timothy S. Fisher, Andrey A. Voevodin, "Temporally and spatially resolved plasma spectroscopy in pulsed laser deposition of ultra-thin boron nitride films," *Journal of Applied Physics* **117,** 16, (2015).

3.1 Motivation and background info

Optical spectroscopy is a non-invasive technique used to evaluate plasma emissions in order to understand nucleation and growth mechanism involved in the high quality growth of thin films. In this case, the relative intensity and dwell time of ionic and neutral boron and nitrogen species is evaluated at different processing conditions to formulate and design the growth conditions in order to optimize film chemistry, thickness, and surface roughness.

3.2 Experimental methodology

Ultra-thin amorphous boron nitride films were deposited in an ultra-high vacuum chamber with residual base pressures of 2×10^{-9} Torr. Ablation from an amorphous

boron nitride target (99.99 % pure) was carried out using a Lambda Physik LPX300 248 nm KrF excimer laser at pulse energies of 900 mJ/pulse, 30 nanosecond duration, and 1 Hz repetition rate. A focusing lens reduced the laser spot size to an area of 2 mm x 3 mm with a flux of 22 J/cm^2 upon impact with the target. All of the samples in this study were grown at room temperature and without rotation of the sample.

Depositions were performed in nitrogen background gas, where pressure was controlled by a butterfly valve to preset values within 10^{-4} to 100 mTorr range and keeping the flow of ultra-high purity nitrogen gas (99.9999%) at 30 sccm. Films were grown at various conditions and the thickness of the films was controlled by the number of laser pulses impacting the target material. After deposition, the substrate was allowed to cool to room temperature before removal from the vacuum chamber. A schematic of the deposition chamber and process is shown in Figure 3.1. Different target-to-substrate working distances of could be adjusted using various spacers that altered the target holder length. The target was oriented 45 degrees to the substrate surface and the substrate was rotated continuously to encourage film thickness uniformity.

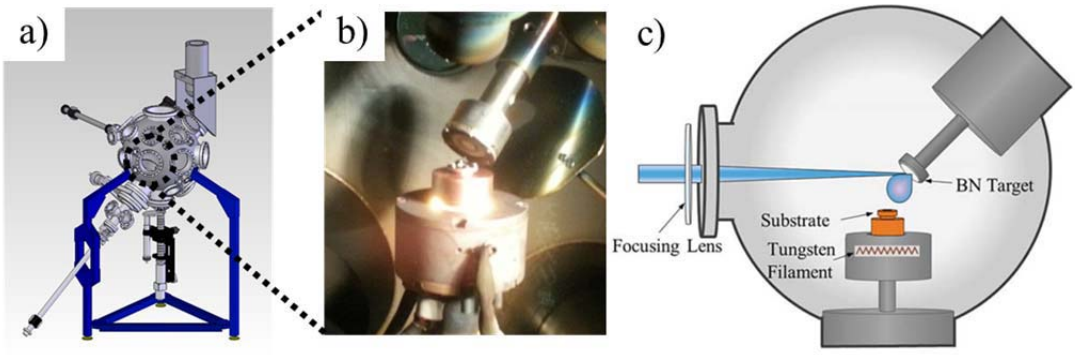

Figure 3.1: a) Computer schematic of deposition chamber setup, b) image of target and substrate inside chamber, and c) schematic of inside the deposition chamber.

Spectroscopic analysis was performed on two distinct regions within the ablated plumes to evaluate plasma compositions both close to the target (Region 1) and adjacent to the substrate (Region 2), as in Figure 3.2. A focusing lens assembly coupled to a fiber optic guide focused the collected area to approximately 2.5 cm in diameter. The fluorescent light was captured by adjusting the slit width between 1 and 20 microns at the entrance of an Acton Research Spectra Pro 150 monochromater connected to a high speed Princeton Instruments 576-S/RBE image intensified charge-coupled device (ICCD) detector. The spectrometer was calibrated using a HeNe light source and maintained a calibration threshold of ±0.1 nm across the spectrum window and in the high resolution scans. A 1200 l/mm grating and a 150 l/mm grating allowed for collection of both high resolution spectra at narrower wavelength windows, and lower resolution spectra at broader windows, respectively. Broad spectra of Region 1 and 2 were initially accumulated upon laser impact on the target and extended to10 μs which was well after any residual plasma emission was detected in either region. Time of flight measurements were performed with the use of a gated pulse generator (Princeton Instruments Model PG-200) at a 200 ns delay from the laser pulse, and high resolution spectra were collected at increments of 200 ns steps and a 200 ns gate width. High resolution spectra were taken at each 200 ns increment for intensity measurements. Peak identification was completed by comparing to spectral lines of atomic excited species in the NIST database [124] and molecular band spectral lines of characteristic N_2 and BN emission systems [125]. Plasma images were captured using a focus zoom lens coupled to the ICCD detector array and each image corresponds to an individual laser pulse. Narrow bandpass filters

(10 nm FWHM) were used for isolation of atomic nitrogen gas emissions (400 nm and 750 nm filter) for imaging, each with a transmittance of approximately 50%.

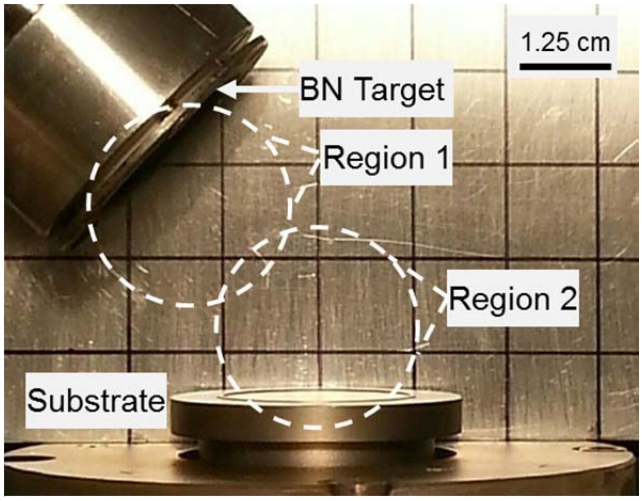

Figure 3.2: Image inside growth chamber indicating locations for BN target, substrate and two collection regions used for spectroscopic analysis.

The numerical intensity values accumulated via spectroscopy techniques are dependent on multiple variables including the spectroscopic data collection setup (i.e. slit width, gain on the detector, gate width, timing mechanism), the Einstein coefficient of the electron transition (rate of photons emitted/time), the concentration of atomic species, the probability of a given electron transition state, and the dwell time of that species within the spectroscopic collection window. Thus, in all comparative studies, the camera and spectrometer settings remained constant within that data set to allow for direct relative comparison of plasma emission phenomena. Scans within each data set were performed in succession and the target was re-polished frequently to avoid any surface morphology changes which can alter the ablation plume dynamics.

3.3 Spatially-dependent plasma behavior

Emission spectra collected at two specific regions between the target and substrate indicate differences in energies and compositions due to collisions of the ablated plasma species with the background gas during initial formation and transport of the plume within the growth chamber (See Figure 3.2). In region 1 of the spectroscopy collection window, localized pressure and temperature increases due to rapid evaporation of target material, typical of those observed in pulsed laser deposition experiments, cause the formation of species including ionized boron B^+ (345.1 nm) and B^{2+}(448.7 nm), ionized nitrogen N^+ (395.5 and 399.5 nm), and lesser emitting excited neutral species B* (582.1 nm) and N*(748.6 nm), as shown in Figure 3.3. The background gas composition and pressure had little influence on the emission spectra close to the target surface because collisional interactions with the nitrogen gas are limited, as the plasma is initially confined within dense adiabatically expanding ablated plume and observed excitations originate from species formed from the BN target. In particular support of this assertion is the observation that the spectra in this region do not indicate the presence of molecular nitrogen in either the vacuum or gas case. The presence of a doubly ionized B^{2+} species is unique to this region close to the target surface, and has been observed in other ablated BN plasmas[47] when laser energies exceed 20 J/cm^2. These B^{2+} ions have a short life time and recombine quickly with plasma electrons, forming the more stable B^+ species. Plasma images shown in the inset of Figure 3.3 depict the similarities in emission intensities and spatial distributions of the plasma at the first 600 ns after the laser pulse when the majority of the plasma is still within the Region 1 collection area.

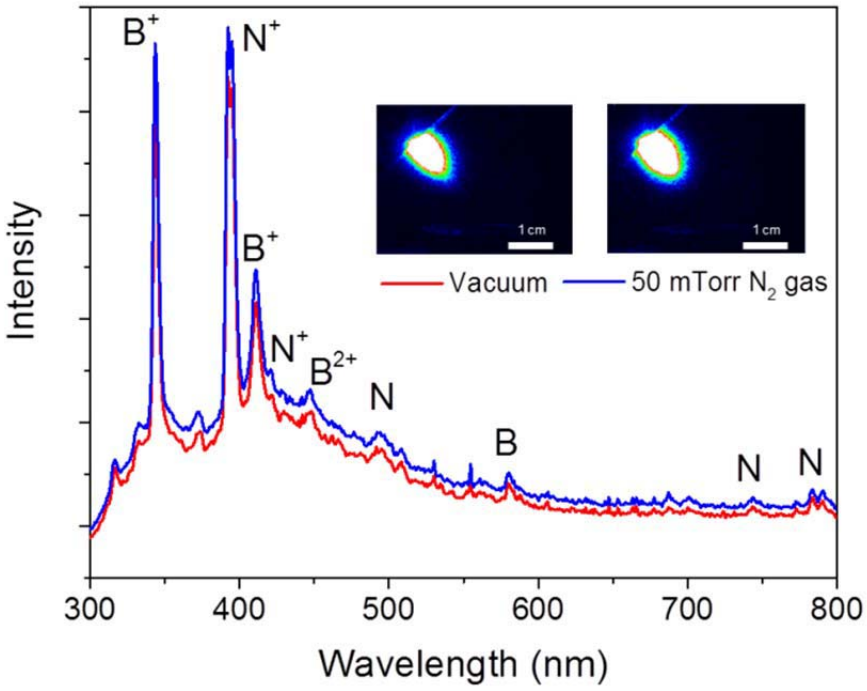

Figure 3.3: Broad spectra from Region 1 of ablated plasma from a BN target in vacuum and in 50 mTorr nitrogen gas, and the inset images depict plasma emission 600 ns after the laser interacts with the target at the indicated pressures.

In the collection region adjacent to the substrate surface (Region 2 in Figure 3.2), the plasma plume experiences changes in energies and compositions as the pressure within the chamber increases. In ultra-high vacuum conditions, the accelerated ablated particles travel quasi-ballistically from target to substrate, as the mean free path for collisional interactions is much larger than the distance between target and substrate. As molecular nitrogen species are added to the chamber, a much shorter mean free path and an increased probability of multiple collisional interactions are expected. Many of the emitted species are common in both the vacuum and gas conditions, however, the peak height of the emission intensities is about an order of magnitude higher with the inclusion

of a background gas at a pressure of 50 mTorr (scale bars in Figure 3.4 for vacuum and 50 mTorr spectra represent 10,000 counts and 100,000 counts, respectively). This change is due to the plume confinement within the collection region, resulting in a longer dwell time and more collisional excitations of ablated species with the nitrogen background gas. A much more comprehensive compilation of individual higher resolution scans of the entire frequency measured are shown in Appendix B.

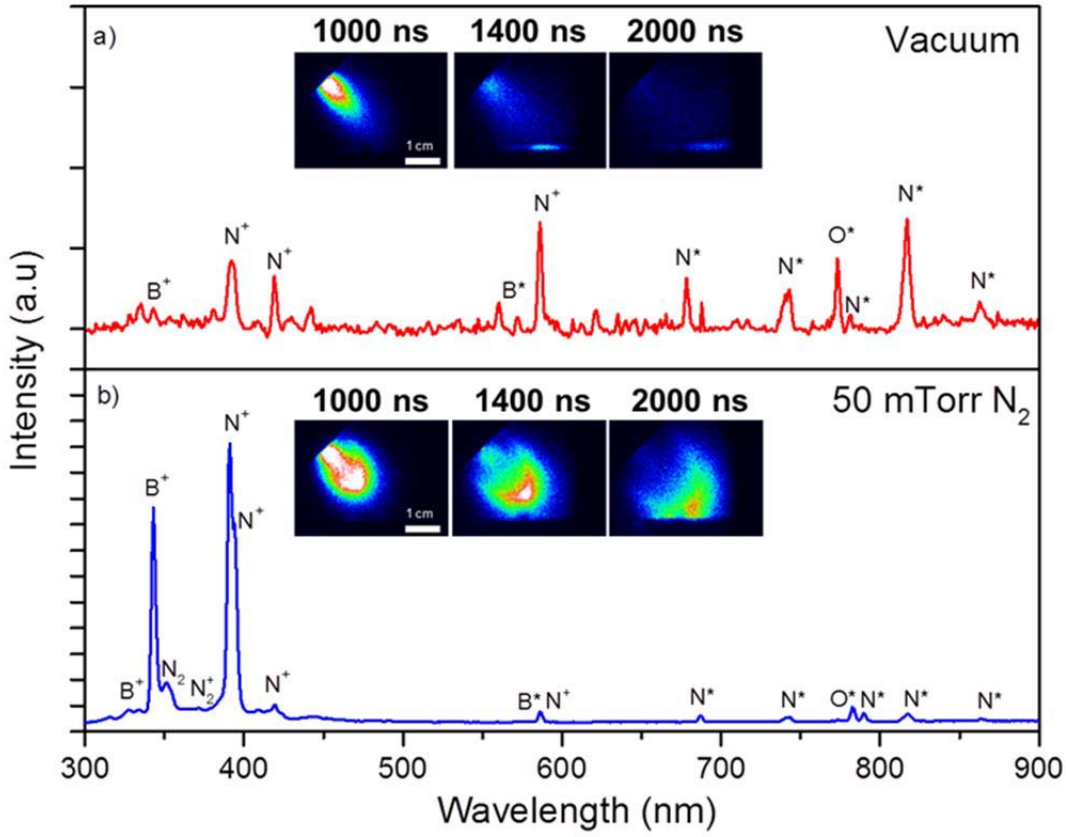

Figure 3.4: Broad spectra from Region 2 of ablated plasma in a) vacuum and b) 50 mTorr. The scale bars for vacuum and 50 mTorr spectra are 10,000 counts and 100,000 counts, respectively. The inset of each graph displays plasma imaging of full spectra as a function of time after the laser pulse for each corresponding pressure condition.

Plasma images in Figure 3.4 also display the confinement of the plume in the collection window and very different plasma distribution at longer times after the laser pulse and in the region close to the substrate surface. The presence of ionized atomic boron B^+ (317.93 and 345.1 nm) and ionized atomic nitrogen N^+ (395.5, 399.5, 422.8, 594.3 nm) dominate the spectra upon the inclusion of nitrogen background gas, as both long-lived species are able to retain their ionization within the collection window at a high concentration. The strongest peaks in the spectrum belong to singly ionized boron and ionized nitrogen, but the contribution to neutral nitrogen is stronger than that of neutral boron, as the presence of excited neutral boron B* (582.1 nm) and nitrogen N* (648.5, 742.4, 744.3, 746.8, 818.5, 820.0, 821.1, 827.6, 822.3, 822.2, and 868.12 nm) are observed mostly in the near-infrared. The presence of the neutral excited nitrogen species is unique to this wavelength region, as many other spectroscopic studies of BN ablated plasma do not report this species in any other frequency range. The first ionization potential for metallic boron of 8.3 eV minimizes the concentration of neutral boron, as the ionization process in high energy plasmas occurs fairly easily. The more electronegative nitrogen is known to have a higher ionization energy of 14.5 eV, which results in the larger number of peaks of the neutral nitrogen than the neutral boron. Unlike region 1, the presence of the doubly ionized species of boron is absent, as the energy required for this ionization is 25.2 eV, more than three times higher than the first ionization energy. Molecular neutral and ionized molecular nitrogen gas, N_2 (313.6, 315.9, and 337.1 nm) and N_2^+ (391.4 , 423.7, and 427.8 nm), respectively are observed, but only in the presence of a background gas and is not observed in the vacuum condition. The primary band system $A^3\Pi \rightarrow X^3\Pi$ of the BN molecule, occurring between 340 and

400 nm, has relatively weak emission intensity compared to the atomic emission, and can be further masked by intense peaks of ionized boron at 345.1 nm and the second positive system $C^3\Pi \rightarrow B^3\Pi$ of excited molecular nitrogen N_2 from 350 nm to 400 nm. This has led to assumptions that the recombination reaction to form BN is not dominant in the plasma [79] and likely to occur at the substrate surface [77]. In select cases, including this study, observation of the boron nitride radical can be resolved. The observed vibrational transitions of BN match fairly well with similar molecular peaks reported by Dutouquet et al. [80] (v'=1,v"=1 at 362.5 , v'=3,v"=3 at 368.2 nm, v'=0,v"=1 at 380.3,and v'=2,v"=3 at 385.6 nm). In the vacuum condition, the BN radical presence was not detected.

3.4 Temporally dependent plasma behavior at the substrate location

Time of flight measurements of the intensity of major peaks associated with B^+ (345.1 nm), N^+ (395.5 nm), and N* (748.8 nm), and N_2^+ (391.4 nm) in region 2 at background pressures from 5 mTorr to 100 mTorr are shown in Figure 3.5. The formation and decay mechanisms for each emitting species change as collisional interactions with the background gas alter plasma energies, concentrations, temperatures, and dwell times within the collection region. Ionized boron, B^+, is formed solely from the target ablation and ionization of small amount of neutral boron in the plasma plume. Boron, being the lighter of the two species (atomic weights: B=10.81, N=14.01), will escape the Knudsen layer of plasma plume at higher velocity and reach the surface before the neutral or ionized nitrogen. However, the atomic radius of the boron is larger than that for nitrogen, as the collisional cross section is approximately 31% larger. The larger

radius, low ionization energy, and the fact that the only creation mechanisms in the plasma are from ionization of neutral boron and from the ablation process, results in a maximum in boron emission intensity at the substrate at a pressure of 50 mTorr. At pressures less than 50 mTorr, the ionized boron species move quickly towards the substrate and are dispersed quickly. The electron density at gas pressures approaching 50 mTorr is sufficient to maximize the number of B^+ ions. At pressures higher than 50 mTorr, the plasma system is becoming depleted of electrons, in part from the dissociative recombination reaction of the background gas, and the plume begins to become thermalized, reducing the concentration of ionized boron. From the maximum locations in time of flight data in Figure 3.5a, kinetic velocity of the majority of the B^+ species arriving at the substrate was found to decrease from about 35 km/s at 5 mTorr pressures to 22 km/s at 100 mTorr, indicating the collisional deceleration of B^+ species in background gas. These estimated average speeds are consistent with that reported in the early studies for BN ablation in nitrogen background [79].

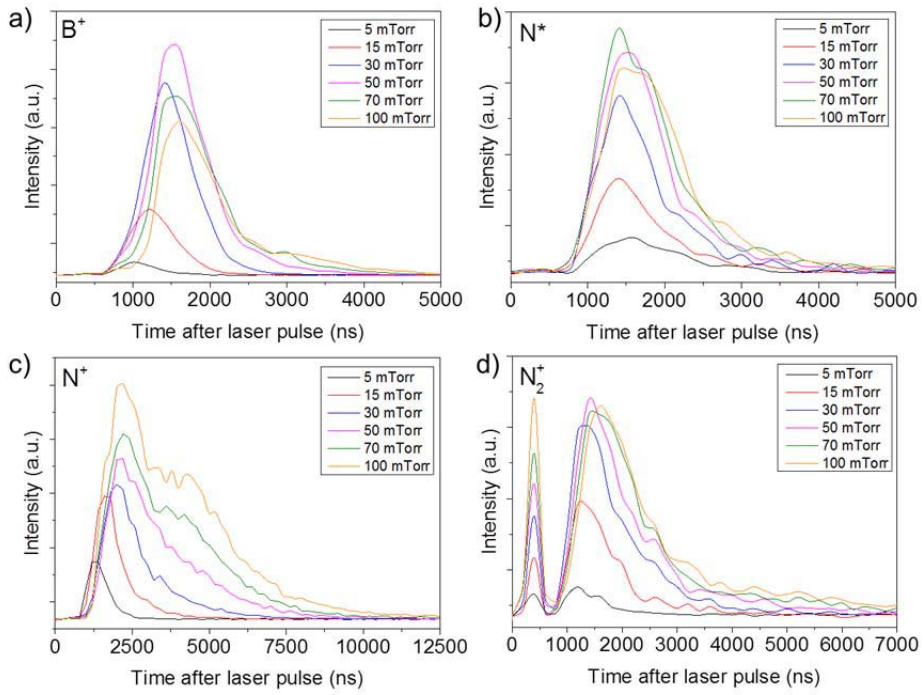

Figure 3.5: Time of flight intensities for a) B^+ (345.1 nm), b) N* (748.8 nm), c) N^+ (395.5 nm), and d) N_2^+ (391.4 nm) peaks in Region 2 from ablation of a BN target.

The near substrate emission from atomic neutral nitrogen species, N*, increases with background pressure, and reaches a maximum at pressures around 50 mTorr. Beyond that pressure, the confinement of the plume is enough to restrict propagation of the N*, as well as increase the reaction time with the ionized boron to form BN at the interface. Unlike the ionized boron species at higher pressures, the maximum intensity of N* saturates beginning around 50 mTorr and the maximum location is not considerably shifted with the increased pressure. This indicates that in addition to atomic nitrogen generated from the target surface, a significant contribution is also due to dissociation and ionization of the background nitrogen in collisions within the shockwave front of the

plasma plume, which formation is confirmed for pressures above 30 mTorr from plasma plume imaging studies discussed later.

Ionized atomic nitrogen is the longest living emitting species characterized within the plasma system, as the decay mechanism is dominated entirely by impact with the substrate and chamber walls [79]. The peak emission time for this species is nearly 600 ns after the peak emission time for both neutral nitrogen and ionized boron. Competing mechanisms for the formation of the ionized nitrogen include species formed from the ablation process, separation of N_2 directly to N^+ from a high energy collision, ionization of neutral nitrogen, secondary ionization from collisions with the substrate, and the following gas dissociation reactions:

$$N_2 \rightarrow N_2^+ + e^- \qquad (1)$$

$$N_2^+ + e^- \rightarrow 2N \qquad (2)$$

$$2N \rightarrow 2N^+ + 2e^- \qquad (3)$$

The proposed reaction mechanism occurs readily in the nitrogen plasma as collisions with electrons, atomic, and molecular species at high energies cause decomposition of molecular nitrogen and quickly form atomic nitrogen, which then lose an electron and form ionized nitrogen. The ionization mechanisms described in reaction (1) and (3) occur fairly rapidly at high electron densities. In addition, the dissociative recombination reaction in (2) has an extremely high reaction rate of 1 x 10-7 $cm^3\ s^{-1}$, and thus the mechanism described here dominates over other possible molecular nitrogen dissociations [126]. Emission from ionized nitrogen in region 2 can be detected only as the neutral nitrogen and ionized boron emission maximize within the same region, at

around 1400 ns, as much of the formation of N^+ is due to the dissociation reaction of molecular nitrogen species.

Molecular emission from ionization of background gas has a strongest band for the transition $B^2\sum_u^+ \rightarrow X^2\sum_g^+$ (v'=0, v"=0) of N_2^+ at 391.4 nm is shown in Figure 3.5d. A large emission peak at 400 ns after the laser pulse is consistent in time for the entire pressure range tested in this study, and increases as the pressure and concentration of gas within the chamber increases. This may be caused by high electron density at the leading edge of the plasma plume that travels collisionlessly to the substrate location, leading to further excitation of the background gas species as they propagate from target to substrate. The leading edge electron densities in laser ablated plasma can be as high as 10^{20} electrons/cm^3, which can be greater than the density very close to the target during ablation [127]. After the leading edge excitation occurs in the background gas at around 400 ns, the main plasma plume flux causes ionization just before 1000 ns. The intensity of ionized molecular nitrogen increases as the gas pressure within the deposition chamber increases and reaches a maximum at values greater than 30 mTorr and at a time of 1600 ns. At pressures higher than 30 mTorr, the behavior of the emission from the ionized molecular nitrogen is very similar up until 100 mTorr, even though the concentration of nitrogen gas is higher. This indicates that above 30 mTorr a transition of plasma plume to a collisional dissociation and recombination process equilibration occurs, which is also linked to an expected transition from direct plume propagation to confined propagation and a shock wave front generation at increased nitrogen background pressure [79].

Spatial emission plasma images of the plume propagation at 50 mTorr pressure appear in Figure 3.6. Narrow bandpass filters of 750 nm and 400 nm isolate the observed

plasma emission to just the individual N* and N^+, respectively. Both species exhibit similar emission behavior shortly after the laser pulse, where the plume is close to the ablation target and is not significantly impacted by the background gas collisions. As the plume begins to form and move toward the substrate location, the atomic neutral nitrogen within the plasma is centralized within the plume and is extinguished as it reacts within the plasma and hits the interface with the substrate, most likely forming BN. The shape of the N* and N^+ distributions in the plasma plume is much different. The exited neutral nitrogen profile is quickly transitioning from a high intensity and directional plume shape to a relatively weak and strongly confined distribution which is mostly extinguished by 2800 ns time at arriving to the substrate location Figure 3.6a. In contrast, the N^+ emission imaging exhibits a clear transition to a reverse cone-shaped distribution and formation of a hemispherical shock front (Figure 3.6b), which is typical for plasma plumes undergoing collisional decelerations in background gas [128]. From the comparison of Figure 3.6a and b, the ionized nitrogen presence considerably lags behind the neutral nitrogen, indicating that the formation of N^+ is primarily from the dissociation and ionization of the background gas caused by the collisions with species in the ablated plume. While the majority of the N^+ is extinguished upon impact with the substrate surface, some deflects and forms a sheath over the far end of the substrate location. This creates an additional extended presence (beyond 6000 ns) of ionized high energy nitrogen at the substrate surface as it diffuses through the plasma sheath [129]. The high energy collisions with substrate can cause desorption of the deposited film and lead to re-ionization of nitrogen species, further extending the lifetime of the plasma sheath at the film growth surface.

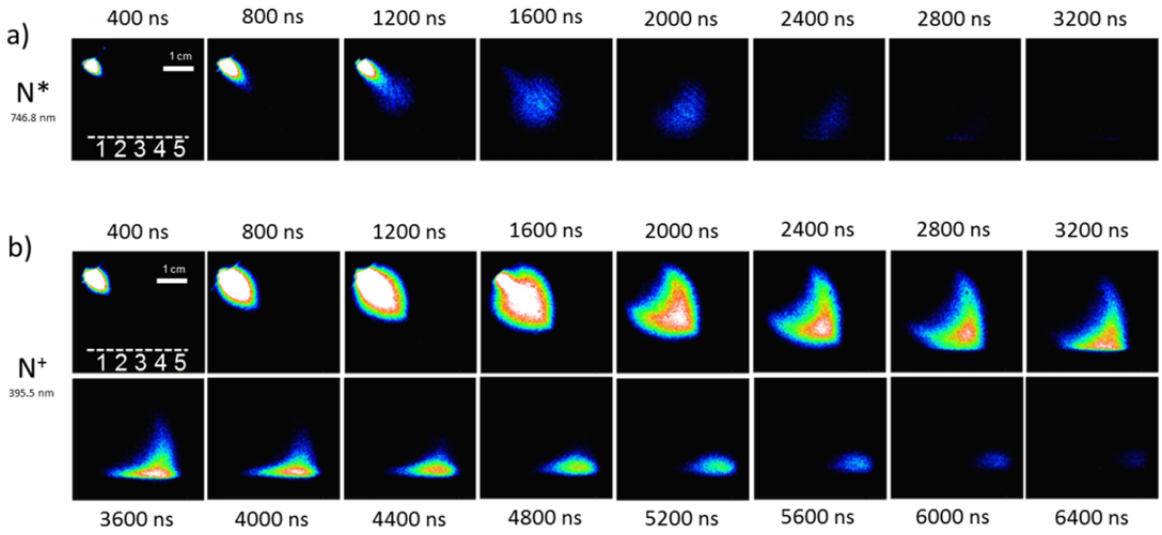

Figure 3.6: Plasma imaging through narrow bandpass filters for a) N* at 746.8 with a 750 nm filter, and b) N^+ at 395.5 nm with a 400 nm filter at 50 mTorr background gas pressure. The dotted line indicates the location of the substrate and numbers indicate locations of the sapphire (0001) samples.

3.5 Impact of plasma conditions on boron nitride film growth

The thickness of the 10 laser pulse ultra-thin BN films varies across the substrate area, shown in Figure 3.7a. The higher gas pressure in the chamber leads to thicker nanoscale films, and the thickness drops off as the distance away from the target is increased. A variation of more than 2 nm thickness is observed in the 5 mTorr depositions, as the higher energy species lead to a lower reaction time in the gas phase and can cause desorption of the nucleated films. The 50 mTorr deposition condition also leads to a smaller delta in thickness across the substrate holder area. Samples at position 1, 2, and 3 have nearly identical thickness for this optimal pressure, and at location 4 and 5 the extended presence of energetic N^+ ions induces significant desorption of nitrogen. This provides a controlled growth of stoichiometric BN and thickness uniformity within 1

nm at 1 cm^2 areas at the 1-3 sample location and 50 mTorr pressures of these studies. There was no observation of a significant change in surface roughness across pressure ranges and all positions from the deposited samples, as measured by AFM, and the average RMS roughness was 0.18 nm.

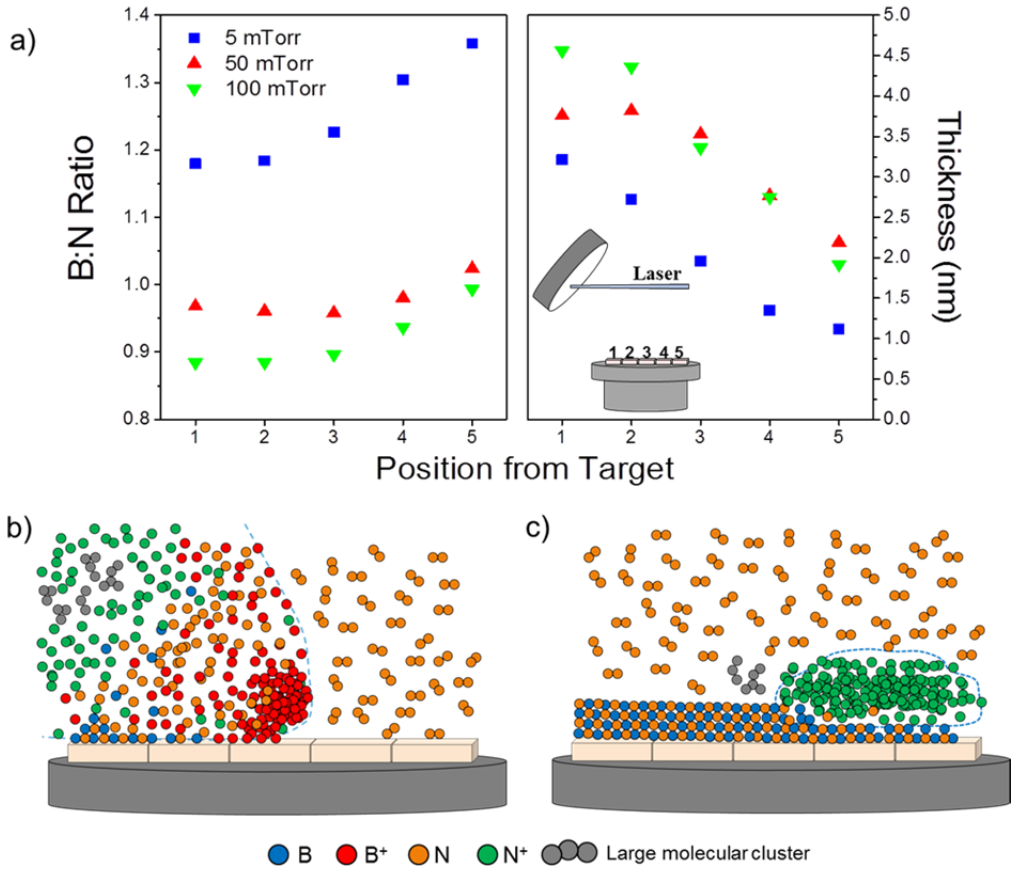

Figure 3.7: a) BN ratio and thickness of laser ablated films grown on five sapphire [0001] substrates at different distances from the target at 5 mTorr, 50 mTorr, 100 mTorr, and b) schematics of plasma plume compositions at approximately 3000 ns, and c) 6000 ns after laser pulse.

Schematics to aid in the understanding of species concentrations and spatial distributions within the plasma plume during deposition appear in Figure 3.7b and c at approximately 3000 ns and 6000 ns after the laser impacts the target. At 3000 ns, the boron and neutral nitrogen species are heavily concentrated at the front of the plume, as

boron reaches the sample first followed by the nitrogen. Molecular boron nitride, BN, is formed mostly at the interface but is represented within the plume at small concentrations. The ionized nitrogen forms from the laser ablation process, as some of the N^+ is present at the front of the plume, but most is localized behind the front of the plume. Large molecular clusters formed by laser ablation are hypothesized to follow behind the front of the plume as well, but are typically not detected in plasma emission studies. The collisions with the large molecular clusters with other molecules and with the background gas species happen readily and frequently, as the collisional cross section is significantly higher than the atomic species. These collisions will lead to further creation of N^+ at the back of the plume.

Figure 3.8 presents an example of a cross-sectional transmission electron microscope (TEM) image from a film grown at room temperature when using the optimized plasma plume conditions discussed in this study. High temperature growth and an appropriate surface template (e.g. highly ordered pyrolytic graphite) facilitates the growth of nanocrystalline *h*-BN with structural and electrical properties close to mechanically exfoliated *h*-BN [130]. The ultra-thin amorphous BN film shown in Figure 3.8 was grown with 5 laser pulses and, consequently, has a thickness of 1.5 nm, corresponding to about 4-5 monolayer thickness of the crystalline 2D equivalent. This dense and fully stoichiometric BN film extends over the entire macroscopic sample area and has a very clean and damage free interface with the underlying sapphire, indicating a negligible impact of the energetic species in laser ablated plasma on the substrate surface. These characteristics and the low temperature growth open new opportunities for integrations of ultra-thin PLD grown BN films in 2D electronic device architectures.

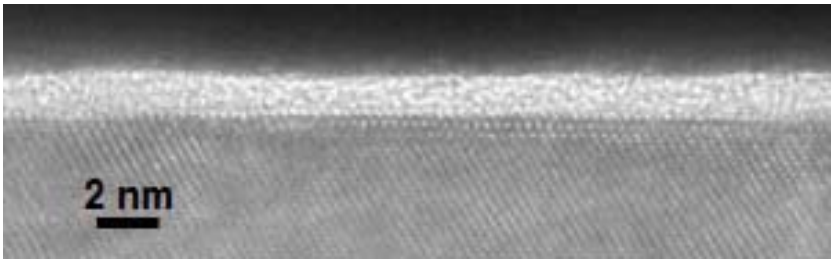

Figure 3.8: Example of a cross sectional TEM image of an amorphous BN film grown at room temperature on a sapphire substrate at 50 mTorr nitrogen background pressure. The shown film morphology and thickness uniformity extends microscopically over the entire 5 mm length of the sample.

One of the major advantages in physical vapor deposition growth of 2D materials is the potential to scale up, as the film coverage is wide-spread over the sample surface, which is required for most industrial applications. In large scale dielectric growth of these films, the sample is rotated and is typically at elevated temperature, which can mitigate the non-uniformity in film thickness and B:N ratio that is observed in these studies [130]. Plasma spectroscopy techniques discussed here can be used to optimize the growth of insulating two-dimensional BN films and provide insights into laser ablation processing of ultra-thin insulating materials.

3.6 Summary of mechanisms for ultra-thin BN growth

Temporally and spatially resolved spectroscopy, coupled with emission wavelength specific imaging of plasma plumes produced by laser ablation of a BN target in vacuum and background nitrogen, were used to identify and track the evolution of ionized and neutral atomic boron and nitrogen as well as molecular N_2, N_2^+, and BN from the initial laser-target interaction to the location of condensation at the substrate surface.

During initial plume formation, the ablated plasma composition is independent of the background gas pressure and originates from laser ablation of the BN target itself. However, as the plume expands from the target, the shockwave front formation and collisional interactions with the background result in ionized boron and nitrogen concentrations increased by about 140 and 30 times, respectively. The emission enhancement from neutral atomic species is impacted to a lesser degree by the background gas presence with about 7 times intensity increase for neutral nitrogen at the substrate location.

Independent of the background nitrogen pressure, ionized boron arrives at the substrate location first, followed closely by neutral nitrogen. The concentration of ionized boron species increases with pressure due to molecular collisions, and the neutral nitrogen concentration remains approximately constant. Atomic nitrogen ions are generated primarily from dissociation and ionization of the background gas, and majority of N+ ions arrive and dwell at the substrate surface for a few microseconds after neutral B and N species arrive. Molecular ionized nitrogen was also in abundance at the substrate location and showed double maxima intensity behavior as a function of time after the laser pulse. This phenomena is explained by the background gas first being ionized with a high density electron flux in the front of the ablated plume, and then followed by ionization collisions with the rest of the plume. Presence of molecular BN was identified, but its intensity was relatively low with a negligible contribution to the film growth.

The performed studies helped to identify that a predominant mechanism for BN film formation is condensation surface recombination of boron ions and neutral atomic nitrogen species arriving nearly simultaneously to the substrate location, and that this

process occurs before arrival of the majority of N^+ ions generated by plume collisions with background nitrogen. Furthermore, the energetic nature and dwelling of incident N+ ions at the substrate location can negatively impact both BN film stoichiometry and thickness. At substrate locations further away from the ablation target where these energetic ions are prevalent, film desorption was linked to the extended N+ bombardment. Growth of stoichiometric and ultra-thin BN films was optimized at enriched concentrations of ionized boron and neutral atomic nitrogen at condensation surfaces. For the plasma – substrate geometry of the present studies, these conditions were at 50 mTorr nitrogen pressure, providing few nanometer thick films with 1:1 BN stoichiometry and good thicknesses uniformity. This study will help direct PLD plasma phenomena in the optimization of stoichiometric BN film growth in both amorphous and hexagonal phases that is a significant addition to the expanding suite of new PVD techniques for 2D heterostructure and device processing.

CHAPTER 4. GROWTH OF FEW-LAYER, LARGE AREA HEXAGONAL BORON NITIRDE BY PULSED LASER DEPOSITION

Chapter 4 derives predominantly from the following manuscript:

Nicholas R. Glavin, Michael L. Jespersen, Michael H. Check, Jianjun Hu, Al M. Hilton, Timothy S. Fisher, Andrey A. Voevodin, "Synthesis of few-layer, large area hexagonal-boron nitride by pulsed laser deposition," *Thin Solid Films*, **572**, 245, (2014).

4.1 Growth of 2D *h*-BN

As discussed in Chapter 3, PLD can be an advantageous technique to grow ultra-thin boron nitride films. In this chapter, this knowledge on plasma reactions and kinetics is used to explore the possibility of growing crystalline hexagonal boron nitride (*h*-BN). Crystalline, two-dimensional (2D) hexagonal boron nitride (*h*-BN) has been investigated for use in nanotechnology applications including high speed transistor devices [3, 47], flexible electronics [97, 131], and high temperature coatings [132, 133]. Structurally similar to graphene, *h*-BN nanosheets consist of alternating B and N atoms arranged in a sp^2-bonded hexagonal lattice structure in-plane, with van der Waals interactions between the layered sheets. The *h*-BN sheets exhibit desirable properties including a wide band gap, high temperature stability, and inertness to many chemical environments. Boron nitride is a complementary dielectric material to graphene in 2D nanoelectronic devices as it provides an atomically smooth surface free of dangling bonds, high surface optical

phonon modes, a good tunneling barrier for electrons, and minimal sites for adsorbed surface impurities [83]. The use of exfoliated *h*-BN as a substrate dielectric material in graphene devices has been shown to markedly increase electron mobility in graphene by several times when compared to traditional dielectric materials such as thermally grown silicon dioxide [91].

Current methods for preparation of *h*-BN nanosheets include mechanical and chemical exfoliation, high temperature chemical vapor deposition (CVD), and PVD techniques including reactive sputtering followed by high temperature annealing, and pulsed laser deposition (PLD) of boron nitride nanosheets, all discussed in detail in earlier sections of this document. Mechanically exfoliated *h*-BN flakes have been used for device-level testing of numerous configurations incorporating graphene and other two-dimensional materials, but the device size is limited to the size of the flake and the exfoliation thickness is not well predictable, which hinders scale-up for device fabrication. Most of the CVD routes for *h*-BN growth include the use of metal substrates or catalysts. Only recently, a direct growth of polycrystalline few-layer *h*-BN on sapphire and silicon substrates using CVD techniques was successfully demonstrated with a deposition of polyborazylene film at moderate temperatures and subsequent conversion to *h*-BN by annealing at 1000 °C [38]. This also includes recent reports on the direct CVD growth of *h*-BN on the surface of epitaxial graphene with an ammonia borane precursor in a vertical tube furnace at 1075 °C [134].

Clearly, one major challenge for large area, 2D *h*-BN material synthesis is the reduction of the growth or annealing temperatures. Alternatively, growth of 2D materials by means of physical vapor deposition (PVD) may offer such a possibility, as these

processes involve energetic plasmas which can add to the surface adatom mobilities and create conditions for *h*-BN growth at lower synthesis temperatures. The attempts with reactive sputtering [68] are promising but yielded amorphous materials which were converted to crystalline BN with the 850 °C anneal, similar to the CVD routes described above.

Pulsed Laser Deposition (PLD) is an alternative PVD technique to reactive sputtering, where a high energy, focused laser beam pulse causes rapid heating on the face of the target, causing both ionized and neutral components to accelerate from the target in the form of a plasma plume normal to the target surface. The plasma plume propagates in the direction of the substrate and can be thermalized by collisions with the background gas, depending on the pressure and target to surface distance. The resulting film quality and composition on the substrate can be affected by parameters including laser wavelength, power, pulse rate, pulse duration, target-to-substrate working distance and relative orientation, background gas type and pressure, and substrate temperature. Whereas alternative PVD techniques present difficulties in preparing complex stoichiometric films due to differing partial pressures of the individual species in the vapor phase, PLD has proven useful in preparing complex thin films due to the rapid, localized heating, and relatively stoichiometric plasmas expelled from the target. This technique has also proven viable for growth of thicker boron nitride films of different crystalline orientations including hexagonal and cubic phases [71], at relatively low temperatures of 650 °C with B:N ratios of approximately one. Nanoscale thicknesses of *h*-BN were synthesized using a high-powered CO_2 pulsed laser and showed a possibility of a reduction of substrate temperature for deposition to around 400°C, and formation of

overlapping boron nitride nanosheets [69, 74]. The nanosheets, however, were non uniform in thickness and morphology over large areas, limiting their ability to be used for electronic applications.

Here, growth of ultra-thin (less than 2 nm) stoichiometric, crystalline hexagonal-phase boron nitride by means of pulsed laser deposition is discussed. To induce the formation of crystalline *h*-BN, surface energetic conditions need to be setup in such a way to promote organization of boron nitride into an ordered structure. This includes the appropriate substrate template to force atomic assembly in a specific manner, altering the energies of plasma species by adjusting the distance between target and substrate, and by varying the pressure for availability of active species such as those discussed in Chapter 3.

4.2 Experimental methodology

Few-layer boron nitride films were deposited in an ultra-high vacuum chamber under the same conditions as described in Chapter 3 and with a setup shown in Figure 3.1. In this case, the substrate was heated to 700°C with the use of a 1000 W Astex ECR power supply supplied heat to the substrate by means of joule heating a tungsten filament. The surface temperature was calibrated using a thermocouple spot-welded on the block just beneath the substrate. After heating each sample to the appropriate temperature, the target was cleaned by laser ablation to remove any adsorbed impurities on the target surface, while the deposition sample stage was covered with a shutter. Depositions were performed in nitrogen background gas, where pressure was controlled by a butterfly valve to preset values within 10^{-4} to 50 mTorr range and keeping the flow of ultra-high purity nitrogen gas (99.9999%) at 30 sccm. After deposition, the substrate was allowed

to cool to room temperature before removal from the vacuum chamber. Two different target-to-substrate working distances of 1 cm and 3 cm were used in the study, with the plume at 45 degrees to the substrate surface. Films were grown for 1 sec at the 1 cm working distance, and 5 sec at 3 cm working distance, in order to achieve the same thickness of BN films.

To guide the PLD process toward the formation of *h*-BN films at reduced substrate temperatures, the ablated plasma dynamic was captured by collecting images of spatial, broadband plasma emission intensities timed from the laser impact on the target. A high-speed Princeton Instruments 576-S/RBE ICCD camera with a 2 ns resolution in gate control was used to collect distributions of emitting species timed to the laser pulse with 100 ns steps and 100 ns gate widths. Plasma images were recorded for all visible emission within 300-900 nm (limited by window and camera bandwidths) with no image averaging, and each image corresponding to a single laser shot.

Highly ordered pyrolytic graphite (HOPG) and sapphire samples with (0001) surface termination and dimensions 5 mm x 5 mm provided atomically smooth surfaces with different lattice constants and electrical properties for deposition substrates. Structurally, HOPG (a-axis lattice constant of 0.246 nm) is very similar to *h*-BN, with a lattice mismatch of less than 2% and similar interlayer spacing. In order to create a clean sp^2-bonded carbon face on the substrate, exfoliation of several layers of material occurred immediately prior to placing in the deposition chamber. Polished sapphire (0001) substrates provided an ultra-smooth, highly crystalline, insulating interface and is used as a substrate material in many transistor fabrications. While c-axis oriented sapphire also provides hexagonal plane template, the sapphire in-plane a-axis lattice constant is 0.476

nm, which is almost twice that of *h*-BN (0.250 nm). Heating the substrate to 700 °C during deposition eliminated all but a minimal amount of adsorbed oxygen contamination on both substrates.

In order to assess film composition, x-ray photoelectron spectroscopic (XPS) analysis was carried out using a Kratos AXIS Ultra spectrometer with a monochromatic Al Kα x-ray source (1486.7 eV) operated at 120 W (12 kV, 10 mA) and at approximately 4 x 10^{-9} Torr. In this system, the analyzer is oriented at 90˚ relative to the sample surface. Survey scans were collected over the binding energy range of -5 to 1200 eV, in 1 eV steps, using a dwell time of 300 ms and an analyzer pass energy of 160 eV. High resolution spectra of the B 1s, N 1s, O 1s, and C 1s regions were acquired using an energy step size of 0.1 eV, a dwell time of 500 ms, and an analyzer pass energy of 20 eV. Since BN is an insulator, a low-energy electron flood source was utilized for charge compensation in cases where differential surface charging was observed. XPS spectra were analyzed using the CasaXPS software. The binding energy scale was calibrated to the C *1s* peak from adventitious carbon at 284.8 eV. The atomic concentration of oxygen atoms was corrected by subtracting the O *1s* contributions from adventitious carbon contamination and from the underlying sapphire substrate (O:Al for clean sapphire measured on this spectrometer was approximately 1.5) [135]. Peak areas were determined using a Shirley background subtraction, and atomic concentrations were calculated by applying relative sensitivity factors specific to the XPS instrument. Curve fits for the B *1s* and N *1s* peaks were obtained by fitting the peaks with a Gaussian-Lorentzian function with a 30% Lorentz contribution.

To determine structural and electrical properties, the films were examined with Raman spectroscopy, AFM topography, TEM, and conductive atomic force microscopy (C-AFM). Raman structural measurements were performed using a Renishaw Raman system with an Ar ion laser at 514 nm and 8 mW input power. AFM topographical images of *h*-BN on HOPG and sapphire were acquired using a Bruker Dimension Icon AFM. For these measurements, the AFM was operated in tapping mode using an AFM tip with a nominal radius of curvature of approx. 2 nm (SNL-10, Bruker). Conductive atomic force microscope (CAFM) measurements were used to verify a large area and pin-hole free *h*-BN films grown on the conductive HOPG substrate, and determine tunneling performance at various locations on the film. Scans were taken using a doped-diamond probe (DDESP-10, Bruker) to avoid tip wear, and electrical current between the biased tip and the grounded HOPG substrate was recorded using a current amplifier having a sensitivity of 1 nA/V.

4.3 Impact of the working distance on plasma dynamics

Altering the working distance as well as changing the background gas pressure within the chamber strongly impacts the incoming plasma energies and local composition in the PLD process. In particular, extending the working distance and increasing background pressure maximizes the probability of collisions between ablated plasma species and background gas, reducing the incoming plasma energies by thermalization, and allowing for a longer reaction time of the energetic ablated species with the background gas species [136]. Depending on the laser energy and target material, there is an optimum pressure-distance parameter space, as the high pressure or longer distance,

the plumes will be fully thermalized without reaching the substrate location, and the benefits of the energetic plasma growth as compared to a CVD will be lost.

Figure 4.1 displays a series of images taken at 3 cm target-to-substrate working distance, depicting broadband plasma emission intensities as a function of time and background pressure of ultra-high purity nitrogen gas. At 600 nanoseconds (ns) after the laser impacts the target, the plume dynamics appear to be fairly similar across the range of pressures examined in this study (10^{-4} mTorr, 5 mTorr, and 50 mTorr). Significant differences are evident at 1200 ns, when the plume is spatially confined due to collisions with other gas molecules inside of the plume and at the plume boundary. At 1800 ns and 2400 ns, plasma confinement is observed at 50 mTorr, in contrast to the diffuse, unconfined plume that has nearly dissipated entirely at the same times at 10^{-4} mTorr. Such plasma confinement is well known for plasma conditions leading to the formation of clusters and radical species from both target atoms and reactive background gas [137]. Furthermore, Figure 4.1 clearly shows the additional excitations of the energetic plasma plume with the substrate. This additional plasma excitation at the substrate surface lasts for relatively long times and with a much stronger intensity when the background pressure is increased. The energetic plume lasted as long as 4 ms after the laser pulse at a pressure of 50 mTorr. Such conditions create the extended presence of chemically reactive species (e.g. atomic boron and nitrogen), and possibly their radicals with increased vibrational temperatures at the film condensation surface. This is supported by earlier reports on PLD process optimization for a low-temperature growth of ceramic and fullerene structures, where plume collisions with the substrates provided reactive species and high vibration energy radicals for increased adatom mobility, extended surface

diffusion times, and reactivity needed for the formation of crystalline films at low substrate temperatures [138, 139]. For the shorter working distances, similar plasma plume evolution processes were observed as in Figure 4.1, but plumes had much less time for collisional reactions with the background gas before reaching the substrate surface.

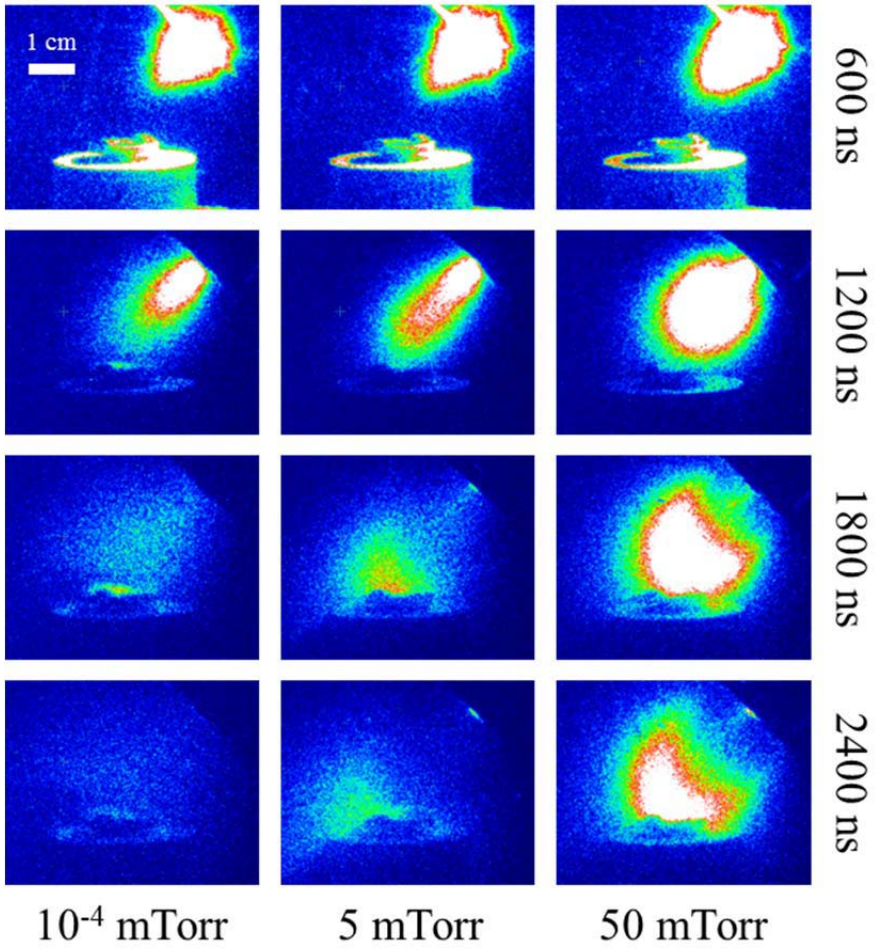

Figure 4.1: CCD camera image of plasma emission intensities for 3 cm target-to-substrate working distance at various pressures and time after impact of the laser pulse on the target.

Representative high resolution spectra of the B1s and N1s regions are shown in Figure 4.2a and Figure 4.2b. The B 1s peak is fit with two components at 190.6 eV and 192.1 eV, corresponding to BN and BN_xO_y, respectively. The small amount of BN_xO_y

observed as a shoulder on the B 1s spectra is observed in other polycrystalline *h*-BN films [38], and is most likely due to exposure to ambient conditions and oxidation at the polycrystalline grain edges. The N 1s peak is fit with a single component at 398.1 eV. High resolution spectra of the B 1s region for films grown on HOPG also revealed a broad satellite peak at 9 eV higher binding energy from the main B 1s line [140]. This energy difference is characteristic of the $\pi \rightarrow \pi^*$ transition in *h*-BN and was only observed for the films grown on HOPG. The crystalline formation on only the lattice matched sp^2-bonded carbon phase indicates an epitaxial-like growth phenomena, where the incoming flux of deposited species has sufficient energy and surface diffusion time to restructure and match the structural template of the substrate material at the condensation surface.

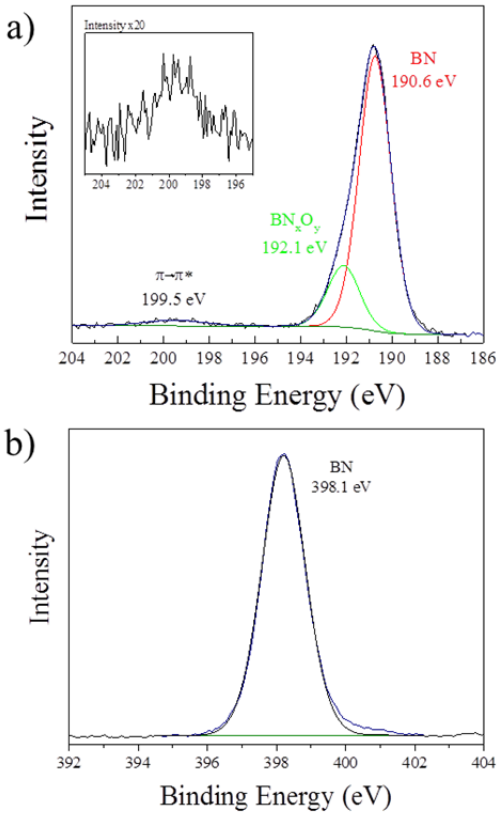

Figure 4.2: a) Representative XPS scan of the B 1s peak as well as the $\pi \rightarrow \pi^*$ satellite shifted 9 eV from the B *1s* peak, and b) a representative scan of the N *1s* peak.

Figure 4.3 depicts the boron-to-nitrogen ratios, calculated from the XPS data, as a function of both working distance and pressure for PLD grown thin films of boron nitride. The B:N ratio decreases with increasing pressure for all deposited films, with the exception of those prepared on sapphire at 1 cm working distance. The decrease in the ratio indicates a more stoichiometric construction of the films as the number of collisions between the plasma and the background gas increases. Independent of the substrate material, a 1:1 B:N stoichiometry is observed in films grown at greater working distance and at 50 mTorr background pressure. The interaction with the background gas at this pressure appears to be optimize generation of BN at the interface between the plasma and substrate. In addition to the proper target-to-substrate working distance, the increased number of collisions with background gas molecules greatly helped in the formation of stoichiometric BN thin films.

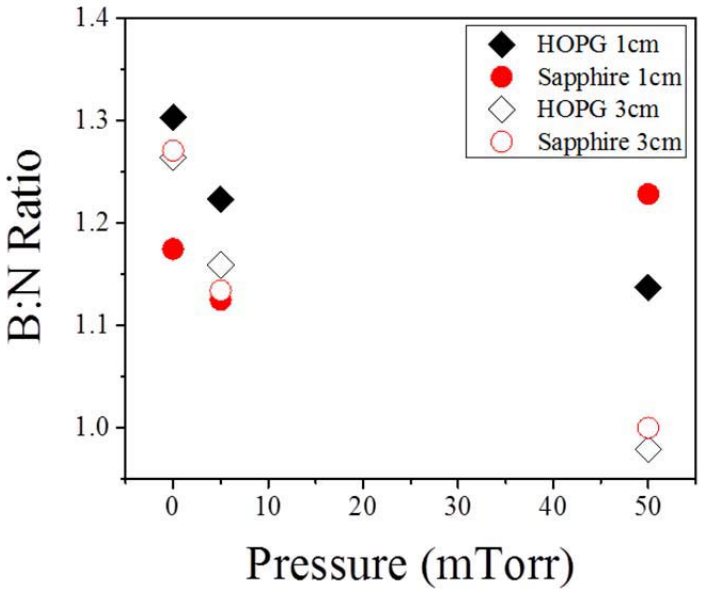

Figure 4.3: Boron to nitrogen ratio as a function of nitrogen background pressure within the deposition chamber.

4.4 Influence of substrate surface templating for *h*-BN formation

The two substrates chosen for comparison of nucleation and growth of boron nitride were sapphire (0001) and HOPG. The sapphire (0001) substrate is hexagonally template, but the lattice spacing is rather large compared to the *h*-BN lattice. In contrast to sapphire, HOPG has a very close lattice match to h-BN, differing by only 1.8%. In addition to the lattice parameter difference, sapphire (0001) surface energy of 1-2 J/m^2 is an order of magnitude larger that of HOPG (0001) surface, where 0.1-0.2 J/m^2 values are typical. From this observation, the HOPG surface with a low surface energy will allow for a longer dwelling of mobile species deposited on the surface from the ablated plasma plumes and a better opportunity for crystalline *h*-BN formation.

From a chemical perspective, as shown in Figure 4.3, the surface template is not influencing the stoichiometry of the film overlayer, as the boron-to-nitrogen ratio is near 1 for both substrates. However, there is expected to be a big difference in film structure as a result of the underlying substrate structure. The E_{2g} shear mode, characteristic of *h*-BN [68], is visible at 1362 cm^{-1} of samples grown on the HOPG substrates only, as shown in Figure 4.4a. The similar peak is not evident for the exact same growth conditions on the sapphire (0001) substrate. Peaks in the Raman spectra of *h*-BN on HOPG include the highly ordered G, G*, and G' bands of HOPG at 1581 cm^{-1}, 2440 cm^{-1}, and 2725 cm^{-1}, respectively. The D band of highly ordered graphite (1352 cm^{-1}) is not evident in scans prior to deposition, as the substrates are very highly ordered, and does not show up post-deposition. The latter is an important observation, as one of the concerns for thin film growth with PLD is a potential substrate damage and defect generation due to the energetic particle bombardment. The background gas collisional

deceleration of the ablated plasma in this study had helped to reduce the kinetic energy of the arrival species to below 7-8 eV de-cohesion energy for carbon atoms from HOPG surface [141]. The observed crystalline *h*-BN Raman signature for the growth on the HOPG substrate further corroborates the XPS $\pi \rightarrow \pi^*$ satellite, suggesting epitaxial-like growth on the lattice matched interface, which was not evident on the sapphire. Similar epitaxial-like growth has been exhibited by cubic boron nitride films on the nearly latticed matched diamond (0001) surface [142].

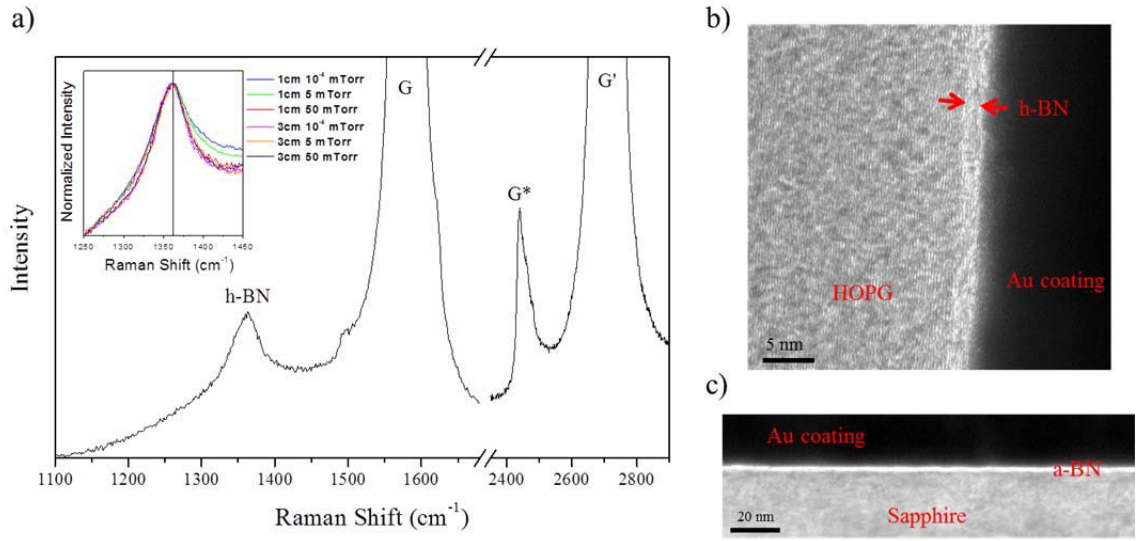

Figure 4.4: a) Raman spectra from polycrystalline *h*-BN on HOPG, and the inset shows the normalized intensity of the E_{2g} shear mode as a function of nitrogen background pressure; b) Cross-sectional TEM image of approximately 2 nm, polycrystalline *h*-BN on HOPG; and c) ultra-smooth amorphous boron nitride on crystalline sapphire (0001).

The different working distances appear to influence the Raman response distribution of grain boundaries, as shown in Figure 4.4a. The longer working distance results in a smaller FWHM for the E_{2g} Raman peak, indicating a larger average grain size within the polycrystalline material. The extremely high intensity Raman shift of the G

peak results in an asymmetric *h*-BN Raman response, making estimation of the FWHM difficult to determine. To correct for this, a background subtraction of the pristine HOPG wafer from the BN Raman signal was performed. The FWHM for the most crystalline sample at 3 cm WD and 50 mTorr was 58 cm^{-1}, indicating an average in-plane domain size to be 2.9 nm for the most crystalline BN film grown at 700 °C on an HOPG substrate, as compared to other polycrystalline BN films [143].

AFM topographical scans indicated large-area film coverage and do not exhibit formation of micron-sized domains of BN, as is the case in many CVD grown BN films [44, 144]. The RMS roughness of the BN films was independent of deposition pressure conditions, and yielded an average of 0.493 nm on HOPG and 0.133 nm on Sapphire for a given 4 μm^2 area.

4.5 Electrical characterization of crystalline *h*-BN

To confirm the film thickness and crystallinity, the samples were cross-sectioned and studied with transmission electron microscopy (TEM). Determination of thickness of the crystalline BN films on HOPG via TEM proved difficult due to similar e-beam absorption coefficients and very close inter-plane lattice spacing between of these materials. Nevertheless, the TEM image in Figure 4.4b clearly indicates a surface layer, where due to the atomic mass contrast an ordered surface layer was determined as that of *h*-BN, and the thickness was estimated to be 2 nm, or about 6 atomic layers. Similarly to XPS and Raman spectroscopy results, TEM studies also confirmed that amorphous BN films were grown on sapphire. The film thickness was approximately 2 nm when grown

at 50 mTorr, with large area coverage and no evidence of pinholes within the amorphous film (Figure 4.4c).

Complementary to TEM, *h*-BN thickness estimations were performed utilizing XPS data based upon the exponential decay of substrate photoelectrons with increasing overlayer thickness due to inelastic scattering effects. Atomic concentration ratios between unique, non-interfering photoelectron peaks from the overlayer (B 1s, N 1s) and the substrate (C 1s, Al 2p) were fit to a homogeneous, flat overlayer model incorporating the inelastic mean free paths (IMFPs) of substrate photoelectrons within the substrate, substrate photoelectrons within the overlayer, and overlayer photoelectrons within the overlayer in order to determine an effective overlayer thickness. This method has been detailed elsewhere [145, 146]. The data confirmed film thicknesses of 1.6 nm on HOPG and 2 nm on Sapphire and show that PLD offers good control over film thickness for macroscopic length scales, as the XPS analysis spot size was at 800 μm^2. TEM and XPS thickness measurements were repeated in multiple locations over the 5 mm x 5 mm sample area, yielding the same results at each spot. It is known from PLD literature that the process allows for good film uniformity, and with the addition of beam rastering and sample motion, larger area samples can potentially be accommodated with similar large area uniformity as those observed in this study [147].

Figure 4.5 shows eight C-AFM scans on the PLD grown *h*-BN films performed over the 5 mm x 5 mm sample that indicate large area coverage free of pin-holes and good electrical performance uniformity. Assuming a 1.8 nm BN film, the average low biased tunneling resistance (R_{LB}) for the polycrystalline *h*-BN film is 1.811 Ω/m, calculated by the slope of the low bias regime, as shown in the inset of Figure 4.5. The

polycrystalline film will most likely exhibit a different electrical response from a pristine flake due to inherent grain boundaries within the film, and thus results in slightly differing low bias I-V characteristics. Pristine *h*-BN flakes have shown to have a high dependence of thickness on the low biased tunneling resistance, in the range of 0.5 Ω/m for 1 nm thick flakes to 100 Ω/m for 2 nm thick flakes [96].

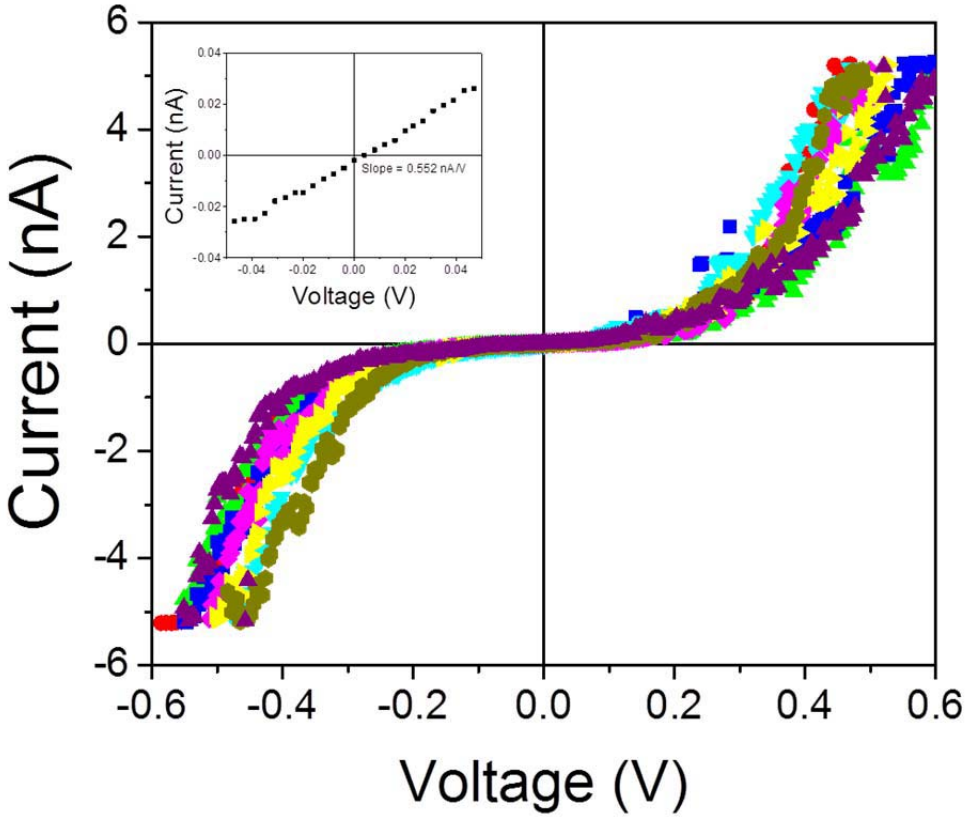

Figure 4.5: Conducting AFM I-V curves of eight spots on a 5 mm x 5 mm BN-coated HOPG sample, and the inset shows the average value of the low-biased tunneling curve.

4.6 Summary for *h*-BN growth by PLD

PLD has been investigated as a new approach for the synthesis of ultra-thin hexagonal boron nitride films in contrast to currently used CVD processes. This

technique has been shown to produce stoichiometric, polycrystalline four-to-six layer BN films within 5 seconds of deposition on 25 mm^2 areas at 700 °C temperatures. This was achieved by in-situ recording and adjusting pulsed plasma plume evolutions to optimize growth conditions at the condensation surfaces with the presence of reactive, thermally excited, high mobility, and long diffusion time species on the condensation surface. Growth of crystalline *h*-BN on both lattice-matched substrates (*e.g.,* HOPG) as well as amorphous, smooth *a*-BN films on crystalline substrates (*e.g.,* sapphire) was demonstrated with complete coverage of the large area without pinholes, or any other cross-thickness defects as confirmed with a number of techniques. When compared to traditional CVD methods, the technique opens up the possibility of preparing high-quality BN films on a wide range of previously incompatible substrates with traditional growth approaches of BN, a possibility to scale the film production to large areas, and achieve very fast growth throughput needed for commercialization benefits.

CHAPTER 5. AMORPHOUS BORON NITRIDE: A UNIVERSAL, ULTRA-THIN DIELECTRIC FOR TWO-DIMENSIONAL NANOELECTRONICS

Chapter 5 derives predominantly from the following published manuscript:

Nicholas R. Glavin, Christopher M. Muratore, Michael L. Jespersen, Jianjun Hu, Phillip T. Hagerty, Al M. Hilton, Austin T. Blake, Christophr A. Grabowski, Michael F. Durstock, Michael E. McConney, Drew M. Hilgefort, Timothy S. Fisher, Andrey A. Voevodin, "Amorphous boron nitride: a universal, ultrathin dielectric for 2D nanoelectronics," Adv. Func. Mat., (2016). doi:10.1002/adfm.201505455

5.1 Background information on reduced temperature boron nitride growth

In Chapter 3 and 4, it was demonstrated that PLD can be used to produce stoichiometric, continuous, crystalline or amorphous boron nitride. Ideally, a versatile synthesis route that facilitates nucleation and coalesce of continuous and large area ultra-thin BN insulating films at low temperatures on all electronic materials of interest (metal, ceramics, polymers, graphene and other 2D materials) at temperatures < 200 ^{o}C, without the requirement of tuning the deposition conditions for every substrate of interest, would facilitate simple integration of ultra-thin dielectrics into 2D devices. This chapter is focused on demonstrating and exploring the applicability of PLD growth mechanisms as described in previous chapter for low temperature growth of dielectric, ultra-thin boron nitride material on a variety of substrates for potential use in flexible 2D devices. While

conducting (e.g., graphene, TaS_2), and semiconducting (e.g., MoS_2, WS_2) 2D materials are being rapidly advanced for next generation 2D devices [2-5, 24, 148], ultra-thin and high strength dielectric materials for transistor gates, capacitors, memory devices, and barrier layers for electrical and ambient environment isolation are far less developed. This circumstance is primarily a result of the fundamental challenge in synthesis of ultra-thin insulating materials at moderate temperatures (< 900 ^{o}C) needed for direct growth over large lateral dimensions [39]. In silicon-based electronics, silicon dioxide (SiO_2) has proven to be an ideal dielectric material due to the large band gap (9 eV), well-matched interfacial properties with silicon, and simple, repeatable processing.

Low temperature synthesis routes including thermal decomposition of Si [149] and plasma enhanced chemical vapor deposition (PECVD) have been extensively studied and are now routine industrial operations. While integration of SiO_2 on silicon-based devices is commonplace, synthesis of ultra-thin dielectrics with interfacial characteristics suitable for use with diverse (i.e., electrically insulating and conducting) 2D materials, without compromising unique 2D benefits such as optical transparency and mechanical flexibility, is critical for realization of flexible electronic devices and other premium areas of nano-technological innovation. Atomic layer deposition of HfO_2 [150, 151] and Al_2O_3 [152], thermal activated growth of *h*-BN by CVD, and other alternatives to SiO_2 are some of the recently reported direct-growth approaches that suffer from significant scaling, process tuning, and pin-hole free uniformity challenges.

Chemical vapor deposition (CVD) is the most widely used direct synthesis method, suitable for use over large areas, of ultra-thin *h*-BN [42], and is discussed extensively in Section 2.2.2. Prior studies reveal that the thermally activated CVD

processes for high quality, 2D *h*-BN growth are strongly substrate-dependent, and require substantial tailoring to accommodate the full range of chemical reactivities and surface energies of the substrate material. Recent progress in direct growth methods of *h*-BN has been reported on insulating Al_2O_3 (0001) and conducting Si (111) using a two-step process of pre-growth annealing at 1000 °C followed by the decomposition of polyborazylene precursor, representing a key advance in few-layer *h*-BN growth prospects [38]. In this chapter we are focusing directly on the low temperature applicability of the PLD growth technique for growing high quality ultra-thin dielectric materials and exploring the device-scale electronic properties such as dielectric constant and dielectric strength.

5.2 Experimental methodology

Growth: Growth of amorphous boron nitride films were performed in an ultra-high vacuum chamber from a 248 nm KrF laser at 1 Hz repetition rate, a laser power of 900 mJ/pulse, and spot size of 2.66mm x 1.5 mm, corresponding to a laser energy of 22.5 J/cm^2. Depositions were performed at a working distance of 3 cm with an amorphous boron nitride target and the chamber was filled with 99.9999% N_2 gas at a pressure of 50 mTorr.

Tungsten films for bottom electrodes were grown in the same chamber with DC magnetron sputtering at a power of 40 W applied to the target, 2.5 mTorr of Argon background pressure and an Argon flow rate at 30 sccm on an SiO_2/Si wafer. Titanium/Gold contacts were grown in a similar manner, with 40 W applied to the titanium and gold targets sequentially, and an argon pressure of 15 mTorr.

Chemical and Structural analysis: X-ray photoelectron spectroscopy (XPS) was carried out using a Kratos AXIS Ultra spectrometer with a monochromatic Al Kα x-ray source (1486.6 eV) operated at 120 W (12 kV, 10 mA) and at approximately 4 x 10^{-9} torr. Survey scans were collected over the binding energy range of -5 to 1200 eV, in 1 eV steps, using a dwell time of 400 ms and analyzer pass energy of 160 eV. High resolution spectra of the B 1s and N 1s regions were acquired using an energy step size of 0.1 eV, a dwell time of 500 ms, and analyzer pass energy of 20 eV. XPS spectra were analyzed using the CasaXPS software. Peak areas were determined using a Shirley background subtraction. The binding energy was calibrated to Al 2p at 74.5 eV where sapphire was present and to Si 2p at 102.4 eV where PDMS was present.

The cross-sectional TEM of BN thin films was performed using a FEI Nova focused ion beam (FIB) microscope equipped with an Omniprobe manipulator for lift-out. Samples were studied in a FEI Titan 80-300 S/TEM operating at 300kV, which was equipped with a Cs-corrector for high-resolution imaging. In addition, cross-sectional microscopy was used in measuring film thickness, and the scatter in the measurements is reflected in Table 5.1.

Device characterization: Resistivities were measured using a Keithley 4200 and using a thin gold filament to make contact onto a 40 μm x 40 μm gold top electrode to facilitate the measurement. Dielectric permittivity characterizations were performed using a Novocontrol Alpha Analyzer. Scans were conducted at discrete frequencies, swept over the range of 10 Hz – 1 MHz, at an AC driving voltage of 100 mV.

5.3 Demonstration of low temperature processing benefits using PLD

For both conducting and semiconducting 2D materials, well ordered structure is essential to obtain the desired electronic, optical, and mechanical properties, as these are dictated by the anisotropy of interatomic bonding arrangements and electron density distributions, which are unique for such 2D materials. This structural anisotropy could be much less essential, however, for wide bandgap materials with no electrons in the conduction band, such as BN. Thus, if (a) atomic order is not necessary to obtain the desired dielectric properties for ultra-thin insulating materials based on BN, and (b) the film growth can be activated by non-thermal means, then the synthesis temperatures can be reduced to allow for direct, large area growth and thus to enable flexible cost-effective 2D device production. The approach described here utilizes a low temperature (<200 °C) pulsed laser deposition of ultra-thin BN dielectric films as a universal means of direct growth of pinhole free, few-nanometer-thick and high dielectric strength films on a number of metal, ceramic, and polymer substrates as well as on the surface of 2D materials including graphene and few-layer MoS_2.

Amorphous boron nitride with a controllable thickness of 2 to 17 nm was synthesized using a pulsed laser deposition method optimized for ultra-thin growth. A comprehensive description of the process development can be found in previous chapters. Benefits of this optimized PLD approach include the inherent ability to commercialize PLD processes to large areas [65, 147], (Figure 5.1b shows *a*-BN grown on a Si/SiO_2 wafer with a cross-section from a similar wafer), stoichiometric *a*-BN growth at significantly reduced temperatures from room temperature to 200 ^{o}C on a diverse range of substrates (Figure 5.1c), and all without modifying the required deposition conditions.

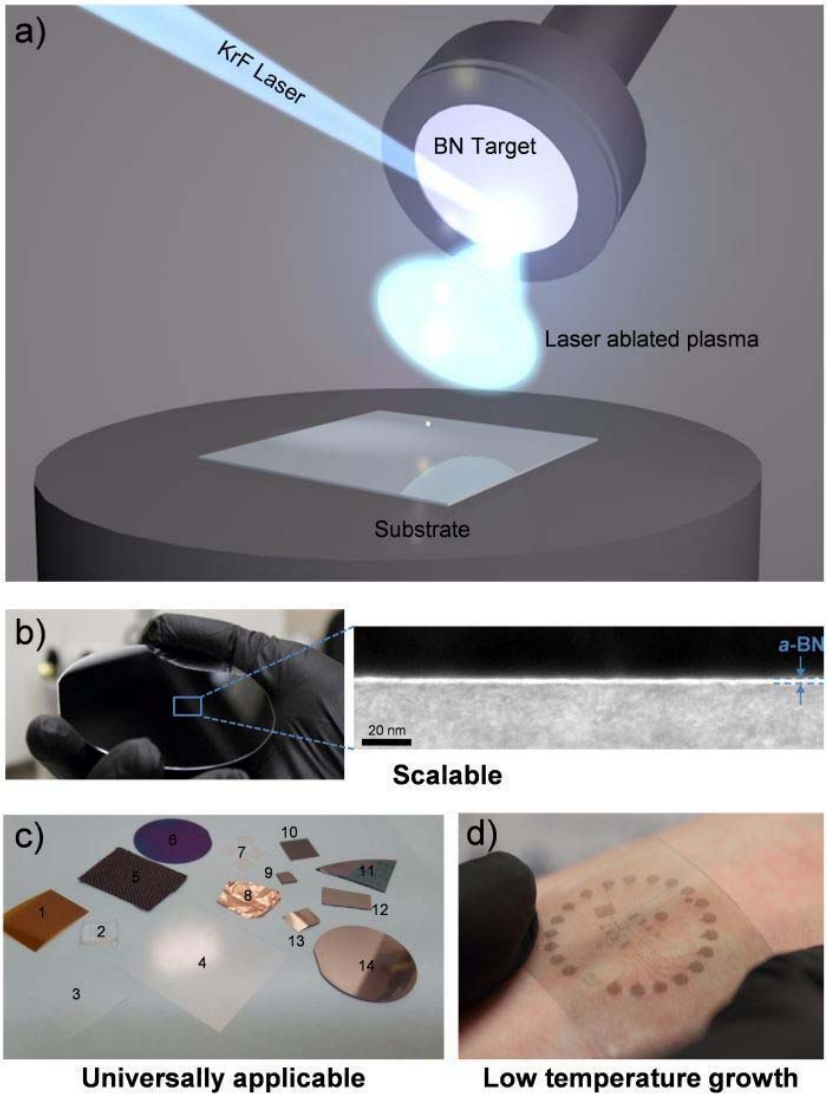

Figure 5.1: a) Schematic representation of the pulsed laser deposition setup, b) *a*-BN grown on a 3 inch SiO2/Si wafer and cross-sectional TEM of *a*-BN on Al_2O_3 showing large area uniformity, c) ultra-thin a-BN applied to diverse substrates, including: (1. Kapton™, 2. PDMS, 3. Willow glass™, 4. Polyethylene terephthalate (PET), 5. Carbon cloth, 6. SiO_2/Si, 7. Al_2O_3, 8. Copper foil, 9. HOPG, 10. SiC, 11. Patterned SiO_2, 12. E-beam evaporated chromium, 13. Nickel foil, 14. Magnetron sputtered tungsten) and d) device construct with directly grown *a*-BN and PVD MoS_2 on flexible PET substrate with magnetron sputtered tungsten contacts.

5.4 Structural and chemical bonding analysis of substrate agnostic *a*-BN films

Figure 5.2 displays eight cross sectional TEM images of the ultra-thin *a*-BN films grown on metals (W, Cu foil), insulators (SiO_2, Al_2O_3), other 2D materials (MoS_2 and graphene), and polymer substrates (Polyethylene terephthalate (PET) and Polydimethylsiloxane (PDMS)). All films were synthesized at < 200 °C without changing any of the *a*-BN deposition parameters (e.g. nitrogen pressure, working distance, laser power, etc. were kept the same), highlighting the versatility and ease of the deposition technique for growth on electrical conductors, insulators, and semiconductors. The presented BN films represented are of thicknesses from 1-5 nm, and which is controlled with at least 0.5 nm precision by the number of laser pulses impacting the target material. Under such process control, *a*-BN with uniform thickness over areas as large as 3 inches can be feasibly synthesized (Figure 5.1c), as PLD has been shown to enable scale-up with advanced processes such as laser beam rastering [147] and other advanced techniques [65]. Additionally, the wafer-scale, direct synthesis approach eliminates limitations associated with alternative transfer processes (via introduction of structural or chemical defects) or high substrate temperature requirements for BN growth in 2D device production. Amorphous BN films were found to be equally uniform and conformal at thicknesses greater than approximately 2 nm on a local scale, and 6 nm on a device-level scale on tested substrates of 1” in diameter, with no evidence of cross thickness defects (e.g., pinholes or domain boundaries), as confirmed by large area AFM scans, dielectric measurements at multiple sample locations, and random probing with cross-sectional TEM studies. The amorphous nature of the films is confirmed by Raman,

XPS, and TEM studies, as no evidence of any hexagonal or cubic crystallographic signatures are revealed.

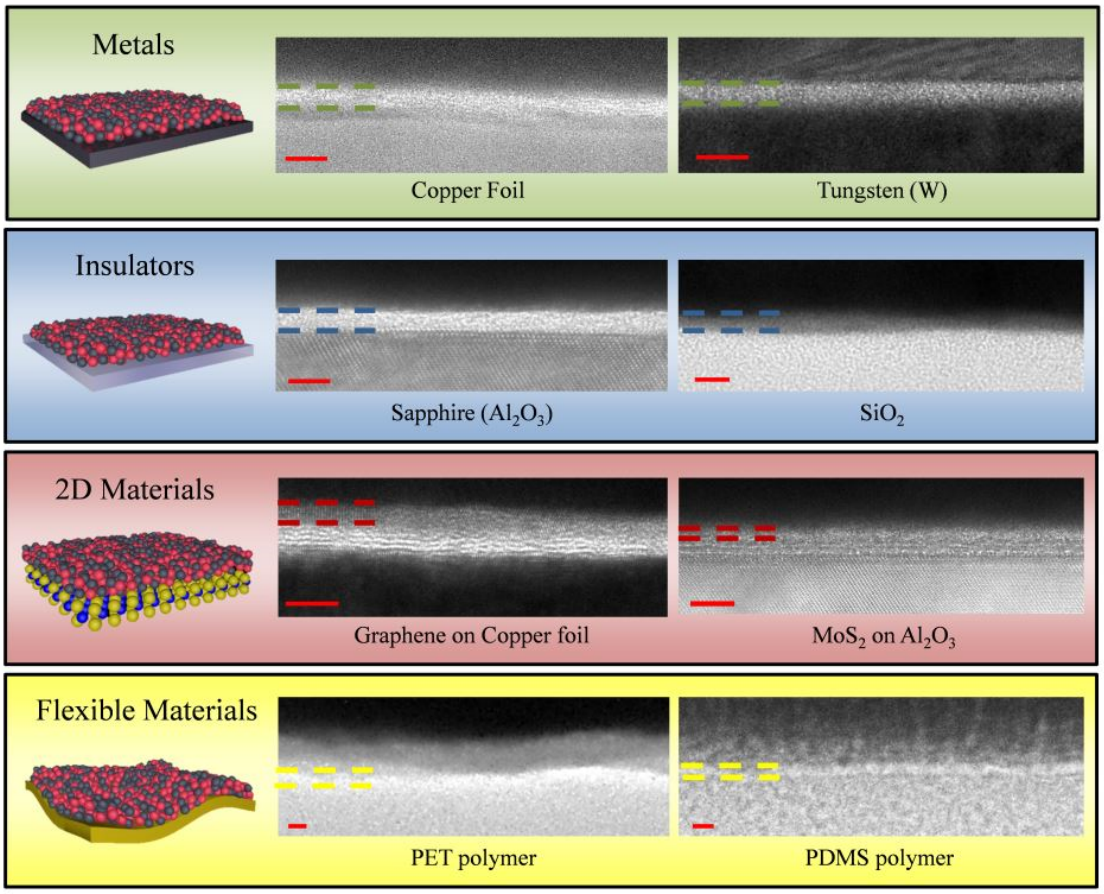

Figure 5.2: Cross-sectional TEM imaging of amorphous boron nitride growth from room temperature to 200 °C on metal, insulating, 2D material, and flexible substrates (with gold cap layers on top of BN), dotted lines are to aid the reader in identifying *a*-BN material location. Larger area cross-sectional TEMs can be viewed in Figure A.1.

The density and composition of ultra-thin *a*-BN films are expected to dictate their insulating properties, as there are no domain boundaries or other well-defined structural features (as shown in Figure 5.1b). The B:N ratio directly influences dielectric behavior, as nitrogen deficiencies promote metallic B-B bonding that can open conductive pathways or mid-gap states in the band structure of the ultra-thin films. High-resolution

XPS data shown in Figure 5.3 (collected *ex-situ*) indicates excellent stoichiometry and homogeneous bonding chemistry within <5 nm *a*-BN films grown on four substrates having diverse electronic properties and surface energies (from 19.8 mJ m^{-2} for PDMS to >60 mJ m^{-2} for tungsten). Single-component B *1s* (190.6 eV) and N *1s* (398.2 eV) photoelectron peaks indicate B-N bonding, independent of the substrate material. In all cases, the *a*-BN films are nearly stoichiometric with no evidence of metallic B-B bonding (B *1s* = 187 eV) [153] or bonding with the substrate material. We attribute the absence of film-substrate bonds to plasma processing conditions that generate abundant N atoms and ions at the surface and promote nitrogen integration at the film interface [154].

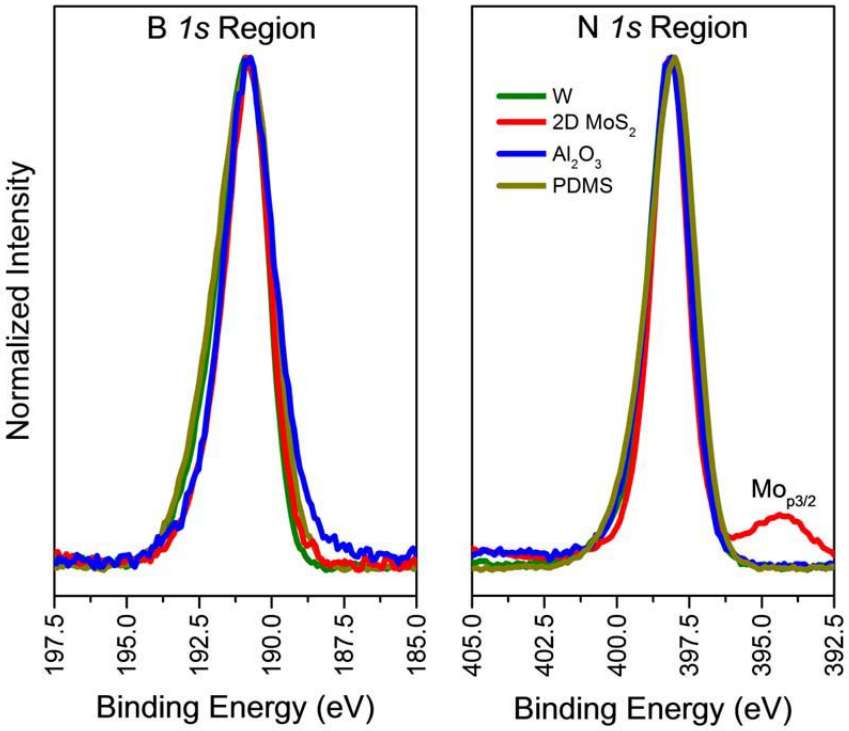

Figure 5.3: XPS B *1s* and N *1s* regions of < 5 nm a-BN films grown at < 200°C on four representative substrates including magnetron sputtered tungsten (W), 2D PVD MoS_2, Al_2O_3, and PDMS.

Homogeneous nucleation and coalescence of ultra-thin *a*-BN are driven primarily by the inert nature and resulting low surface energy as compared to the substrate materials, facilitating continuous film formation by the reduction of the condensation surface energy during the film growth. Indicated in Figure 5.3, the films are stoichiometric on each of the examined substrates as the B:N ratio is near 1:1 and found to be uniform over large areas, confirmed by random sampling of XPS data collection. While uniform growth occurs on all substrates shown in Figure 5.1c, the initial nucleation stage and deposition rate are, as expected, highly influenced by the substrate surface energy. Surfaces with a higher surface energy (such as metals) were found to delay the continuous *a*-BN film formation. However after a critical thickness >1-2 nm films on all substrates are continuous and the growth rate is subsequently linear.

5.5 Correlation of nucleation and growth behavior of ultra-thin boron nitride with localized electrical performance

The initial growth mechanism proposed for *a*-BN films is two-stage, evidenced by two independent studies employing 2D MoS_2 produced by physical vapor deposition [66] and tungsten substrates. PVD-grown MoS_2 was covered with *a*-BN films, where film thickness was controlled by varying the number of laser pulses. *Ex situ* XPS studies reveal significant oxidation of the few-layer MoS_2 for *a*-BN overlayers of less than 1 nm thickness (achieved with under 20 laser pulses on the BN target). Once the *a*-BN films reached 1 nm or thicker (TEM of *a*-BN on MoS_2 from Figure 5.2 is at 20 pulses), the MoS_2 oxidation rate dropped substantially (40% oxidized non-covered versus no apparent oxidation with 1 nm *a*-BN, after 1 week ambient), indicating the minimum number of

pulses to reach full coverage of underlying layers is achieved on a large probing area. The proposed initial island nucleation mechanism is also confirmed by localized IV curves, shown in Figure 5.4a, performed using through-thickness C-AFM of *a*-BN on magnetron sputtered tungsten and a measuring technique similar to Lee et al. [96] The initial growth stage films (produced at < 20 pulses) demonstrate small pinholes within the ultra-thin layer, evidenced by areas of high conduction shown in Figure 5.4b. The similarity of the IV curves for the 2-20 pulse growth samples indicate that there is not much change in thickness, as small gaps and pinholes are preferentially filled during the initial growth stage. Once full surface coverage of *a*-BN is achieved (>20 pulses or 1.67 nm), the breakdown potential dramatically increases (Figure 5.4a), and the film is found to be cohesive, with no evidence of pinholes present on a microscopic area, as indicated in Figure 5.4c. Beyond this initial nucleation and coalescence stage, the *a*-BN growth enters uniform growth mode, where subsequent laser pulses result in increased thicknesses and corresponding film breakdown voltages as the deposition rate becomes linearly dependent on the number of laser pulses. Topographical AFM scans of *a*-BN on Al_2O_3 are shown in Figure A.2, where the locations of these scans were taken in 5 locations spaced 5 mm apart on a 30 mm sample surface.

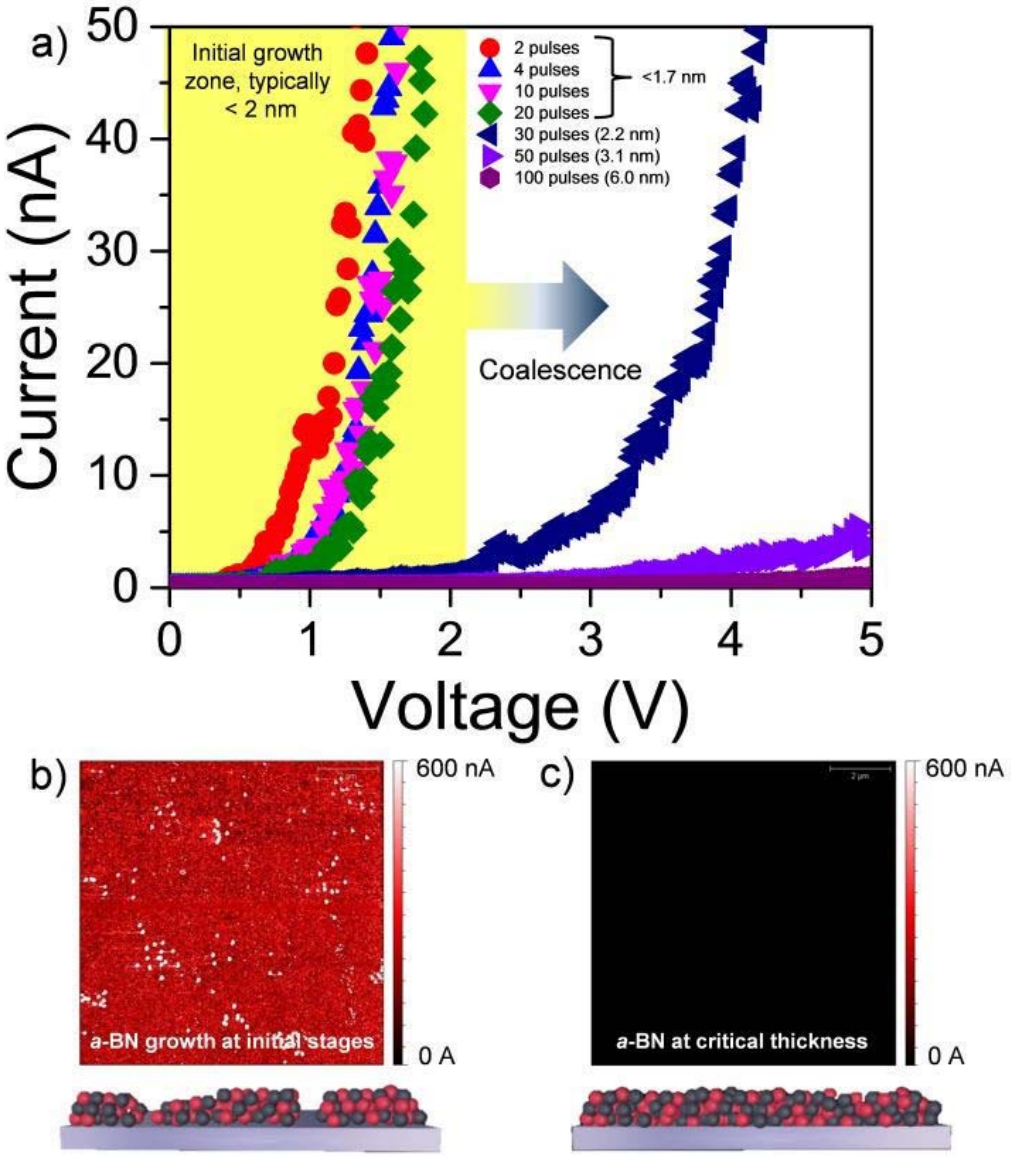

Figure 5.4: a) C-AFM I-V curves of *a*-BN on tungsten and corresponding number of laser pulses, b) C-AFM image and schematic of initial growth stages at 2 pulses, and c) C-AFM image and schematic of cohesive *a*-BN film at critical thickness of 20 pulses.

Beginning at the point of coalescence, the measurement of dielectric breakdown strength for films over a range of thicknesses was completed with the C-AFM technique

using the linear breakdown method when the current reaches 1 nA [101]. The breakdown is characterized by a sharp increase in current as the electronic behavior enters a regime commonly analyzed using Fowler-Nordheim tunneling theory. The dielectric breakdown strength measured from C-AFM curves at the nearly fully formed samples (< 20 pulses) is near 5 MV/cm, and an increase in the dielectric breakdown to of 9.8 ± 1.0 MV/cm is observed in the fully coalesced 2.2 nm and 3.1 nm samples (corresponding to 30 and 50 laser pulses, respectively). This value is substantially higher than the breakdown voltage measured in thicker (20 nm) CVD *h*-BN films and approaching the values for that of mechanical exfoliated, single crystal *h*-BN flakes of similar thicknesses.

5.6 Device-scale electronic behavior and properties

While C-AFM studies can provide insights into initial growth mechanisms as well as intrinsic material properties, pulsed laser deposited of *a*-BN is uniform and cohesive over a much larger areas on all tested substrates and amenable to wafer-scale testing. To demonstrate the large area applicability and device production applicability, a simple back-gated device was fabricated using *a*-BN as the active resistor material, a tungsten bottom electrode, and Ti/Au contacts, as shown in the schematic of Figure 5.5a. Fabrication of these devices was conducted in a single chamber and not in a cleanroom facility, highlighting all-PVD direct growth advantage with no transfer/lift off or lithography required to avoid introduction of contamination or other defects. Top contacts of Ti/Au pads were deposited using a TEM mesh, where the contact pads were 40 μm x 40 μm, as shown in Figure 5.5a. A cross-sectional view of the 6.0 nm thick *a*-BN integrated into the device appears in Figure 5.5b and a 16.5 nm *a*-BN in Figure A.1.

The resistivity measurements in devices with thinner *a*-BN samples were insulating, but less so than the reported resistivities for various phases of BN (10^{13}-10^{15} ohm·cm) [155] as pathways through ultra-thin insulators at areas of 1600 μm^2 are predominantly caused by extrinsic effects such as dust particles and substrate topography imperfections that induce micro-scopic leakage pathways. The performance is believed to be amenable to improvement by additional cleaning procedures, as well as processing in a cleanroom facility. Beyond this critical thickness, average resistivity values of 7.22 * 10^{11} ohm·cm at 6 nm thickness (100 laser pulses) and 2.98 * 10^{12} ohm·cm at 16.5 nm (200 laser pulses) were measured, which is near an expected value for a bulk BN film [155].

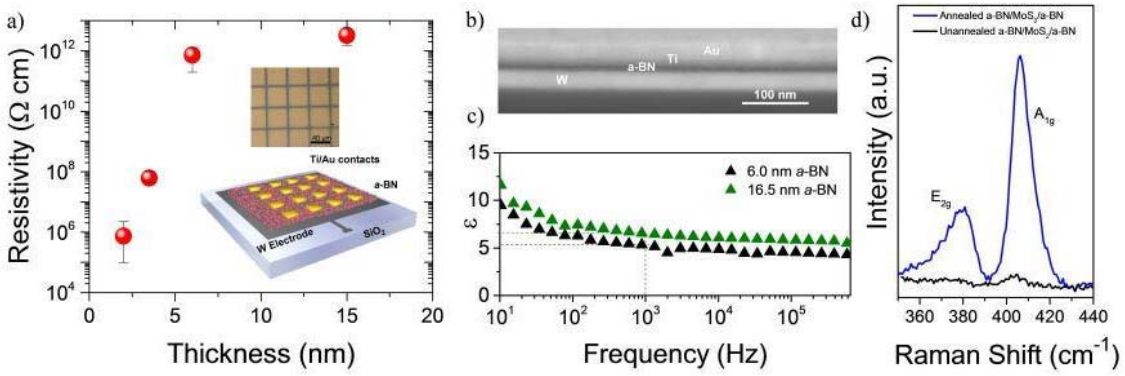

Figure 5.5: a) Electrical resistance measurements of continuous *a*-BN films on metallic tungsten at different thicknesses using 40 μm x 40 μm Ti/Au contacts shown in the inset, b) cross-sectional image of the 6 nm *a*-BN device, c) dielectric constant measurements for 6 nm and 16.5 nm films, and d) MoS_2 raman signature of as-deposited (black) and laser annealed (blue) in BN/MoS_2/BN heterostructured stack.

In addition to resistivity, the same device was used for dielectric constant measurements of the 6 and 16.5 nm samples (Figure 5.5c). A dielectric constant of 3 ± 1.0 has been reported in a polycrystalline CVD film of 15-19 nm thickness [98], as leakage pathways at the grain boundaries can lead to charge dissipation within the

material. In highly dense 6 and 16.5 nm *a*-BN films grown at 200 °C the measured dielectric constant was 5.2 and 6.5 at 1 kHz, respectively, with an average of 5.9, which approaches the dielectric constant of pure, single crystal *h*-BN. An increase in dielectric constant can be attributed to higher resistivity of the film, where it is a bulk value, where the electrical properties are not as influenced by surface defects and other contaminant species. Device-scale dielectric breakdown measurements indicate an E_{BD} value of 9.1 MV/cm for the 2.2 nm sample, as presented in the Weibull distribution in Figure 5.6, which is consistent with the constant current C-AFM measurements of breakdown strength. Subsequent testing on the thicker W/*a*-BN/metal contact devices were inclusive, as the metal contacts failed consistently near 8 V by delamination before breakdown of the *a*-BN material occurred.

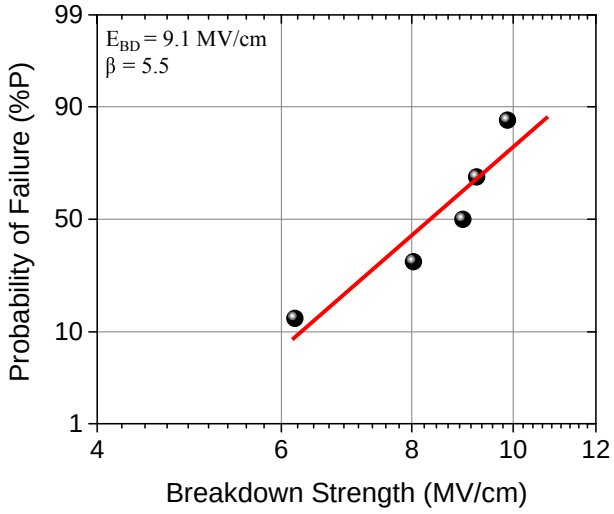

Figure 5.6: Weibull distribution of device dielectric breakdown measurements on 2.2 nm (30 pulse) *a*-BN sample using Au/Ti contact pads of 40 µm x 40 µm in area.

Finally, optical bandgap measurements were performed on an 8 nm *a*-BN film grown on Al_2O_3 (0001), and resulted in a measured absorption bandgap of 4.5 eV, as shown in Figure 5.7. A bandgap of 4.5 eV is well within the reported values for thin film amorphous boron nitride of 3.8-5.05 eV, as compared in Table 5.1. The bandgap measured here for ultra-thin *a*-BN is slightly below that of the hexagonal phase of boron nitride, as both the bulk single crystal and polycrystalline *h*-BN produced by CVD exhibit a bandgap of 5.2-5.9 eV. Efforts to model and understand electronic properties of *h*-BN have been well explored [13, 156]; however, comparable model for *a*-BN has yet to be fully developed. A reduction in band gap has been observed in other crystalline-to-amorphous phase transitions, as the amorphous phase results in both a reduction in coordination of the bonding species, as well as random orientation of atomic orbitals [157]. The values for dielectric constant, dielectric breakdown strength, and bandgap of the *a*-BN material in this work are listed in Table 5.1, as presented earlier, along with a comparison to other state-of-the-art ultra-thin BN dielectrics and thermally grown SiO_2 thin films. These values reported are higher than those of previously measured *a*-BN thicker films and are believed to be due to the defect free, large area, atomic-scale roughness and stoichiometry tuned precisely to applications in nanoelectronic systems.

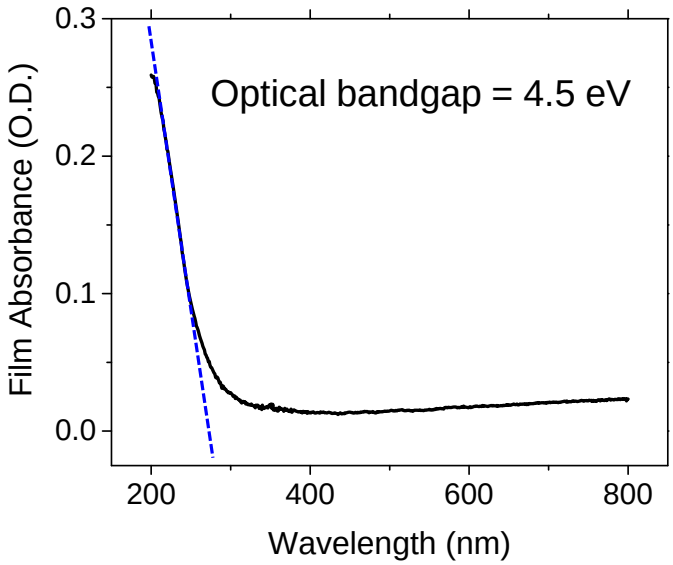

Figure 5.7: Bandgap measurement of 8 nm ultra-thin BN on Sapphire (0001) by UV-Vis spectroscopy.

As discussed, significant advantages of the laser deposited *a*-BN films over traditional ultra-thin or two-dimensional dielectrics includes large area nucleation and coalescence on diverse substrates at low temperatures (<200°C). To demonstrate these advantages, in addition to retention of optical transparency of heterodevices on a polymer substrate, an *a*-BN/amorphous MoS_2/*a*-BN heterostructure was synthesized on PDMS with low temperature PVD methods. The MoS_2 was grown via PVD [66], however, at much lower temperatures than described in the previous work, the MoS_2 film is amorphous and insulating. Recent studies have proven successful in the laser annealing and crystallization of such amorphous MoS_2 layers by photonic curing on a flexible PDMS substrate [158]. In the present here, a 514 nm laser was used to crystallize the

amorphous MoS_2 into the 2H phase through the transparent *a*-BN film of approximately 2 nm, without any evidence damage to the dielectric film properties, evidenced by the E2g and A1g characteristics peaks of MoS_2 in Figure 5.5d. This capability is an important advantage in low-temperature processing of 2D materials, as the crystallization of MoS_2 sandwiched between low-temperature grown *a*-BN layers will significantly hinder oxidation of the environmentally sensitive MoS_2, and allow for direct-write manufacturing of MoS_2 transistors on flexible substrates with well-defined gate dielectrics and without degradation from exposure to the ambient environment.

5.7 Comparison of device-scale electrical properties of current dielectric materials

Table 1 compares physical properties of various insulating BN materials (from bulk to ultra-thin) to that of thermally grown SiO_2. Bulk amorphous boron nitride is characterized by predominantly sp^2 bonding, is transparent and insulating, and is typically used as an intermediate layer in *c*-BN synthesis processes in prior works [130, 154]. The reported measured electronic properties of these thin film *a*-BN (films with thickness > 600 nm) are nearly identical to thermal activated growth of *h*-BN by CVD, in terms of measured dielectric strength, dielectric constant, and bandgap energy values (see Table 5.1). The amorphous material possesses a density similar to the crystalline phases, and retains much of the valued chemical inertness and high thermal stability characteristics of its hexagonal counterpart. The electronic properties of *a*-BN where the device measurements were made (6 and 17 nm) described throughout this work are reported in the final column of Table 1 and will be discussed later.

Table 5.1: Comparison of electronic properties of thin film *a*-BN, CVD deposited *h*-BN, single crystal *h*-BN, thermally grown SiO_2, and ultra-thin *a*-BN described in this work

Property	Thin film (>600nm) *a*-BN†	CVD *h*-BN[a)]	Single crystal *h*-BN	Thermal SiO_2	Ultra-thin *a*-BN (this work)
Density	2.28	---	2.0-2.28	2.27	---
Dielectric Constant	3.5	3 ± 1.0	6.85	3.9	5.9 ± 0.65
Dielectric Strength (MV/cm)	2.2-5.0	2 - 3.8	7.9-12	9 ± 1.0	9.8 ± 1.0
Bandgap (eV)	3.8-5.05	5.92	5.2-5.9	9	4.5
Direct growth synthesis temperature and compatibility	Typically 200-600°C, By-product of desired *c*-BN synthesis	CVD at >900°C, refractory metal foils and some insulators	Exfoliation required to create ultra-thin layers	Thermal decomposition of Silicon at >700 °C	<200 °C, wide range of substrates

[a)] Measured dielectric constant and strength of CVD *h*-BN of thickness approx.15-19 nm
† Thin film *a*-BN data from [159, 160], CVD *h*-BN data from [42, 98, 161], single crystal *h*-BN from [94-96, 162], and thermal SiO_2 from [149, 163].

5.8 Summary of low temperature growth of *a*-BN for flexible nanoelectronics

The new low-temperature processing route towards ultra-thin and continuous *a*-BN described in this work, represents a significant breakthrough in dielectric processing necessary for next-generation 2D material heterostructure systems. The *a*-BN ultra-thin dielectric material deposited at 200 °C is universal in structure and chemistry on numerous substrates including flexible PDMS, traditional insulating electronic substrates such as SiO_2 and Al_2O_3, other 2D materials including graphene, 2D MoS_2, and conducting metals. A dielectric constant of 5.9 ± 0.7 at 1 kHz and breakdown voltage at

9.8 ± 1.0 MV/cm were measured for *a*-BN films, representing values higher than previously reported for CVD *h*-BN and close to that of single crystal *h*-BN, as shown in Table 5.1. The electronic properties of ultra-thin continuous *a*-BN produced by PLD, coupled with the versatility in materials processing and adaptability, the optical transparency, as well as the large-area and uniform coverage at low temperatures, make integration of *a*-BN into 2D nanoelectronic systems and devices a very exciting and appealing possibility.

CHAPTER 6. TRANSPORT BEHAVIOR IN NANOELECTRONIC BORON NITRIDE FILMS AND DEVICES

The previous chapters have elaborated on the space and time-dependent characterization of optimal plasma conditions required for growth of stoichiometric, high quality BN films (Chapter 3), the synthesis and characterization of 2D *h*-BN and ultra-thin *a*-BN films grown by this PLD technique (Chapter 4), and the first demonstration and measurements of the properties of low temperature growth of ultra-thin *a*-BN (Chapter 5). The amorphous phase of BN appears to have some significant advantageous over the state of the art directly-grown crystalline *h*-BN by chemical vapor deposition, including ease of the deposition technique, lower required substrate temperatures, and enhanced dielectric constant and breakdown strength. Little is known, however, as to how the crystalline structure of the two dielectric variants (i.e. crystalline *h*-BN compared to ultra-thin *a*-BN) might behave both in the degree in which the crystallinity impacts electron transport in the active material and how well heat dissipates in a typical 2D device setup, such as one shown in Figure 6.1. This chapter elucidates on these concepts in the following sections:

Section 6.1: Impact of boron nitride crystallinity on graphene device performance

Section 6.2: In-plane thermal conductivity of boron nitride films by PLD

Section 6.3: Thermal interface transport in BN/metal and BN/substrate interactions

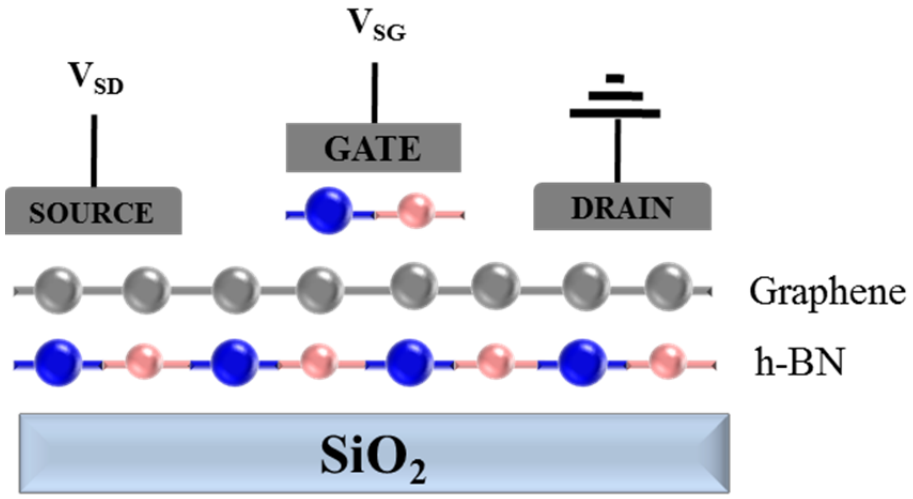

Figure 6.1: Typical *h*-BN/graphene/*h*-BN "sandwich" device setup, with *h*-BN set up as a smooth, lattice-matched substrate template for graphene devices and as a gate dielectric material.

6.1 Graphene device performance on ultra-thin *h*-BN and *a*-BN films

Some of the content in Section 6.1 describe elements of a previously published manuscript: Uddin, A., Glavin, N., et al., *Applied Physics Letters*, **107**, 203110 (2015).

The performance of graphene-based transistor devices is strongly impacted by the interactions with the substrate and gate dielectric material, as evidenced by the 2-8 times enhancement in electron mobility when the graphene is transferred either on a bulk *h*-BN substrate [90], or placed between two highly crystalline *h*-BN sheets [91] (see Section 2.4.1). The increase in mobility is presumed to be attributed to the atomically smooth, inert *h*-BN surface free of dangling bonds, as well as high energy surface optical phonon modes in the dielectric for reduced scattering in the graphene layer [164, 165] and high in-plane thermal conductivity of *h*-BN. The energy of the surface optical phonon modes

in the dielectric material has been shown to influence the saturation velocity due to charge carrier scattering. It has been predicted that the saturation velocity of future graphene devices can be enhanced by selecting dielectric materials with much higher optical phonon energies than the 55 meV surface phonon energy in SiO_2 [165].

With the advances in deposition technology discussed in sections of this manuscript (i.e. the use of PLD to form atomically smooth *a*-BN and *h*-BN films), isolation of the individual metrics that allow for enhanced graphene transport can be better understood. More specifically, with the *a*-BN and *h*-BN films having similar surface roughness, as well as inert chemistry at the interface, if an enhancement in graphene transport is measured in one case rather than the other, then it can be determine that structural components including lattice matching, van der Waals surface termination, and high surface optical phonon modes in *h*-BN are the dominant factors in influencing graphene behavior.

6.1.1 Preparation of boron nitride and graphene for device testing

In this study, 5 nm (20 laser pulses) boron nitride films were grown directly onto amorphous SiO_2 (300 nm)/Si substrates by pulsed laser deposition at temperatures of 200 °C and conditions discussed in Chapter 5. The highly doped silicon substrates (0.008 Ω cm) allowed for back-gate contact with the SiO_2/BN structure as the dielectric layer in the device. The highly dense, amorphous BN material was shown to convert to nanocrystalline *h*-BN films as a result of annealing at 400°C for 2 hours in forming gas. The grain sizes of the *h*-BN thin films were approximately 20 to 40 nm, as shown in the AFM image in Figure 6.2a, with an RMS roughness of 1.9 nm. It is important to note

that this annealing procedure was not necessarily successful on all attempts, and it is believed that the activation energy required for this grain conversion is a very tight window highly dependent on substrate conditions, film thickness, and surface roughness. Of the successful film conversions, a Raman peak was able to be distinguished that is characteristic of the *h*-BN E2g shear mode, and is shown in Figure 6.2b, and a SEM surface image is shown in Figure 6.2c.

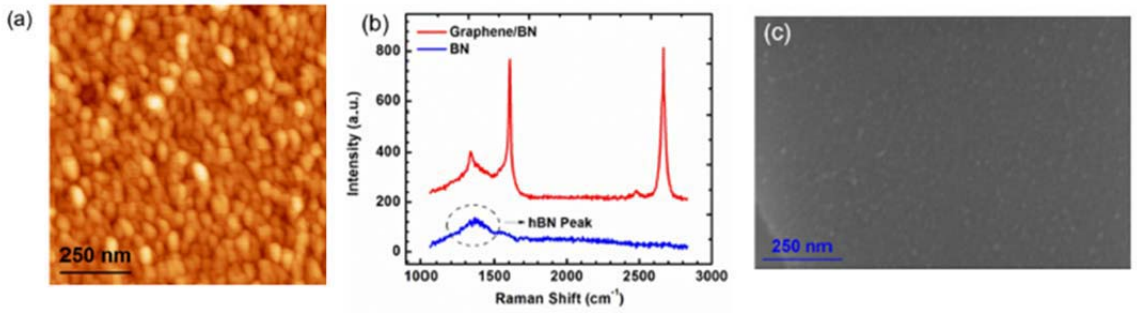

Figure 6.2: a) AFM topographical image of annealed BN showing grains with diameter varying from 20 to 40 nm, b) Raman spectra of graphene/BN (red) showing overlap of BN E_{2g} shear mode peak and graphene D peak and *h*-BN film showing E_{2g} peak, and c) SEM image of graphene/BN showing BN grains.

Few-layer graphene films for device testing were grown on Cu foil by CVD and transferred to the annealed h-BN and non-annealed *a*-BN films by the conventional PMMA assisted wet transfer method [166]. The 2D graphene was patterned using a photolithographic pattern and an O_2 plasma etch, followed by Ti/Au metal contacts and the lift-off in resist remover to make up the graphene devices. To compare the device performance, the same procedure was performed on an SiO_2/Si wafer without the 5 nm *a*-BN or *h*-BN material. A schematic of the back-gated device setup can be viewed in Figure 6.4a. After transfer of the entire device was transferred onto the substrate of interest, the samples were annealed again for 2 h at 400°C at 100 mTorr base pressure to

remove the polymer residue and for better adhesion of graphene to the substrate [167]. At this point the devices were fully constructed, and the annealing step did not influence the underlying boron nitride crystallinity.

Hole and electron mobility were extracted by using the following relationship:

$$\mu_{FET} = \frac{g_m L_C}{W_C C_{ox} V_{DS}}, \tag{6.1}$$

where the hole and electron mobilities were calculated using the left and right branches of the IV curve, respectively. In this evaluation, g_m is the transconductance, C_{ox} is the oxide capacitance, and L_c and W_c are the length and width of the graphene channel, respectively (7 μm length, 6 μm width).

6.1.2 Graphene device performance

Back-gated graphene devices on SiO_2, 5 nm *a*-BN, and 5 nm *h*-BN were evaluated by critical performance metrics including the Dirac point of graphene, as well as the electron and hole mobility in the device. Immediately upon evaluating the device performance on the 5 nm amorphous boron nitride films, it was observed to have very similar electronic behavior to that of graphene devices on traditional SiO_2. Thirty of these devices were constructed on each substrate, and an example drain current and back gate voltage curve of a representative device from each is shown in Figure 6.3b. The Dirac point, in this case, is shifted to a non-optimal voltage of >60 V, which is the maximum observable voltage for the testing system. This Dirac point shifting away from 0V is an indicator that the graphene is considerably influenced by extrinsic doping in the dielectric as well as a substantial amount of Coulombic scattering [168]. The polar

nature of the bonding in amorphous materials including *a*-BN and SiO_2 can additionally lead to enhanced scattering events due to surface optical phonon interactions, impacting the performance of the graphene material [169]. The hole mobility in the device structure is approximately the same in the presence of *a*-BN material compared to that of the traditional SiO_2 substrate. The lack of enhanced performance in graphene on the highly smooth, inert *a*-BN material indicates that the electronic performance depends on the surface bonding (i.e. van der Waals terminated vs. covalently terminated), as well as the lack of high energy surface optical phonon modes in *a*-BN that is exhibited by the crystalline *h*-BN.

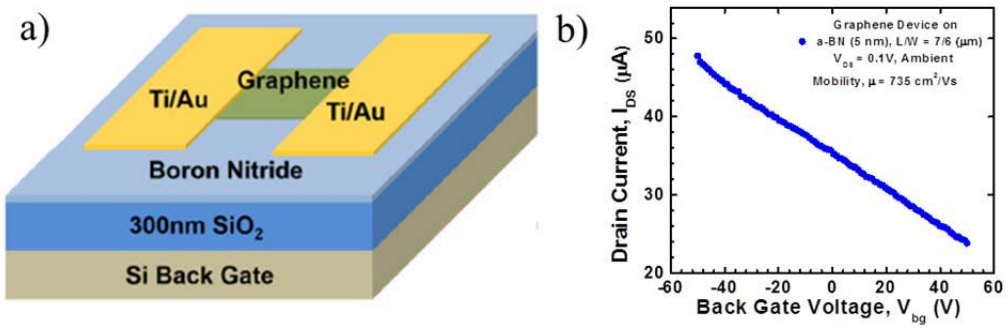

Figure 6.3: a) Graphene device setup on boron nitride thin films, and b) a representative I-V curve of graphene on 5 nm *a*-BN films, revealing poor performance of the graphene device and observable Dirac point shift.

The transistor device performance on the 5 nm *h*-BN on SiO_2 reveals that there is a stark difference in the graphene transistors on the poly-crystalline *h*-BN material. This performance enhancement results in a Dirac point shift for graphene, evident in Figure 6.4a, where the Dirac point for graphene is shifted to an average value of 3.5 V in the case of the *h*-BN coated back-gated device, compared to >60 V on the SiO_2 and *a*-BN

devices. The shift in Dirac point from a large positive value (in this case, greater than the measurable voltage) to approaching 0 V can be attributed to the reduction of the extrinsic impurity induced doping and charge inhomogeneity in graphene. Comparison of the hole mobility of 35 constructed devices on the *h*-BN and SiO_2 is shown in Figure 6.3b, where the average hole mobility was 1410 cm^2/Vs and 2854 cm^2/Vs on SiO_2 and *h*-BN, respectively, indicating a 2 fold improvement. The maximum measured hole mobility of graphene on *h*-BN was as high as 4980 cm^2/Vs, compared to a maximum of 1810 cm^2/Vs on SiO_2. Unfortunately, due to the Dirac point shift of greater than 60 V for graphene on bare SiO_2, a comparison of the electron mobility cannot be measured using the same techniques and equipment as described here because the dominant carrier type has not been switched to electrons in a readable voltage range. However, because the Dirac point in graphene is shifted to near 0 V for the case of the *h*-BN back-gated device, the right side of the IV curve can be evaluated for electron mobilities, which are plotted in Figure 6.3c. Extracted electron mobilities reveal an average of 1560 cm^2/Vs, and a maximum of 4200 cm^2/Vs. The last key observation for these films is the reduction in carrier concentration in the crystalline *h*-BN films, which also contributes to a reduction in the electron and hole scattering in the graphene layer.

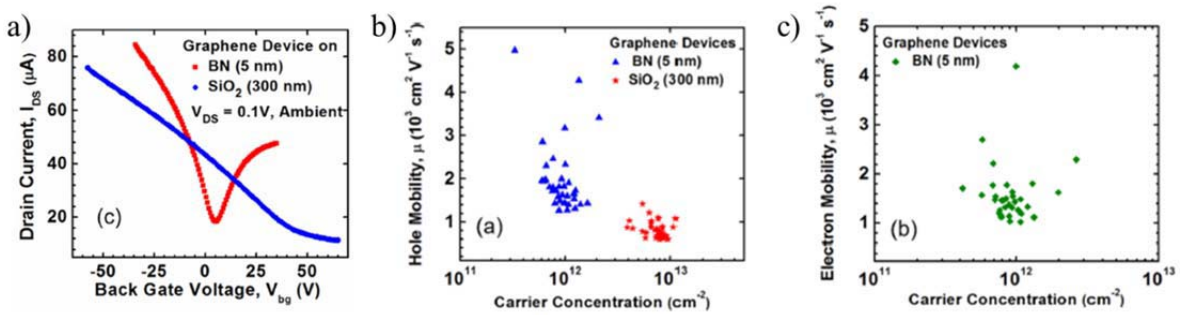

Figure 6.4: Graphene device performance on 5 nm *h*-BN compared to traditional SiO_2, with a) a representative IV curve of drain current and back gate voltage, b) hole mobility of graphene on *h*-BN and SiO_2, and c) electron mobility of graphene on the 5 nm *h*-BN.

It is clear that the electronic transport behavior in graphene is greatly affected by the interfacial bonding properties and structure of the dielectric material. For amorphous dielectrics including SiO_2 and *a*-BN, the increased scattering from Coulombic effects, the low energy surface phonon modes do not enhance the graphene thermal transport in comparison to nanocrystalline *h*-BN in this study. The weak bonding of the van der Waals terminated *h*-BN material was shown to be successful in improving graphene device behavior with regard to the Dirac point, hole and electron mobility. In high speed and, in particular, RF devices with short gate lengths, this mobility increase seen on crystalline *h*-BN is extremely crucial for pushing the limits of electrical performance. Additionally important in these potential device setups is the thermal transport behavior of the materials including the ability to conduct heat both in the 2D sense and eventually 3D.

6.2 Thermal conductivity of pulsed laser deposited boron nitride thin films

Elements from this section involving the technique used to freely suspend PLD BN films are highlighted in Alam, T., Wang, B., Pulavarthy, R., Haque, M. A., Muratore,

C., Glavin, N., Roy, A., Voevodin, A., "Domain engineering of physical vapor deposited two-dimensional materials," *Applied Physics Letters*, **105**, 213110 (2014).

6.2.1 Formulation of bridge structure and annealing of BN thin films

The thermal conductivity in BN films, like many other materials, is highly dependent on crystallinity, and the understanding of how the *a*-BN and nanocrystalline *h*-BN films synthesized by PLD will behave is crucial in determining the viability of these film structures as a dielectric material in a 2D device. In order to evaluate the thermal conductivity of the thin BN films, the specimen is ideally situated as a freestanding bridge in order to separate the thermal transport from the underlying substrate, as discussed early in Section 2.5.1 of this manuscript. To do this, a nanofabricator/manipulator, designed with the help of Aman Haque at Penn State University and represented in Figure 6.5, was used to create a freestanding BN and allow for IR microscopy thermal conductivity measurements. To create this elaborate structure, the boron nitride was first deposited on an SiO_2 wafer at 200 °C and various thicknesses of interest. Immediately following the PLD growth of boron nitride, titanium thin films of thicknesses approximately 10 nm were sputtered on the BN to aid in the manufacturing process and ensure no damage to the *a*-BN material upon subsequent removal of the photoresist. The material stack required for the devices is shown in Figure 6.5a. Following the titanium deposition, photolithography and reactive ion etching were used to pattern the rectangular bridge structures of 10 μm in width and 100 μm in length in a pattern depicted in Figure 6.5b. The bridges can then be micromechanically cleaved, lifted out, and placed on a micromechanical device portrayed in Figure 6.5c. Deposition

of carbon anchors at the end of the bridge represented in green in Figure 6.5d and e, the BN freely suspended bridges are mechanically secure in the desired bridge structure. At this point, a hydrofluoric acid vapor was used to remove the titanium without damaging the BN thin films and leaving no evidence of the Ti layer, as confirmed by energy filtered chemical elemental mapping in the TEM. The final configuration of the boron nitride thin films is represented in Figure 6.5e.

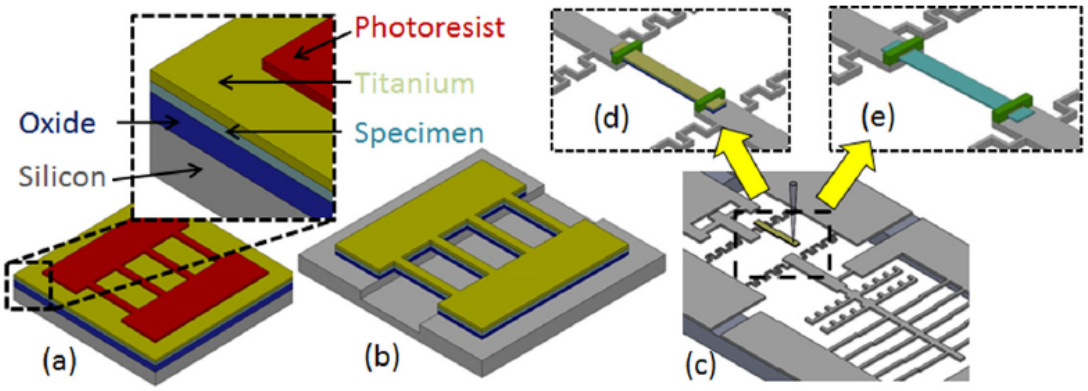

Figure 6.5: a) Material stack for freestanding films with initial PLD of BN film grown on SiO_2, then a titanium capping protection layer, followed by a patterned photoresist, b) then the specimen is etched and photoresist removed and c) micromechanically cleaved bridge structure transferred to nanomanipulation stage, d) securing the ends of the BN/Ti specimen and e) removal of the Ti layer for final boron nitride freestanding structure.

The custom designed TEM specimen holder and nanomanipulator stage design was inserted in to a JOEL 2010 TEM and had the unique ability to apply tensile strain as well as to pass current to induce Joule heating throughout the 40 μm long, 10 μm wide freestanding structure. In the as-deposited case, the 10 nm film is clearly amorphous, as evidenced by the low magnification TEM image in Figure 6.6a of the freestanding film at room temperature. In this configuration, a tensile strain of 1% was first applied to the specimen. Upon passing a current through the freestanding film (on the order of 10's of

mA), the amorphous material was successfully converted to nanocrystalline *h*-BN after 30 minutes at temperatures around 625 °C with domains on the order of as large as 100 nm. A top view TEM image in Figure 6.6b and corresponding diffraction pattern in Figure 6.6c depicts the beginning of nanocrystalline domains within the *a*-BN material, with a complete transformation to large nanocrystalline domains at 650 °C in Figure 6.6d and the diffraction pattern reminiscent of hexagonal lattice structure in Figure 6.6e. The film appears to be composed of an amorphous matrix with well-defined crystalline domains within the structure such as that portrayed in the TEM image in Figure 6.6f. This is an important processing achievement, as crystallization of amorphous structures typically require extremely high temperatures and/or pressures, and the observed crystalline change here is less than the normally >1000 °C temperatures required in other boron nitride studies [17]. The reduction in required temperature is explained by the role of surface diffusion at these temperatures, which has been shown to be the fastest pathway for atomic migration in comparison to grain boundary or bulk diffusion [170]. Due to the freely suspended nature of the films in this study, two of these boundaries are exposed (top and bottom), allowing for a substantial increase in surface diffusion from typical film growth on a substrate, which would just expose one surface condition.

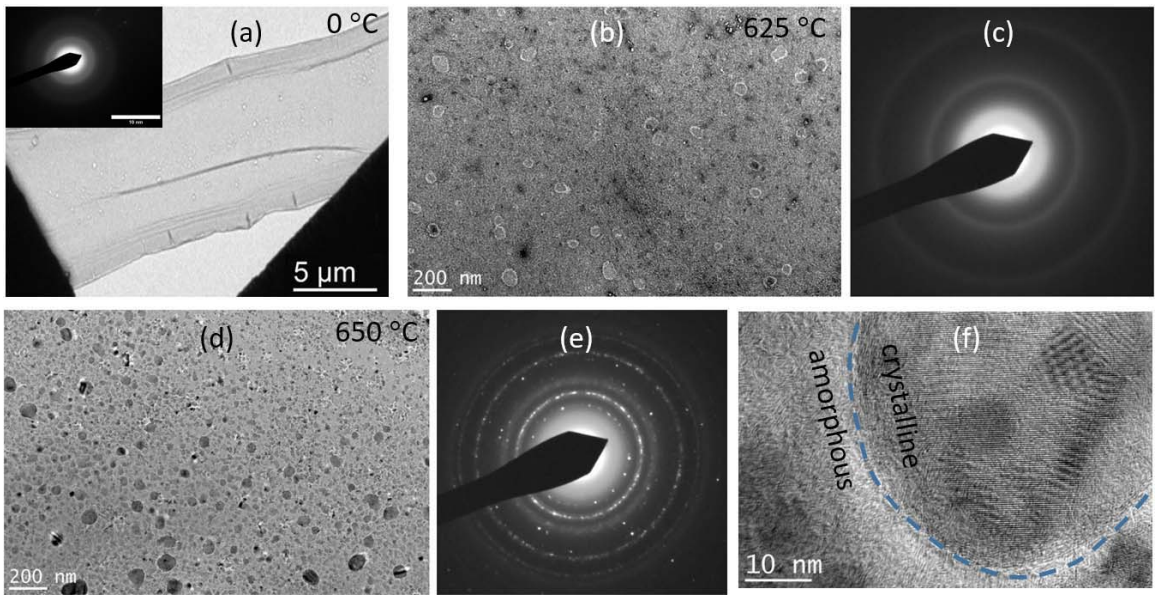

Figure 6.6: TEM images of a) freestanding amorphous BN specimen at room temperature (b) first observed crystallization change at 625 °C and c) corresponding diffraction pattern, d) image of annealed specimen at 650 °C (e) corresponding diffraction pattern showing amorphous to nanocrystalline phase transformation (f) high magnification image showing growth of a crystallite in the amorphous matrix.

The annealing of *a*-BN into an amorphous matrix with crystallite domains on the order of 100 nm at temperatures as low as 650°C was demonstrated only upon creation of a free-standing film to heighten the ability for surface diffusion to play a role. Additional time or added temperature did not enhance the crystallinity further, and it is apparent that the activation energies required for subsequent crystallization are not possible with this setup.

6.2.2 Thermal transport measurements in suspended films

In the freestanding bridge configuration, the BN films synthesized by PLD are amenable to measure thermal transport properties with the use of an IR imaging microscope, as described in Alam et al. [118]. With a pin-fin analysis and incorporating

Fourier's law for one dimensional heat conduction, two points using a 1D temperature gradient model using the expression below:

$$kA\left.\frac{dT}{dx}\right|_{x} - kA\left.\frac{dT}{dx}\right|_{x+\Delta x} = h_T P \Delta x (T - T_\infty), \tag{6.2}$$

where k is the thermal conductivity, A is the area, P is the perimeter length, h_T is the convective heat transfer coefficient from the specimen to the air, and T_∞ is the ambient temperature. The heat transfer coefficient is important in analyzing what extrinsic effects (i.e. convection and radiation) are lost to the ambient and to what extent it impacts thermal transport in-plane. In this case, Alam et al. [118] incorporated convection and radiation into the heat transfer coefficient through the following relation

$$h_T = \varepsilon\sigma 4T^4 + h_c, \tag{6.3}$$

where ε is the emissivity (0.8 for h-BN) and σ is the Stefan Boltzmann constant (5.670373×10^{-8} W m^{-2} K^{-4}). The general solution to Eqn. 6.2 is the following:

$$T - T_\infty = C_1 e^{mx} + C_2 e^{-mx};\ \ m = \sqrt{\frac{hP}{kA}}, \tag{6.4}$$

from the boundary conditions T_1 and T_2, at the two ends of the bridge structure, the final expression is given by

$$\frac{T - T_\infty}{T_1 - T_\infty} = \frac{[(T_2 - T_\infty)/(T_1 - T_\infty)]\sinh mL + \sinh m(L - x)}{\sinh mL}. \tag{6.5}$$

This expression has the unknown variables of the heat transfer coefficient, h, and the temperature at any given point, T. In order to determine the convective heat transfer, h, the convection parameter, h_c, must be evaluated given the expression $h_c = k_{air} * s$. The s parameter is from the thermal boundary layer profile from

$$T = T_\infty + (T_s - T_\infty) * e^{-sy}. \tag{6.6}$$

where y is the height from the specimen, and T_s is the specimen temperature. The s term in this expression is evaluated by measuring this thermal boundary profile as the slope of the graph in Figure 6.7.

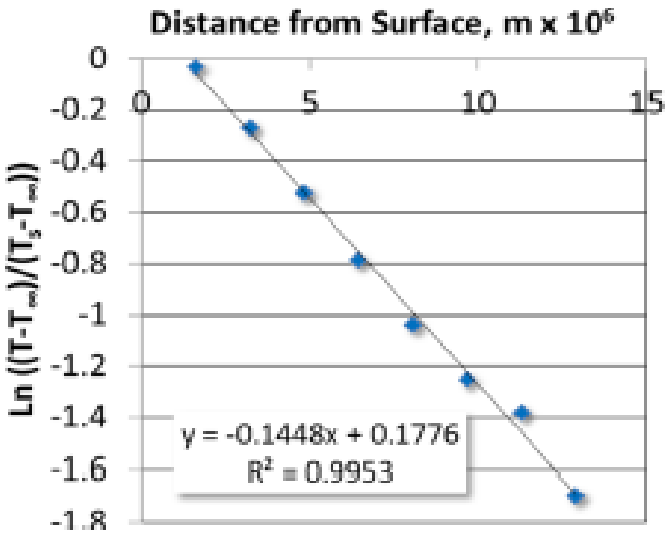

Figure 6.7: Thermal boundary layer profile from near the micro-heater surface to calculate the s term in the heat transfer coefficient, used by permission from [118] and AIP Publishing.

The thermal analysis was conducted both before and after crystallization, as the formation of any *h*-BN crystallinity would be expected to enhance the thermal transport dramatically. This expectation stems from the fact that bulk amorphous boron nitride has an estimated thermal conductivity of <1 W m^{-1} K^{-1} [171], whereas the in-plane conductivity of crystalline *h*-BN is measured to be as high as 360 W m^{-1} K^{-1}.

The nanomanipulator stage was removed from the TEM and the temperature profile was characterized using an Infrascope II thermal microscope (Quantum Focus Instruments Corporation) on the 15x setting, with a pixel to pixel resolution of 1.66

microns. The focal plane array type detector measures the amount and signature of the radiation from the specimen and calculates the film temperature with 0.1 K resolution. Heating occurred by passing a current through the sample at much smaller currents than was necessary for crystallization, and the ends were heated to between 50 and 75°C. In this narrow temperature range, the thermal profile was repeatable and no effect on the temperature-dependence of the thermal conductivity was observed.

The temperature profiles of the 10 nm as-grown *a*-BN and annealed *h*-BN samples in the freestanding configuration are shown in Figure 6.8. In the graph below, the symbols indicate experimentally measured temperature using the IR microscope and the lines represent the modeled thermal response using the approach described in Alam et al. [118]. An equal amount of current was placed on each end of the bridge, and Joule heating resulted in heat dissipation into the material. From the drop in temperature from the contact to the center of the bridge structure, the analysis described earlier can be used to quantify the in-plane thermal transport. Clearly, the crystallinity has a dramatic effect on the thermal distribution within the film structure. The thermal conductivity of the as-deposited *a*-BN film is derived to be 5 W m^{-1} K^{-1}, which is higher than previously reported values for measured bulk *a*-BN of <1 W m^{-1} K^{-1} [171]. The observed increase in thermal conductivity could be due to some hexagonal or ordered bonding formed due to the high kinetic energies associated with the plasma-based deposition process. This type of bonding is not observed in the Raman spectra at these thicknesses and the intensity of the phonon response is expected to be fairly low and potentially non-observable.

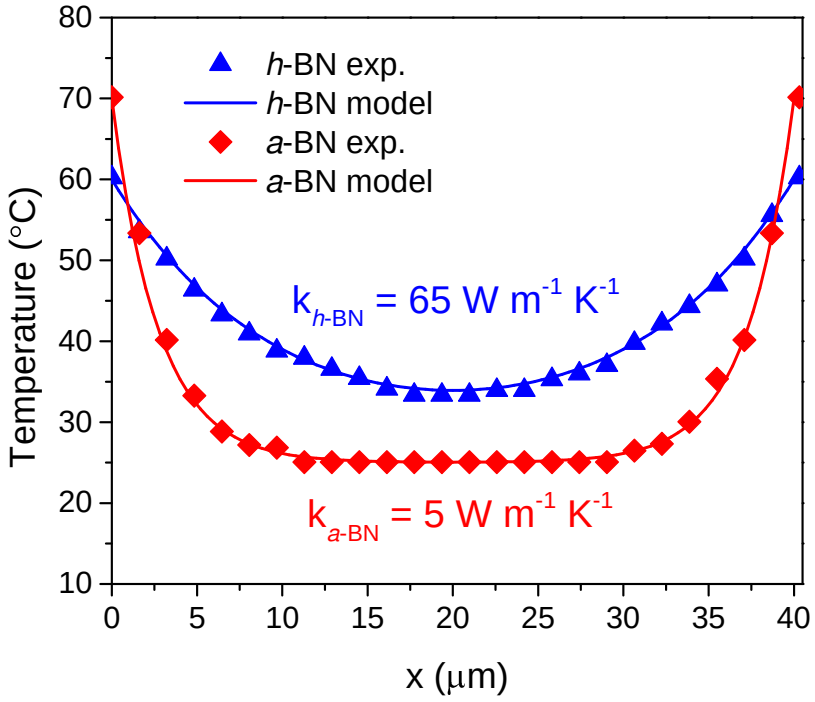

Figure 6.8: IR temperature measurements of *a*-BN and *h*-BN suspended thin films along with derived thermal conductivity.

The modeled estimated thermal conductivity of the annealed samples with hexagonal domain sizes as large as 100 nm was 65 ± 0.65 W m^{-1} K^{-1}. The increase in conductivity by a factor of 13 is a remarkable improvement, which we attribute to the crystalline domains with higher in-plane thermal transport than the amorphous matrix of surrounding material. The nanocrystalline material exhibits a 35% lower measured conductivity value than CVD grown *h*-BN, and nearly 5.5 times lower than exfoliated single crystal *h*-BN [108]. This is undoubtedly due to the boundary scattering and resultant reversal of the phonon momentum from both the grain boundaries inside the crystalline domains as well as the crystalline/amorphous boundary.

The in-plane thermal conductivity of the dielectric material is expected to contribute strongly to the lateral heat spreading in the device. As the device length-scales continue to diminish and the increasing demand to fit more transistors on a singular chip design, lateral heat spreading may turn out to be insufficient as a means to mitigate hot spots in graphene devices. Thus, 3D heat transport will become increasingly important, as elaborated on in the following section.

6.3 Engineering thermal interface conductances at boron nitride device interfaces

Thermal management in 2D devices will become increasingly important as the material and device length scales are continually reduced, resulting in heat to propagate into the substrate or metal contacts, as discussed in Section 2.5.2. In graphene devices similar to the one portrayed in Figure 6.1, the choice of dielectric interfacial material will be crucial in mitigating hot spots, which can ultimately lead to premature device failure.

It is well known that by varying the gate voltage in an ambipolar graphene field effect transistor (GFET) with respect to the source and drain voltage, the dominant carrier can be switched from electrons to holes, and vice versa [165]. The dominant carrier type and effective energy of each carrier leads to a shift in the hot spot location, caused by Joule heating within the graphene device, from near the electrodes to in the middle of the channel [172]. Upon evaluating the interface thermal conductance behavior in graphene devices, and under the assumption of heating in the center of the channel in the device, it was predicted that at source-to-drain length scales less than 600 nm the interface transport will especially become a major contributing factor for heat mitigation [119]. While many current graphene devices have gate lengths approaching this length-scale,

future devices are expected to require significantly smaller gate lengths, thus enhancing the need to understand thermal transport at interfaces.

The area near the gate dielectric typically experiences very high electric fields and as a result, hot-spot formation under or on the drain-side of the gate can lead to degraded device operation and reliability. Considering graphene devices with very short channel lengths (< 600 nm), the interface thermal transport between the gate dielectric and the metallic gate contact is essential for dissipation of heat away from the channel material. As 2D BN may be considered to be an ideal dielectric material for such a purpose, the van-der Waals terminated *h*-BN is hypothesized to have a weak interaction both electrically and thermally with the metallic contact in contrast to strong covalent or ionic bonding. Bresnehan et al. [38] evaluated such a hypothesis by measuring the effective thermal conductance of various degrees of crystallinity, stoichiometry, and interfacial roughness in *h*-BN that was directly grown by CVD on Si (111) and Al_2O_3 (0001) substrates. TEM images in Figure 6.9a-d from [38] demonstrate the crystallinity dependence upon applied surface temperature during growth, where *h*-BN grown at 1000°C show a high degree of hexagonal crystallinity, with a reduced degree of crystallinity at lower growth temperatures. The Al_2O_3 (0001) and Si (111) substrates do not provide for an epitaxial surface template for *h*-BN growth, and therefore even the high temperature grown material is very rough (> 3 nm RMS) and exhibits nanocrystalline grains. In addition, the coefficient of thermal expansion (CTE) mismatch between the substrate and *h*-BN film results in vertical c-axis growth caused by strain in the film upon cooling, as *h*-BN has a negative CTE [61]. Complimentary to the structure analysis, XPS analysis determined that there was small evidence of oxidation (typically

observed in *h*-BN films upon exposure to air) in the 1000°C as well as the 250°C with anneal, but the 400°C and 250°C processing conditions produced significant modification of the bonding chemistry. A combination of the surface roughness, crystal size, and chemistry synergistically contribute to an overall trend of increasing effective thermal conductance upon decreasing crystal size and surface roughness. Potentially, the amorphous boron nitride material synthesized by pulsed laser deposition can provide for this optimal thermal interface with metallic contacts due to strict control of stoichiometric chemistry, atomic-scale roughness, and lack of weak van der Waals surface termination.

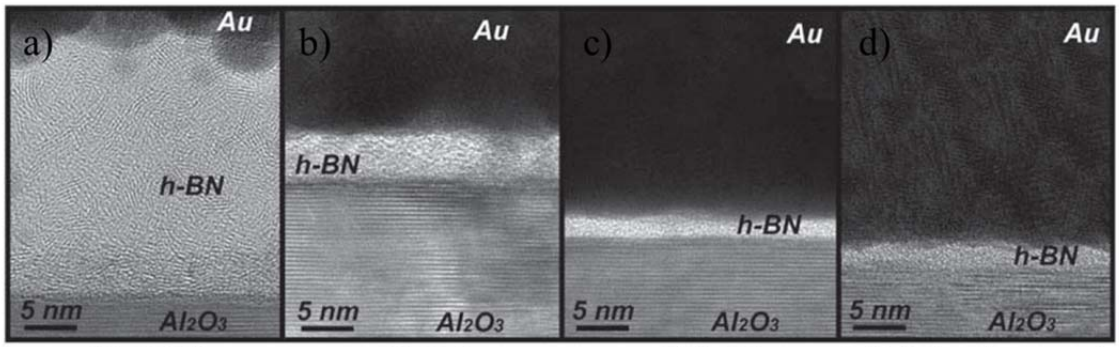

e)

Substrate	Growth condition	Thickness (nm)	Interface thermal conductance ($MW/m^2/K$)[a]	BN thermal conductivity (W/m/K)
Si(111)	1000 °C	25	17 ± 1	0.46 ± 0.01
	400 °C	7	51 ± 2	…
	250 °C	2	65 ± 2	…
	250 °C with anneal	2	72 ± 2	…
Al_2O_3(0001)	1000 °C	25	20 ± 1	0.57 ± 0.02
	400 °C	7	58 ± 1	…
	250 °C	2	98 ± 6	…
	250 °C with anneal	2	88 ± 3	…

[a]Effective conductance, including thermal transport through film thickness and interfaces.

Figure 6.9: TEM images of *h*-BN directly grown by CVD on Al_2O_3 at a) 1000°C and 25 nm thickness, b) 400°C and 7 nm thickness, c) 250°C and 2 nm thickness, d) 250°c and 2 nm thickness followed by post-annealing at 1000°C, and e) table of effective interface thermal conductance measurements of the films grown on Si (111) and Al_2O_3 (0001), all reprinted by permission from [38].

6.3.1 Experimental setup for thermal conductance measurements

Due to the amorphous nature of the pulsed laser deposited *a*-BN, the structure and chemistry can potentially be expanded without much change from the ultra-thin form to create thick dielectric layers. This is not the case in crystalline BN growth, as tertiary systems are common with transitions to c-axis growth of turbostratic *h*-BN after only several nanometers of growth at the interface [73]. In the metal/*a*-BN interface, the thermal transport can be specifically isolated using the time domain thermal reflectance (TDTR) technique presented in Section 2.5.2. If the *a*-BN material is grown to be thicker than the thermal penetration depth of the femtosecond laser, *l*, where $l = \sqrt{\frac{\alpha}{\pi * f}}$, α is the thermal diffusivity, and f is the laser frequency. Beyond this thickness *l*, the *a*-BN material is treated thermally as a "substrate," because the thermal input pulse will not penetrate to the underlying Al_2O_3 substrate. In this study, the "thick" *a*-BN was grown to thicknesses about 60 nm, verified by cross-section SEM microscopy, and was thicker than the thermal penetration depth of the laser.

The *a*-BN thick films were grown by a total of 500 laser pulses (60 nm BN) impacting the target, with an Al_2O_3 [0001] substrate temperature of 200°C and depositions were performed in succession to ensure repeatable film growth for testing. Figure 6.10 depicts the required sample stack for BN/metal conductance evaluation by the TDTR technique. To apply metal contacts, the films were left in vacuum after PLD processing (< 10^{-6} Torr), and allowed to cool to room temperature before metal deposition. Magnetron sputtering by both DC (Direct Current) and HIPIMS (High Power Impulse Magnetron Sputtering) were performed in the same chamber as the PLD

processing without exposing the sample to air. HIPIMS is used oftentimes for metal deposition in TDTR measurements, as the high current density applied to the target generates a substantially higher density of ionic species, resulting in low surface roughness of the metal contact and good signal to noise of the reflectance signal. Stabilizing and adjusting the plasma conditions to just the right regime for optimal growth depends on ionization energy, atomic mass, and thermal conductivity of the target material. In the HIPIMS of gold, tantalum, and aluminum metals, relatively higher energies (450V applied, 90 μs pulse width, 120 Hz repetition rate) were used to create a stable plasma at a pressure at 15 mTorr. The overall flux of material is decreased due to the short "on" time of the sputtering target, with required overall deposition rates of the metals varying greatly from 1.5 hours to 2.5 hours in order to reach thicknesses of 75-100 nm. With the case of titanium, the low thermal conductivity of the metallic target (17 W m^{-1} K^{-1}) resulted in excessive heating during the high energy HIPIMS deposition. To overcome this, the pulse width and repetition rate were reduced to 30 μs (67% reduction) and 60 Hz (50% reduction) for a titanium growth process at lower energies. Conventional DC magnetron sputtering was also used for growth of the high Debye temperature, very reactive metals (Ti and Al) to evaluate the impact on deposition conditions on interface transport behavior. Conventional DC sputtering reduces the amount of ions relative to excited neutrals in the plasma plume, and greatly increases the flux of material, cutting down the deposition times to 10 and 5 minutes for Ti and Al, respectively.

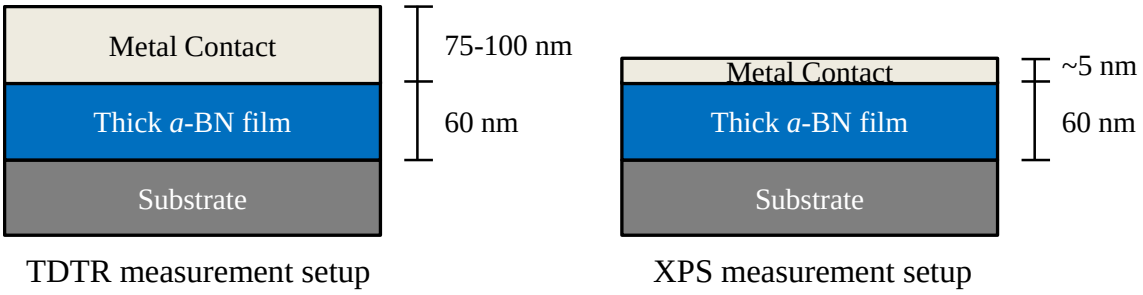

Figure 6.10: a) TDTR Device setup for *a*-BN/metal contact thermal conductance evaluation, and b) XPS setup for chemical analysis of BN/metal interface.

Time domain thermoreflectance (TDTR) measurements were recorded in a process similar to that described in [120] and modeled in [121]. A total of five scans were taken for each sample, and error bars accommodate for the variation in thermal conductance values to one standard deviation. To aid in the understanding of interfacial surface bonding, XPS analysis of the BN/metal interface was made possible by reducing the deposition times of the metal contact to coat the sample surface with 5 nm of metal, as shown in Figure 6.10. This distance is small enough to capture and examine photoelectrons from the boron nitride underlying surface, as the escape depth of these photoelectrons is typically around 10 nm depending upon the material properties and the electron mean free path.

6.3.2 Optimization of thermal conductance at *a*-BN/metal interfaces

In Debye theory, the Debye temperature, Θ_D, can be expressed as the following:

$$\theta_D = \frac{h\nu_m}{k_B}, \tag{6.7}$$

where h is Planck's constant, ν_m is the Debye frequency, and k_B is the Boltzmann constant. The Debye temperature and frequency terms are brought about using the Debye

approximation. In this analysis, the sinusoidal phonon dispersion relationship seen in real materials is simplified using a linear approximation, where $\omega(K) \approx v_{g,avg}K$, where $v_{g,avg}$ is the constant average group velocity, and *K* represents the position in K-space. The allowable number of states in a 3D metallic material as a function of the wavevector, K, is expressed as $K_{D,3D} = (6\pi^2\eta_{a,})^{1/3}$, where η_D is the number of unit cells per volume. The Debye frequency, then, is evaluated by substituting the $K_{D,2D}$ expression into the dispersion relation shown below:

$$\omega_{D,3D} = v_{g,avg}(6\pi^2\eta_a)^{1/3}, \tag{6.8}$$

The Debye temperature, shown in Eqn. 6.7, is simply the Debye frequency multiplied by the reduced Planck's constant, divided by Boltzmann's constant such that $\theta_D = \frac{\hbar\omega_{D,3D}}{k_B}$.

In these approximations the higher Debye temperature metals are directly related to an increase in average phonon group velocities. This increase in acoustic phonon average group velocity is hypothesized to be a driving reason for the observed increase in thermal conductance in high Debye temperature metal contacts on graphene [119] and graphite [122]. Thermal interface conductance measurements of thick *a*-BN/metal interfaces are plotted in Figure 6.11 as a function of increasing metal Debye temperature. An overall increase in interface conductance with an increasing Debye temperature is evident, with the BN/Au and BN/Ta conductance at approximately 20 MW m^{-2} K^{-1} and the BN/Ti and BN/Al conductances greater than 50 MW m^{-2} K^{-1}. The thermal transport at the interfaces of these more reactive and lighter metals, Ti and Al, depends on the metal deposition conditions, as the low energy (LE) HIPIMS deposition of Ti enhances the thermal conductance, while the DC sputtering is optimal for Al contacts.

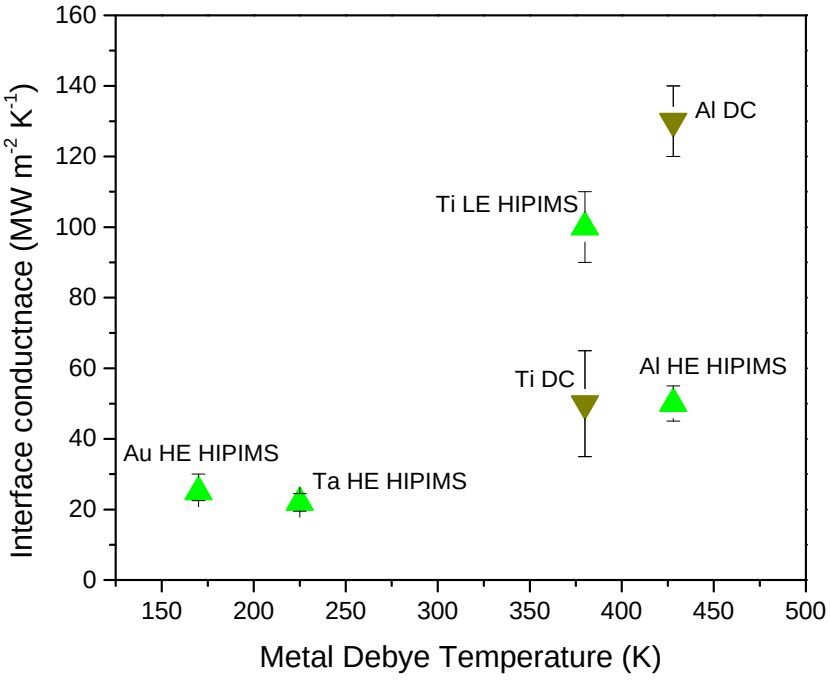

Figure 6.11: Interface conductance TDTR measurements of various metals and metal deposition processes, where "LE" designates low energy, and "HE" designates high energy.

The atomic mass of the metals chosen in this study are inversely proportional to the Debye temperature. Due to the very small atomic masses of boron and nitrogen, the smaller atomic mass of a metal atom results in a reduction in the anharmonic losses at the interface, further enhancing thermal conductance. To elaborate on this phenomena, elements of the Acoustic Mismatch Model (AMM) can be used to describe impedance matching at the interface of two materials. In the AMM evaluation, the acoustic impedance, Z, and the matching of such impedances is extremely important, and directly influences the transmission across the interface. The impedance term is related to the

acoustic velocity, v_a, and mass density of the spring, μ, by $Z = \mu v_a$. The transmission probability, t_{12}, across the gap is depicted below:

$$t_{12} = \frac{4Z_1Z_2}{(Z_1+Z_2)^2}. \tag{6.9}$$

Where Z_1 is the impedance of material 1, Z_2 is the impedance of material 2. In this expression, t_{12} is maximized only when the impedance on both sides are equivalent. The impedances here are directly relatable to the phonon behavior on each side of the interface, which is a function of the atomic mass and arrangement of the atoms within the unit cell. Thus, by choosing metals with better acoustic impedance matches (e.g. smaller atomic mass, bond stiffness), an increase in thermal transport across the interface is expected. This effect will be maximized if the acoustic phonon group velocities are very high as well, such in the case of those with small atomic masses and high Debye temperature metals.

Chemical analysis by XPS can potentially elucidate mechanisms as to the differences in interfacial bonding chemistries and the impact on thermal transport behavior. The 60 nm as-deposited *a*-BN displays the same bonding characteristics and chemical stoichiometric construction, shown in Figure 6.12, as the ultra-thin form described in Chapter 5 in this document. The B*1s* and N*1s* high resolution scan depicts singly distributed boron and nitrogen atoms bound to one another, with an atomic boron-to-nitrogen ratio of 1.00. A slight shoulder on the higher binding energy end of both spectra indicates a slight surface oxidation due to ambient exposure, commonly observed in boron nitride films of similar composition [38, 61]. By reducing the metal deposition time and synthesizing a very thin metal film of approximately 5 nm on the *a*-BN material,

the chemical bonding behavior at the interface can be evaluated by XPS. The deposition of gold by the HIPIMS process leads to a slight change in the bonding chemistry of the BN material, evidenced by an increase in B:N ratio to 1.07. The main chemistry of the underlying film is relatively unchanged, as the B*1s* and N*1s* scans indicate signatures of BN, with a slight increase in oxidation at the higher binding energy shoulder of both peaks. The increase in oxidation is most likely due to film damage from the bombardment of large Au ions and subsequent increase in surface roughness as well as removal of nitrogen atoms from the BN lattice structure. Also, the oxidation can be due to voids or non-uniform film growth, as gold tends to form islands and leave the underlying film not entirely covered and exposed to the environment in this case [173]. Spectra of metallic tantalum films do not show any abnormal surface chemistry as well, leading to the assumption that the limited thermal conductance at these two interfaces is primarily due to low metal Debye temperatures, potentially non-uniform coverage, and anharmonic losses due to large atomic mass differentials.

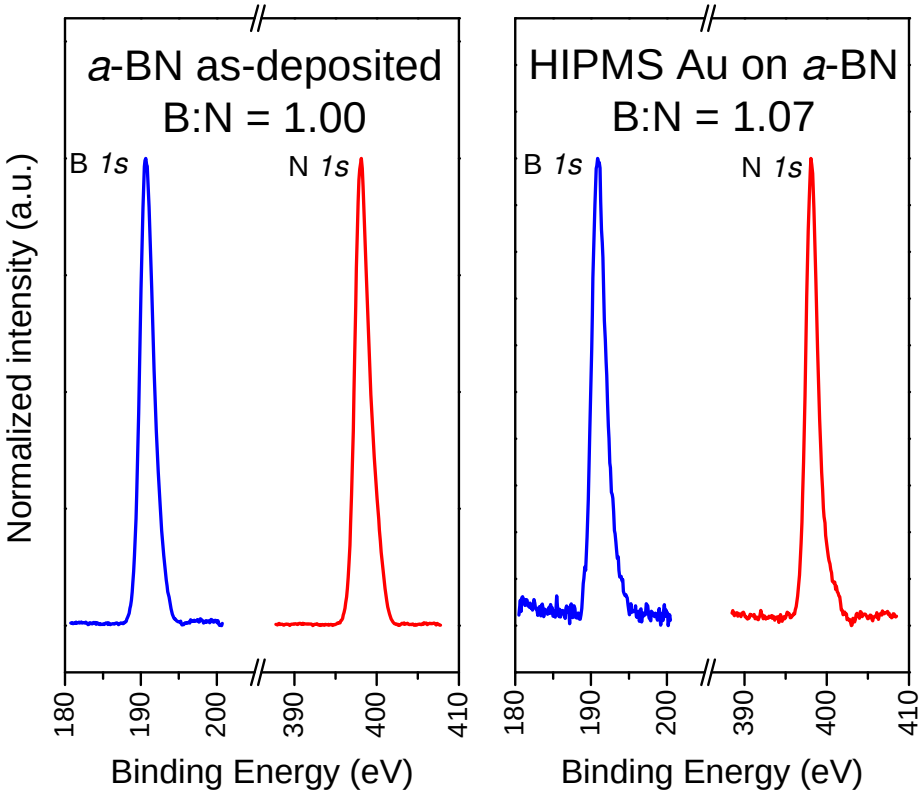

Figure 6.12: XPS scans of B*1s* and N*1s* areas of the spectra of as-deposited *a*-BN and chemical signature of *a*-BN under a 5 nm Au film deposited by HIPIMS.

A more intensive analysis is required for the highly reactive titanium and aluminum samples, especially considering the enthalpy of formation for titanium nitride and aluminum nitride is very favorable, and therefor one might expect to see interfacial bonding [174]. The analysis of the DC and low energy HIPIMS deposition on *a*-BN is in Figure 6.13. The DC Ti metal contact proved to be a relatively poor interface conductance material, with a thermal conductance of 50 W m^{-2} K^{-1}, and the evidence is clearly shown from the chemical bonding behavior that a destruction of the underlying BN film was the primary cause. The B *1s* spectra reveals a significant change in BN

chemistry, with nearly all of the boron removed due to Ti bombardment, and a B:N ratio of 0.07. The residual nitrogen is bound up in a TiN layer at the interface, corresponding to an emergence of a new peak in the XPS spectra corresponding to the same. A thin layer of TiN is also formed in the low energy HIPIMS, however the underlying BN film retains much of the chemistry and does not show as much evidence of extreme alterations in surface chemistry. The thermal conductance in this case is nearly 100 W m^{-2} K-1, and an increase in thermal transport is presumed to be due to this TiN layer and the fact that the underlying BN layer is not completely destroyed. In addition, titanium nitride is a unique ceramic nitride in that the thermal conductivity of TiN is similar to the metallic Ti (both near 20 W m^{-1} K^{-1}), but the electrical properties and hardness or significantly higher [175]. In the case of HIPIMS Ti deposition, the metallic-like hard ceramic interface with stiff bonds is hypothesized to encourage phonon transport in comparison to the TiN layer that is destructive to the BN surface chemistry. Titanium is a very commonly used adhesive layer especially for Ti/Au contacts, and it is clear that the surface chemistry of nitrides can be significantly altered by the favorable TiN formation. Understanding this phenomena and how the deposition conditions impact the formation of this layer is extremely important, and this study is a step forward in understanding mechanisms for thermal transport across these boundaries.

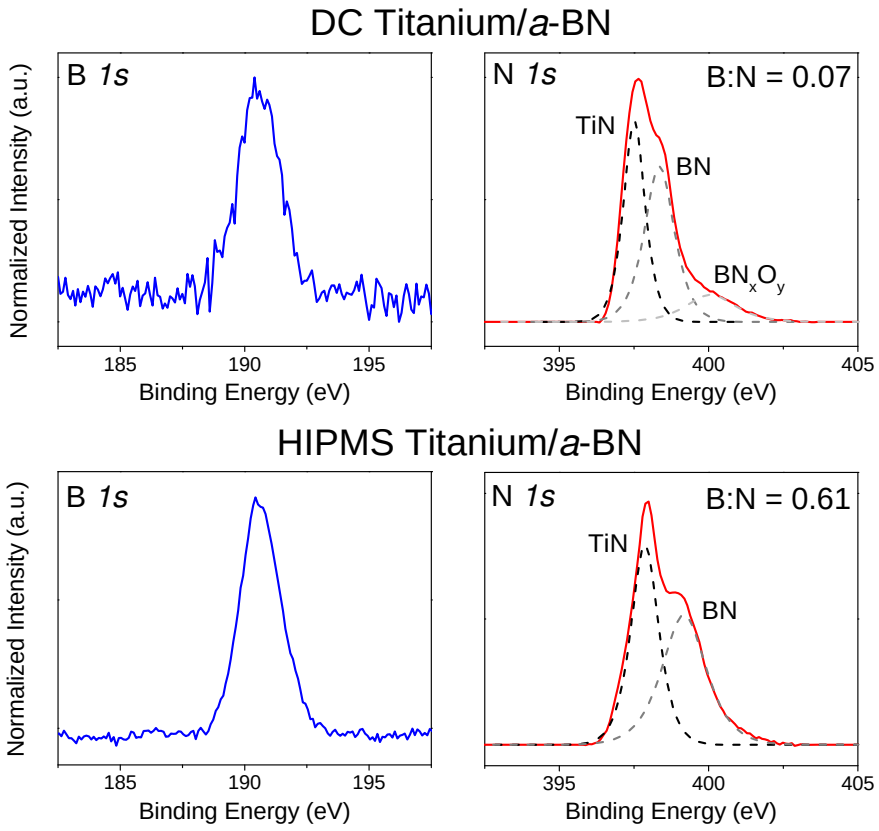

Figure 6.13: XPS spectra of DC and HIPIMS Ti coated *a*-BN films.

The metal deposition technique appears to have a great effect on the measured conductance values of titanium contacts. The aluminum capped *a*-BN shares a similar response to the sensitivity to deposition techniques, however, shows an inverse dependence than was observed in titanium. The DC coated aluminum sample resulted in a high thermal interface conductance of 130 MW m^{-2} K^{-1}, and the surface chemistry reveals a pristine preservation of boron nitride, free from damage or oxidation. No evidence of surface oxidation at higher binding energies is present, which is believed to be a major factor for inhibiting thermal transport in other measured metal contacts. The DC coated aluminum material creates a pristine, highly conformal coating, where even at

5 nm no evidence of oxidation is present. In contrast to that, the HIPIMS aluminum does appear to retain the boron nitride chemical signature, but does show significant surface oxidation at the higher binding energy tail of the B *1s* and N *1s* spectra in Figure 6.14. This is presumed to be a factor in the observed decrease in thermal conductance of approximately 60%. Evidence of surface oxidation in the underlying *a*-BN at nearly the same thickness of Al could be the evidence of voids or non-complete surface coverage, such as the case of Au thin films discussed earlier. It is thought that a combination of surface oxidation and voids observed in the case of HIPIMS Al can reduce the effective contact area, and thus reducing the overall thermal conductance at the interface.

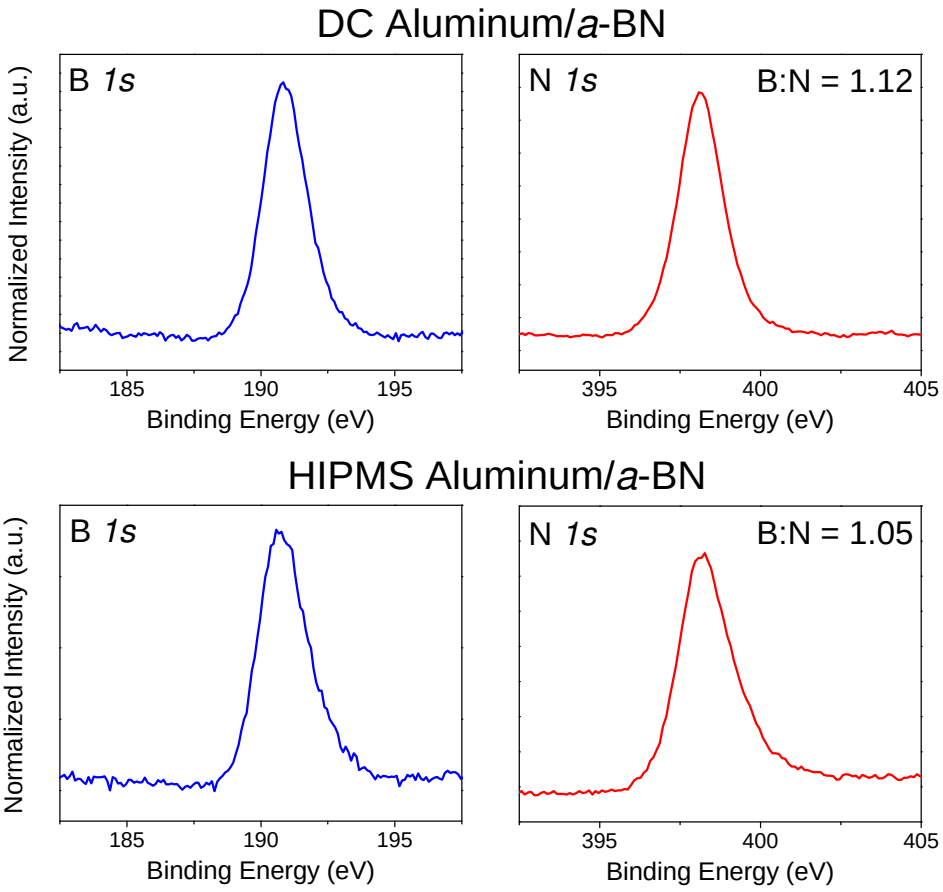

Figure 6.14: XPS Spectra of DC and HIPIMS Al coated *a*-BN films.

It is very clear that the choice of metallic gate contacts in a short channel device can have a drastic effect on the thermal conductance away from the channel material. By choosing metals with high Debye temperatures (e.g. Ti, Al), and ensuring the deposition conditions facilitate an optimal interface, engineering of contacts in these devices is possible to enhance the 3D heat transport at the gate/metal interface. The surface oxidation appears to be a major limiter for thermal transport, as the surface layer provides for another resistance in the transmittance of phonons through the interface. Figure 6.15 presents the calculated surface oxidation from the N *1s* spectra for the various thin metals, displaying a clear trend of decreasing thermal conductance upon observance of the BN surface oxidation. Controlling the oxidation is possible through careful choice of deposition technique and ensuring uniform coverage without voids, which can potentially lead to weak interactions or a reduction in effective surface area. In the future, understanding the metal/dielectric interface transport, and limitations for transport, will be vital in ensuring that thermal management is not limiting the performance of the device.

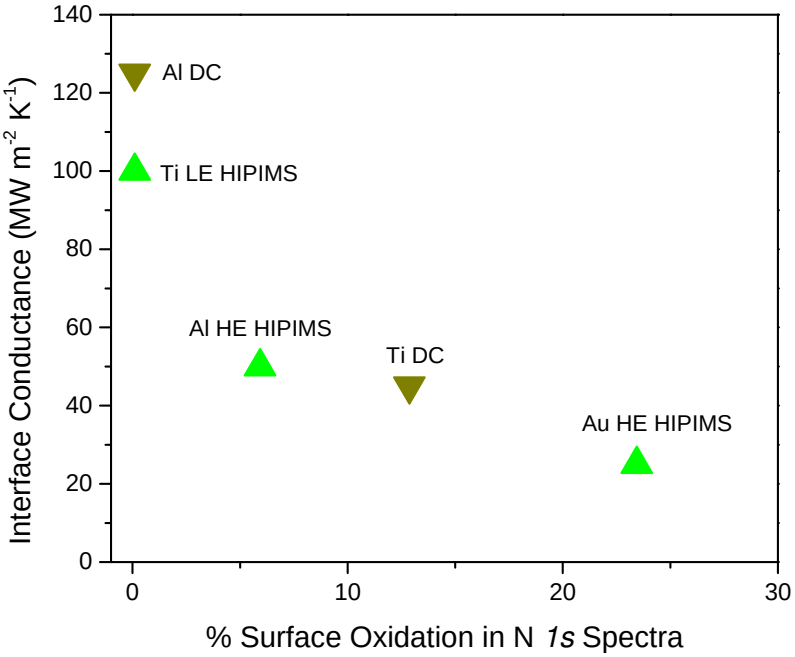

Figure 6.15: The impact of observed *a*-BN surface oxidation to the interface thermal conductance of metal/*a*-BN interfaces with various thin (5 nm) metal contacts and at the performed deposition conditions.

6.4 Summary of transport in *a*-BN and *h*-BN dielectrics for graphene devices

In semiconducting and conducting 2D materials, the interplay between film crystallinity and electronic properties is vital to understand, as a reduction in grain size typically leads to many more spots for electron and phonon scattering events to occur. In the case of 2D insulating materials, where there are no free or easily thermalized electrons, the impact on grain size is not as well understood. The section here is an attempt to understand some of the impacts that the dielectric structure and properties can have on device metrics including electronic properties of the active material, in-plane thermal transport, and thermal conductance at critical interfaces. Nanocrystalline *h*-BN performed exceptionally well in regards to both positively influencing graphene transport

in a 2D device structure, as well as providing for an efficient lateral heat spreader, evidenced by a 13 times increase in thermal conductivity than the amorphous material. Amorphous boron nitride, due to the fact that the top surface is not van der Waals terminated, allows for an exceptionally high thermal conductance upon coming in contact with a high Debye temperature metal with the appropriate deposition conditions. Moving forward in device fabrication, these individual studies can be key in providing for a template as to the dielectric influence on device performance.

CHAPTER 7. CONCLUSIONS

Two-dimensional materials systems lead the way in one of the most intriguing fields of scientific research, as physics at the atomic-scale can provide a means to revolutionize the field of electronics, optoelectronics, human performance monitoring, frictional and high temperature coatings, and many more. Of these materials, hexagonal-boron nitride continues to be one of the most desired, as properties including high temperature resistance, good dielectric performance, and structural similarities to graphene naturally hint at use of this material for a dielectric partner in 2D van der Waals systems. The results found in the studies highlighted in this dissertation may be the key to opening this possibility, as many of the material limitations are overcome with the use of plasma processing and a very fine control of chemistry and properties.

The fundamental understanding of nucleation and growth by means of optical spectroscopy during plasma conditions can be challenging, but the knowledge gained by this process can be exceptionally enlightening. In this case, the plasma spectroscopy over a wide wavelength range and plasma imaging at the substrate location have been utilized to elucidate mechanisms that promote nucleation and growth of ultra-thin (< 5 nm), stoichiometric, and uniform BN films by PLD. Specifically, by measuring space and time-dependent plasma behavior during growth it was determined that the arrival of B^+ and N* at approximately 800-1000 ns after the laser impacted the target was the primary mechanism for formation of cohesive BN films at the processing conditions analyzed. At

a pressure of 50 mTorr N_2 gas pressure, the B^+ and N* conditions at the substrate were favorable for high kinetic energy species, without too much energy as to cause damage to the substrate. The much higher concentration of N^+ ions proved to have a minimal positive impact on film growth, and actually could be a detriment to film growth, as these ions arrived at the substrate location at a much later time and with high kinetic energies through the plasma sheath. Future studies in growth optimization could specifically isolate each of these atomic, neutral, and molecular fluxes by means of magnetic fields or shadow masks and build on this initial optical study.

The pulsed laser deposition technique is significant in that the resulting films are highly uniform, large area, and amenable to commercialization much more than typical lab-scale synthesis processes. For the first time, in this study, the hexagonal phase of boron nitride (*h*-BN) was shown to nucleate and grow at large areas and with strict control of layer thickness at temperatures much lower than conventional CVD processing (700°C compared to >1000°C). The key to formation of hexagonal crystallinity is providing for template epitaxial-like growth, which in this case was facilitated through the use of an HOPG substrate. The additional kinetic energies within the plasma, specifically tuned to input activation energy for crystal formation, allow for the possibility of this growth of nanocrystalline *h*-BN with grain boundaries of approximately 5 nm. The film was demonstrated to be completely covering the substrate with no evidence of cross-plane voids or defects by evaluation with XPS, TEM, and C-AFM conductivity measurements. In comparison to conventional preparation methods for *h*-BN, the technique described herein is an exciting step forward for large area, fast throughput growth of a very exciting 2D material.

On non-lattice matched substrates at the same plasma processing conditions and at temperatures <200°C, a highly dense, substrate-agnostic amorphous boron nitride (*a*-BN) was observed to nucleate and grow. Up until this work, the phase of boron nitride has yet to be investigated for the purposes of nanoelectronics research. The crystalline allotrope, *h*-BN, is one of the most intriguing possibilities for dielectric materials in 2D devices, but the synthesis and processing is very difficult in the sense that high temperatures and specific substrate templates are required. The *a*-BN demonstrate here can be grown at very low temperatures, and on just about any substrate with atomic or near atomic-scale roughness. The amorphous material was shown to nucleate and grow at thicknesses from 2 to 17 nm on diverse substrates including crystalline Al_2O_3, amorphous SiO_2, various metals such as tungsten and copper, and other 2D materials, while all retaining the same chemical and structural properties. This is a very exciting revelation, as the ease in processing makes it much more favorable for 2D devices in certain circumstances. The device scale electronic properties were evaluated, and a dielectric constant of 5.9 ± 0.65 at 1 kHz, breakdown voltage of 9.8 ± 1.0 MV/cm, and bandgap of 4.5 further expands on the previous affirmations of the *a*-BN material as being a high quality dielectric.

Finally, the work described here attempts to elucidate mechanisms for device performance based on the crystallinity or properties of the dielectric material. Graphene FET performance was evaluated on the *a*-BN and *h*-BN material, with the nanocrystalline van der Waals terminated *h*-BN providing for a surface free from many scattering events, evidenced by a 2 fold improvement of mobility and significant changes in Dirac point in comparison to conventional SiO_2 substrates and *a*-BN.

Thermal management in these high speed graphene devices will become especially important as the gate lengths are reduced to only a few nanometers. To combat this, understanding the thermal transport in the dielectric as well as from the dielectric/interfaces will be key in extended the lifetime and reliability of devices. In-plane thermal conductivity measurements were made possible with the use of a nanofabricator designed to create a free-standing BN film with a thickness of 5 nm. The annealing temperature can be reduced to only 650°C due to the presence of two boundary conditions for surface diffusion (top and bottom of film). The thermal conductivity of pre-annealed *a*-BN and post-annealed *h*-BN were found to be 5 W m^{-1} K^{-1} and 65 W m^{-1} K^{-1}, respectively. The high in-plane thermal conductivity is attributed to the 2D structure of *h*-BN, which is known to have high thermal conductivities due to the layered structure. In addition to in-plane transport, the 3D transport is especially important to understand and one of these interfaces that is critical is the gate dielectric/metal interface. The *a*-BN grown by PLD provides for an exceptionally good interface conductance material, as the atomic-scale roughness provides for a great template for metal deposition. The experimentation described here determined that not only is the choice of contact material important, but the deposition technique used for that metal must be considered. For these studies, a metal with a high Debye temperature (Ti, Al) and low atomic mass resulted in the highest thermal conductances, with an interface conductance of 130 MW m^{-2} K^{-1} observed in the case for DC sputtering aluminum on *a*-BN.

The technique extensively described in this manuscript for growth of boron nitride nanomaterials potentially has an exceptionally bright future for revolutionary dielectric processing for next generation 2D devices. By providing a template for

understanding the mechanisms associated with PLD plasma-based synthesis, elaborating on synthesis techniques and the impact on crystal structure and properties, and evaluating the impact of the films on device performance, the integration of *h*-BN and *a*-BN films is an exciting possibility one step closer to implementation into nanoelectronic systems.

LIST OF REFERENCES

LIST OF REFERENCES

1. Mas-Balleste, R., et al., *2D materials: to graphene and beyond.* Nanoscale, 2011. **3**(1): p. 20-30.

2. Geim, A.K. and I.V. Grigorieva, *Van der Waals heterostructures.* Nature, 2013. **499**(7459): p. 419-425.

3. Hsu, A., et al., *Large-area 2-D electronics: materials, technology, and devices.* Proceedings of the IEEE, 2013. **101**(7): p. 1638-1652.

4. Roy, T., et al., *Field-effect transistors built from all two-dimensional material components.* ACS Nano, 2014. **8**(6): p. 6259-6264.

5. Fiori, G., et al., *Electronics based on two-dimensional materials.* Nature Nanotechnology, 2014. **9**(10): p. 768-779.

6. Ohno, Y., K. Maehashi, and K. Matsumoto, *Chemical and biological sensing applications based on graphene field-effect transistors.* Biosensors & Bioelectronics, 2010. **26**(4): p. 1727-1730.

7. Dongyuan, C., et al., *Graphene-like layered metal dichalcogenide/graphene composites: synthesis and applications in energy storage and conversion.* Materials Today, 2014. **17**(4): p. 184-193.

8. Zhou, D., Y. Cui, and B. Han, *Graphene-based hybrid materials and their applications in energy storage and conversion.* Chinese Science Bulletin, 2012. **57**(23): p. 2983-2994.

9. Kumar, A., et al., *Direct synthesis of lithium-intercalated graphene for electrochemical energy storage application.* ACS Nano, 2011. **5**(6): p. 4345-4349.

10. Xu, C., et al., *Graphene-based electrodes for electrochemical energy storage.* Energy and Environmental Science, 2013. **6**(5): p. 1388-1414.

11. Wang, X. and F. Xia, *van der Waals heterostructures: Stacked 2D materials shed light.* 2015.

12. Xia, F., et al., *Two-dimensional material nanophotonics.* Nature Photonics, 2014. **8**(12): p. 899-907.

13. Miro, P., M. Audiffred, and T. Heine, *An atlas of two-dimensional materials.* Chemical Society Reviews, 2014. **43**(18): p. 6537-6554.

14. Das, S., et al., *All two-dimensional, flexible, transparent, and thinnest thin film transistor.* Nano Letters, 2014. **14**(5): p. 2861-2866.

15. Balmain, W.H., *Bemerkungen über die Bildung von Verbindungen des Bors und Siliciums mit Stickstoff und gewissen Metallen.* Journal für Praktische Chemie, 1842. **27**(1): p. 422-430.

16. Monteiro, S.N., et al., *Cubic boron nitride competing with diamond as a superhard engineering material – an overview.* Journal of Materials Research and Technology, 2013. **2**(1): p. 68-74.

17. Solozhenko, V.L., V.Z. Turkevich, and W.B. Holzapfel, *Refined phase diagram of boron nitride.* Journal of Physical Chemistry B, 1999. **103**(15): p. 2903-2905.

18. Pakdel, A., Y. Bando, and D. Golberg, *Nano boron nitride flatland.* Chemical Society Reviews, 2014. **43**(3): p. 934-959.

19. Gorbachev, R.V., et al., *Hunting for Monolayer Boron Nitride: Optical and Raman Signatures.* Small, 2011. **7**(4): p. 465-468.

20. Song, Y., et al., *Triggering the atomic layers control of hexagonal boron nitride films.* Applied Surface Science, 2014. **313**: p. 647-53.

21. Novoselov, K.S., et al., *Electric Field Effect in Atomically Thin Carbon Films.* Science, 2004. **306**(5696): p. 666-669.

22. Novoselov, K.S., et al., *Two-dimensional gas of massless Dirac fermions in graphene.* Nature, 2005. **438**(7065): p. 197-200.

23. Pop, E., V. Varshney, and A.K. Roy, *Thermal properties of graphene: Fundamentals and applications.* MRS Bulletin, 2012. **37**(12): p. 1273-1281.

24. Akinwande, D. *Two-dimensional atomic sheets for heterogeneous flexible high-frequency and low-power nanoelectronics*. in *Micro- and Nanotechnology Sensors, Systems, and Applications VI, May 5, 2014 - May 9, 2014*. SPIE.

25. Kim, S.J., et al., *Materials for Flexible, Stretchable Electronics: Graphene and 2D Materials.* Annual Review of Materials Research, 2015. **45**(1): p. 63-84.

26. Novoselov, K.S., et al., *Two-dimensional atomic crystals.* Proceedings of the National Academy of Sciences of the United States of America, 2005. **102**(30): p. 10451-10453.

27. Das, S., et al., *Beyond Graphene: Progress in Novel Two-Dimensional Materials and van der Waals Solids.* Annual Review of Materials Research, 2015. **45**(1): p. 1-27.

28. Yamada, T., et al., *A roll-to-roll microwave plasma chemical vapor deposition process for the production of 294 mm width graphene films at low temperature.* Carbon, 2012. **50**(7): p. 2615-19.

29. Yi, M. and Z. Shen, *A review on mechanical exfoliation for the scalable production of graphene.* Journal of Materials Chemistry A, 2015. **3**(22): p. 11700-11715.

30. Zhu, J., et al., *Solution-Processed Dielectrics Based on Thickness-Sorted Two-Dimensional Hexagonal Boron Nitride Nanosheets.* Nano Letters, 2015. **15**(10): p. 7029-7036.

31. Kosynkin, D.V., et al., *Longitudinal unzipping of carbon nanotubes to form graphene nanoribbons.* Nature, 2009. **458**(7240): p. 872-876.

32. Norimatsu, W. and M. Kusunoki, *Epitaxial graphene on SiC{0001}: advances and perspectives.* Physical Chemistry Chemical Physics, 2014. **16**(8): p. 3501-3511.

33. Gao, G., et al., *Artificially Stacked Atomic Layers: Toward New van der Waals Solids.* Nano Letters, 2012. **12**(7): p. 3518-3525.

34. Gayathri, S., et al., *Synthesis of few layer graphene by direct exfoliation of graphite and a Raman spectroscopic study.* AIP Advances, 2014. **4**(2): p. 027116.

35. Varrla, E., et al., *Large-Scale Production of Size-Controlled MoS2 Nanosheets by Shear Exfoliation.* Chemistry of Materials, 2015. **27**(3): p. 1129-1139.

36. Kang, J., et al., *Solvent Exfoliation of Electronic-Grade, Two-Dimensional Black Phosphorus.* ACS Nano, 2015. **9**(4): p. 3596-3604.

37. Fan, X., et al., *Fast and Efficient Preparation of Exfoliated 2H MoS2 Nanosheets by Sonication-Assisted Lithium Intercalation and Infrared Laser-Induced 1T to 2H Phase Reversion.* Nano Letters, 2015. **15**(9): p. 5956-5960.

38. Bresnehan, M.S., et al., *Prospects of Direct Growth Boron Nitride Films as Substrates for Graphene Electronics.* Journal of Materials Research, 2013.

39. Osada, M. and T. Sasaki, *Two-dimensional Dielectric Nanosheets: Novel Nanoelectronics From Nanocrystal Building Blocks.* Advanced Materials, 2012. **24**(2): p. 210-228.

40. Nagashima, A., et al., *Electronic states of monolayer hexagonal boron nitride formed on the metal surfaces.* Surface Science, 1996. **357-358**(1-3): p. 307-311.

41. Rokuta, E., et al., *Phonon dispersion of an epitaxial monolayer film of hexagonal boron nitride on Ni(111).* Physical Review Letters, 1997. **79**(23): p. 4609-4609.

42. Shi, Y., et al., *Synthesis of Few-Layer Hexagonal Boron Nitride Thin Film by Chemical Vapor Deposition*, in *Nano Letters*. 2010, American Chemical Society. p. 4134-4139.

43. Song, L., et al., *Large scale growth and characterization of atomic hexagonal boron nitride layers.* Nano Letters, 2010. **10**(8): p. 3209-3215.

44. Kim, K.K., et al., *Synthesis of monolayer hexagonal boron nitride on Cu foil using chemical vapor deposition.* Nano Letters, 2012. **12**(1): p. 161-166.

45. Vlassiouk, I., et al., *Graphene Nucleation Density on Copper: Fundamental Role of Background Pressure.* The Journal of Physical Chemistry C, 2013. **117**(37): p. 18919-18926.

46. Bhaviripudi, S., et al., *Role of Kinetic Factors in Chemical Vapor Deposition Synthesis of Uniform Large Area Graphene Using Copper Catalyst.* Nano Letters, 2010. **10**(10): p. 4128-4133.

47. Lee, K.H., et al., *Large-Scale Synthesis of High-Quality Hexagonal Boron Nitride Nanosheets for Large-Area Graphene Electronics.* Nano Letters, 2012. **12**(2): p. 714-718.

48. Tang, S., et al., *Precisely aligned graphene grown on hexagonal boron nitride by catalyst free chemical vapor deposition.* Scientific Reports, 2013. **3**: p. 2666.

49. Liu, Y., S. Bhowmick, and B.I. Yakobson, *BN White Graphene with "Colorful" Edges: The Energies and Morphology.* Nano Letters, 2011. **11**(8): p. 3113-3116.

50. Stehle, Y., et al., *Synthesis of Hexagonal Boron Nitride Monolayer: Control of Nucleation and Crystal Morphology.* Chemistry of Materials, 2015. **27**(23): p. 8041-8047.

51. Yin, J., et al., *Large Single-Crystal Hexagonal Boron Nitride Monolayer Domains with Controlled Morphology and Straight Merging Boundaries.* Small, 2015. **11**(35): p. 4497-4502.

52. Lee, Y.-H., et al., *Growth selectivity of hexagonal-boron nitride layers on Ni with various crystal orientations.* RSC Advances, 2012. **2**(1): p. 111-115.

53. Cho, H., et al., *Growth kinetics of white graphene (h-BN) on a planarised Ni foil surface.* Scientific Reports, 2015. **5**: p. 11985.

54. Yang, Y., et al., *Creating a Nanospace under an h-BN Cover for Adlayer Growth on Nickel(111).* ACS Nano, 2015. **9**(12): p. 11589-11598.

55. Preobrajenski, A.B., A.S. Vinogradov, and N. Mårtensson, *Monolayer of h-BN chemisorbed on Cu(1 1 1) and Ni(1 1 1): The role of the transition metal 3d states.* Surface Science, 2005. **582**(1–3): p. 21-30.

56. Kim, G., et al., *Growth of High-Crystalline, Single-Layer Hexagonal Boron Nitride on Recyclable Platinum Foil.* Nano Letters, 2013. **13**(4): p. 1834-1839.

57. Morscher, M., et al., *Formation of single layer h-BN on Pd(1 1 1).* Surface Science, 2006. **600**(16): p. 3280-3284.

58. Lu, G., et al., *Synthesis of large single-crystal hexagonal boron nitride grains on Cu–Ni alloy.* Nat Commun, 2015. **6**.

59. Goriachko, A., et al., *Self-Assembly of a Hexagonal Boron Nitride Nanomesh on Ru(0001),* in *Langmuir*. 2007, American Chemical Society. p. 2928-2931.

60. Corso, M., et al., *Boron Nitride Nanomesh.* Science, 2004. **303**(5655): p. 217-220.

61. Bresnehan, M.S., *Synthesis and characterization of hexagonal boron nitride for integration with graphene electronics,* in *Engineering*. 2013, Pennsylvania State University.

62. Barth, J.V., G. Costantini, and K. Kern, *Engineering atomic and molecular nanostructures at surfaces.* Nature, 2005. **437**(7059): p. 671-679.

63. Barth, J.V., *Transport of Adsorbates at Metal Surfaces: From Thermal Migration to Hot Precursors*. 2000: Elsevier.

64. Muratore, C., et al., *Thermal anisotropy in nano-crystalline MoS2 thin films.* Physical Chemistry Chemical Physics, 2014. **16**(3): p. 1008-14.

65. Panzner, M., et al. *Scale-up of pulsed laser deposition (PLD) for 4"-wafer coating*. in *Laser Ablation. Symposium F: Third International Symposium on Laser Ablation (COLA'95) 1995 E-MRS Spring Conference, 22-26 May 1995*. 1996. Netherlands: Elsevier.

66. Muratore, C., et al., *Continuous ultra-thin MoS2 films grown by low-temperature physical vapor deposition.* Applied Physics Letters, 2014. **104**(26): p. 261604.

67. Voevodin, A.A., et al., *Magnetic field argon ion filtering for pulsed magnetron sputtering growth of two-dimensional MoS2.* Surface and Coatings Technology, 2015. **280**: p. 260-267.

68. Sutter, P., et al., *Scalable synthesis of uniform few-layer hexagonal boron nitride dielectric films.* Nano Letters, 2013. **13**(1): p. 276-281.

69. Sajjad, M., G. Morell, and P. Feng, *Advance in novel boron nitride nanosheets to nanoelectronic device applications.* ACS Applied Materials and Interfaces, 2013. **5**(11): p. 5051-5056.

70. Nakhaie, S., et al., *Synthesis of atomically thin hexagonal boron nitride films on nickel foils by molecular beam epitaxy.* Applied Physics Letters, 2015. **106**(21): p. 213108.

71. Acacia, N., et al., *Pulsed laser deposition of boron nitride thin films.* Radiation Effects and Defects in Solids, 2008. **163**(4-6): p. 293-298.

72. Mirkarimi, P.B., K.F. McCarty, and D.L. Medlin, *Review of advances in cubic boron nitride film synthesis.* Materials Science & Engineering R: Reports, 1997. **R21**(2): p. 1-54.

73. Zhang, X.W., et al., *Microstructure of the intermediate turbostratic boron nitride layer.* Diamond and Related Materials, 2005. **14**(9): p. 1474-1481.

74. Sajjad, M., et al., *Effect of Substrate Temperature in the Synthesis of BN Nanostructures.* Physica Scripta, 2011. **83**(6): p. 065601.

75. Wei, P.S., D.J. Nelson, and R.B. Hall, *Laser-induced Evaporation of Solid Surfaces.* J.of Chem.Phys., 1975. **62**(8): p. 3050.

76. Murray, P.T., M.S. Donley, and N.T. McDevitt. *Growth of Stoichiometric BN Films by Pulsed Laser Evaporation*. in *Materials Research Society*.

77. Doll, G.L., et al. *Laser Deposited Cubic Boron Nitride Films*. in *Materials Research Society Symposium Proceedings*.

78. Shin, K.B., S.M. Park, and Y.M. Kim, *Pulsed Laser Ablation of Boron Nitride*, in *Advanced Laser Processing of Materials - Fundamentals and Applications*, R. Singh, et al., Editors. 1995, Materials Reaserch Society Symposium Proceedings: 1995. p. 265-270.

79. Angleraud, B., et al., *Study of the expansion of the laser ablation plume above a boron nitride target*, in *Applied Surface Science Proceedings of the 1995 E-MRS Spring Conference, May 22, 1995 - May 26, 1995*. 1996, Elsevier Science B.V. p. 117-121.

80. Dutouquet, C., S. Acquaviva, and J. Hermann. *Detection of boron nitride radicals by emission spectroscopy in a laser-induced plasma*. in *1st International Conference on Laser Induced Plasma Spectroscopy and Applications, October 8, 2000 - October 12, 2000*. Elsevier.

81. Chrenko, R.M., *Ultraviolet and infrared spectra of cubic boron nitride.* Solid State Communications, 1974. **14**(6): p. 511-515.

82. Slack, G.A., *Nonmetallic crystals with high thermal conductivity.* Journal of the Physics and Chemistry of Solids, 1973. **34**(2): p. 321-335.

83. Britnell, L., et al., *Electron tunneling through ultrathin boron nitride crystalline barriers.* Nano Letters, 2012. **12**(3): p. 1707-1710.

84. Bolotin, K.I., et al., *Temperature-dependent transport in suspended graphene.* Physical Review Letters, 2008. **101**(9): p. 096802-1.

85. Lei, L., et al., *High-speed graphene transistors with a self-aligned nanowire gate.* Nature, 2010. **467**(7313): p. 305-8.

86. Lin, Y.M., et al., *100-GHz transistors from wafer-scale epitaxial graphene.* Science, 2010. **327**(5966): p. 662.

87. Chen, J.-H., et al., *Intrinsic and extrinsic performance limits of graphene devices on SiO2.* Nature Nanotechnology, 2008. **3**(4): p. 206-209.

88. Martin, J., et al., *Observation of electron-hole puddles in graphene using a scanning single-electron transistor.* Nat Phys, 2008. **4**(2): p. 144-148.

89. Morozov, S.V., et al., *Giant Intrinsic Carrier Mobilities in Graphene and Its Bilayer.* Physical Review Letters, 2008. **100**(1): p. 016602.

90. Dean, C.R., et al., *Boron nitride substrates for high-quality graphene electronics.* Nature Nanotechnology, 2010. **5**(10): p. 722-726.

91. Han, W., et al., *BN/Graphene/BN Transistors for RF Applications.* IEEE Electron Device Letters, 2011. **32**(9): p. 1209-1211.

92. Gannett, W., et al., *Boron nitride substrates for high mobility chemical vapor deposited graphene.* Applied Physics Letters, 2011. **98**(24): p. 242105.

93. Nayfeh, O.M., et al., *Increased mobility for layer-by-layer transferred chemical vapor deposited graphene/boron-nitride thin films.* Applied Physics Letters, 2013. **102**(10): p. 103115.

94. Watanabe, K., T. Taniguchi, and H. Kanda, *Direct-bandgap properties and evidence for ultraviolet lasing of hexagonal boron nitride single crystal.* Nature Materials, 2004. **3**(6): p. 404-409.

95. Rumyantsev, S.L., et al., *Properties of Advanced Semiconductor Materials GaN, AlN, InN, BN, SiC, SiGe*, M.E. Levinshtein, S.L. Rumyantsev, and M.S. Shur, Editors. 2001, John Wiley & Sons: New York. p. 67-92.

96. Lee, G.H., et al., *Electron tunneling through atomically flat and ultrathin hexagonal boron nitride.* Applied Physics Letters, 2011. **99**(24).

97. Lee, G.H., et al., *Flexible and Transparent MoS2 Field-Effect Transistors on Hexagonal Boron Nitride-Graphene Heterostructures*, in *ACS Nano*. 2013, American Chemical Society. p. 7931-7936.

98. Kim, K.K., et al., *Synthesis and characterization of hexagonal boron nitride film as a dielectric layer for graphene devices.* ACS Nano, 2012. **6**(10): p. 8583-8590.

99. Bumm, L.A., et al., *Electron Transfer through Organic Molecules.* The Journal of Physical Chemistry B, 1999. **103**(38): p. 8122-8127.

100. Fowler, R.H. and L. Nordheim, *Electron Emission in Intense Electric Fields.* Proceedings of the Royal Society of London A: Mathematical, Physical and Engineering Sciences, 1928. **119**(781): p. 173-181.

101. Boucart, K. and A.M. Ionescu, *A new definition of threshold voltage in Tunnel FETs.* Solid-State Electronics, 2008. **52**(9): p. 1318-1323.

102. Pierson, H.O., *Handbook of Chemical Vapor Deposition: Principles, Technology and Applications: Materials Science and Process Technology Series*. 1999: William Andrew. 460.

103. Liu, Z., et al., *Ultrathin high-temperature oxidation-resistant coatings of hexagonal boron nitride.* Nature Communications, 2013. **4**.

104. Jacobson, N., et al., *High-Temperature Oxidation of Boron Nitride: I, Monolithic Boron Nitride.* Journal of the American Ceramic Society, 1999. **82**(2): p. 393-398.

105. Liu, G., et al., *Selective Gas Sensing With h-BN Capped MoS2 Heterostructure Thin-Film Transistors.* Electron Device Letters, IEEE, 2015. **36**(11): p. 1202-1204.

106. Lee, C., et al., *Frictional Characteristics of Atomically Thin Sheets.* Science, 2010. **328**(5974): p. 76-80.

107. Ouyang, T., et al., *Thermal transport in hexagonal boron nitride nanoribbons.* Nanotechnology, 2010. **21**(24).

108. Jo, I., et al., *Thermal Conductivity and Phonon Transport in Suspended Few-Layer Hexagonal Boron Nitride*, in *Nano Letters*. 2013, American Chemical Society. p. 550-554.

109. Balandin, A.A., *Thermal properties of graphene and nanostructured carbon materials.* Nature Materials, 2011. **10**(8): p. 569-581.

110. Lindsay, L., D.A. Broido, and T.L. Reinecke, *Phonon-isotope scattering and thermal conductivity in materials with a large isotope effect: a first-principles study.* Physical Review B (Condensed Matter and Materials Physics), 2013. **88**(14): p. 144306.

111. Singh, D., J.Y. Murthy, and T.S. Fisher, *Mechanism of thermal conductivity reduction in few-layer graphene.* Journal of Applied Physics, 2011. **110**(4).

112. Singh, D., J.Y. Murthy, and T.S. Fisher, *Spectral phonon conduction and dominant scattering pathways in graphene.* Journal of Applied Physics, 2011. **110**(9).

113. Singh, D., J.Y. Murthy, and T.S. Fisher, *On the accuracy of classical and long wavelength approximations for phonon transport in graphene.* Journal of Applied Physics, 2011. **110**(11).

114. Lindsay, L. and D.A. Broido, *Enhanced thermal conductivity and isotope effect in single-layer hexagonal boron nitride.* Physical Review B (Condensed Matter and Materials Physics), 2011. **84**(15): p. 155421.

115. Lindsay, L. and D.A. Broido, *Theory of thermal transport in multilayer hexagonal boron nitride and nanotubes.* Physical Review B (Condensed Matter and Materials Physics), 2012. **85**(3): p. 035436.

116. Fisher, T.S., *Thermal Energy at the Nanoscale*. 2014: Work Scientific Publishing Co.

117. Ecsedy, D.J. and P.G. Klemens, *Thermal resistivity of die ectric crystals due to four-phonon processes and optical modes.* Phys.Rev.B, 1977. **15**: p. 5957.

118. Alam, M.T., et al., *Thermal conductivity of ultra-thin chemical vapor deposited hexagonal boron nitride films.* Applied Physics Letters, 2014. **104**(1): p. 013113.

119. Koh, Y.K., et al., *Heat conduction across monolayer and few-layer graphenes.* Nano Letters, 2010. **10**(11): p. 4363-4368.

120. Muratore, C., et al., *Cross-plane thermal properties of transition metal dichalcogenides.* Applied Physics Letters, 2013. **102**(8): p. 081604.

121. Cahill, D.G., *Analysis of heat flow in layered structures for time-domain thermoreflectance.* Review of Scientific Instruments, 2004. **75**(12): p. 5119-5122.

122. Gengler, J.J., et al., *Limited thermal conductance of metal-carbon interfaces.* Journal of Applied Physics, 2012. **112**(9).

123. Pop, E., et al. *Electrical and thermal transport in metallic single-wall carbon nanotubes on insulating substrates*. 2007. American Institute of Physics.

124. *NIST Atomic Spectra Database Lines Form*. 2014 9/16/2014; Available from: www.nist.gov/pml/data/asd.cfm.

125. R.W.Pearse and A.G.Gaydon, *The Identification of Molecular Spectra*. 3 ed. 1963, London: Chapman and Hall LTD.

126. Mehr, F.J. and M.A. Biondi, *Electron Temperature Dependence of Recombination of O2+ and N2+ Ions with Electrons,* in *Physical Review 270*. 1969. p. 264.

127. Rajendiran, S., et al., *Modelling of laser ablation and reactive oxygen plasmas for pulsed laser deposition of zinc oxide,* in *Surface and Coatings Technology, The 41st International Conference on Metallurgical Coatings and Thin Films*. 2014. p. 417-423.

128. Geohegan, D.B., *Diagnostics and Characteristics of Pulsed Laser Deposition Laser Plasmas,* in *Pulsed Laser Deposition of Thin Films*. 1994, John Wiley & Sons, Inc.: New York. p. 115-165.

129. Muratore, C., et al., *Effect of plasma flux composition on the nitriding rate of stainless steel.* Journal of Vacuum Science & Technology A (Vacuum, Surfaces, and Films), 2004. **22**(4): p. 1530-1535.

130. Glavin, N.R., et al., *Synthesis of few-layer, large area hexagonal-boron nitride by pulsed laser deposition.* Thin Solid Films, 2014. **572**: p. 245-250.

131. Guo, N., et al., *Fabrication of large area hexagonal boron nitride thin films for bendable capacitors,* in *Nano Res.*
Nano Research. 2013, Springer Berlin Heidelberg. p. 602-610.

132. Barboza, A.P., et al., *Dynamic negative compressibility of few-layer graphene, h-BN, and MoS 2.* Nano Letters, 2012. **12**(5): p. 2313-2317.

133. Changgu, L., et al., *Frictional Characteristics of Atomically Thin Sheets.* Science, 2010. **328**(5974): p. 76-80.

134. Lin, Y.C., et al., *Direct Synthesis of van der Waals Solids*, in *ACS Nano*. 2014, American Chemical Society.

135. Payne, B.P., M.C. Beisinger, and N.S. McIntyre, *X-ray photoelectron spectorscopy studies of reactions on chromium metal and chromium oxide surfaces.* J.Electron Spectrosc.Relat.Phenom., 2011. **184**(1-2): p. 29-37.

136. *Pulsed Laser Deposition of Thin Films: Applications-Led Growth of Functional Materials*. 2007: Wiley-Interscience.

137. Lowndes, D.H., et al., *Synthesis of novel thin-film materials by pulsed laser deposition.* Science, 1996. **273**(5277): p. 898-903.

138. Voevodin, A.A., J.G. Jones, and J.S. Zabinski, *Characterization of ZrO2/Y2O3 laser ablation plasma in vacuum, oxygen, and argon environments.* Journal of Applied Physics, 200. **88**: p. 1088.

139. Voevodin, A.A., et al., *Plasma Characterization during laser ablation of graphite in nitrogen for the growth of fullerene-like CNx films.* Journal of Applied Physics, 2002. **92**: p. 724.

140. Trehan, R., Y. Lifshitz, and J.W. Rabalais, *Auger and X-ray electron spectroscopy studies of hBN, cBN, and N2+ ion irradiation of boron and boron nitride.* Journal of Vacuum Science & Technology A (Vacuum, Surfaces, and Films), 1990. **8**(6): p. 4026-4032.

141. Ooi, N., A. Rairkar, and J.B. Adams, *Density Functional Study of Graphite Bulk and Surface Properties.* Carbon, 2006. **44**(2): p. 231-242.

142. Zhang, X.W., et al., *Epitaxy of cubic boron nitride on (001)oriented diamond.* Nature Materials, 2003. **2**(5): p. 312-315.

143. Nemanich, R.J., S.A. Solin, and R.M. Martin, *Light scattering study of boron nitride microcrystals.* Physical Review B (Condensed Matter), 1981. **23**(12): p. 6348-6356.

144. Tay, R.Y., et al., *A systematic study of the atmospheric pressure growth of large-area hexagonal crystalline boron nitride film.* Journal of Materials Chemistry C, 2014. **2**(9): p. 1650-1657.

145. Smith, K.C., et al., *XPS Thickness Solver*. 2012.

146. Powell, C.J. and A. Jablonski. *NIST Electron Inelastic-Mean-Free-Path Database*. National Institute of Standards and Technology 2010 2010.

147. Greer, J., *Large-Area Commercial Pulsed Laser Deposition*, in *Pulsed Laser Deposition of Thin Films*. 2006, John Wiley & Sons, Inc. p. 191-213.

148. Jariwala, D., et al., *Emerging device applications for semiconducting two-dimensional transition metal dichalcogenides.* ACS Nano, 2014. **8**(2): p. 1102-1120.

149. Wolf, S. and R.N. Tauber, *Thermal Oxidation of Silicon*, in *Silicon Processing for the VLSI Era: Volume 1 - Process Technology*. 2000, Lattice Press: Sunset Beach, CA. p. 265-323.

150. Kamiyama, S., T. Miura, and Y. Nara, *Electrical properties of ultrathin HfO2 films for replacement metal gate transistors, fabricated by atomic layer deposition using Hf (N(CH 3)(C2H5))4 and O3.* Applied Physics Letters, 2005. **87**(13): p. 1-3.

151. Gu, D., et al., *Experimental study of ALD HfO2 deposited on strained silicon-on-insulator and standard SOI.* Journal of the Electrochemical Society, 2008. **155**(6): p. G129-G133.

152. George, S.M., *Atomic layer deposition: An overview.* Chemical Reviews, 2010. **110**(1): p. 111-131.

153. *NIST X-ray Photoelectron Spectroscopy Database*. National Institute of Standards and Technology, 2012.

154. Glavin, N.R., et al., *Temporally and spatially resolved plasma spectroscopy in pulsed laser deposition of ultra-thin boron nitride films.* Journal of Applied Physics, 2015. **117**(16).

155. Steinborn, C., et al., *Correlation between microstructure and electrical resistivity of hexagonal boron nitride ceramics.* Journal of the European Ceramic Society, 2013. **33**(6): p. 1225-1235.

156. Wu, J., et al., *Mechanics and Mechanically Tunable Band Gap in Single-Layer Hexagonal Boron-Nitride.* Materials Research Letters, 2013. **1**(4): p. 200-206.

157. De Jamblinne de Meux, A., et al., *Comparison of the electronic structure of amorphous versus crystalline indium gallium zinc oxide semiconductor: structure, tail states and strain effects.* Journal of Physics D: Applied Physics, 2015. **48**(43): p. 435104 (10 pp.).

158. McConney, M.E., et al., *Direct Synthesis of Ultra-thin Large Area Transition Metal Dichalcogenides and their Heterostructures on Stretchable Polymer Surfaces.* Journal of Materials Research, 2015.

159. Rand, M.J. and J.F. Roberts, *Preparation and properties of thin film boron nitride.* Journal of the Electrochemical Society, 1968. **115**(4): p. 423-429.

160. Zedlitz, R., M. Heintze, and M.B. Schubert, *Properties of amorphous boron nitride thin films*, in *Journal of Non-Crystalline Solids, Proceedings of the 1995 16th International Conference on Amorphous Semiconductors - Science and Technology, ICAS 16. Part 1 (of 2), September 4, 1995 - September 8, 1995*. 1996, Elsevier Science B.V. p. 403-406.

161. Orofeo, C.M., S. Suzuki, and H. Hibino, *Ultrathin chemical vapor deposition (CVD)-grown hexagonal boron nitride as a high-quality dielectric for tunneling devices on rigid and flexible substrates.* Journal of Physical Chemistry C, 2014. **118**(6): p. 3340-3346.

162. Hattori, Y., et al., *Layer-by-Layer Dielectric Breakdown of Hexagonal Boron Nitride*, in *ACS Nano*. 2015, American Chemical Society. p. 916-921.

163. Mohammad, S.N., F.J. Kub, and J. Eddy, *Field-plate design for edge termination in silicon carbide high-power Schottky diodes.* Journal of Vacuum Science and Technology B:Nanotechnology and Microelectronics, 2011. **29**(2).

164. Meric, I., et al., *Graphene Field-Effect Transistors Based on Boron Nitride Dielectrics.* Proceedings of the IEEE, 2013. **101**(7): p. 1609-1619.

165. Meric, I., et al., *Current saturation in zero-bandgap, top-gated graphene field-effect transistors.* Nat Nano, 2008. **3**(11): p. 654-659.

166. Uddin, M.A., et al., *Functionalized graphene/silicon chemi-diode H2 sensor with tunable sensitivity.* Nanotechnology, 2014. **25**(12): p. 125501.

167. Pirkle, A., et al., *The effect of chemical residues on the physical and electrical properties of chemical vapor deposited graphene transferred to SiO2.* Applied Physics Letters, 2011. **99**(12): p. 122108.

168. Wang, M., et al., *A Platform for Large-Scale Graphene Electronics – CVD Growth of Single-Layer Graphene on CVD-Grown Hexagonal Boron Nitride.* Advanced Materials, 2013. **25**(19): p. 2746-2752.

169. Konar, A., T. Fang, and D. Jena, *Effect of high-K gate dielectrics on charge transport in graphene-based field effect transistors.* Physical Review B, 2010. **82**(11): p. 115452.

170. Antczak, G.E., Gert, *Surface Diffusion: Metals, Metal Atoms, and Clusters*. 2010, New York: Cambridge University Press.

171. Henager, C.H. and W.T. Pawlewicz, *Thermal conductivities of thin, sputtered optical films.* Applied Optics, 1993. **32**(1): p. 91-101.

172. Bae, M.-H., et al., *Imaging, Simulation, and Electrostatic Control of Power Dissipation in Graphene Devices.* Nano Letters, 2010. **10**(12): p. 4787-4793.

173. Tai, K., et al., *Integration of microplasma with transmission electron microscopy: Real-time observation of gold sputtering and island formation.* Scientific Reports, 2013. **3**: p. 1325.

174. Niessen, A.K. and F.R. De Boer, *The enthalpy of formation of solid borides, carbides, nitrides, silicides and phosphides of transition and noble metals.* Journal of the Less Common Metals, 1981. **82**: p. 75-80.

175. Sundgren, J.E., *Formation and characterization of titanium nitride and tittanium carbide films prepared by reactive sputtering*, in *Dept. of Physics and measurement Technology*. 1982, Linkoeping Univ. (Sweden). p. 201.

APPENDICES

APPENDIX A. Large area *a*-BN growth

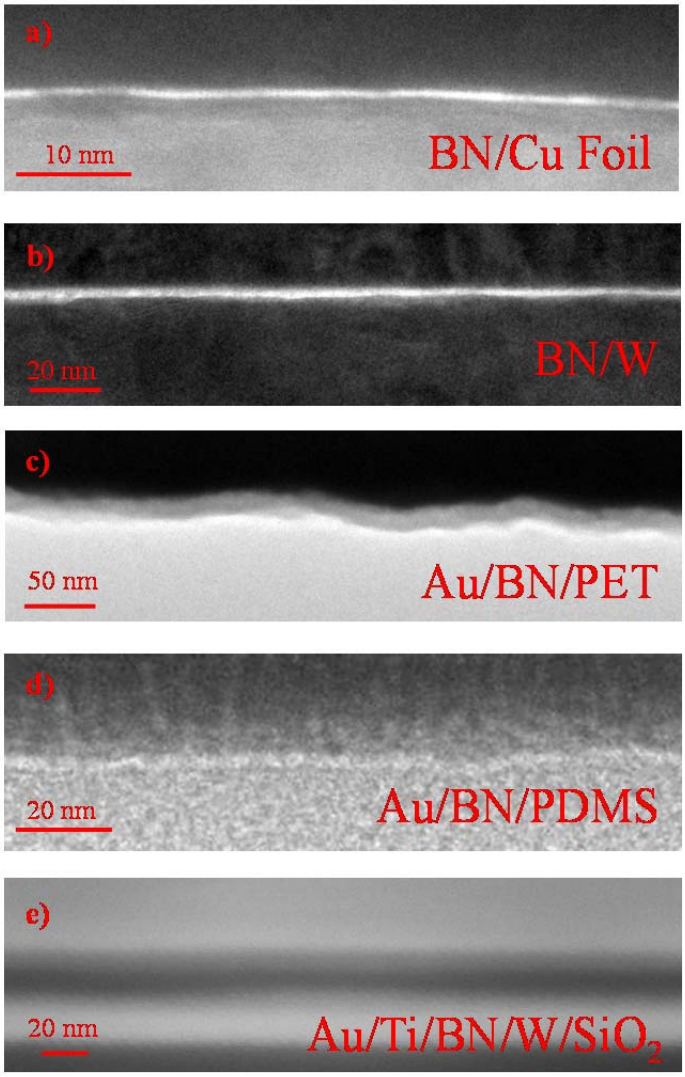

Figure A.1: Cross-sectional SEM imaging confirming thicknesses and large area uniformity for various BN samples of a) *a*-BN on copper foil, b) BN on W (30 pulses), c) Gold on *a*-BN on PET, d) Gold on *a*-BN on PDMS, and e) Gold/Titanium contacts on BN grown on magnetron sputtered tungsten on an SiO_2 wafer. A higher resolution image of this sample labeled e) was used to verify the thickness of *a*-BN at 16.47 nm for dielectric measurements.

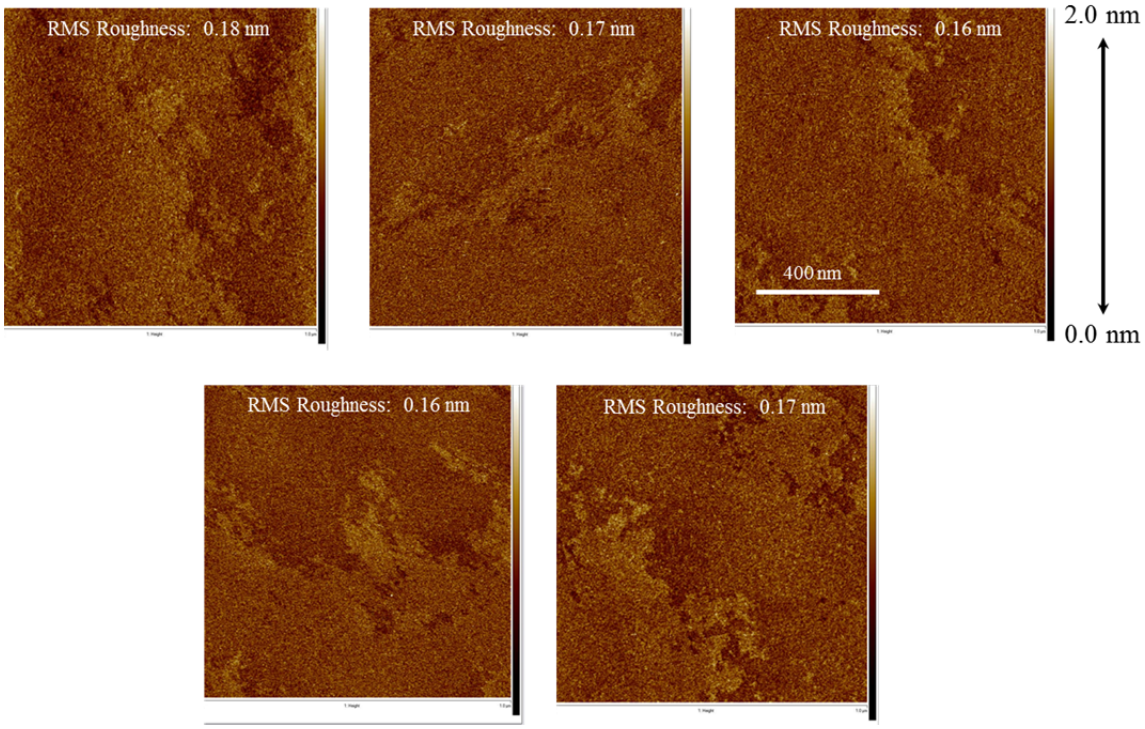

Figure A.2: Five topographical AFM images of ultra-thin (< 5 nm) *a*-BN grown on Al_2O_3 at 5 mm separation distances on a 30 mm diameter sample setup.

APPENDIX B: Steady State Plasma Emission Spectra

The following appendix presents extensive optical emission spectra collected at steady state at the substrate location. The camera and collection settings are labeled for each spectra, and contrasting scans with and without background gas are presented.

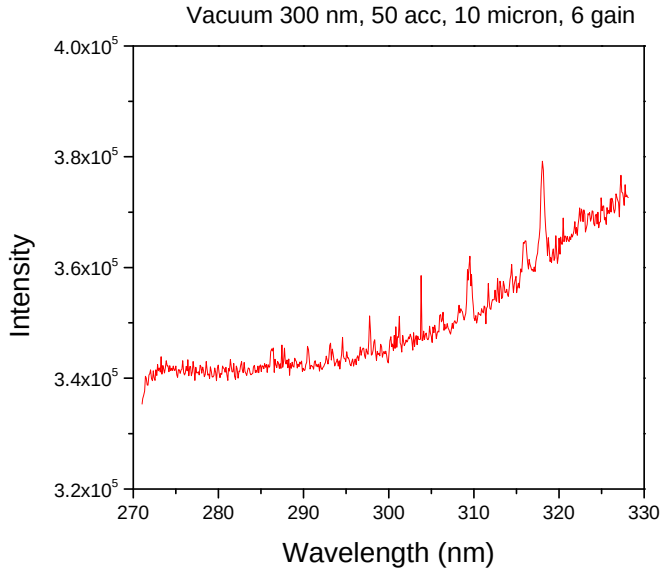

Figure B.1: Collected spectra centered at 300 nm at vacuum conditions.

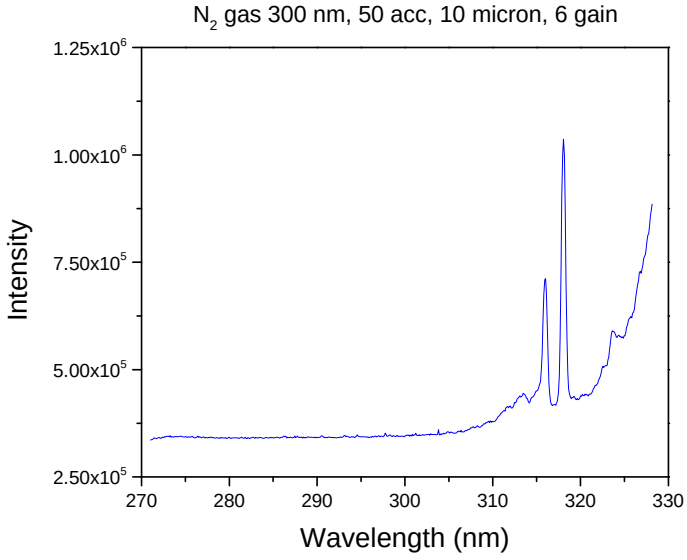

Figure B.2: Collected spectra centered at 300 nm at 50 mTorr N_2 gas.

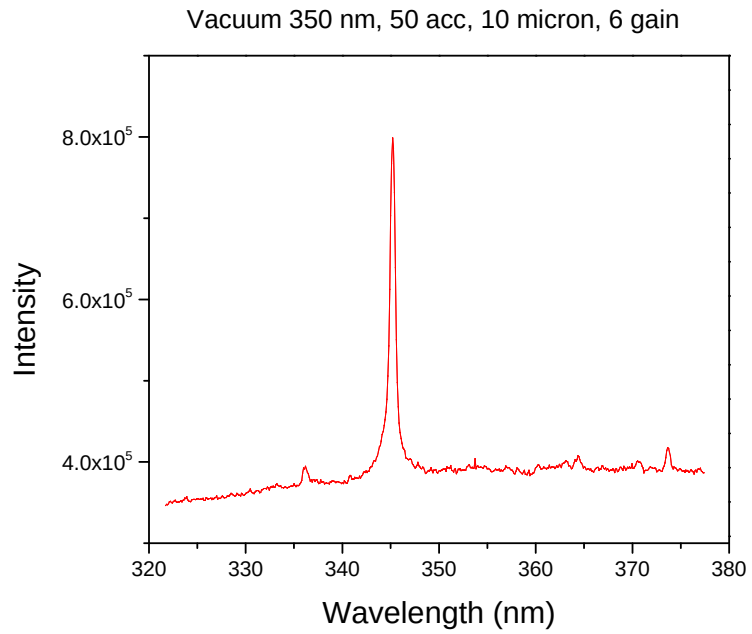

Figure B.3: Collected spectra centered at 350 nm at vacuum conditions.

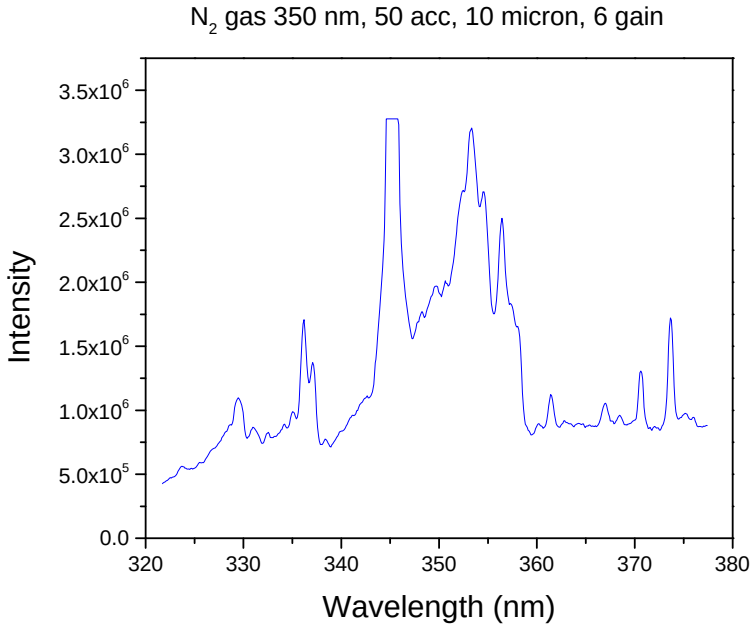

Figure B.4: Collected spectra centered at 350 nm at 50 mTorr N_2 gas.

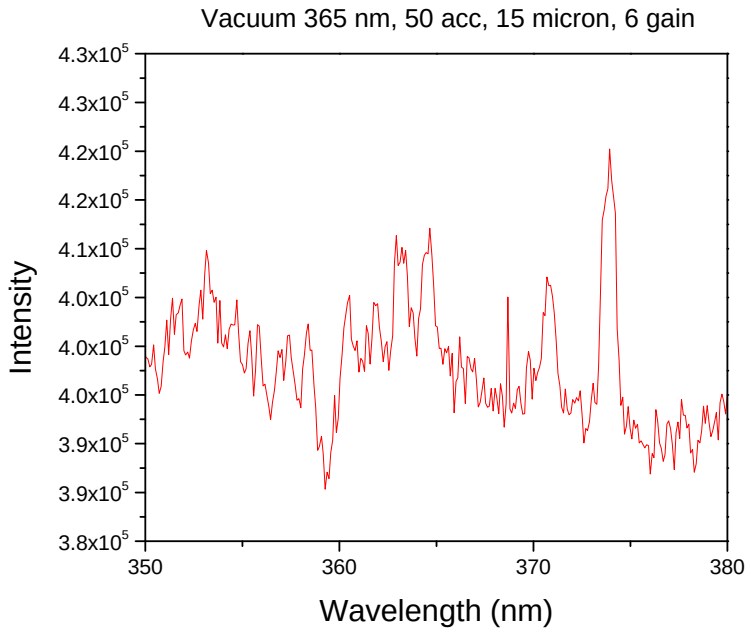

Figure B.5: Collected spectra centered at 365 nm at vacuum conditions.

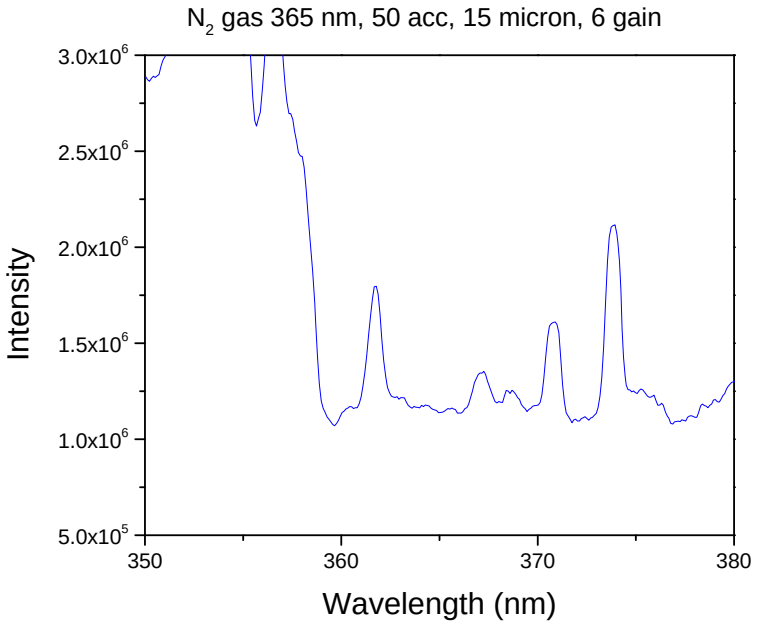

Figure B.6: Collected spectra centered at 365 nm at 50 mTorr N_2 gas.

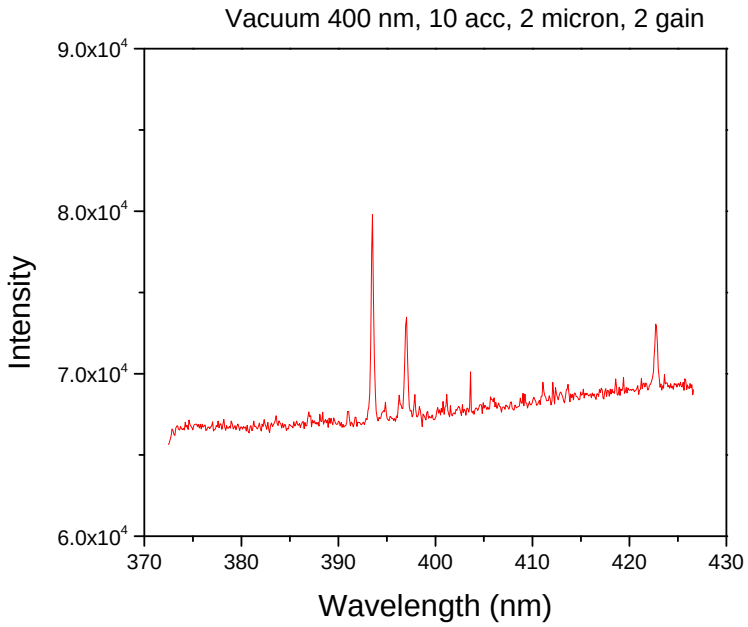

Figure B.7: Collected spectra centered at 400 nm at vacuum conditions.

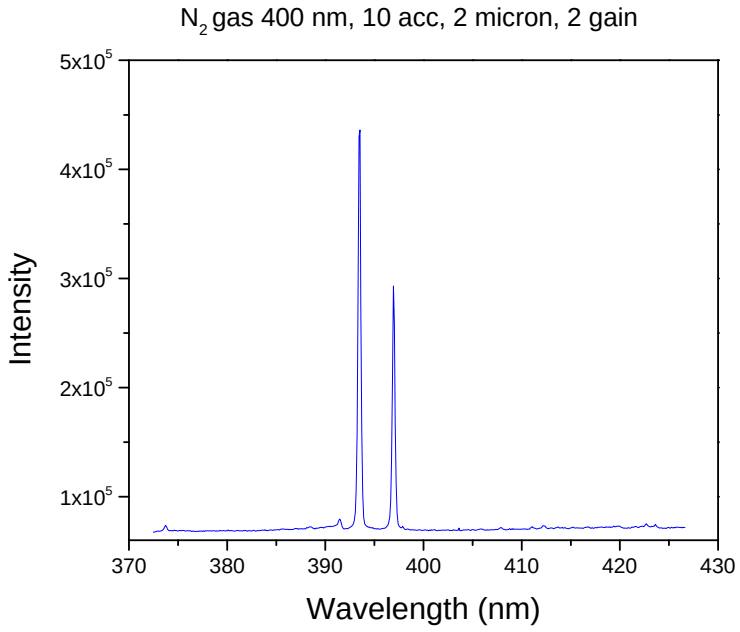

Figure B.8: Collected spectra centered at 400 nm at 50 mTorr N_2 gas.

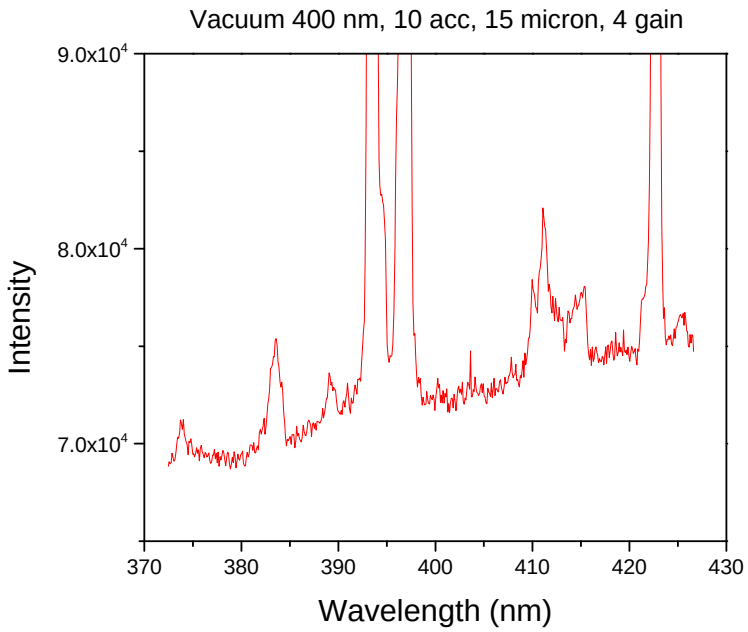

Figure B.9: Collected spectra centered at 400 nm at vacuum conditions (high resolution).

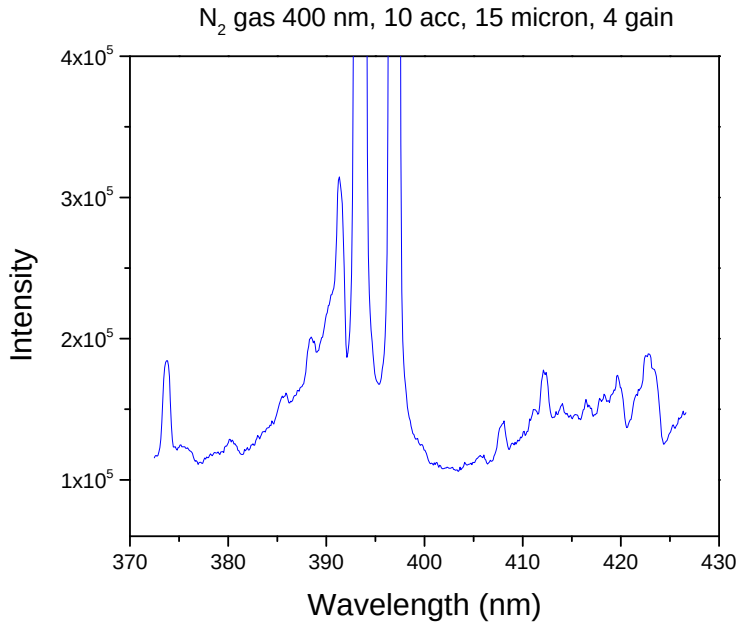

Figure B.10: Collected spectra centered at 400 nm at 50 mTorr N_2 gas (high resolution).

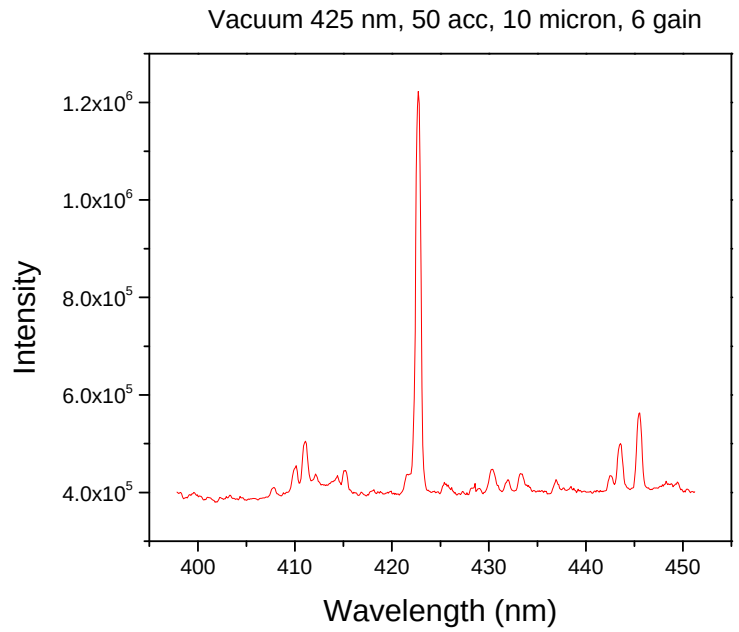

Figure B.11: Collected spectra centered at 425 nm at vacuum conditions.

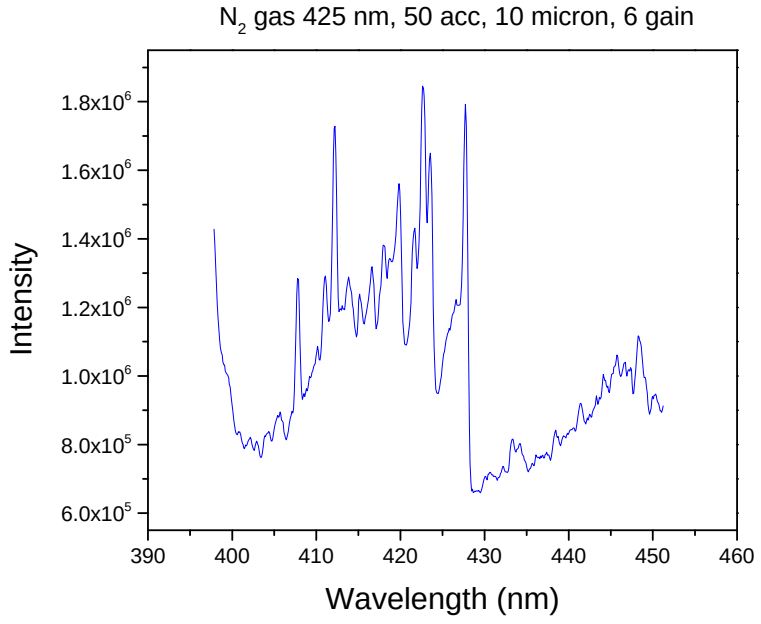

Figure B.12: Collected spectra centered at 425 nm at 50 mTorr N_2 gas.

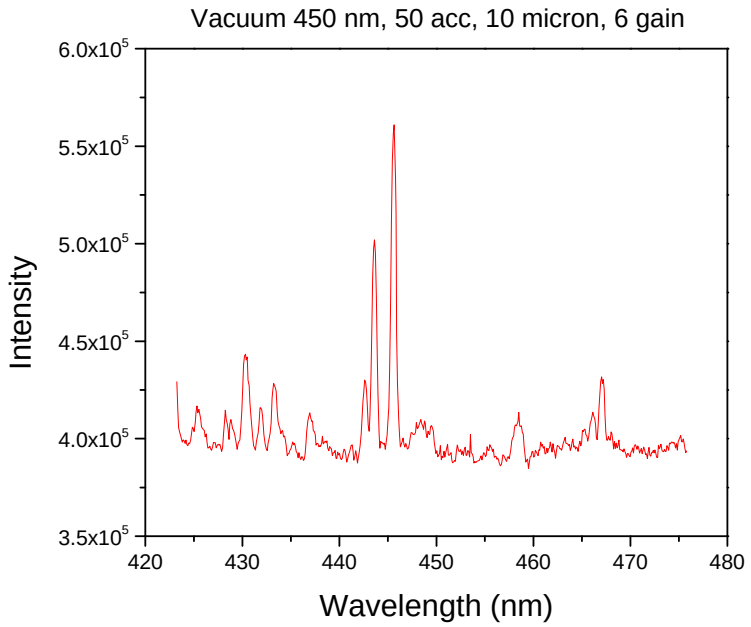

Figure B.13: Collected spectra centered at 450 nm at vacuum conditions.

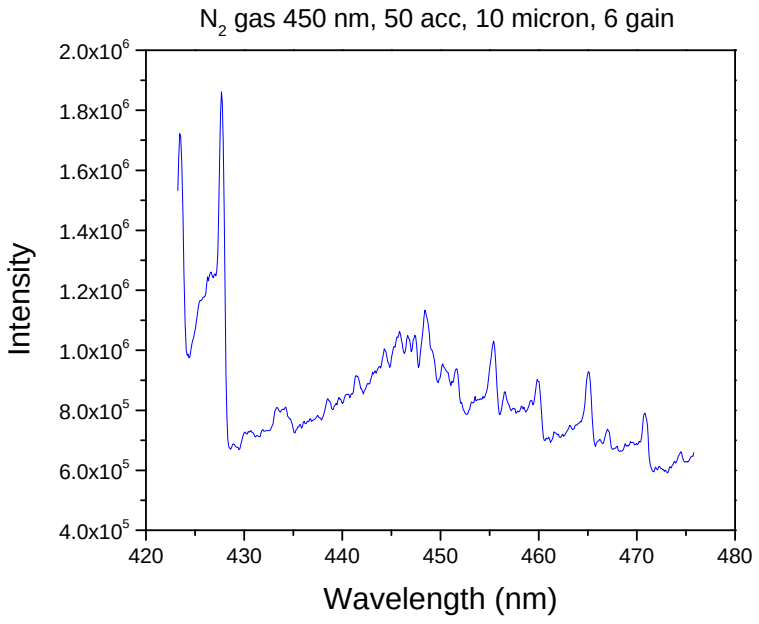

Figure B.14: Collected spectra centered at 450 nm at 50 mTorr N_2 gas.

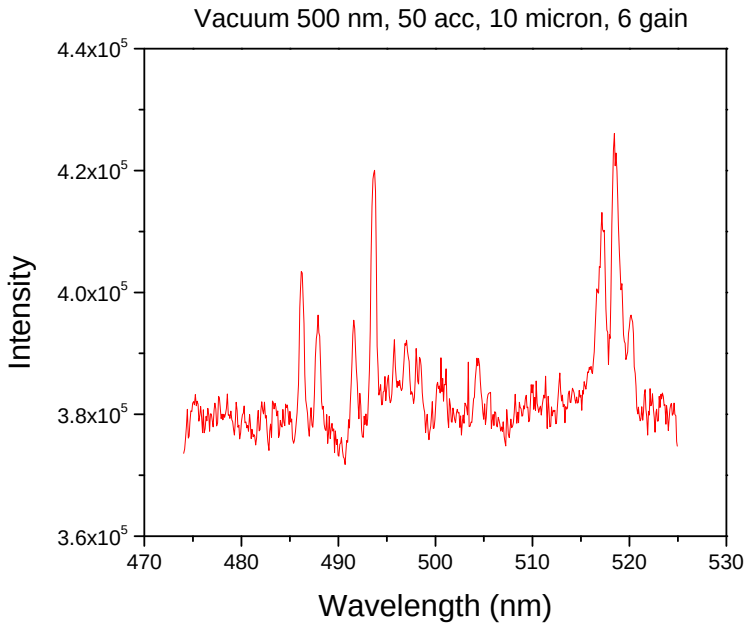

Figure B.15: Collected spectra centered at 500 nm at vacuum conditions.

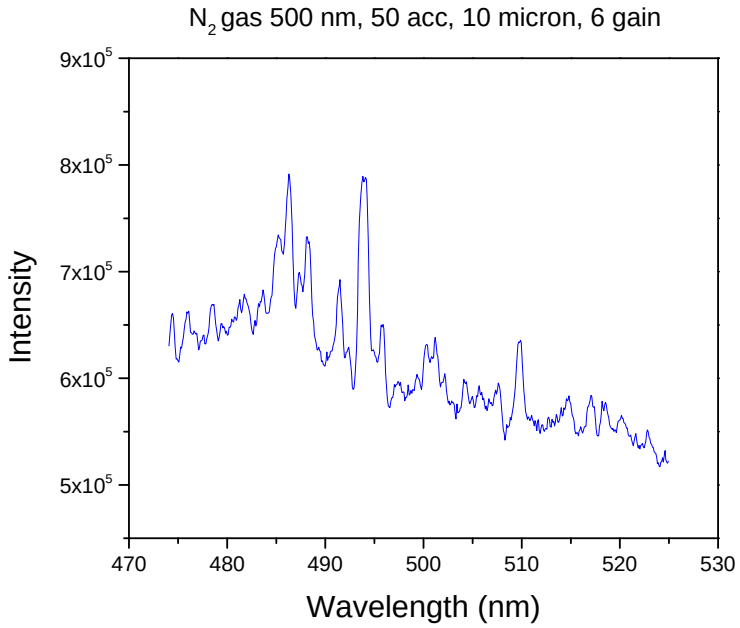

Figure B.16: Collected spectra centered at 500 nm at 50 mTorr N_2 gas.

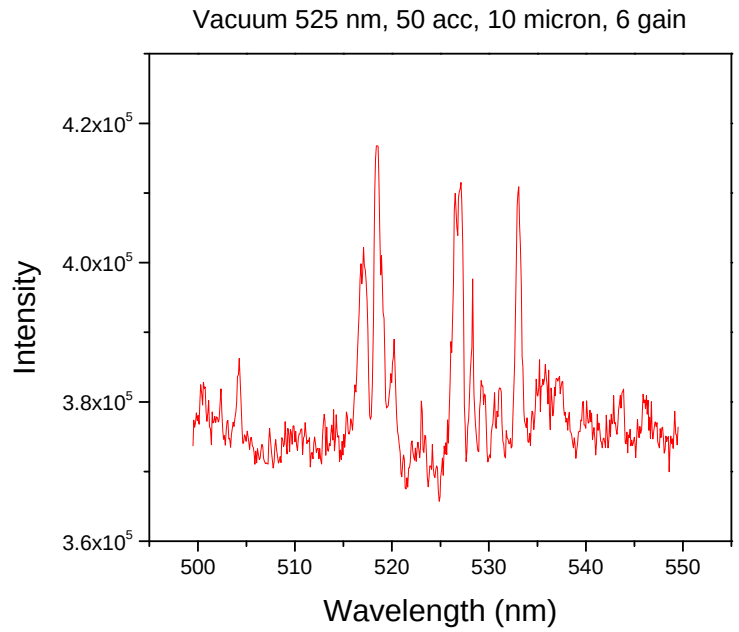

Figure B.17: Collected spectra centered at 525 nm at vacuum conditions.

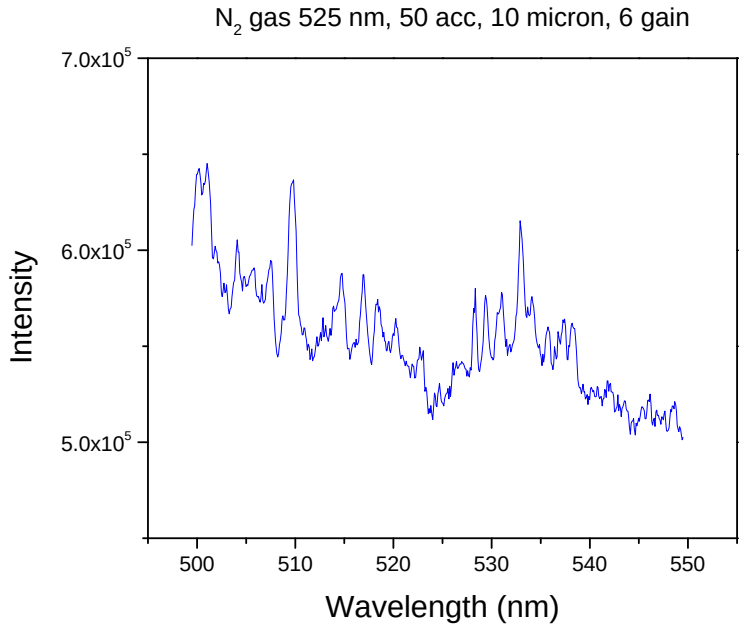

Figure B.18: Collected spectra centered at 500 nm at 50 mTorr N_2 gas.

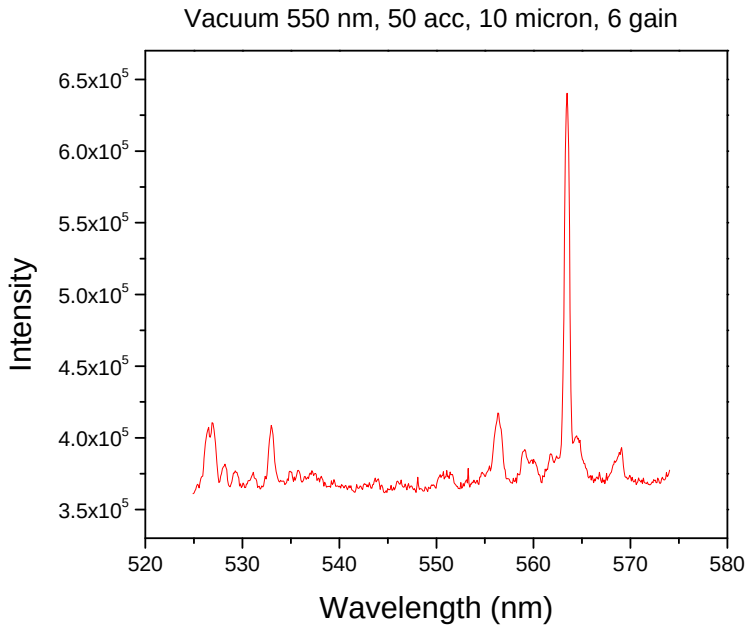

Figure B.19: Collected spectra centered at 550 nm at vacuum conditions.

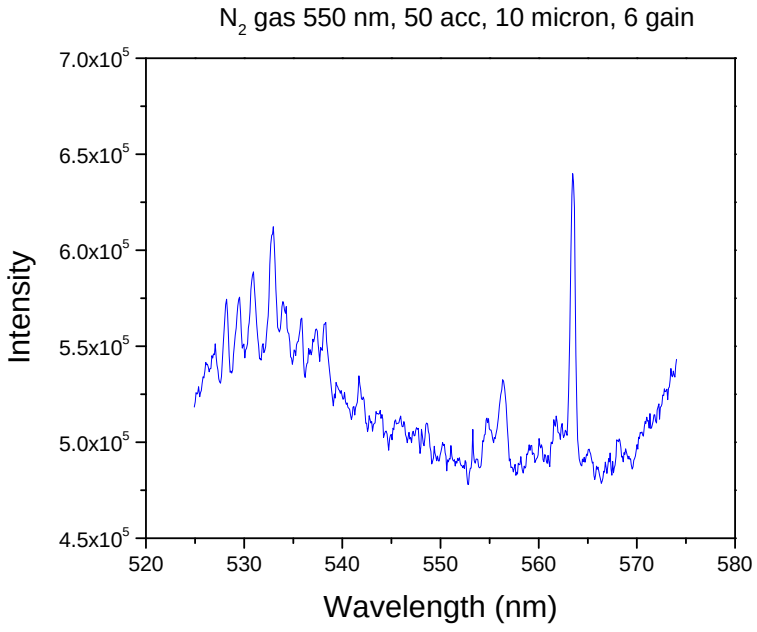

Figure B.20: Collected spectra centered at 550 nm at 50 mTorr N_2 gas.

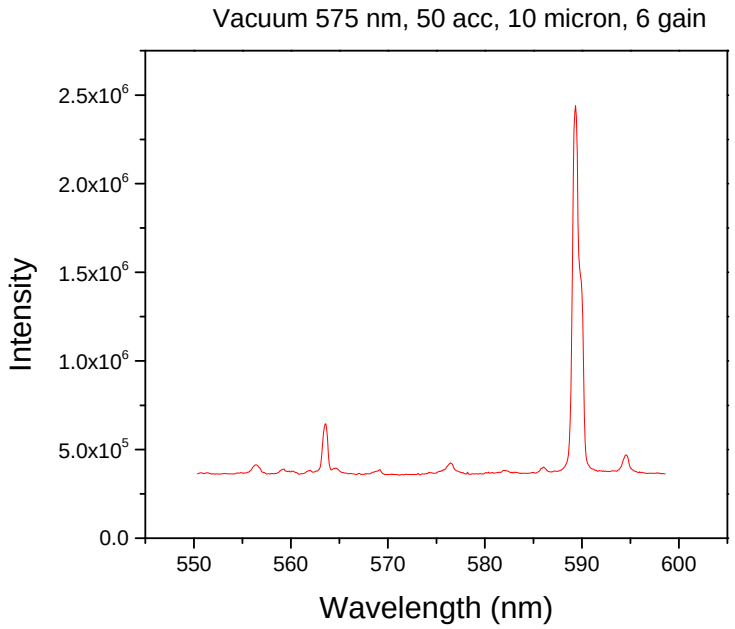

Figure B.21: Collected spectra centered at 575 nm at vacuum conditions.

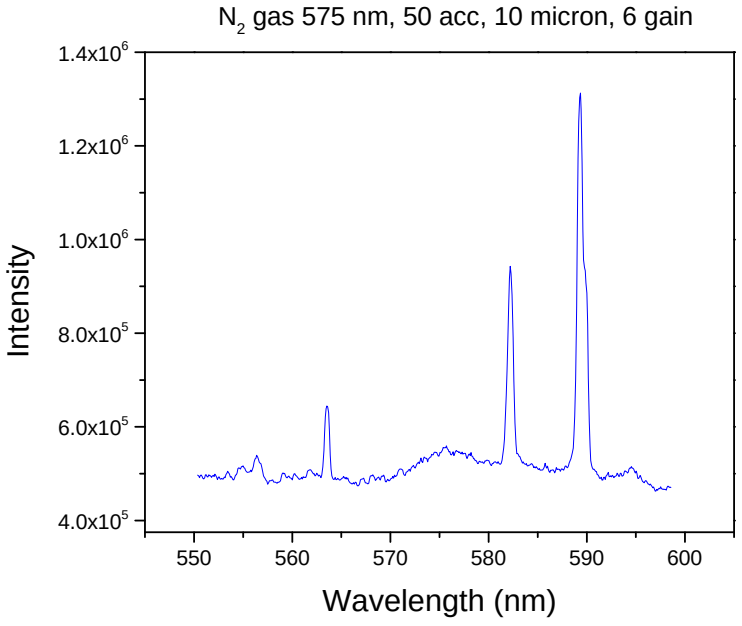

Figure B.22: Collected spectra centered at 575 nm at 50 mTorr N_2 gas.

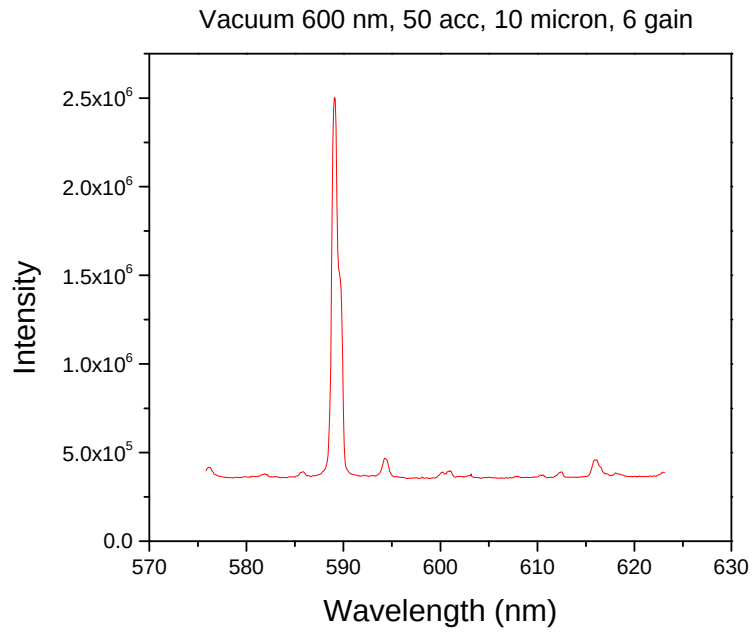

Figure B.23: Collected spectra centered at 600 nm at vacuum conditions.

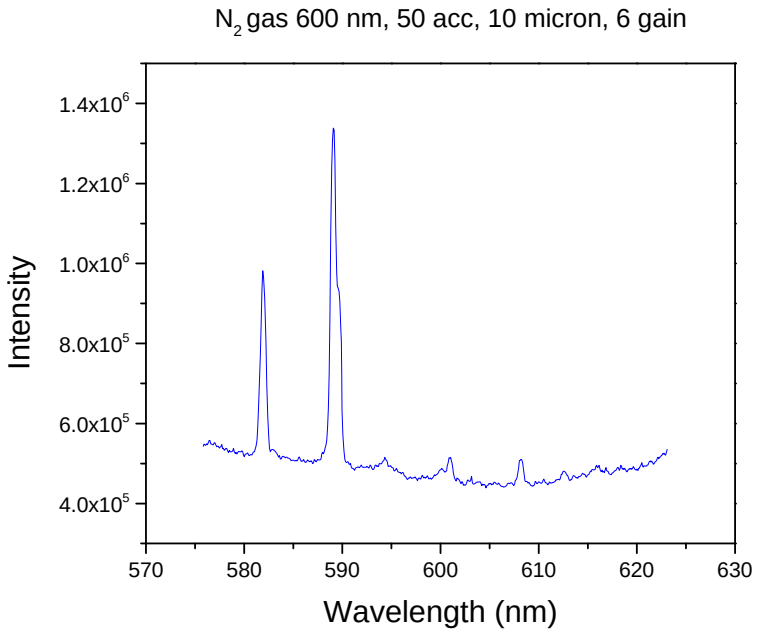

Figure B.24: Collected spectra centered at 600 nm at 50 mTorr N_2 gas.

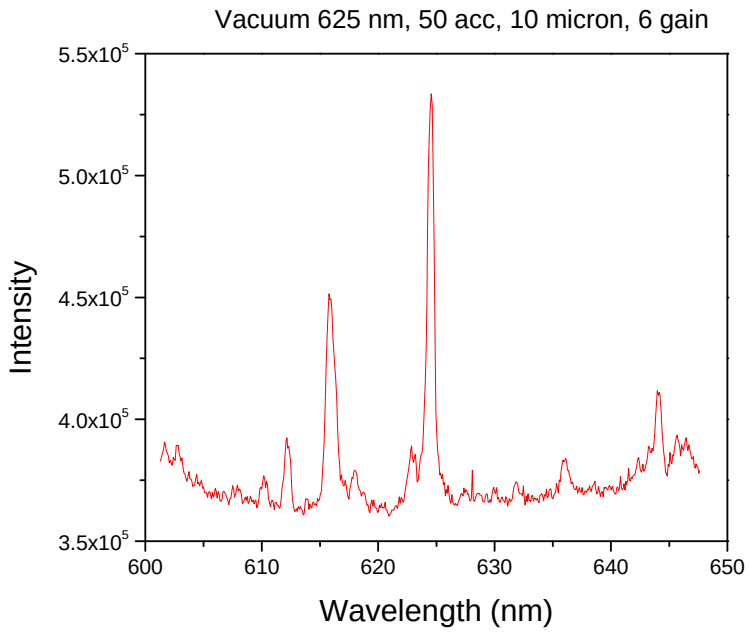

Figure B.25: Collected spectra centered at 625 nm at vacuum conditions.

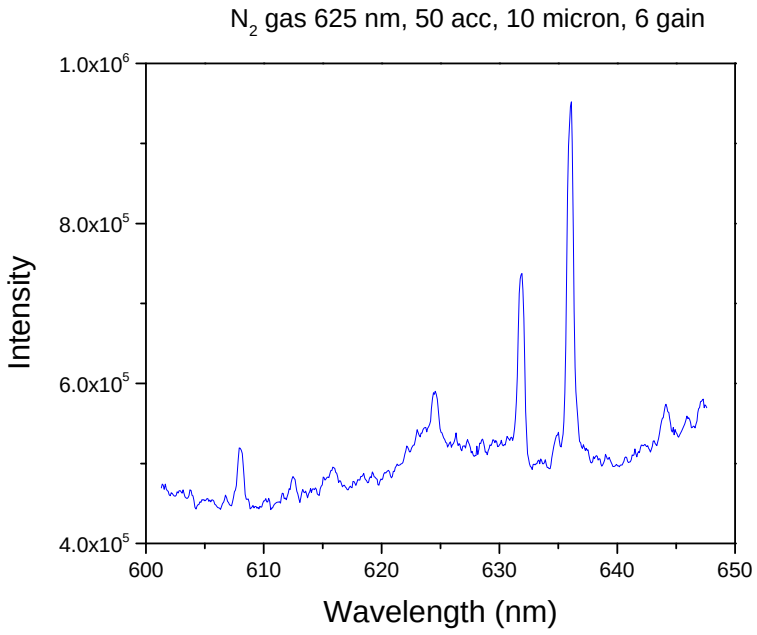

Figure B.26: Collected spectra centered at 625 nm at 50 mTorr N_2 gas.

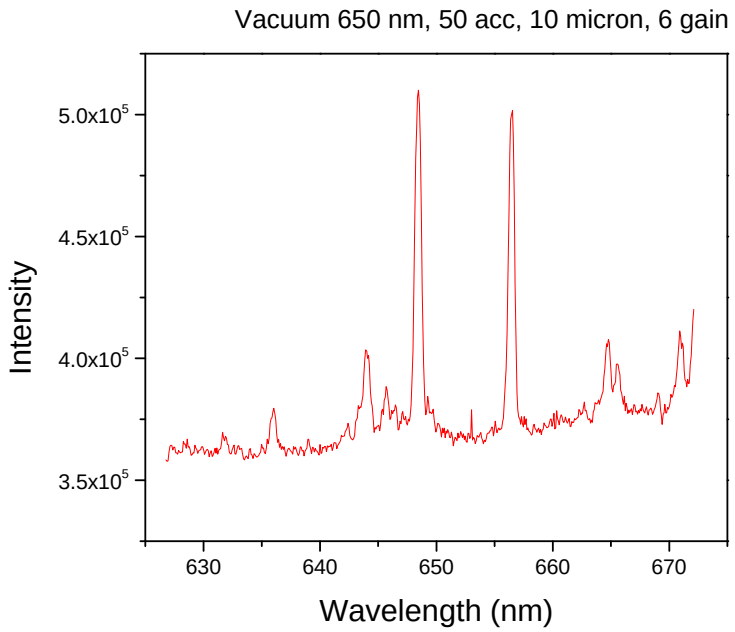

Figure B.27: Collected spectra centered at 650 nm at vacuum conditions.

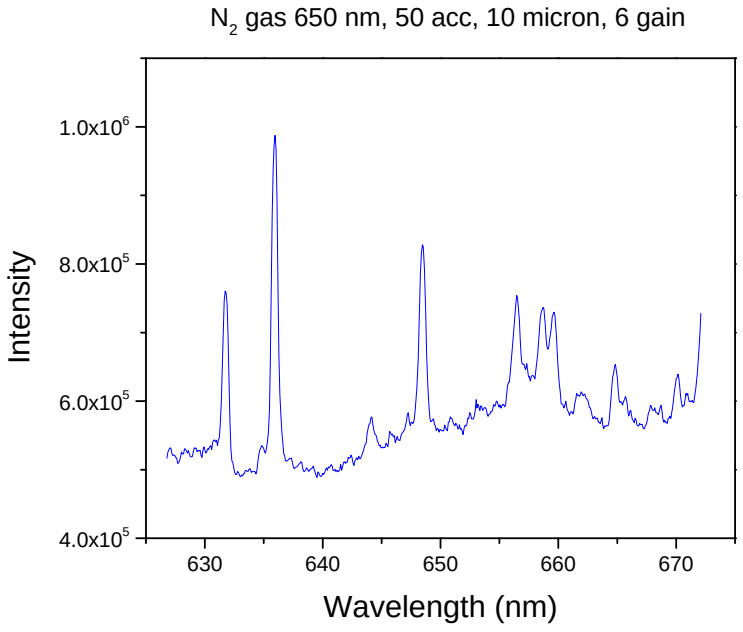

Figure B.28: Collected spectra centered at 650 nm at 50 mTorr N_2 gas.

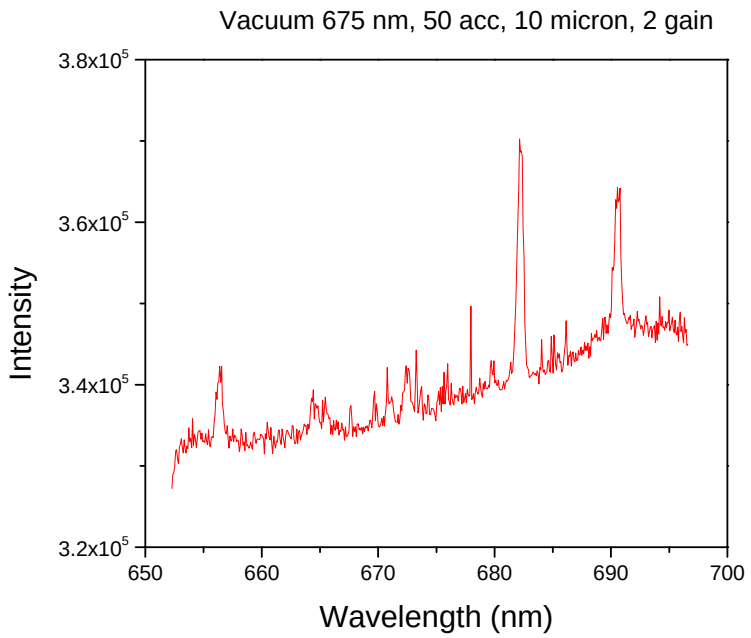

Figure B.29: Collected spectra centered at 675 nm at vacuum conditions.

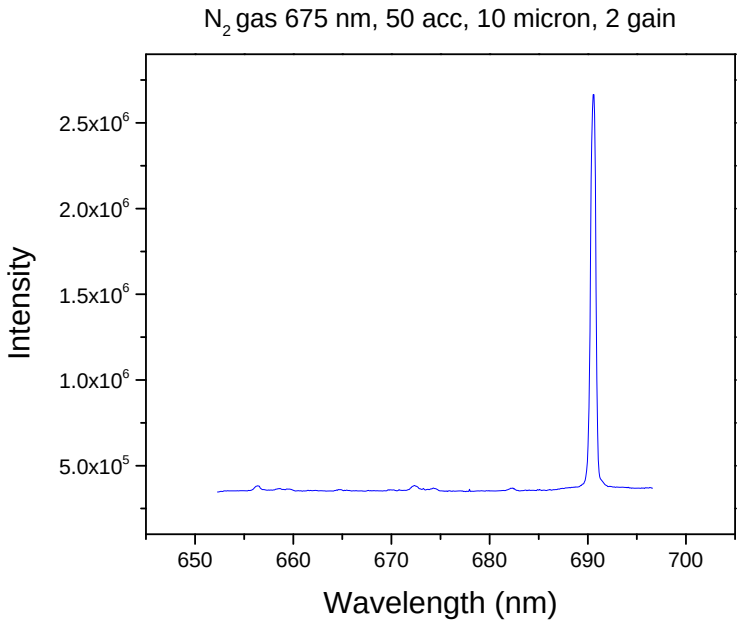

Figure B.30: Collected spectra centered at 675 nm at 50 mTorr N_2 gas.

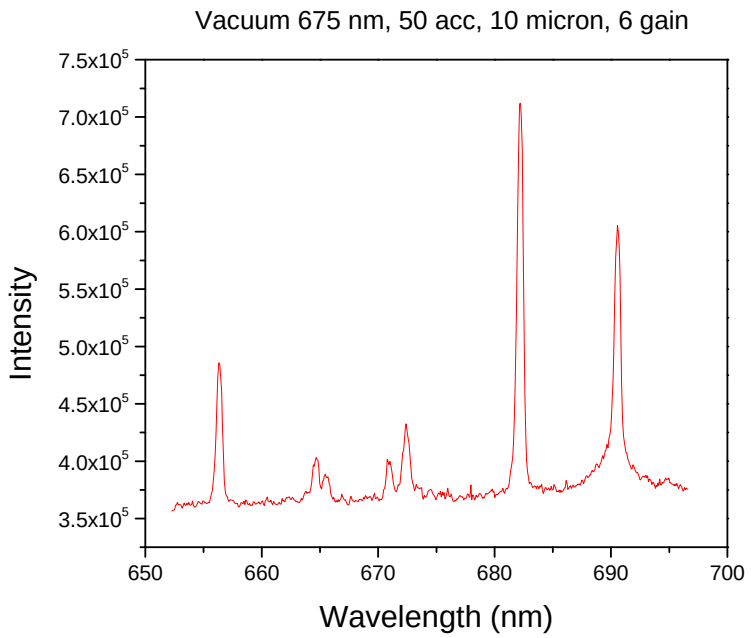

Figure B.31: Collected spectra centered at 675 nm at vacuum conditions (high resolution).

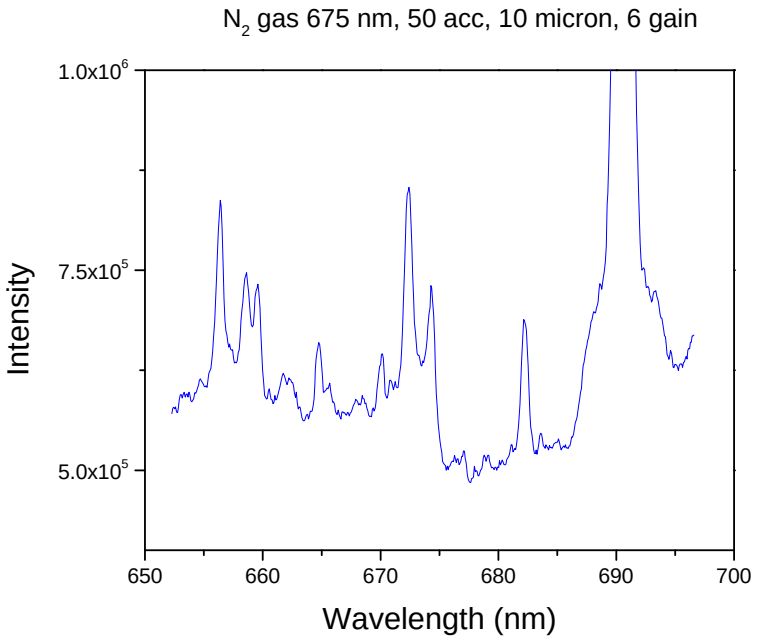

Figure B.32: Collected spectra centered at 675 nm at 50 mTorr N_2 gas (high resolution).

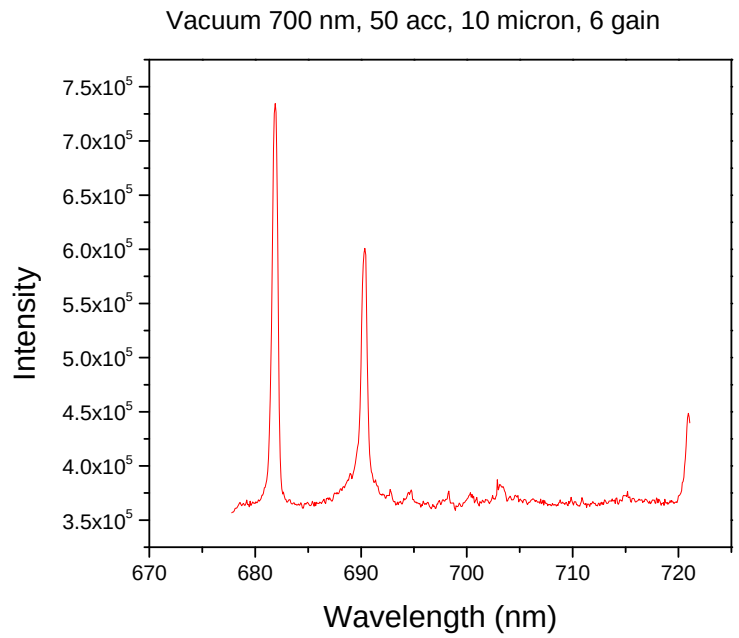

Figure B.33: Collected spectra centered at 700 nm at vacuum conditions.

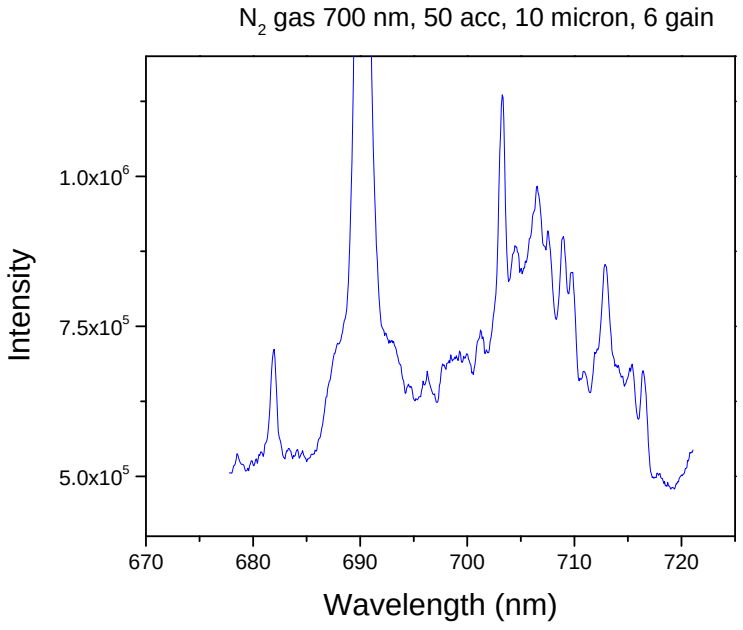

Figure B.34: Collected spectra centered at 700 nm at 50 mTorr N_2 gas.

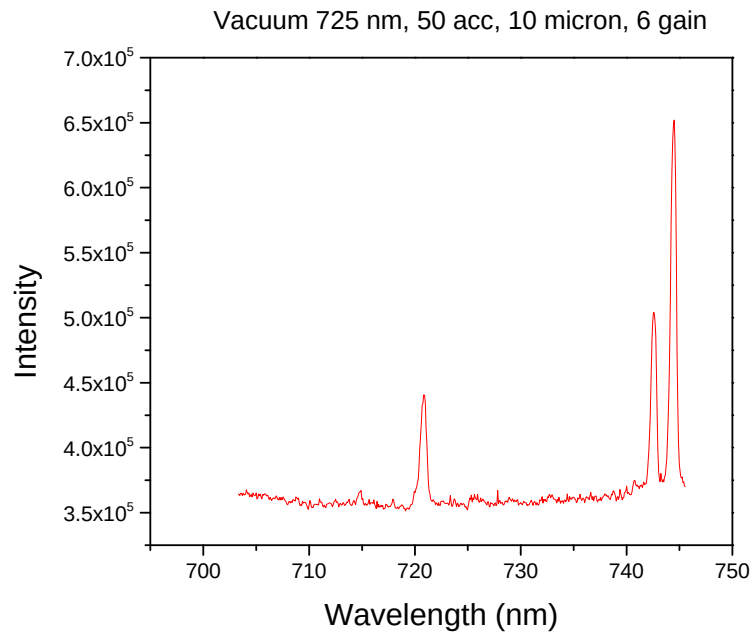

Figure B.35: Collected spectra centered at 725 nm at vacuum conditions.

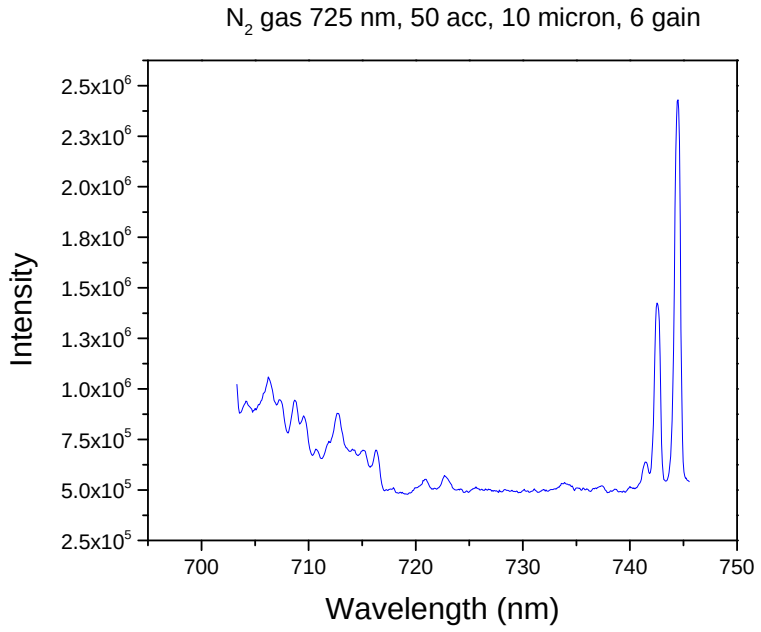

Figure B.36: Collected spectra centered at 725 nm at 50 mTorr N_2 gas.

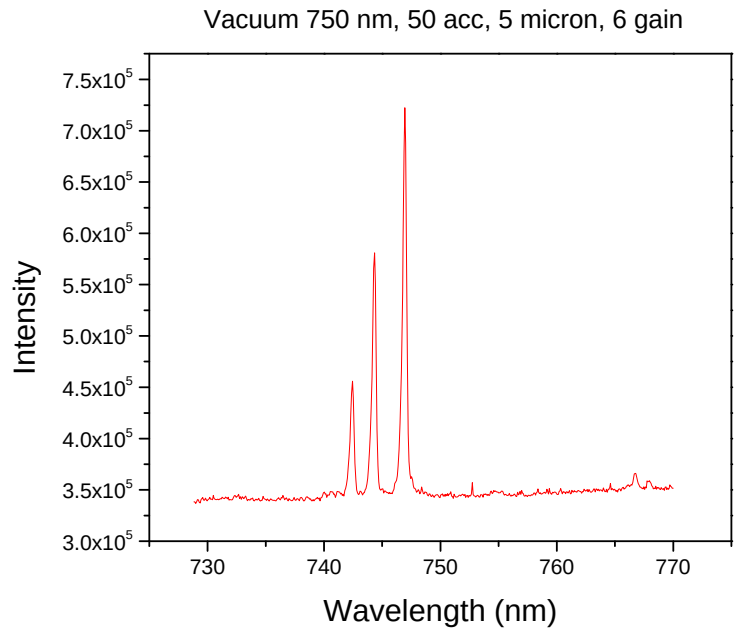

Figure B.37: Collected spectra centered at 750 nm at vacuum conditions.

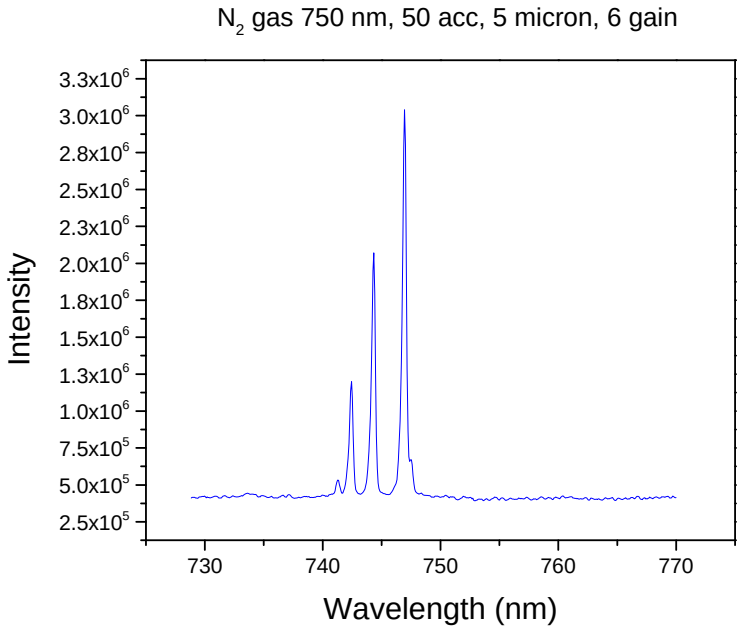

Figure B.38: Collected spectra centered at 750 nm at 50 mTorr N_2 gas.

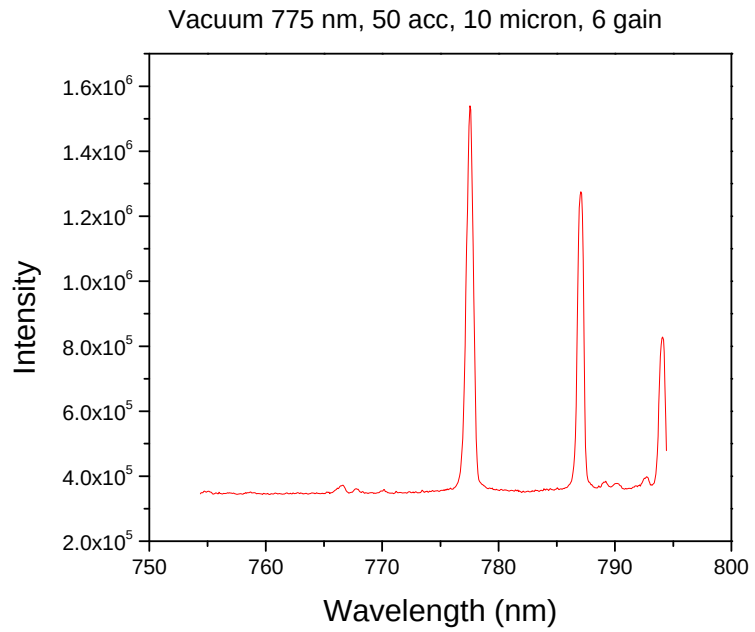

Figure B.39: Collected spectra centered at 775 nm at vacuum conditions.

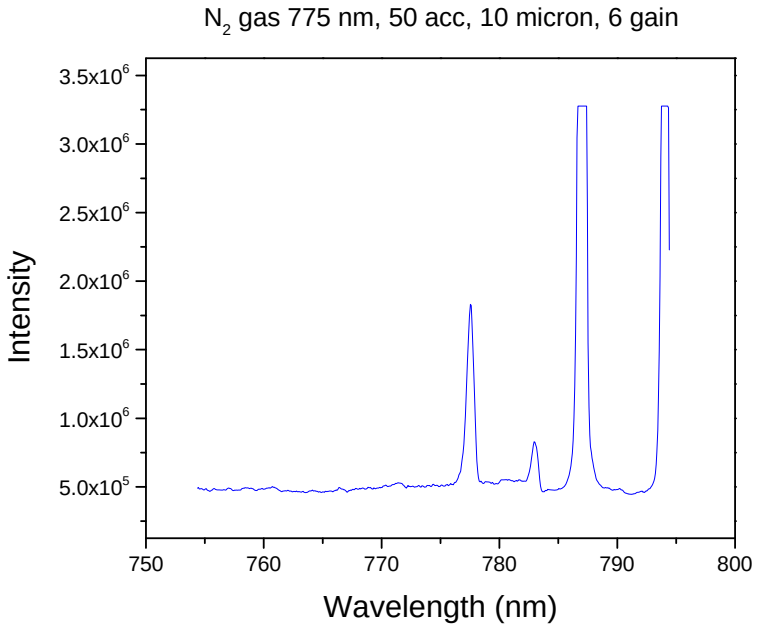

Figure B.40: Collected spectra centered at 725 nm at 50 mTorr N_2 gas.

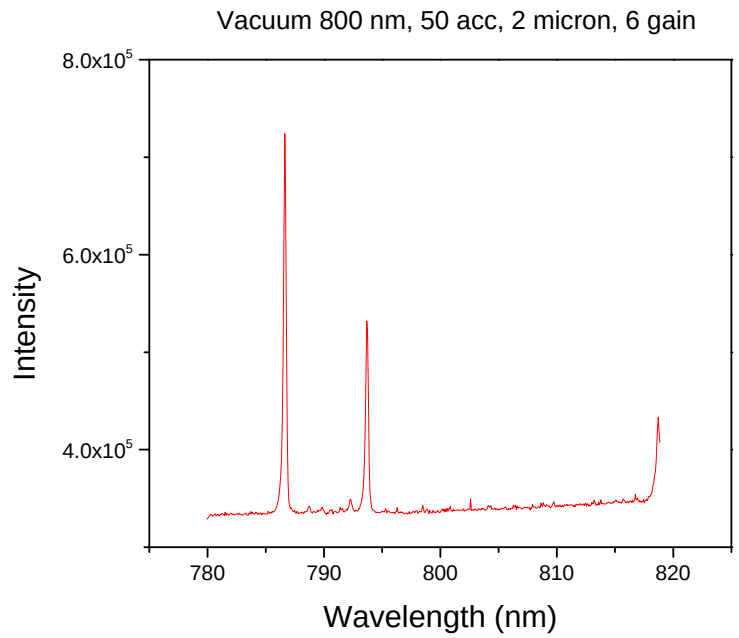

Figure B.41: Collected spectra centered at 800 nm at vacuum conditions.

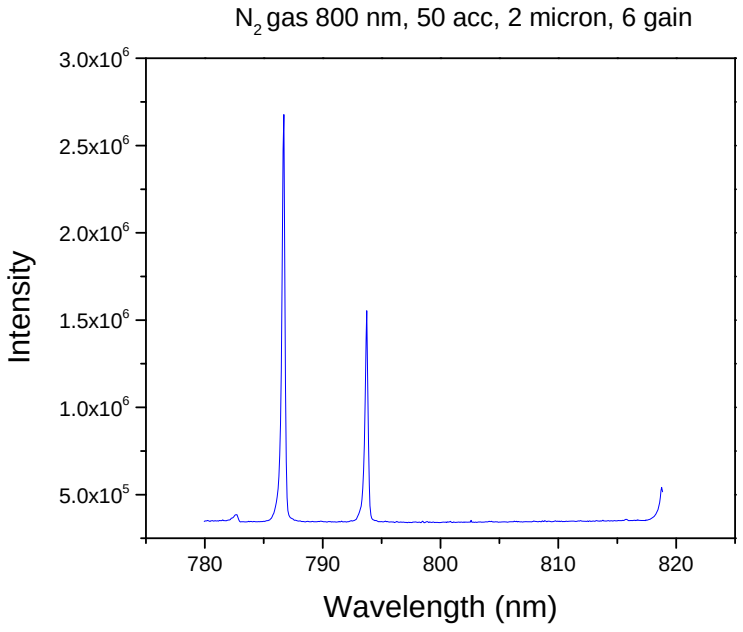

Figure B.42: Collected spectra centered at 800 nm at 50 mTorr N_2 gas.

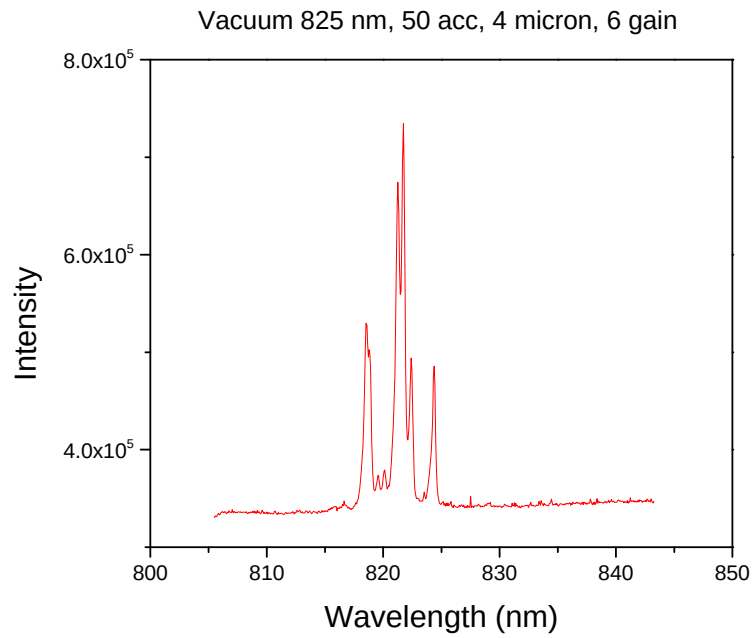

Figure B.43: Collected spectra centered at 825 nm at vacuum conditions.

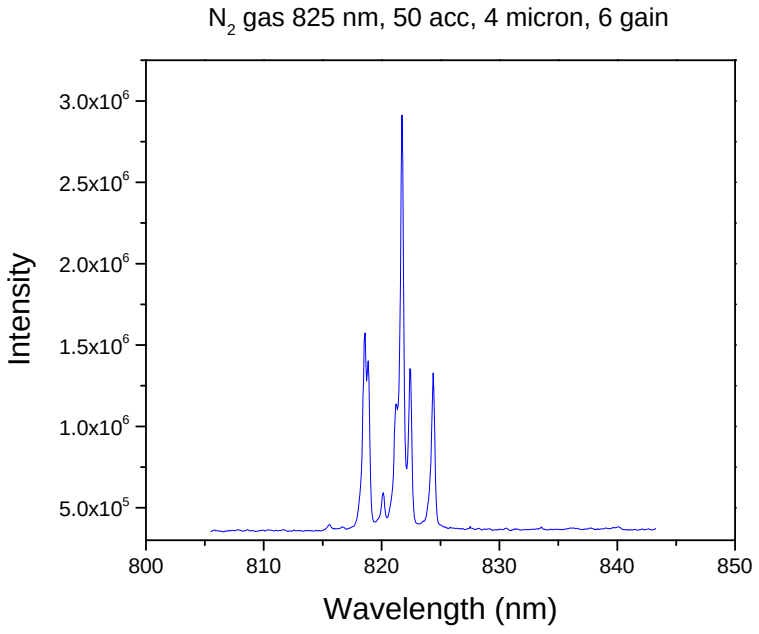

Figure B.44: Collected spectra centered at 825 nm at 50 mTorr N_2 gas.

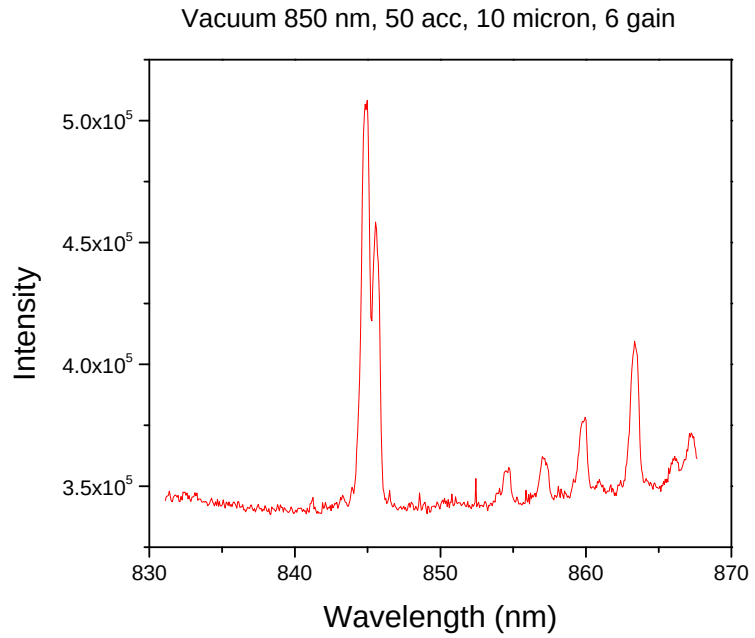

Figure B.45: Collected spectra centered at 850 nm at vacuum conditions.

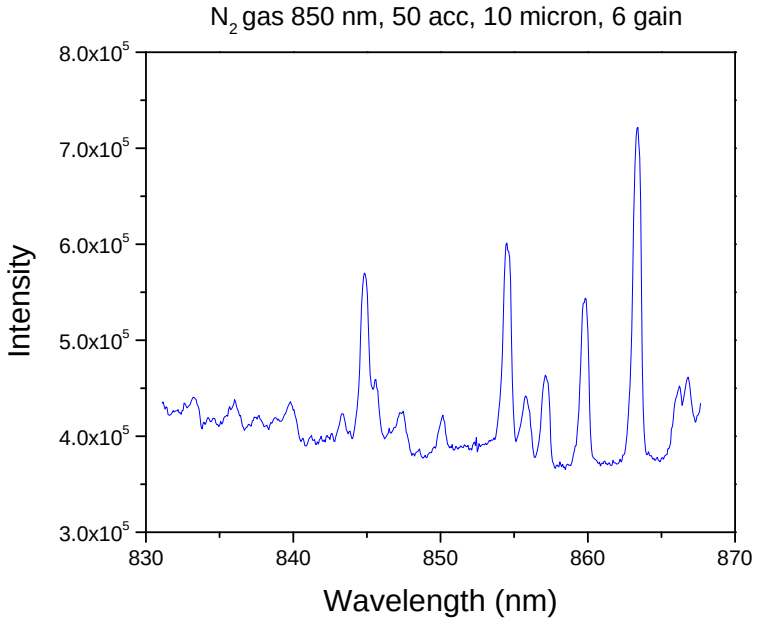

Figure B.46: Collected spectra centered at 850 nm at 50 mTorr N_2 gas.

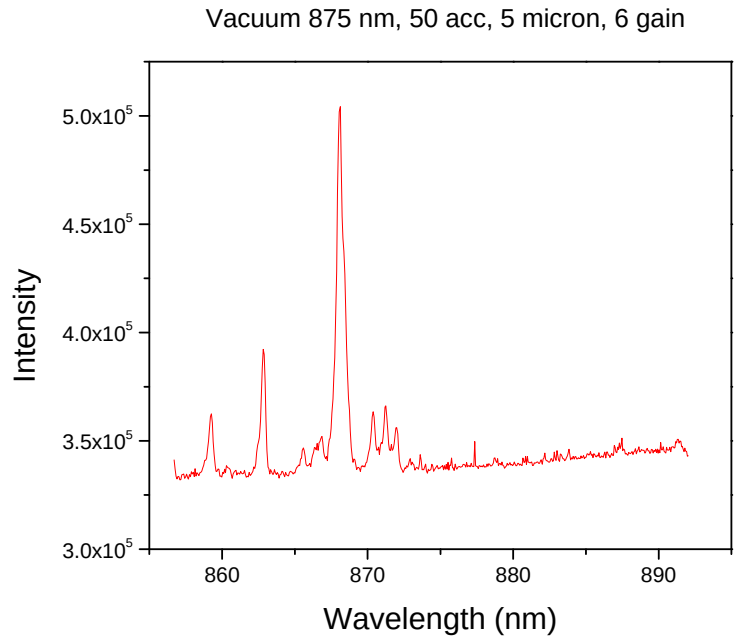

Figure B.47: Collected spectra centered at 875 nm at vacuum conditions.

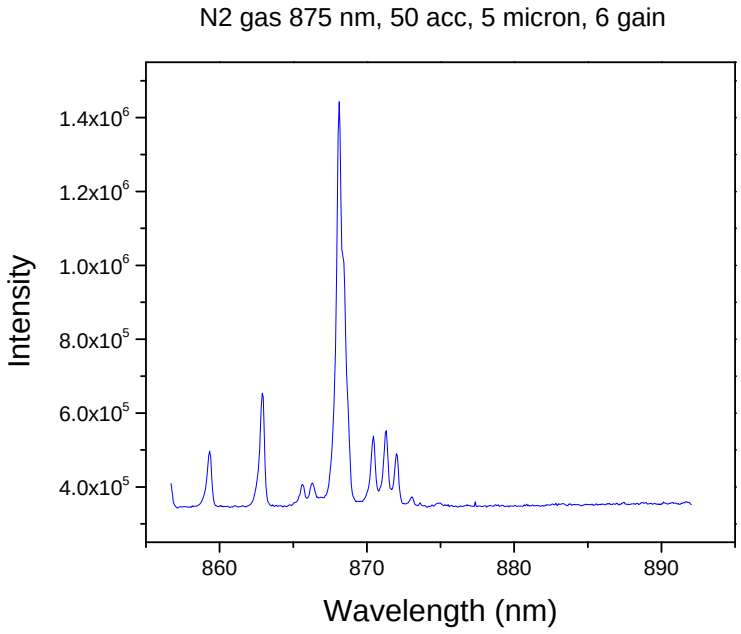

Figure B.48: Collected spectra centered at 875 nm at 50 mTorr N_2 ga.s

VITA

VITA

Nicholas Glavin was born in Dayton, OH, where he attended Archbishop Alter High School. Upon graduation, he began a college career in pursuit of his Chemical Engineering Degree from the University of Dayton while excelling as a student athlete playing for the varsity football program. He completed his degree in 2010 and continued his studies by joining the Masters of Chemical Engineering program while working as a civilian co-op student at the Air Force Research Laboratory in the Materials and Manufacturing Directorate in the Thermal Management branch. Here, he worked on multiphase flow dynamics with Dr. Fisher from Purdue University, where his interest in nanomaterials and synthesis began to take shape. He completed his Masters in 2012 and joined Dr. Fisher's group at Purdue University in pursuit of his PhD in Mechanical Engineering. Upon graduation, Nicholas will start his full time career at the Air Force Research Laboratory working in nanomaterial synthesis and growth with a special focus in flexible, high power RF electronics.

PUBLICATIONS

PUBLICATIONS

1. Nicholas R. Glavin, Michael L. Jespersen, Michael H. Check, Jianjun Hu, Al M. Hilton, Timothy S. Fisher, Andrey A. Voevodin, "Synthesis of few-layer, large area hexagonal-boron nitride by pulsed laser deposition," *Thin Solid Films*, **572**, 245, (2014).

2. Tarek Alam, Baoming Wang, Raghu Pulavarthy, MA Haque, Christopher Muratore, Nicholas R. Glavin, Ajit K. Roy, Andrey A. Voevodin, "Domain engineering of physical vapor deposited two-dimensional materials," *Applied Physics Letters*, **105**, 21, 213110 (2014).

3. Nicholas R. Glavin, Christopher Muratore, Michael L. Jespersen, Jianjun Hu, Timothy S. Fisher, Andrey A. Voevodin, "Temporally and spatially resolved plasma spectroscopy in pulsed laser deposition of ultra-thin boron nitride films," *Journal of Applied Physics* **117,** 16, (2015).

4. M. Uddin, N. Glavin, A. Singh, R. Naguy, M. Jespersen, A. Voevodin, G. Koley, "Mobility enhancement in graphene trasnsistors on low temperature pulsed laser deposited boron nitride," *Appied. Physics Letters*, **107**, 20, 203110, (2015).

5. J. DiStefano, Y. Lin, J. Robinson, N. Glavin, A. Voevodin, J. Brockman, M. Kuhn, B. French, S. King, "Band alignment at molbdenum disulphide/boron nitride/aluminum oxide interfaces," *Journal of Electronic Materials*, **45**, 2, 983-988, (2016).

6. Nicholas R. Glavin, Christopher M. Muratore, Michael L. Jespersen, Jianjun Hu, Phillip T. Hagerty, Al M. Hilton, Austin T. Blake, Christophr A. Grabowski, Michael F. Durstock, Michael E. McConney, Drew M. Hilgefort, Timothy S. Fisher, Andrey A. Voevodin, "Amorphous boron nitride: a universal, ultrathin dielectric for 2D nanoelectronics," *Advanced Functional Materials*, (2016). doi:10.1002/adfm.201505455